Sources of vibrations and their impact on the environnement

Abdul Karim Jamal Eddine

To cite this version:

Abdul Karim Jamal Eddine. Sources of vibrations and their impact on the environnement. Géotechnique. Université Paris-Est, 2017. English. NNT : 2017PESC1111 . tel-01744297

HAL Id: tel-01744297
https://theses.hal.science/tel-01744297v1

Submitted on 21 May 2018

UNIVERSITE PARIS-EST

Ecole Doctorale Sciences, Ingénierie et Environnement

Thèse de doctorat

Présentée pour l'obtention du grade de

Docteur de l'Université Paris-Est

Spécialité : Génie Civil

Par :

Abdul Karim Jamal Eddine

Sujet :

Sources vibratoires et effets sur l'environnement

Thèse soutenue le 25 Septembre 2017 devant le jury composé de :

M. Etienne Bertrand	CEREMA	Rapporteur
Mme Gaëlle Lefeuve-Mesgouez	Université d'Avignon	Rapporteure
M. Emmanuel Chaljub	ISTerre	Examinateur
M. Cyrille Fauchard	CEREMA	Président du jury
M. Jean-François Semblat	IFSTTAR	Directeur de thèse
M. Luca Lenti	IFSTTAR	Co-Directeur de thèse

Acknowledgments

First and foremost I thank the Lord Almighty who inspired patience to finish this work and for his continuous guidance in my life.

I am ever indebted to my family for their continuous support and patience during my studies.

I would like to thank the thesis director Mr. Jean-Francois Semblat for welcoming me in the lab and for the good advices that made this work better. Thanks are also extended to Mr. Luca Lenti for his supervision of the thesis. I would like to express my sincere gratitude to Mrs. Gaëlle Lefeuve-Mesgouez and Mr. Etienne Bertrand for taking the time to review this work and provide helpful feedback. I would like to thank Mr. Cyrille Fauchard for presiding over the examination jury and for his useful advices regarding the manuscript. Thanks to Mr. Emmanuel Chaljub for accepting to examine my work and for the interesting discussions and ideas.

Sincere thanks go to Mr. Hazem Khaled for the interesting discussions regarding artificial intelligence and his very good advices regarding the neural networks code. The ANN work wouldn't be accomplished without him.

Special thanks go to Mr. Youssef Abboud, my officemate for three years, a good friend at all levels.

I would like to thank all the friends I have met during this thesis inside and outside the workplace whether they are researchers, technicians or students. These thanks are especially extended to the lab’s secretary Mrs. Jeannine Leroy and my shifting officemates Rym, Chiara and Gisela.

Abstract

Ground vibration is an increasingly important environmental problem. This study investigates multiple aspects of ground vibration. Local site conditions and the related amplification of seismic waves represent a widely studied topic in seismology and earthquake engineering. While most of the studies are dedicated to engineering seismology and earthquake engineering, similar approaches for soil classification and site amplification have not been yet fully established in the field of urban vibrations.

First an improvement strategy for absorbing layer method was developed in order to enhance precision of the FEM models. The design of simple absorbing layers in FEM through the nullification of the real part of reflected waves in the complex number domain proved to be efficient when coupled with the stiffness reduction of the absorbing layer. Excessive reduction of the stiffness along with the excessive increase of the stiffness factor in the attenuation matrix enabled a large reduction in the size of the absorbing layer and therefore the design of an inexpensive absorbing layer.

Afterwards an important part of the work was dedicated to the derivation of a new set of parameters of the velocity-gradient type that controls the vibration transfer through multilayered soil. The absence of a well-structured comprehensive approach for prediction and site classification for vibration problems leaves the problem broad and complicated. Different sites with different mechanical and geometrical properties were examined using FEM and their surface response was studied. Sites responses were formulated in simple time domain and spectral approaches. The newly derived proxies along with the spectral laws serve as a classification mean for multilayered soils in the vibration problem and may even be used for design purposes.

An artificial intelligence tool for predicting soil response using the previously derived proxies coupled with the geometrical properties of the surface layer was later developed. The neural networks tool was used to analyze the parametric effects of the velocity-gradient proxies versus that of the surface layer's depth. Important conclusions were derived from the analysis regarding the mechanical and geometrical properties of multiple layers and their varying effects with distance from the source.

Finally multiple sources recordings were studied through comparing them with the spectral responses of different sites defined in the previous sections. The rate of matching between the spectral content of a particular source and a given site serves as a mean to assess the vibration hazard caused by this source to the corresponding site. The vibration hazard assessment leads to a classification link between sources in one hand and sites characterized by velocity-gradient proxies on the other hand.

Résumé étendu

Contexte

Cette thèse porte sur la prédiction des vibrations et leurs effets sur l'environnement, en particulier sur les sols. Cette problématique est de plus en plus intéressante dans le domaine du génie civil, à cause de la croissance rapide des méthodes de transport et de construction. En effet, des nuisances croissantes au voisinage d'une source sont associées avec un grand niveau des vibrations ; et l'absence d'un cadre cohérent pour la prédiction des vibrations dans les sols et d'une classification des sites représente un problème à résoudre pour arriver à une prédiction fiable de leurs effets.

Ce travail avait donc plusieurs objectifs en se basant sur des travaux antérieurs. D'une part, une stratégie d'absorption des ondes a été mise en place dans les modèles par éléments finis établis et étudiés. Ensuite, une approche pour la prédiction des niveaux des vibrations a été présentée en adaptant des paramètres issus de la sismologie. Cette nouvelle approche sera utilisée pour analyser les différentes sources et pour développer un outil de prédiction.

Améliorations des méthodes de couches absorbantes

L'objectif de cette partie est de développer une stratégie de calibration pour des couches absorbantes aux bords du domaine, afin d'atténuer le plus possible les réflexions parasites. Cette stratégie reste simple d'application et permet un abaissement du coût de calcul. La réflexion des ondes sur les frontières, due au contraste des propriétés entre le domaine physique et la couche absorbante, est traitée avec l'approche de réduction de la rigidité suggérée précédemment dans la littérature. L'annulation de la partie réelle des ondes réfléchies dans le domaine du nombre d'onde complexe ainsi que la réduction de la rigidité s'est avérée être une combinaison très efficace. Ces hypothèses ont été étudiées à l'aide d'une formulation de type Rayleigh pour l'amortissement d'un modèle rhéologique (modèles généralisés de Maxwell) aux éléments finis. Des études paramétriques concernant l'effet de plusieurs facteurs influençant l'atténuation ont été menées conduisant à la meilleure procédure de calibration.

Lois de propagation et classification des sites

Les conditions locales du site et l'amplification des ondes sismiques constituent un sujet largement étudié en sismologie et en génie parasismique. Les amplifications/effets du site sont directement dépendantes de l'impédance du matériau et/ou des irrégularités géométriques. Afin de quantifier les effets de site et donc classifier les différents sols, de multiples approches et divers paramètres sont suggérés dans la littérature. Dans la littérature et remarquablement dans l'EC8 (Eurocode pour le domaine sismique), des paramètres comme Vs_{30} sont adaptés pour la classification des sites vis-à-vis des séismes. Néanmoins, d'autres facteurs tels que la fréquence fondamentale f_0 et les gradients de vitesses peuvent être utilisés pour plus de précisions dans le problème de classification. Les paramètres de type gradient de vitesse constituent un très bon outil pour la classification des sites dans le contexte des problèmes des vibrations. Deux paramètres principaux ont été adoptés, Vs_3 et B_{10}, qui décrivent respectivement les propriétés de la couche superficielle et le changement d'impédance avec la profondeur. Il a été conclu que les sites avec des gradients plus grands sont plus vulnérables aux fréquences plus élevées et vice versa. La réponse de différents sites dépend fortement de la distance de la source. Des formulations simples dans le domaine temporel et des graphiques de réponses spectrales sont fournis et peuvent être utilisés à des fins de conception.

Prédiction des vibrations par réseaux de neurones

Le paramètre de gradient-B_{10} est influencé par deux facteurs, la profondeur et le contraste des propriétés mécaniques. Un contraste fort à une grande profondeur et un contraste faible à une petite profondeur peuvent donner une valeur de ce gradient très similaire. Bien que l'effet des couches profondes dans le sol soit très important, la première couche joue un rôle critique dans la détermination de la réponse en fréquences et pour les niveaux d'amplitudes. Afin de surmonter un tel problème, l'ajout d'un facteur h_1 décrivant la profondeur de la première couche aidera à affiner le processus de prédiction. Un facteur de profondeur est capable de séparer les effets de la profondeur et du contraste dans le gradient B_{10}. Un outil de prédiction utilisant des réseaux de neurones est suggéré. La flexibilité, le coût et la vitesse de résolution l'ont rendu plus adapté pour un grand nombre d'analyses en comparaison avec les simulations par éléments finis. L'outil a permis une analyse plus approfondie du problème et des conclusions importantes ont été tirées. L'effet des propriétés géométriques de la première couche s'est révélé être important avec des gradients. La profondeur de la première couche de surface et le gradient conduisent à des effets différents en fonction de la vitesse d'onde Vs et de la distance à la source.

Classification des sources et des sites

Dans cette partie, les enregistrements des vibrations provenant des sources d'infrastructure seront utilisés ainsi que les résultats numériques pour établir un lien de classification entre les sources et les sites. La correspondance entre les propriétés spectrales des sources et celles d'un site donné exprimées pour ces dernières par la fonction de transfert facilitera l'évaluation de l'aléa dans un site. Les données enregistrées provenaient principalement de quatre types de sources: battage, vibro-fonçage, circulation des poids lourds et circulation des trains. En utilisant les paramètres de gradient de vitesse, les propriétés spectrales des enregistrements, des sources multiples ont été déterminées. Une classification de l'aléa dans un site en considérant une source donnée est proposée.

Conclusions

Pour la conception de couches absorbantes simples dans les modèles numériques, l'annulation de la partie réelle des ondes réfléchies dans le domaine du nombre d'onde complexe et la réduction de la rigidité des matériaux dans les couches absorbantes sont apparus comme des facteurs clés. Réduire fortement la rigidité et augmenter fortement le facteur C_k permet une grande réduction de la taille de la couche absorbante. Les paramètres de gradient de vitesse se sont avérés être un très bon outil pour la classification des sites dans le contexte des problèmes de vibrations. Des formulations simples dans le domaine temporel et spectrales établissent une base de normalisation pour les problèmes de conception. L'outil de prédiction par réseaux de neurones a permis une analyse plus approfondie des réponses des sites. L'effet des propriétés géométriques de la première couche s'est avéré important vis-à-vis des effets des gradients. En utilisant les paramètres de gradient de vitesse, les propriétés spectrales des enregistrements de sources multiples ont été évaluées. Une classification des sources et des sites du point de vue de l'aggravation du niveau de vibrations est fournie.

Perspectives

D'autres études plus approfondies permettant une interprétation physique d'une plus grande efficacité des couches absorbantes plus fines avec l'approche de calibration actuelle sont jugées nécessaires. L'établissement d'une formulation cohérente devrait être envisagé afin de calibrer les couches absorbantes en tenant compte des différents matériaux, du niveau de réduction de la rigidité, des fréquences et des facteurs d'amortissement de Rayleigh. En ce qui concerne la réponse spectrale des sols, une campagne expérimentale est nécessaire pour compléter les simulations numériques et mieux évaluer les paramètres proposés. Il est impératif d'évaluer les fonctions de transfert en fonction de nouvelles définitions des multiples champs sur des segments de longueur inférieure à 20 mètres. Une analyse sur la possibilité d'adapter des paramètres de gradient plus flexibles en fonction des propriétés des sites peu profonds est recommandée. Les gradients comme, B_7 ou B_5, par exemple peuvent présenter une bonne efficacité dans certains cas de sols faibles. Certaines sources importantes sont des sources souterraines comme les tunnels ferroviaires par exemple. La réponse des sols sous excitation issue de sources souterrains peut être différente de celle due à des sources de surface. En ce qui concerne la classification des sources et des sites, le facteur d'aggravation suggéré devrait être étudié plus en profondeur. Une approche de la quantification du risque de résonance et des amplifications dans les sols en fonction du taux de concordance entre la source et les propriétés du site devrait être formulée. La connexion des résultats de ce travail aux effets sur les structures n'a pas été étudiée dans cette thèse. Une telle analyse est fortement recommandée.

Table of Contents

1. **Introduction……………………………………………………..……………………1**
   - 1.1 Motivation and context of the research ………………………….….………....…..….2
   - 1.2 Problematic and objectives…………………………………….………………....2
   - 1.3 Outline of the dissertation……………………………………………………….3

2. **State of the Art…………………………………………………………………...5**
   - 2.1 Introduction ...…………………..…………………………………………………6
   - 2.2 Impact of ground vibration……….……………………………………..………6
   - 2.3 Sources of ground vibration……...…………………………………………………7
   - 2.4 Attenuation of ground vibration.……………………………………………......10
   - 2.5 Simulating ground vibration……..……………………………………………..13
     - 2.5.1 Mechanical idealization……..……………………………….....……….13
     - 2.5.2 Analytical approaches……..……………………………………………15
     - 2.5.3 Numerical approaches……..………………………………...…………..16
   - 2.6 References……………………………………………………..…….………21

3. **FEM Modeling Methodology Development…………………………………...…….35**
   - 3.1 Introduction……………………………………………………………………..36
   - 3.2 Key assumptions for FEM models …..……………………………………………37
   - 3.3 Absorbing layer methods for vibrations propagation...….………………………...38
   - 3.4 Improving Rayleigh-based absorbing layers methods…………………………..…40
     - 3.4.1 Stiffness reduction in absorbing layers…………….………………………40
     - 3.4.2 Mathematical formulation of attenuation…………………………….…41
     - 3.4.3 Influence of pertinent parameters on the absorbing layer efficiency………...46
       - 3.4.3.1 Effect of density (ρ)……….……...……………………………………..46
       - 3.4.3.2 Effect of modulus of elasticity (E)……….…………………………..….48
       - 3.4.3.3 Effect C_M and C_K interrelation…………………………………………...50
       - 3.4.3.4 Effect of layer size……..….……………………………………………...55
     - 3.4.4 Sensitivity to different materials………...…………………………….…58
     - 3.4.5 Sensitivity to frequency content………….……………………….………59
     - 3.4.6 Absorbing Layers for 2D-models……………..……………………………59
   - 3.5 Validation of the modelling considering a canonical problem………….…………62
   - 3.6 Conclusions and recommendations……………………...………………………...63
   - 3.7 References………………………………………………………………………....65

4. **Vibration Attenuation and Amplification in Soils……68**
    4.1 Introduction……69
    4.2 Velocity-Gradient proxies suggestion……70
    4.3 Testing program for the analysis of different sites……72
    4.4 Simple laws of attenuation and amplification in time domain……74
    4.5 Spectral approach……82
        4.5.1 Adopted procedure……82
        4.5.2 Near field response……84
        4.5.3 Mid-field response……86
        4.5.4 Far-field response……89
    4.6 H/V spectral ratios from numerical results……92
    4.7 Conclusions……95
    4.8 References……95

5. **Analysis of Vibration in Soils through Artificial Neural Networks……98**
    5.1 Introduction……99
    5.2 Theoretical background and model architecture……100
    5.3 Assessment and validation of the neural network……105
    5.4 Effects of B_{10} and h_1……107
        5.4.1 Effects of B_{10} and $h_1$in the near field……109
        5.4.2 Effects of B_{10} and $h_1$in the mid field……109
        5.4.3 Effects of B_{10} and $h_1$in the far field……111
    5.5 References……112

6. **Classification of Sources and Sites……113**
    6.1 Introduction……114
    6.2 Spectral matching of sources and sites……114
    6.3 Sites classification by source……116
        6.3.1 Pile driving……116
        6.3.2 Vibro-driving……118
        6.3.3 Trucks traffic……121
        6.3.4 Railways……122
    6.4 Refinement method for spectral matching of sources and sites……124
    6.5 Conclusion and recommendation……126
    6.6 References……127

7. **Conclusions and Recommendations……129**
    7.1 Conclusion……130
    7.2 Recommendations for Future Works……130

Appendices

A. 3D SPECTRAL MAPS FOR VIBRATION PROPAGATION…..…..…...….…….…..……133
B. H/V INVESTIGATION EXAMPLES IN 3D……….…..……..…………………....……..146
C. NEURAL NETWORKS RESULTS……………..……....……..………………………..…….148
D. SOURCE-SITE CLASSIFICATION CURVES USING σ'……………………………...166

Chapter 1

Introduction

The aim of this chapter is to discuss the reasons motivating this research, to lay the problematic and objectives of the work, and to set up a brief outline of the following chapters.

1.1 Motivation and context of the research

This work investigates vibrations and their effects on the environment, mainly in soils. The transmission of vibration in urban areas is a rapidly rising issue and its study is gaining an increasing importance from an engineering point of view.

The quick development of the transportation infrastructures and of the construction works is associated with an increase of complaints from the population concerning vibrations. While sleep disturbance and noise annoyance are the main complaints, effects on livestock and wildlife are also reported. This thesis falls within the research program “VIBREN”, resulting from the collaboration between two French national institutes IFSTTAR and CEREMA and which deals specifically with the problem of vibration: in terms of the characterization of sources, observation of effects and mitigation.

1.2 Problematic and objectives

The scope of this thesis is to establish a coherent framework for a prediction of vibrations induced by the use of infrastructures. Unlike earthquake engineering, the absence of a well-structured approach to predict the transfer through the soil of the ground-borne vibration leaves the prediction problem largely broad and complicated. The thesis focuses on the propagation of vibrations in soils in the most problematic range of frequency (0 to 120 Hz).

The first objective is to produce precise finite element models that can simulate the response of real soils under vibrations. The precision of FEM models is associated with the implementation of absorbing layers in order to simulate an infinite space. Improvement for existing absorbing layer methods is one of the aims of the present work.

The main objective of this thesis is to derive a set of parameters that would help in the prediction of vibration induced by the use of infrastructures through a better comprehension and consideration of the attenuation and amplification features of the waves propagation in soils. Another objective will be a tentative classification of sites with respect to vibrations depending on their susceptibility to a certain range of frequencies and therefore certain kinds of sources.

A deeper analysis of the sites responses to vibration depending on their material and geometrical properties is of a particular importance for a reliable prediction of ground vibration. Performing such analysis through an accelerated method is envisaged.

1.3 Outline of the dissertation

This work comprises seven chapters. Chapter 2 reviews the state of the art of ground borne vibration. It focuses, in particular, on the impact of vibration, the main sources of vibration, attenuation laws and modelling approaches.

Chapter 3 deals with the methodology of simulating vibrations in soil. The development of FEM model is discussed through the definition of the various materials, of the surface sources and absorbing layer conditions. The part on the absorbing layers is detailed to include the development of an improvement strategy for absorbing layers such as so-called CALM approaches.

Chapter 4 is dedicated to the derivation of velocity-gradient proxies that control the vibration transfer through multilayered soils. Different sites with different mechanical and geometrical properties are examined and the vibration induced at the soil surface is analyzed as function of the distance from the source. Sites responses are then considered in the time and spectral domain. The derived parameters along with the spectral laws serve as a preliminary classification mean for multilayered soils.

An artificial intelligence based tool for predicting soil response using the previously derived parameters coupled with the geometrical properties of the surface layer is developed in chapter 5. The tool is then used to analyze the parametric effects of the velocity-gradients values versus the depth of the surface layer. Important conclusions are derived from the analysis considering the mechanical and geometrical properties and their effects depending on the distance from the source.

Chapter 6 examines recordings associated to multiple sources belonging to the CEREMA database comparing them with the spectral responses of multiple sites found in chapter 4. The rate of matching between the spectral content of the particular source and the transfer function for a given site serves as a mean to assess the vibration hazard of a source to a given site. The vibration hazard assessment leads to a classification relating sources on one hand and sites characterized by velocity-gradient proxies on the other hand.

Finally, based on the work detailed in the previous chapters, general conclusions and suggestions for a further development of this research are presented in chapter 7.

Chapter 2

State of the Art

2.1 Introduction

This chapter reviews the problem of ground-borne vibration from a large perspective. The problem is discussed first in terms of the impact of ground borne vibration on humans, structures and sensitive equipment. Secondly the sources of excitation are discussed especially from a civil engineering point of view. The main discussed sources are pile driving, road traffic and trains. Then theoretical and empirical formulations for wave's attenuation in soils are reviewed. Ultimately methods for simulating wave propagation in soils are addressed in details through their mechanical idealization, analytical and numerical approaches.

2.2 Impact of ground vibration

The impact of vibration varies widely depending on the receptors. The main effects fall usually under three categories: effects on humans, effects on structures and effects on sensitive equipment.

Impacts of vibration on humans vary between the disturbance of sleep, interruption of concentration and interference with speech and communication (Öhrström, 1997). Berglund et al. (2000) considered sleep disturbance as one of the most serious effects of traffic noise. Duarte and Filho (2003) concluded that humans are sensitive to certain frequency ranges. For instance frequencies between 20 and 40 Hz are more annoying since the resonance of the human head falls in this frequency band. Between 50-100 Hz the sensitivity of humans is also important since it is the range of resonance of the chest wall and ocular globe. However the response of residents to vibration and re-radiated noise depends also on non-acoustic factors. For instance the attitude of the residents toward railways depends on the neighborhood environment and their sensitivity to noise (Knall, 1996).

Structures represent an important field of study for the impact of vibrations. Hildebrand (2001) reported that historic buildings are more vulnerable to ground borne vibration when compared to ordinary buildings. Vibrations associated to lower frequencies tend to impose larger strains on structures (BSI, 1990). Dawn and Stanworth (1979) reported that in order to excite a foundation or a building, the wavelength of the vibration in soil must be matching the dimension of the structure. Watts and Krylov (2000) noticed that the impact of vibration depends on the soil composition. Soil layering, they observed, would increase the magnitudes of vibrations due to wave reflections from stiff soils. Moreover they reported that soft soils tend to produce larger responses than strong soils. François et al. (2010) proved that differential settlement of foundations leading to structural damage could be caused by repeated dynamic excitations having low amplitudes.

The effects of vibration on sensitive equipment were discussed in details in Gordon (1999). Effects of vibration vary and can ultimately cause malfunctioning of sensitive equipment. Hao et al. (2001) concluded that ground vibrations corresponding to normal traffic conditions might impede the normal operations of sensitive equipment. Gupta et al. (2008) concluded the necessity of isolating the sensible materials from vibration after the study of metro induced vibration in physics laboratory of the University of Beijing.

2.3 Sources of ground vibration

The interest of civil engineers in ground vibration is usually related to construction works and the utilization of infrastructure. Multiple sources of induced vibration exist, characterized by different mechanisms of excitation and different effects. This section will focus on three of the most important sources of ground-induced vibration: piling, road traffic and railways.

The pile driving excitation at the head of the pile will generate stress waves inside the pile itself. A part of the energy will be dissipated ensuring the penetration of the pile in the soil, another small amount of energy will be reflected toward the pile head and the remaining will be transformed into elastic waves in the soil (Ramshaw et al., 1998). Due to the dynamic resistance, vibrations will be emitted from the part of the pile in contact with the surrounding soil, i.e. the shaft and the toe (Massarsch and Fellenius, 2008). The shaft resistance increases due to the penetration of the pile in soil, since the shaft area in contact with the surrounding soil increases. Toe resistance is equal to zero when the pile is not moving downward and varies during the driving process (Whenham, 2011).

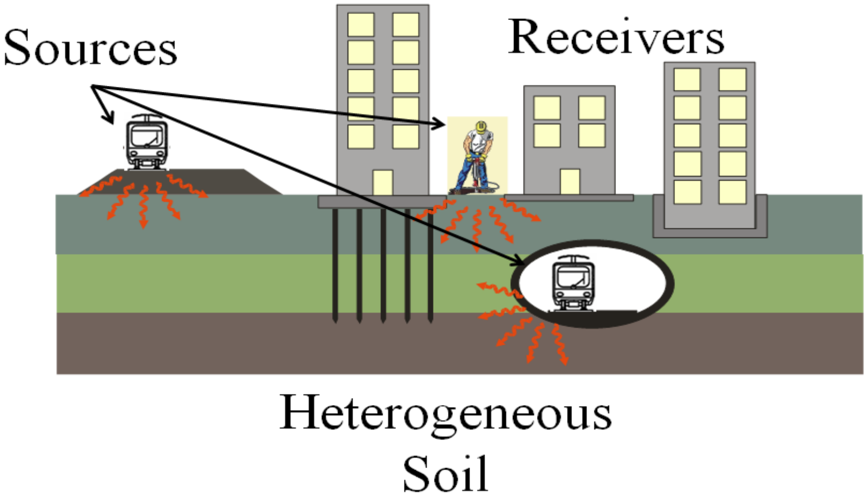

Fig. 2.1: Components of the vibration problem: the sources, receivers and the transfer media (soils).

Furthermore, soil stratification plays an important role in vibration generation. The contact of the pile with a stiffer layer in the driving process raises vibration problems (Woods, 1997). Masoumi et al. (2006) reported that in inhomogeneous soils the top layer is affected by the reflection of body waves and that the shear wave front is affected by reflected and refracted waves around the shaft. Massarsch (2004) identified three common cases during piles installation which can cause excessive vibrations, all related to soil stratification and change of impedance.

Vibrations induced by road traffic are mainly generated by heavy vehicles (Watts, 1992; Hunaidi, 2000). According to Hunaidi (2000) the predominant frequencies and amplitude of vibration from traffic sources depends on multiple factors including for instance the condition of the roads, the vehicle weight, the speed of the vehicle, the suspension system, soil type and stratification. Similar factors were discussed by Hajek et al. (2006). These factors could be interrelated: for instance the effect of vehicle speed depends on road conditions and the effect of the suspension system depends on road conditions and the vehicle speed (Hunaidi, 2000).

Excitations caused by traffic are mainly divided into static and dynamic components. The static component is due to the mass distribution of the vehicle on the axles while the dynamic component is due to pavement irregularities. Lombaert (2001) reports that when the vehicle speed is low compared to that of waves in soil, the static components contribution is negligible. Hajek et al. (2006) stated that compared to the static force, the dynamic force may be up to 50 to

80 percent higher. He further distributed the dynamic tire forces into three types: impact forces of the individual parts of the tire tread, the impact forces linked to the unsuspended mass of the vehicle and the impact forces linked to the fundamental frequency of trucks. The three types of forces simultaneously produce vibration of dominant frequencies around 10-15 Hz at highway speeds.

Railways are one of the most important sources of vibration, whether underground or surface railways. Trains generate vibration through mainly two excitation mechanisms: quasi static excitation and dynamic excitation.

The quasi-static excitation, also called wheel-passing frequency, arises due to static train load generating deflection around the wheel. The effect of this excitation mechanism is dominant close to the track and generates excitation within a range of 0-20 Hz (Jones and Block, 1996; Sheng et al., 2003). Auersch (2005) reported that for a European Intercity train having a speed of 200 Km/h, the wheel-passing frequency is in the range of 18-20 Hz.

Dynamic excitation is generated from the wheel/rail contact and excites higher frequencies when compared to quasi-static excitation (Knothe and Grassie, 1993). The dynamic excitation mechanism could be divided into the parametric excitation and general wheel/rail roughness.

Heckl et al. (1996) stated that the best known example of the parametric excitation is the sleeper passing frequency which is due to the passage of train wheels over the sleepers. Other examples for the parametric excitation are related to the variations in the mechanical properties of the soil or in the ballast stiffness. On the other hand, the passage of a train over wheel/rail roughness generates forces and creepages, such roughness irregularities are usually present because of manufacturing defects or re-grinding of the rail (Nielsen et al., 2003). For railway induced vibrations, wheel/rail roughness is considered to be the governing excitation mechanism (Thompson and Jones, 2000).

“Mach cone excitation” is one of the most hazardous excitation mechanism but also one of the less frequent. High speed trains exceeding the velocity of Rayleigh waves, usually in weak soils, cause very large amplitudes of vibration to propagate in the soil. Over a soil having a Rayleigh speed wave equal to 162 Km/h near Ledsgard in Sweden, a train speed increase from 140 km/h to 180 Km/h caused ground vibration levels to increase about ten times (Krylov et al., 2000).

Multiple studies were dedicated to the analysis and discussion of this phenomenon (Kaynia et al., 2000; Madshus and Kaynia, 2000; Paolucci et al., 2003).

2.4 Attenuation of ground vibration

Attenuation due to geometrical effects, also called attenuation by radiation, was given by different authors under different forms. Attewell and Farmer (1973) stated that surface wave's amplitude diminishes proportionally to the square root of the distance from the source. In the other hand body wave's amplitude diminishes proportionally to the distance from the source.
Woods (1968) formulated the geometrical attenuation in relation with the wave type and distance from source:

Attenuation of body waves in the near field as amplitude $A=f(1/r^2)$ (2.1)

Attenuation of body waves in the far field as amplitude $A=f(1/r)$ (2.2)

Attenuation of surface wave as amplitude $A=f(1/\sqrt{r})$ (2.3)

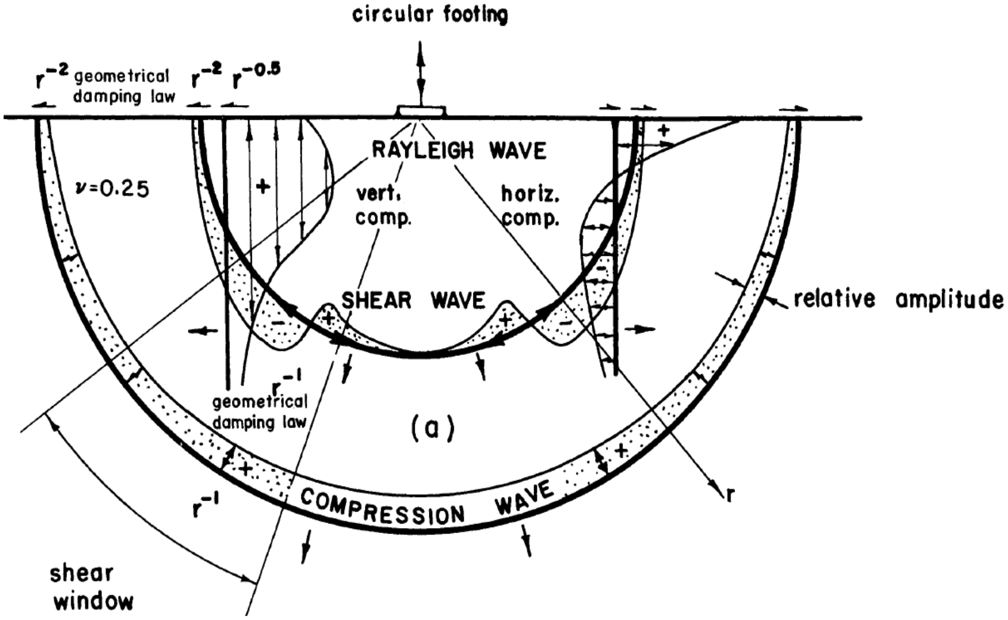

Fig. 2.2: Distribution of displacement waves from a circular footing on a homogeneous, isotropic, elastic half space (modified from Woods, 1968).

Athanasopoulos et al. (2000) described the geometrical attenuation laws as shown in equation (2.4):

$$A_2 = A_1 \left(\frac{r_1}{r_2} \right)^n \tag{2.4}$$

Where A_1 and A_2 are respectively the vibration amplitudes at distances r_1 and r_2 . The factor n depends on the source position and wave type and observation point. Table 2.1 summarizes the values of n.

Source Position	**Wave Type**	**Observation Point**	**n**
Point on surface	Rayleigh Wave	Surface	0.5
Point on surface	Body Wave	Surface	2
Point in depth	Body Wave	Surface	1
Point in depth	Body Wave	Depth	1

Table 2.1: Factor n variation for the description of the geometrical attenuation (from Amick and Gendereau, 2000).

Furthermore alongside the geometrical attenuation, material attenuation which depends on soil type and wave frequency plays an important role in the attenuation of vibration. Attewell and Farmer (1973) suggested, for a given frequency, a factor α (in m^{-1}) which combined with the geometric attenuation could be formulated as shown in equation (2.5):

$$W_r = W_0 . e^{-\alpha(r-r_0)} \tag{2.5}$$

Where W_r and W_0 are respectively the vibration energies at the distances r and r_0, where the latter is supposed to be the source location.

Woods and Jedele (1985) provided a set of values for α for frequencies of 5 and 50 Hz and for different soils with varying stiffness.

Massarsch (1995), Jongmans (1996) and Athanasopoulos et al. (2000) provided the following formulation for α:

$$\alpha = \frac{\pi . f}{Q . C} \tag{2.6}$$

Where f is the frequency, C is the wave velocity and Q the quality factor of the soil.

The theoretical formulation of Bornitz which is the most widely used formula describes the combination of both geometrical and material attenuation. The formulations along with the relevant parameters were summarized by Kim and Lee (2000) as it appears in equation (2.7):

$$A_2 = A_1 \left(\frac{r_1}{r_2} \right)^n e^{-\alpha (r_2 - r_1)} \tag{2.7}$$

Where A_1 and A_2 are the vibration amplitudes respectively at distance r_1 and r_2 from the source of vibration; n is a geometrical damping coefficient (Table 2.2); and α is the material damping coefficient defined similarly to equation (2.6).

Physical sources	**Type of source**	**Wave**	**Location**	**n**
Highway/Rail line footing array	Line	Surface	Surface	0
		Body	Surface	1
Car in pothole, Single footing	Point	Surface	Surface	0.5
		Body	Surface	2
Tunnel	Buried Line	Body	Interior	0.5
Buried explosion	Buried point	Body	Interior	1

Table 2.2: Geometrical damping coefficients (from Kim and Lee, 2000).

Some empirical formulations and studies dedicated to specific sources could also be found in the literature, following some examples. For instance an empirical formulation for traffic vibration amplitude in the free field taking into consideration some specific factors (Watts, 1990; Watts and Krylov, 2000) is shown in equation (2.8).

$$A = 0.028H\left(\frac{V}{48}\right)sp\left(\frac{r}{6}\right)^n \tag{2.8}$$

H describes the irregularity size in mm, V the speed of the vehicle in km/h, r the distance from the source, p is a constant that describes the position of irregularity to wheels, s and n are constants associated to the type of soil considered.

Similarly, such formulations exist for pile driving sources. An example is the formulation provided by Attewell and Farmer (1973) given in equation (2.9) which is considered as the basis of most of the other formulation that followed.

$$V = K\frac{\sqrt{W_0}}{r} \tag{2.9}$$

V is the vibration level in mm/s, r is the distance in meters from the source, W_0 is the energy at the source position and K an empirical coefficient recommended to be equal to 0.75.

Another example is a formulation provided by Attewell et al. (1992) shown in equation (2.10).

$$\log V = -0.296 + 1.38\log\left(\frac{\sqrt{W_0}}{r}\right) - 0.234\log^2\left(\frac{\sqrt{W_0}}{r}\right) \tag{2.10}$$

Where V is the amplitude in mm/s, r is the distance in meters from the source. W_0 is the energy at the source expressed in Joules.

Empirical prediction methods for train vibrations could also be found in the literature. Such models for instance were developed by Madshus et al. (1996) and Rossi and Nicolini (2003).

2.5 Simulating ground vibration

Modeling vibrations in soils can involve a large number of parameters and usually encloses a certain level of complexity. Numerous methods and approaches have been developed in order to simulate wave propagation in solids. The following discussion reviews the common approaches used for the simulation of vibrations in soils and structures.

2.5.1 Mechanical idealization

Simulating dynamic problems may be computationally demanding. A number of assumptions are often made to reduce the computational efforts. Along with 3D models which are the most expensive idealization, 2D and 2.5D models are widely used in the assessment of vibration problems in soils and structures.

The aim of using 2D models is to reduce the number of calculations and therefore the computation time and storage cost comparing to the more realistic 3D-models. A disadvantage of such models is the disregard of one dimension and therefore the risk of overestimating the damping in certain problems (Wolf et al., 1994), or overestimating the response in other problems (Makra and Chavez-Garcia, 2016). For instance Paolucci et al. (2003) developed a 2D model using the finite element method in order to study vibrations caused by high-speed trains on soft soils. Yang et al. (2009) used 2D finite element models to study stress changes in railway track bed for various train speeds.

3D models can achieve the highest accuracies in modeling vibrations, since all the three dimensions are explicitly modeled and no assumptions are made on the dimensionality of the problem. However the computational cost of 3D models is dramatically higher than the 2D method. Katou et al. (2008) studied ground vibrations caused by high-speed trains using a 3D finite difference method. Galvin et al. (2010) developed a full 3D FE-BE model for high speed train enabling him to study the interaction between the different elements of the model and the multiple excitation mechanisms generated by trains. Andersen and Jones (2002, 2006) used coupled FE-BE models in 2D and 3D to model vibrations from railway tunnels, deducing by comparison both similarities and differences between the two methods. Grasso et al. (2012) used fast multipole BEM to simulate seismic waves with viscoelastic behavior in 3D.

2.5D models have been developed in order to overcome the lack of precision in 2D models while avoiding the high calculation cost of 3D models. In this approach, the analyzed system is assumed invariant in one direction. For longitudinally invariant structures the Fourier transform is usually applied on the longitudinal direction in order to represent the three dimensional response of the structure (Tadeu et al., 2001). For periodic structures, Floquet transform is usually applied for a unit cell solution in order to generalize the structural response and the radiated wave-field (Gupta et al., 2007; Chebli et al., 2008). 2.5D models can achieve high precision level comparable to 3D models. Multiple examples of 2.5D models can be found in the literature. 2.5D finite element models were developed to study vibratory waves in structures by Gavrić (1994, 1995). Andersen and Nielsen (2005) studied isolation techniques along railway tracks using 2.5D approach. Lombaert et al. (2000) used the 2.5D technique to numerically model traffic induced vibrations. A spatial windowing technique in 2.5D problems was proposed by Coulier et al. (2014). This technique allows accounting for a structure's length, while maintaining the efficiency of a 2.5D approach and it proved to be appropriate as long as the response is not dominated by individual modes.

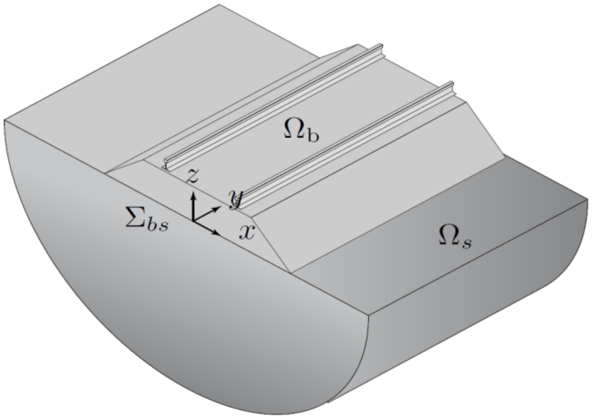

Fig. 2.3: A 2.5D coupled FE-BE model example of a ballasted track at grade invariant with respect to the coordinate y in the longitudinal direction (modified from Galvin et al., 2010).

2.5.2 Analytical approaches

The flexibility matrix method was first formulated by Haskell (1953) and Thompson (1950). It is based on the use of transfer matrices in the frequency-wave number domain. This method satisfies the interface continuity between the layers while doing the transition of field variables between them. In other words the matrices which are deduced from the exact solution of wave equation can precisely describe the displacement relation at the layers interface. This approach was used by Jones et al. (1998) for studying vibrations caused by rectangular harmonic loads at the surface. Sheng et al. (1999) used the flexibility matrix to model harmonic loads on railway tracks.

Direct stiffness method was proposed by Kausel and Roësset (1981) to solve the wave problem in soil. The viscoelastic multilayered soil with a point load was solved through finding a global stiffness matrix, assembled from smaller matrices, each representing a layer. The solution in this method, similarly to other methods is based on the determination of the displacement at each point along the surface of each layer. This method was used in analyzing different cases and problems: Jones and Petyt (1993) employed it for half-space underground vibration and elastic layer over a half-space respectively. Jones et al. (1997) modeled a rectangular load on a viscoelastic layer over a rigid foundation. Jones et al. (1998) modeled one elastic layer over a half-space subjected to rectangular harmonic loads. A well-established application of this method for high speed rectangular loads over a layered soil was done by Lefeuve-Mesgouez et al. (2002).

Lumped mass method unlike the previous methods doesn’t use the displacement potentials to solve the propagation problems and instead leads to simple eigenvalue problem. Lumped mass is a finite element approach where the soil is divided into a finite number of elements (usually rectangular) with the mass of each element concentrated at its corners. The lumped masses are the elements describing and transmitting the motion and forces. The application of the lumped mass method in the wave propagation appears in Lysmer (1970) for the first time. The method is also used in Lysmer and Waas (1972) for studying the efficiency of trenches in reducing the horizontal shear wave motion.

The thin layer method (TLM) solves the wave problem in soil in both time and frequency domains through the discretization of the soil in the vertical direction in a similar way to that done in the finite element method, while the equations are solved analytically in the horizontal direction. TLM as the method’s name indicates discretizes the soil into thin layers and not elements. The thickness of each layer should be small enough compared to the wavelength of the S-wave in the layer in order to comply with the linearity assumption in the behavior of the material which is necessary in the formulation of the problem. The most important developments of this method were done in the early eighties by Kausel (1981). Kausel (1994, 1999) provided the formulation in the time domain for thin layer method and for dynamic point sources in laminated media. TLM could be coupled with other methods like FEM; for instance Hanazato et al. (1991) used a thin layer method along with finite element method in order to analyze in 3D the traffic induced ground vibration. Celebi and Schmid (2005) used the thin layer method coupled with flexible volume method in order to investigate ground vibrations induced by moving loads along with the use of boundary element method.

2.5.3 Numerical approaches

Certain complexity levels can arise when modeling wave propagation in soils. Analytical methods are usually dedicated to rather simple problems and are unable to solve complex problems. Numerical models such as FEM, FDM, BEM and other advanced formulations are commonly used to overcome the complexities faced in wave propagation modeling in solids.

The **finite element method** is a technique that solves the physical problems in a differential form (Bathe, 1982). FEM is about discretizing the problem into finite small elements and solve their governing equations. FEM application in dynamics is based on discrete approximation of the motion equations in their weak formulation (Hughes, 1987; Zienkiewicz and Taylor, 2000).

The FEM main advantages are the capability to model finite extent problems with complex geometries, heterogeneous media and complicated constitutive laws (Hughes 1987, Curnier 1993).

Even though FEM is quite a powerful method for wave propagation problems, many drawbacks exist. Main drawbacks are related to the wave reflection from the artificial boundaries leading to errors in results (Costantino, 1967; Semblat and Pecker, 2009) and related to the numerical dispersion in the classical low-order approximations (Marfurt, 1984; Mullen and Belyteschko, 1982; Semblat and Briost, 2000; Semblat and Pecker, 2009). Other numerical problems that may reduce the precision of the results are numerical damping, polarization errors, numerical anisotropy, phase and group velocities errors, spurious diffraction and scattering or extraneous parasitic modes (Semblat and Pecker, 2009).

The boundary reflection problems have led to the development of absorbing boundaries solutions. Lysmer and Khulmeyer (1969) developed the “standard viscous boundary” technique through adding a series of dashpots with specific viscosity in order to absorb the incoming spurious P- and S- waves. Lysmer et al. (1969) and Lysmer and Drake (1971) developed an absorbing boundary method in the frequency wave number domain based on the stiffness matrix techniques of Haskell (1953) and Thomson (1950). Further developments were introduced to the “viscous boundaries” technique. For instance, White et al. (1977) developed better approximations for the dashpots that led to the “unified viscous boundary” technique. Deeks and Randolph (1994) extended the use of the method in finite elements to plane-strain and axisymmetric models. Perfect matched layer (PML) is another solution for the boundary reflection problems. Initially developed by Berenger (1994) in the field of electromagnetics, it was later adopted and widely used in the elastodynamics and wave propagation in soil (Collino and Tsogska, 2001; Basu and Chopra, 2003; Festa and Nielsen, 2003). A simple multi-directional absorbing layer method in unbounded domains was developed by Semblat et al. (2011).

Numerical dispersion leads to an artificial change in the wave velocities through propagation (Ihlenburg and Babuska, 1995; Semblat, 1998; Semblat and Pecker, 2009). Even though the change is generally weak, the accumulation of the errors during the propagation will lead to a major perturbation and modification in the results. The main cause of numerical dispersion is the lack of coherence between the geometrical and time discretization (Bamberger et al., 1980). Mesh refinement and higher order finite element are generally considered the best ways to reduce the dispersion since numerical dispersion is higher for a larger element size compared to wavelength (Semblat and Brioist, 2000). Mesh refinement is nevertheless associated with higher computational costs.

Vibrations caused by trains and traffic can be modeled using FEM, some examples could be found in Hall (2003), Paolucci (2003) and Ju (2009).

The **finite difference method**, unlike the FEM, uses the most direct approach for discretizing the partial differential equations instead of derivatives to solve the propagation problem at each node in the continuously meshed body. Staggered grids are usually associated with FDM, and are used to optimize the calculations. Spatial derivatives between grids points are calculated using staggered grids (Virieux, 1986; Graves, 1996).

In addition to its capacity to deal with elastic materials, FDM showed good potentials in solving wave propagation problems in viscoelastic media (Robertsson et al., 1994). Katou et al. (2008) state that FDM performs faster and consume less memory than FEM with a comparable accuracy even with free surface calculation.

The use of grids limits the ability of FDM in dealing with heterogeneities and complicated geometries. Staggered grids may reduce the numerical dispersion but in the case of high contrast in materials, the dispersion may arise along with the numerical instability. Many approaches were developed in order to overcome such difficulties through new types of staggered grids (Liszka and Orkisz, 1980; Saenger and Bohlen, 2004). Boundary reflections in FDM are also considered a major problem similarly to FEM. The use of FDM is generally limited in modeling vibrations caused by surface sources; however some studies were done using it, mainly in modeling railway induced vibrations (Thornely-Taylor, 2004; Katou et al., 2008).

The **boundary element method** (BEM) formulation is based on the boundary integral equations (Bonnet, 1999), making its approach quite different than “volumetric” methods i.e FEM an FDM. Instead of meshing the whole volume or body in the problem, only the boundaries and interfaces of discontinuity are meshed and the dimensions of the problem are reduced by one. The radiation condition in the BEM is automatically satisfied (Dominguez and Meise, 1991). This fact leads to the advantage of the absence of boundary reflection problems that usually affect the precision of the results (Aubry and Clouteau, 1991; Bonnet, 1999), thus avoiding the need for absorbing boundary conditions as for the FEM and FDM. Another advantage of the BEM is the absence of cumulative errors during the propagation or, in other words, the numerical dispersion (Semblat and Pecker, 2009).

While it is a very efficient method in terms of describing radiations and avoiding numerical dispersions, BEM is limited to weak heterogeneities and linear models (Gaul and Schanz, 1994; Semblat and Pecker, 2009). Another drawback of the BEM is that it leads to unsymmetric fully populated matrices, which means that in the case of large scale models, the computation requirements in terms of time and memory will be huge. In order to overcome such a disadvantage, more advanced methods involving the BEM will be discussed later in this review.

BEM is widely used to model vibrations from different sources. Interesting applications of BEM can be found in Banerjee et al., (1988); Kattis et al., (1999); Al Hussaini et al., (2000) and François et al., (2005).

The **fast multipole methods** (FMM) appeared when Rokhlin (1985) introduced it to solve the Laplace equation, and it was further developed by Greengard and Rokhlin (1987) in order to solve multibody problem in physics.

The idea of using the FMM came from the fact that, although the BEM is efficient in simplifying the problems dimension and easiness of mesh, it is still limited for large scale models. BEM produces dense and non-symmetric matrices requiring huge CPU time and memory, then limiting its capacity to model with few thousand DOFs.

Matrix vector product computation required in the iterative solution of BEM discretized equation is accelerated using FMM. Moreover the storage requirement is reduced below the O(N^2) memory requirement for BEM full matrix, since the governing matrix is not explicitly formulated. CPU time and memory storage are therefore largely reduced using FM-BEM if compared to classical BEM (Chaillat et al., 2008; Bonnet et al., 2009; Semblat and Pecker, 2009). Very large problems beyond the limited few thousand DOF's are thus solvable using the FM-BEM.

The FM-BEM is today a widely used method in the domain of elastodynamics despite its novelty. Fujiwara (2000) used the FMM to solve 3D topography and basin problems. Chaillat et al. (2008, 2009) used the FM-BEM for wave propagation and amplification problems in geological structures. Bapat et al. (2009) studied acoustic propagation problems using fast multipole methods. Fischer and Gaul (2005) applied fast multipole methods for structural-acoustic interaction problems.

Coupling methods are becoming more and more popular in the domain of wave propagation and soil-structure interaction. FE-BE coupling is widely used and considered very successful for waves propagation in unbounded domains.

As mentioned in the previous part, FEM is very useful when dealing with heterogeneities, complex geometries but limited in terms of spurious reflections. On the other hand, the BEM can deal with the radiation conditions but with limited flexibility in terms of modeling thin domains, non-linear and heterogeneous materials, etc. Therefore the coupling of the two methods gives the opportunity to benefit from the advantages of both of them.

The first approach of coupling FEM and BEM was proposed by Zienkiewicz at al. (1977). One of the first applications of such method in the wave propagation problem was done by Dangla (1988).

The problem solving is done through decomposing the problem into sub problems or sub domains where FEM or BEM will be utilized depending on the convenience of each method with the nature of the subdomain. After that the coupling of the subdomains equations could be performed "directly" what mean that the equation of all subdomains are assembled into one global equation system (Karabalis and Beskos, 1985; Von Estorff and Prabucki, 1990; Pavlatos and Beskos, 1994)

The coupling of FEM matrices which are usually sparse and symmetric with the fully populated non-symmetric matrices of BEM, will lead to computational difficulties and therefore expensive time and memory consumption. The difficulties will increase each time the problem is more detailed (non-linearities, different materials, etc...) since more subdomains and time-steps are needed.

Alternative approaches were developed in order to overcome these difficulties, which were known as the staggered and iterative approaches. The approaches are about solving the equations of each subdomain separately instead of assembling all the coupled equations in one system. Solving for each domain separately gives the advantage of benefiting from the matrix characteristics independently through using the appropriate solver, time steps (since each may require different time step), etc. In a staggered approach, equations for each subdomain are solved only once for each time step. While in an iterative approach the same equations are solved iteratively for each time step. In the first approach the boundary conditions are estimated for the structure subdomain from previous time steps and then applied as a boundary condition to the soil subdomain. On the other hand the iterative approach, the boundary conditions are updated at the interface between subdomains at each time step. Good examples for the staggered coupling could be found in Felippa and Park (1980), Rizos and Wang (2002), O'Brien and Rizos (2005). Iterative solutions for the coupling method could be found in Soares et al. (2004), Von Estorff and Hagen (2006).

Coupled FE-BE method is one of the most used in the domain of vibration modeling. The literature is full with applications of this method; some recommended examples are in O'Brien and Rizos (2005); Masoumi et al., (2007) and Galvin et al., (2010).

2.6 References

Al-Hussaini T.M., Ahmad S., and Baker J.M. (2000). Numerical and experimental studies on vibration screening by open and in-filled trench barriers. pages 241–250, 2000. Wave 2000 International Workshop, Bochum, Germany, Dec 13-15.

Amick, H., and Gendreau, M. (2000). Construction vibrations and their impact on vibration-sensitive facilities. In *Construction Congress VI: Building Together for a Better Tomorrow in an Increasingly Complex World* (pp. 758-767).

Andersen, L. and Jones, C. J. C. (2002) Vibration from railway tunnel predicted by coupled finiteelement and boundary element analysis in two and three dimensions. *In Proceedings of Structural Dynamics-EuroDyn'02,* 1131–1136

Andersen, L., and Nielsen, S. R. (2005). Reduction of ground vibration by means of barriers or soil improvement along a railway track. *Soil Dynamics and Earthquake Engineering*, *25*(7), 701-716.

Andersen, L., and Jones, C. J. C. (2006). Coupled boundary and finite element analysis of vibration from railway tunnels—a comparison of two-and three-dimensional models. *Journal of sound and vibration*, *293*(3), 611-625.

Athanasopoulos, G. A., Pelekis, P. C., and Anagnostopoulos, G. A. (2000). Effect of soil stiffness in the attenuation of Rayleigh-wave motions from field measurements. *Soil Dynamics and Earthquake Engineering*, *19*(4), 277-288.

Attewell P.B and Farmer I.W. (1973). Attenuation of ground vibrations from pile driving, *Ground Engineering*, Vol.6, No.4, pp.26-29

Attewell, P. B., Selby, A. R., and O'Donnell, L. (1992). Estimation of ground vibration from driven piling based on statistical analyses of recorded data. *Geotechnical and geological engineering*, *10*(1), 41-59.

Aubry, D., and D. Clouteau (1991). A regularized bound-ary element method for stratified media, *1st Int. Conf. on Mathematical and Numerical Aspects of Wave Propagation*, SIAM.

Auersch, L. (2005). The excitation of ground vibration by rail traffic: theory of vehicle–track–soil interaction and measurements on high-speed lines. *Journal of Sound and Vibration*, *284*(1), 103-132.

Bamberger A., Chavent G. and Lailly P. (1980). Analysis of numerical schemes for linear elastodynamics equations (in french), *INRIA*, Report No.41.

Banerjee P.K., Ahmad S., and Chen K. (1988). Advanced application of bem to wave barriers in multi-layered 3-dimensional soil media. *Earthquake Engineering & Structural Dynamics,* 16:1041–1060.

Bapat, M. S., Shen, L., and Liu, Y. J. (2009). Adaptive fast multipole boundary element method for three-dimensional half-space acoustic wave problems. *Engineering Analysis with Boundary Elements*, *33*(8), 1113-1123.

Basu, U., and Chopra, A. K. (2003). Perfectly matched layers for time-harmonic elastodynamics of unbounded domains: theory and finite-element implementation. *Computer methods in applied mechanics and engineering*, *192*(11), 1337-1375.

Bathe K.-J. (1982). Finite element procedures in engineering analysis. *Prentice-Hall*.

Berglund B., Lindvall T., Schwela D., and Kee-Tai G.(2000) Guidelines for community noise. *World Health Organization,* Geneva.

Berenger, J. P. (1994). A perfectly matched layer for the absorption of electromagnetic waves. *Journal of computational physics*, *114*(2), 185-200.

Bonnet, M. (1999). Boundary integral equation methods for solids and fluids. *Meccanica, 34(4)*, 301-302.

Bonnet, M., Chaillat, S., and Semblat, J. F. (2009). Multi-level fast multipole BEM for 3-D elastodynamics. In *Recent advances in boundary element methods* (pp. 15-27). Springer Netherlands.

BSI-British Standards Institution (1990). Evaluation and measurement for vibration in buildings. London

Celebi, E., and Schmid, G. (2005). Investigation of ground vibrations induced by moving loads. *Engineering Structures*, *27*(14), 1981-1998.

Chaillat S., Bonnet M. and Semblat J. F. (2008). A multi-level fast multipole BEM for 3-D elastodynamics in the frequency domain. *Comp. Meth. Appl. Mech. Engng.,* 197:4233–4249.

Chaillat, S., Bonnet, M., and Semblat, J. F. (2009). A new fast multi-domain BEM to model seismic wave propagation and amplification in 3-D geological structures. *Geophysical Journal International*, *177*(2), 509-531.

Chebli, H., Othman, R., Clouteau, D., Arnst, M., and Degrande, G. (2008). 3D periodic BE–FE model for various transportation structures interacting with soil. *Computers and Geotechnics*, *35*(1), 22-32.

Collino, F., and Tsogka, C. (2001). Application of the perfectly matched absorbing layer model to the linear elastodynamic problem in anisotropic heterogeneous media. *Geophysics, 66*, 294–307

Costantino C. (1967). Finite element approach to stress wave problem. *Journal of Engineering Mechanics ASCE*, 93(EM2):153-176

Coulier, P., Dijckmans, A., François, S., Degrande, G., and Lombaert, G. (2014). A spatial windowing technique to account for finite dimensions in 2.5 D dynamic soil–structure interaction problems. *Soil Dynamics and Earthquake Engineering*, *59*, 51-67.

Curnier, A. (1993). Méthodes numériques en mécanique des solides. *PPUR presses polytechniques.*

Dangla, P. (1988). A plane strain soil-structure interaction model. *Earthquake engineering and structural dynamics*, 16(8), 1115-1128.

Dawn, T. M., and Stanworth, C. G. (1979). Ground vibrations from passing trains. *Journal of sound and vibration*, *66*(3), 355-362.

Deeks, A. J. and Randolph, M. F. (1994), Axisymmetric time-domain transmitting boundaries. *Journal of Engineering Mechanics Division, ASCE*, 120, 25–42.

Dominguez, J., and Meise, T. (1991). On the use of the BEM for wave propagation in infinite domains. *Engineering Analysis with Boundary Elements*, *8*(3), 132-138.

Duarte M.L.M. and Filho M. R. (2003), Perception threshold of people exposed to sinusoidal vibration.*Proceedings of the Tenth International Congress on Sound and Vibration*, pp. 3791-3798.

Felippa, C. A., & Park, K. C. (1980). Staggered transient analysis procedures for coupled mechanical systems: formulation. *Computer Methods in Applied Mechanics and Engineering*, *24*(1), 61-111.

Festa, G., and Nielsen, S. (2003). PML absorbing boundaries. *Bulletin of the Seismological Society of America*, *93*(2), 891-903.

Fischer, M., and Gaul, L. (2005). Application of the fast multipole BEM for structural–acoustic simulations. *Journal of Computational Acoustics*, 13(01), 87-98

François, S., Lombaert, G., and Degrande, G. (2005). Local and global shape functions in a boundary element formulation for the calculation of traffic induced vibrations. *Soil dynamics and earthquake engineering*, 25(11), 839-856.

François, S., Karg, C., Haegeman, W., and Degrande, G. (2010). A numerical model for foundation settlements due to deformation accumulation in granular soils under repeated small amplitude dynamic loading. *International journal for numerical and analytical methods in geomechanics*, *34*(3), 273-296.

Fujiwara, H. (2000). The fast multipole method for solving integral equations of three-dimensional topography and basin problems. *Geophysical Journal International*, *140*(1), 198-210.

Galvin, P., François, S., Schevenels, M., Bongini, E., Degrande, G., and Lombaert, G. (2010). A 2.5 D coupled FE-BE model for the prediction of railway induced vibrations. *Soil Dynamics and Earthquake Engineering*, *30*(12), 1500-1512.

Gaul L. and Schanz M. (1994). Dynamics of viscoelastic solids treated by boundary element approaches in time domain. *Eur. J. Mech. A/Solids*, 13:43–59.

Gavrić, L. (1994). Finite element computation of dispersion properties of thin-walled waveguides. *Journal of sound and vibration*, *173*(1), 113-124.

Gavrić, L. (1995). Computation of propagative waves in free rail using a finite element technique. *Journal of Sound and Vibration*, *185*(3), 531-543.

Gordon, C. G. (1999, July). Generic vibration criteria for vibration-sensitive equipment. In *Proc. SPIE* (Vol. 3786, pp. 22-39).

Grasso, E., Chaillat, S., Bonnet, M., and Semblat, J. F. (2012). Application of the multi-level time-harmonic fast multipole BEM to 3-D visco-elastodynamics. *Engineering Analysis with Boundary Elements*, *36*(5), 744-758.

Graves, R. W. (1996). Simulating Seismic Wave Propagation in 3D Elastic Media Using Staggered-Grid Finite Differences. *Bulletin of the Seismological Society of America*, *86*(4), 1091–1106.

Greengard, L., and Rokhlin, V. (1987). A fast algorithm for particle simulations. *Journal of computational physics*, *73*(2), 325-348.

Gupta, S., Hussein, M. F. M., Degrande, G., Hunt, H. E. M., and Clouteau, D. (2007). A comparison of two numerical models for the prediction of vibrations from underground railway traffic. *Soil Dynamics and Earthquake Engineering*, *27*(7), 608-624.

Gupta, S., Liu, W. F., Degrande, G., Lombaert, G., and Liu, W. N. (2008). Prediction of vibrations induced by underground railway traffic in Beijing. *Journal of Sound and Vibration*, *310*(3), 608-630.

Hajek, J. J., Blaney, C. T., and Hein, D. K. (2006). Mitigation of highway traffic-induced vibration. In *Session on Quiet Pavements: Reducing Noise and Vibration Annual Conference of the Transportation Association of Canada*.

Hall, L. (2003). Simulations and analyses of train-induced ground vibrations in finite element models. *Soil Dynamics and Earthquake Engineering*, *23*(5), 403-413.

Hanazato, T., Ugai, K., Mori, M., and Sakaguchi, R. (1991). Three-dimensional analysis of traffic-induced ground vibrations. *Journal of geotechnical engineering*, *117*(8), 1133-1151.

Hao, H., Ang, T. C., and Shen, J. (2001). Building vibration to traffic-induced ground motion. *Building and Environment*, *36*(3), 321-336.

Haskell, N. A. (1953). The dispersion of surface waves on multilayered media. *Bulletin of the seismological Society of America*, *43*(1), 17-34.

Heckl, M., Hauck, G., and Wettschureck, R. (1996). Structure-borne sound and vibration from rail traffic. *Journal of sound and vibration*, *193*(1), 175-184.

Hildebrand, R. (2001). *Countermeasures against railway ground and track vibrations* (Doctoral dissertation, Institutionen för farkostteknik).

Hughes, T.J.R. (1987). *Linear static and dynamic finite element analysis*, Prentice-Hall, Englewood Cliffs, N-J

Hunaidi, O. (2000). *Traffic vibrations in buildings*. Institute for Research in Construction, National Research Council of Canada.

Ihlenburg, F., and Babuška, I. (1995). Dispersion analysis and error estimation of Galerkin finite element methods for the Helmholtz equation. *International journal for numerical methods in engineering*, *38*(22), 3745-3774.

Jones, D. V., and Petyt, M. (1993). Ground vibration in the vicinity of a strip load: an elastic layer on an elastic half-space. *Journal of Sound and Vibration*, *161*(1), 1-18.

Jones, C. J. C., and Block, J. R. (1996). Prediction of ground vibration from freight trains. *Journal of sound and vibration*, *193*(1), 205-213.

Jones, D. V., Laghrouche, O., Le Houedec, D., and Petyt, M. (1997). Ground vibration in the vicinity of a rectangular load acting on a viscoelastic layer over a rigid foundation. *Journal of Sound and Vibration*, *203*(2), 307-319.

Jones, D. V., Le Houedec, D., and Petyt, M. (1998). Ground vibrations due to a rectangular harmonic load. *Journal of Sound and Vibration*, *212*(1), 61-74.

Jongmans, D. (1996). Prediction of ground vibrations caused by pile driving: a new methodology. *Engineering Geology*, *42*(1), 25-36.

Ju, S. H. (2009). Finite element investigation of traffic induced vibrations. *Journal of Sound and Vibration*, *321*(3), 837-853.

Karabalis, D. L. et Beskos, D. E.(1985) Dynamic response of 3-D flexible foundations by time domain BEM and FEM. *International Journal of Soil Dynamics and Earthquake Engineering*, , vol. 4, no 2, p. 91-101.

Katou, M., Matsuoka, T., Yoshioka, O., Sanada, Y., and Miyoshi, T. (2008). Numerical simulation study of ground vibrations using forces from wheels of a running high-speed train. *Journal of Sound and Vibration*, *318*(4), 830-849.

Kattis, S. E., Polyzos, D., and Beskos, D. E. (1999). Vibration isolation by a row of piles using a 3-D frequency domain BEM. *International Journal for Numerical Methods in Engineering*, *46*(5), 713-728.

Kausel, E. (1981). *An explicit solution for the Green functions for dynamic loads in layered media*. Department of Civil Engineering, School of Engineering, Massachusetts Institute of Technology.

Kausel, E., and Roësset, J. M. (1981). Stiffness matrices for layered soils. *Bulletin of the Seismological Society of America*, *71*(6), 1743-1761.

Kausel, E. (1994). Thin-layer method: Formulation in the time domain. *International journal for numerical methods in engineering*, *37*(6), 927-941.

Kausel, E. (1999). Dynamic point sources in laminated media via the thin-layer method. *International Journal of Solids and Structures*, *36*(31), 4725-4742.

Kaynia, A. M., Madshus, C., and Zackrisson, P. (2000). Ground vibration from high-speed trains: prediction and countermeasure. *Journal of Geotechnical and Geoenvironmental Engineering*, *126*(6), 531-537.

Kim, D. S., and Lee, J. S. (2000). Propagation and attenuation characteristics of various ground vibrations. *Soil Dynamics and Earthquake Engineering*, *19*(2), 115-126.

Knall, V. (1996). Railway noise and vibration: effects and criteria. *Journal of sound and vibration*, *193*(1), 9-20.

Knothe, K., and Grassie, S. (1993). Modelling of railway track and vehicle/track interaction at high frequencies. *Vehicle System Dynamics*, *22*, 209–262.

Krylov, V. V., Dawson, A. R., Heelis, M. E., and Collop, A. C. (2000). Rail movement and ground waves caused by high-speed trains approaching track-soil critical velocities. *Proceedings of the Institution of Mechanical Engineers, Part F: Journal of Rail and Rapid Transit*, *214*(2), 107-116.

Lefeuve-Mesgouez, G., Peplow, A. T., and Le Houédec, D. (2002). Surface vibration due to a sequence of high speed moving harmonic rectangular loads. *Soil Dynamics and Earthquake Engineering*, *22*(6), 459-473.

Liszka, T., and Orkisz, J. (1980). The finite difference method at arbitrary irregular grids and its application in applied mechanics. *Computers and Structures*, *11*(1-2), 83-95.

Lombaert, G., Degrande, G., and Clouteau, D. (2000). Numerical modelling of free field traffic-induced vibrations. *Soil Dynamics and Earthquake Engineering*, *19*(7), 473-488.

Lombaert G. (2001): *Development and experimental validation of a numerical model for the free field vibrations induced by road traffic*. Thèse de doctorat, Université Catholique de Louvain, département de génie civil.

Lysmer, J., and Kuhlemeyer, R. L. (1969). Finite dynamic model for infinite media. *Journal of the Engineering Mechanics Division*, *95*(4), 859-878.

Lysmer, J. (1970). Lumped mass method for Rayleigh waves. *Bulletin of the Seismological Society of America*, *60*(1), 89-104.

Lysmer, J., and Drake, L. A. (1971). The propagation of Love waves across nonhorizontally layered structures. *Bulletin of the Seismological Society of America*, *61*(5), 1233-1251.

Lysmer, J., and Waas, G. (1972). Shear waves in plane infinite structures. *Journal of Engineering Mechanics*.

Madshus, C., Bessason, B., and Hårvik, L. (1996). Prediction model for low frequency vibration from high speed railways on soft ground. *Journal of sound and vibration*, *193*(1), 195-203.

Madshus, C., and Kaynia, A. M. (2000). High-speed railway lines on soft ground: dynamic behaviour at critical train speed. *Journal of Sound and Vibration*, *231*(3), 689-701.

Makra, K., and Chávez-García, F. J. (2016). Site effects in 3D basins using 1D and 2D models: an evaluation of the differences based on simulations of the seismic response of Euroseistestf. *Bulletin of Earthquake Engineering*, *14*(4), 1177.

Marfurt, K. J. (1984). Accuracy of finite-difference and finite-element modeling of the scalar and elastic wave equations. *Geophysics*, *49*(5), 533-549.

Masoumi, H.R., Degrande, G. and Lombaert, G. (2006). Free field vibrations due to vibratory pile driving in a layered soil medium. *Proceedings of TRANSVIB 2006*, Paris 21-22 September.

Masoumi, H. R., Degrande, G., and Lombaert, G. (2007). Prediction of free field vibrations due to pile driving using a dynamic soil–structure interaction formulation. *Soil dynamics and earthquake engineering*, *27*(2), 126-143.

Massarsch. K. R. (1995). Engineering vibrations and solutions. General Report, *Third International Conference on Recent Advances in Geotechnical Earthquake Engineering and Soil Dynamics*, April 2 - 7, 1995, St. Louis, Mo., Vol. III., pp. 1349 -1353.

Massarsch, K.R. and Fellenius, B.H. (2008). Ground Vibrations Induced by Impact Pile Driving. *Proceedings of the 6th International Conference on Case Histories in Geotechnical Engineering*, Arlington, August 11-16, 2008.

Massarsch, K.R. (2004). Vibrations Caused by Pile Driving. *Deep foundations*, summer 2004 and fall 2004 (two parts).

Mullen, R., and Belytschko, T. (1982). Dispersion analysis of finite element semidiscretizations of the two-dimensional wave equation. *International Journal for Numerical Methods in Engineering*, *18*(1), 11-29.

Nielsen, J. C., Lundén, R., Johansson, A., and Vernersson, T. (2003). Train-track interaction and mechanisms of irregular wear on wheel and rail surfaces. *Vehicle System Dynamics*, *40*(1-3), 3-54.

O'Brien, J., and Rizos, D. C. (2005). A 3D BEM-FEM methodology for simulation of high speed train induced vibrations. *Soil Dynamics and Earthquake Engineering*, *25*(4), 289-301.

Öhrström, E. (1997). Effects of exposure to railway noise—A comparison between areas with and without vibration. *Journal of Sound and Vibration*, *205*(4), 555-560.

Paolucci, R., Maffeis, A., Scandella, L., Stupazzini, M., and Vanini, M. (2003). Numerical prediction of low-frequency ground vibrations induced by high-speed trains at Ledsgaard, Sweden. *Soil Dynamics and Earthquake Engineering*, *23*(6), 425-433.

Pavlatos, G. D., and Beskos, D. E. (1994). Dynamic elastoplastic analysis by BEM/FEM. *Engineering Analysis with Boundary Elements*, *14*(1), 51-63

Ramshaw C.J. Selby A.R., Bettess P. (1998) Computed ground waves due to piling. *Proc. of the conference on geotechnical earthquake engineering and soil dynamics,* Seattle, Washington, August 3-6th, pp.1484-1495

Rizos, D. C., and Wang, Z. (2002). Coupled BEM–FEM solutions for direct time domain soil–structure interaction analysis. *Engineering Analysis with Boundary Elements*, *26*(10), 877-888.

Robertsson, J. O., Blanch, J. O., and Symes, W. W. (1994). Viscoelastic finite-difference modeling. *Geophysics*, *59*(9), 1444-1456.

Rokhlin, V. (1985). Rapid solution of integral equations of classical potential theory. *Journal of computational physics*, *60*(2), 187-207.

Rossi, F., and Nicolini, A. (2003). A simple model to predict train-induced vibration: theoretical formulation and experimental validation. *Environmental Impact Assessment Review*, *23*(3), 305-322.

Saenger, E. H., and Bohlen, T. (2004). Finite-difference modeling of viscoelastic and anisotropic wave propagation using the rotated staggered grid. *Geophysics*, 69(2), 583-591.

Semblat J.F. (1998). Waves attenuation and dispersion: physical and numerical points of view (in french). *Revue Française de Génie Civil* 2(1), 91-111

Semblat, J. F., and Brioist, J. J. (2000). Efficiency of higher order finite elements for the analysis of seismic wave propagation. *Journal of Sound and Vibration*, *231*(2), 460-467.

Semblat, J. F., and Pecker, A. (2009). Waves and vibrations in soils: earthquakes, traffic, shocks, construction works. IUSS Press

Semblat, J. F., Lenti, L., and Gandomzadeh, A. (2011). A simple multi-directional absorbing layer method to simulate elastic wave propagation in unbounded domains. *International Journal for Numerical Methods in Engineering*, *85*(12), 1543-1563.

Sheng, X., Jones, C. J. C., and Petyt, M. (1999). Ground vibration generated by a harmonic load acting on a railway track. *Journal of sound and vibration*, *225*(1), 3-28.

Sheng, X., Jones, C. J. C., and Thompson, D. J. (2003). A comparison of a theoretical model for quasi-statically and dynamically induced environmental vibration from trains with measurements. *Journal of Sound and Vibration*, *267*(3), 621-635.

Soares Jr, D., Von Estorff, O., & Mansur, W. J. (2004). Iterative coupling of BEM and FEM for nonlinear dynamic analyses. *Computational Mechanics*, 34(1), 67-73.

Tadeu, A., António, J., and Godinho, L. (2001). Green's function for two-and-a-half dimensional elastodynamic problems in a half-space. *Computational Mechanics*, *27*(6), 484-491.

Thompson, W. T. (1950). Transmission of elastic waves through a stratified soil medium. *J Appl Phys*, *21*, 89-93.

Thompson, D. J., and Jones, C. J. C. (2000). A review of the modelling of wheel/rail noise generation. *Journal of sound and vibration*, *231*(3), 519-536.

Thornely-Taylor, R. (2004). Numerical modelling of ground borne noise and vibration from underground railways: geotechnical consideration. *12th International Congress on Sound and Vibration, Lisbon*

Virieux, J. (1986). P-SV wave propagation in heterogenous media: Velocity stress finite-difference method. *Geophysics*, *51*, 889–901.

Von Estorff, O., and Prabucki, M. J. (1990). Dynamic response in the time domain by coupled boundary and finite elements. *Computational mechanics*, *6*(1), 35-46.

Von Estorff, O., and Hagen, C. (2006). Iterative coupling of FEM and BEM in 3D transient elastodynamics. *Engineering Analysis with Boundary Elements*, *30*(7), 611-622.

Watts, G. R. (1990). *Traffic induced vibrations in buildings* (No. 46).

Watts, G. R. (1992). The generation and propagation of vibration in various soils produced by the dynamic loading of road pavements. *Journal of Sound and Vibration*, *156*(2), 191-206.

Watts, G. R., and Krylov, V. V. (2000). Ground-borne vibration generated by vehicles crossing road humps and speed control cushions. *Applied Acoustics*, *59*(3), 221-236.

Whenham, V. (2011). *Power Transfer and Vibrator-Pile-Soil Interactions within the framework of vibratory pile driving* (Doctoral dissertation, Doctoral Thesis, University of Louvain, Belgium).

White, W., Lee, I. K., and Valliappan, S. (1977). Unified boundary for finite dynamic models. *Journal of the Engineering Mechanics Division*, *103*(5), 949-964.

Wolf, J. P., and Meek, J. W. (1994). Insight on 2D-versus 3D-modelling of surface foundations via strength-of-materials solutions for soil dynamics. *Earthquake engineering and structural dynamics*, *23*(1), 91-112.

Woods, R.D. (1968), Screening of surface waves in soils, *Tech. Rep. IP-804, University of Michigan, Ann Arbor.*

Woods, R. D., and Jedele, L. P. (1985, October). Energy—Attenuation relationships from construction vibrations. In *Vibration problems in geotechnical engineering* (pp. 229-246). ASCE.

Woods, R.D. (1997). Dynamic Effects of Pile Installations on Adjacent Structures. NCHRP Synthesis 253, *National Cooperative Highway Research Program*, Transportation Research Board, National Academy Press, Washington D.C., USA.

Yang, L. A., Powrie, W., and Priest, J. A. (2009). Dynamic stress analysis of a ballasted railway track bed during train passage. *Journal of Geotechnical and Geoenvironmental Engineering*, *135*(5), 680-689.

Zienkiewicz, O. C., Kelly, D. W., and Bettess, P. (1977). The coupling of the finite element method and boundary solution procedures. *International Journal for Numerical Methods in Engineering*, *11*(2), 355-375.

Zienkiewicz, O. C., and Taylor, R. L. (2000). *The finite element method: solid mechanics* (Vol. 2). Butterworth-heinemann.

Chapter 3

Proposed FEM Modeling Methodology

3.1 Introduction

The absence of a comprehensive site classification for the vibration problem in civil engineering makes harder establishing attenuation and amplification laws in a parametric way depending on the geometrical and mechanical properties of soil. The ambiguous characterization of soils using terms like soft and hard soils, or clay sand and rock limits the ability of engineers in terms of precise quantification of vibrations in soils. Nevertheless site classifications could be found for earthquake engineering in construction codes, for instance the Eurocode 8.

Moreover the amplification of vibrational waves, a very important aspect of vibration prediction along with attenuation, usually depends not only on the simple characteristics of the surface soil layer but also on the characteristics of soils beneath it in certain cases. The characteristics of the deeper layers will participate in the definition of the seismic impedance contrast with the upper layer, and represent the material on which the down coming waves will reflect. In earthquake engineering the problem of site amplification and amplitudes prediction has received considerable attention but far less for problems of environmental ground vibration involving waves with higher frequencies and smaller wavelengths. The fact of dealing with high frequencies with very small wavelengths makes the numerical modeling more challenging in terms of defining appropriate meshes, memory storage and computing time requirements.

For the aim of studying the soil response under vibrations, the finite element method has been used (CESAR-LCPC, Humbert et al., 2005). The analysis has been performed in the time domain, using DYNI module that performs a direct time integration. The FEM models were to be optimized on multiple levels. This chapter will discuss the features of the FEM models with respect to the sources imposed and to the mechanical parameters of the soils considered. An important aspect of this work was also to increase the precision of the FEM results through eliminating the spurious reflections due to the non-physical spatial limitations of the models. Therefore, this chapter will present and discuss the methodology for simulating infinite boundaries. After the presentation of this material, the chapter ends with a validation of the hypothesis introduced in the first part considering the canonical Lamb problem for which an analytical solution is available.

3.2 Key Assumptions for FEM models

The considered source of excitation was in the form of a 5 meters wide foundation, loaded with an imposed vertical displacement at the surface. The choice of the source is done to take into account the wide frequency band content characterizing the vibrational real sources. The input was defined as a wavelet of the zero-order Ricker type (Semblat and Pecker, 2009; see Fig. 3.1).

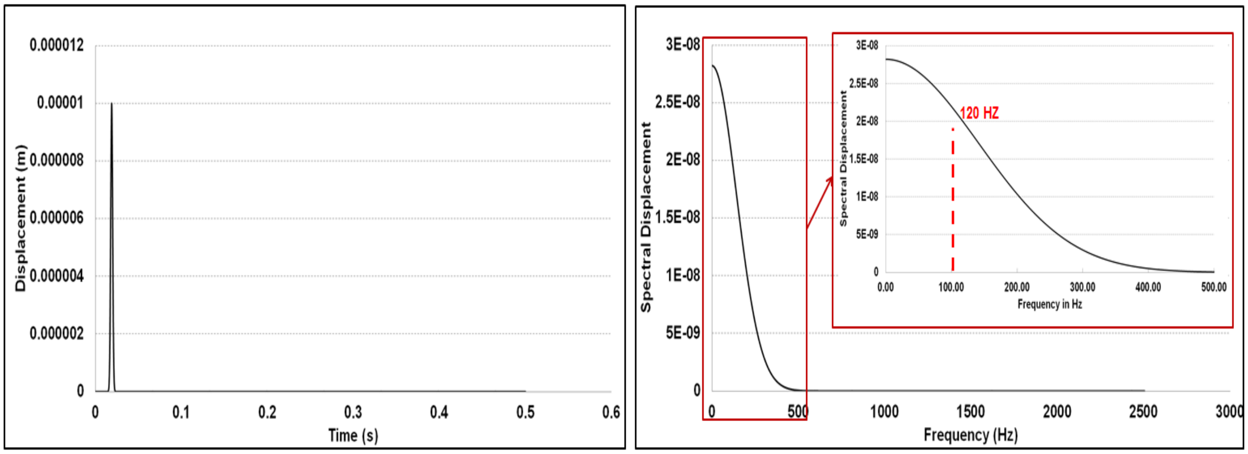

Fig. 3.1: Ricker Pulse Input in time domain (left) and frequency domain (right).

For the rheology of materials, a viscoelastic behavior was assumed. Plasticity and non-linearity effects are insignificant in the case of vibrations problems due to the small strains generally induced into the soils. The main parameters that have to be given to the FEM model for the elastic behavior are: Young's modulus E, density ρ, Poisson's ratio υ. More particularly we considered:

- υ fixed at 0.3 ;
- ρ for stiffer soils ($V_P > 1500 m/s$) defined following Gardner et al (1974)'s formula, $\rho = 0.31 V_P^{0.25}$, where V_P the P-wave velocity ; as Gardner's formula underestimates ρ for V_P below 1500m/s, ρ will be calculated in these cases in an alternative manner following this relation in which appears the S-wave velocity, $\rho = (V_S/4) + 1750$ (finally to be intended in Kg/m^3);
- E is related to ρ, υ and Vs parameters in the form $E = 2G(1+\nu)$ where $G = \rho V_S^2$

Concerning the meshing problems, the highest frequency to be solved was fixed at 120 Hz and all the meshes were calibrated accordingly in order to avoid dispersion problems (Semblat and Briost, 2000). As a consequence, the resulting wavelengths will depend on the minor wave velocity; *Vs*. Considering for each model the value of S-wave velocity and the fixed 120 Hz frequency, the minimum wavelength could be defined. The maximum inter-nodal distance was calculated considering the ratio $\lambda_{\min}/12$ as an upper limit. A second order quadratic interpolation discretization of elements was adopted instead of a linear one in order to enhance the precision of the propagation model.

For the viscous behavior of the materials, the Rayleigh formulation (Semblat, 1997) was used. In this regard, hereafter the definition of the damping coefficients in the Rayleigh formulation for the real soils is discussed. However, as already mentioned in the introduction, the problem of the energy dissipation has to be solved also in the supplementary absorbing layers surrounding the physical model.

Starting with the real soils, the Rayleigh damping coefficients, α_M and α_K that appears in the damping matrix, $C = c_M M + c_K K$, are related to the specific loss factor by the formula $Q^{-1} = 2\xi = c_M / \omega_{\min} + c_K \omega_{\min}$ where Q is assumed equal to $V_S/10$ (Olsen et al. 2003). ξ and $\omega_{\min}$ are the damping and the reference circular frequency respectively. The value of $\omega_{\min}$ for a given Q value was chosen to ensure a nearly constant damping for most of the frequencies below the maximum targeted one in the input loading (120Hz). The $\omega_{\min}$ value for most of the simulations was taken around 60 Hz. Fig. 3.2 shows two examples (*Vs*=200m/s and 400m/s) of the Rayleigh damping where it can be seen that, between 10 and 120 Hz, the value of Q^{-1} is around the constant value given by $10/V_S$.

3.3 Absorbing layer methods for vibrations propagation

Removing spurious reflections when modeling viscoelastic wave propagation has proven to be a challenging task especially with the quick rise of finite element methods due to the advanced computational capacities. Multiple approaches have been adopted in order to deal with this problem. For example, infinite elements may be used around the model in order to emulate the

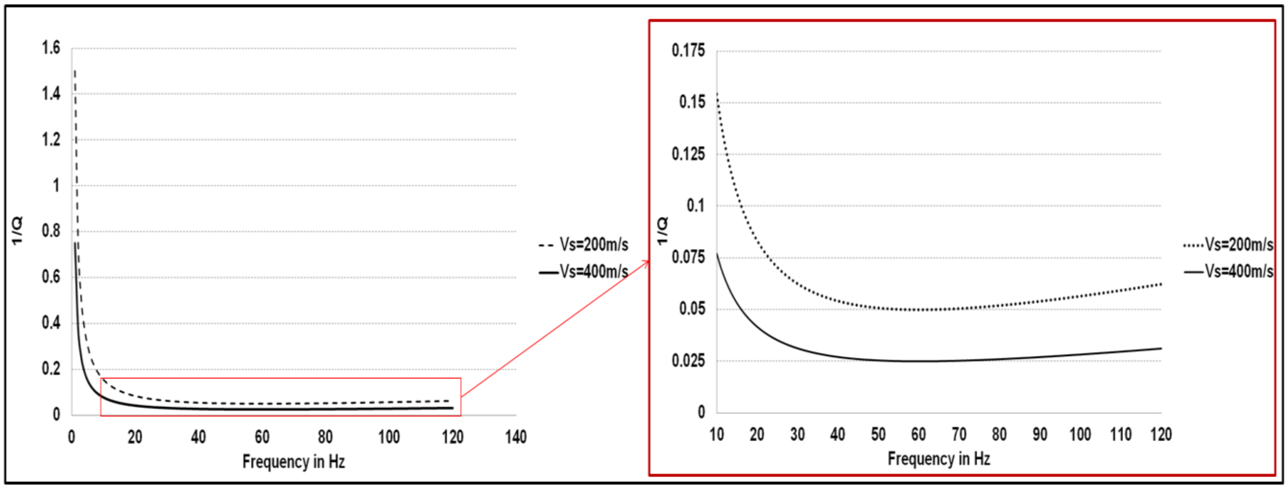

Fig. 3.2: Examples of the Rayleigh attenuation for Vs=200m/s (dotted line) and 400m/s (solid line); Q^{-1} *is given by* $10/V_S$.

infinite space and therefore absorb the incident waves (Bettess, 1992; Chadwick et al., 1999); absorbing boundary conditions aim to prevent reflections through the reduction of the reflection process (Engquist and Majda, 1979; Semblat and Pecker, 2009). Absorbing layers based on the perfectly matched layer (PML) technique were developed in electromagnetics (Berenger, 1994) and were later adopted in elastodynamic problems. Among the first attempts to use PMLs in elastodynamics, there was the one by Hastings et al. (1996) and Chew et al. (1996). Further developments devoted to implement PMLs in the finite difference method were carried by Wang et al. (2003). Meza-Fajardo et al. (2008) later developed the multiaxial perfectly matched layer (M-PML), which could be applied in multiple directions and is considered as a generalization of the standard PML. On the other hand, Rayleigh-based absorbing layer methods were widely considered thanks to their ease of implementation in FEM packages. The main issue rising from this type of methods is the spurious residual reflection due to the impedance contrast at the boundary of the physical domain. Among simpler methods for absorbing waves the Caughey Absorbing Layer Method (CALM) was first developed by Semblat et al. (2011), in which the viscoelastic constitutive relation is constructed considering the Maxwell rheological model to choose the Rayleigh coefficients in the damping matrix in FEM. Generalization of the CALM are nowadays abundant. Among these farther developments, ALID methods (Absorbing Layers with Increasing Damping) are basically very similar to CALM methods; they are based on the

Rayleigh matrix with a progressively increasing damping. ALID methods for instance were used by Liu and Jerry (2003), Drozdz (2008) and Rajagopal et al. (2012). A Rayleigh based absorbing layer method using both strategies, constant and increasing damping, was investigated by Zafati et al. (2014). Pettit et al. (2014) suggested a Rayleigh based absorbing layer with a stiffness reduction that proved to be very efficient.

3.4 Improving Rayleigh-based absorbing layers methods

The aim of this section is to develop a calibration strategy for a simple absorbing layer that could be easily applied at the boundaries of the model in existing FEM packages. Along with simplicity, the model size should remain reasonable. The reflection on the boundaries due to material contrast between the physical domain and the absorbing layer is more specifically addressed along with the stiffness reduction approach previously suggested by Pettit et al. (2014).

3.4.1 Stiffness reduction in absorbing layers

The idea of reducing the stiffness of the absorbing layer in this work is inspired from the physical phenomena of wave refraction and trapping. In other words an absorbing layer will be more efficient if it is able not only to attenuate waves inside of it but also trap the incident wave within.

However the idea of reducing the stiffness in the absorbing layer was recently used in FEM modeling. Pettit et al. (2014) suggested that reducing the stiffness of the layer along with manipulating some other parameters in an ALID (Absorbing Layers by Increasing Damping) would improve the efficiency of the absorbing layer.

In order to assess the idea of stiffness reduction from a rheological point of view, a generalized Maxwell model has to be considered which connects, in parallel, a classical Maxwell cell to a single dashpot as shown in Fig. 3.3 (Semblat, 1997).

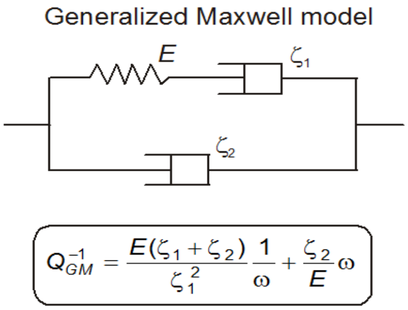

Fig. 3.3: The Generalized Maxwell model.

Studying the Maxwell model through a parametric analysis, while varying the three parameters, it becomes clear that for frequencies above 1 Hz, the maximum attenuation is at the smallest value of E and ζ_1 and the largest value of ζ_2, therefore taking this form $Q^{-1} = \frac{\zeta_2\,\omega}{E}$. Fig. 3.4 shows the variation of attenuation as a function of E and frequency for equal fixed values of ζ_1 and ζ_2. It could be noted that the attenuation increases with the increase of f and the decrease of E respectively. It is worth noticing that in the Generalized Maxwell model, $C_K = (\zeta_2/E)$ and $C_M = [E(\zeta_1 + \zeta_2)/{\zeta_1}^2]$, therefore C_K is inversely proportional to E while C_M is not.

This work aims also for the design of an absorbing layer where the reflections on the boundaries are maximally reduced. This will be described in details in the next section in terms of FEM wave propagation formulation. For the purpose of simplifying the calculations for the rheological model, a factor χ_3 is introduced which is equal to ζ_2/ζ_1.

3.4.2 Mathematical formulation of attenuation

In the following equations, a brief reminder and summary is provided on how the attenuation for Rayleigh damping works in FEM.

$$-\omega^2[M]u + i\omega[C]u + [K]u = [F] \tag{3.1}$$

Where

$$[C] = C_M[M] + C_K[K] \tag{3.2}$$

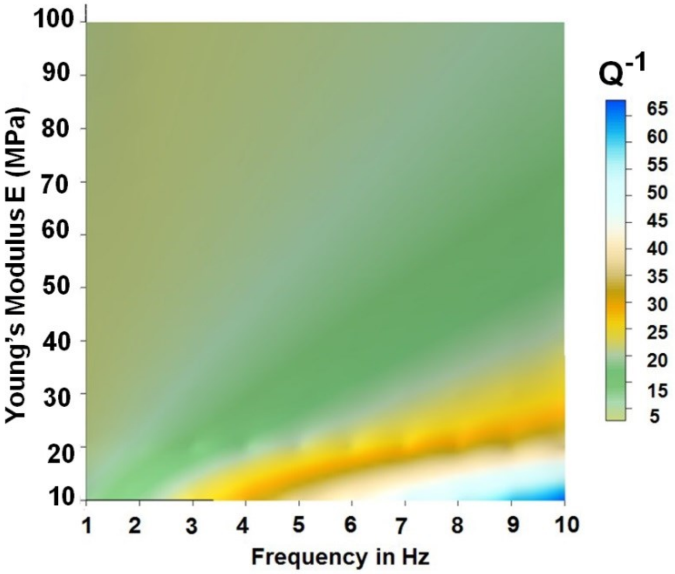

Fig. 3.4: Q^{-1} as a function of E and frequency for fixed ζ_1 and ζ_2.

Replacing the matrix [C] inside the equation (3.1)

$$-\omega^2(1+i\frac{C_M}{\omega})[M]u+(1-i\omega C_K)[K]u=[F] \tag{3.3}$$

Inside the absorbing layer, the attenuation is controlled by the imaginary part of the wave number *k*, while the real part causes impedance mismatch and generates the reflections.

Inside the absorbing layers

$$\boldsymbol{k} \propto k_{real} + ik_{imaginary} \tag{3.4}$$

And *k* is approximated with the definition for compression waves in a rod as

$$\boldsymbol{k} \propto \sqrt{\frac{\boldsymbol{\rho}}{\boldsymbol{E}}} \tag{3.5}$$

Where in complex domain

$$\boldsymbol{\rho} \rightarrow \rho\left(1+i\frac{C_M}{\omega}\right) \text{ and } \boldsymbol{E} \rightarrow E(1-iC_K) \tag{3.6 a,b}$$

In order to optimize the absorbing layer, the imaginary part should be raised without raising the real part as suggested by Pettit et al. (2014).

In order to better understand the problem, and better separate the imaginary and real parts, the expression of wavenumbers in the absorbing layer is developed in equation (3.7):

$$\boldsymbol{k} \propto \sqrt{\frac{\boldsymbol{\rho}}{\boldsymbol{E}}} = \sqrt{\frac{\rho\left(1+i\frac{C_M}{\omega}\right)}{E(1-iC_K)}} = \sqrt{\frac{\rho E-\rho EC_M C_K+i\rho E\omega C_K+\rho E\frac{iC_M}{\omega}}{E^2+E^2\omega^2 C_K{}^2}} =$$
$$= \sqrt{\frac{\rho E(1-C_M C_K)}{E^2+E^2\omega^2 C_K{}^2}+\frac{i\left(\rho E\omega C_K+\rho E\frac{C_M}{\omega}\right)}{E^2+E^2\omega^2 C_K{}^2}} = \sqrt{\frac{\rho(1-C_M C_K)}{E(1+\omega^2 C_K{}^2)}+\frac{i\rho(\omega C_K+\frac{C_M}{\omega})}{E(1+\omega^2 C_K{}^2)}} \tag{3.7}$$

Setting C_K=0 as in Pettit et al.(2014), equation (3.7) becomes

$$\boldsymbol{k} \propto \sqrt{\frac{\rho}{E}+\frac{i\rho C_M}{E\omega}} \tag{3.8}$$

Setting C_M=0, we get:

$$\boldsymbol{k} \propto \sqrt{\frac{\rho}{E(1+\omega^2 C_K{}^2)}+\frac{i\rho(\omega C_K)}{E(1+\omega^2 C_K{}^2)}} \tag{3.9}$$

Pettit et al. (2014) previously suggested putting C_K to zero and controlling the attenuation using C_M only. This will lead to sensitivity in choosing the parameters since reducing E will increase the imaginary part which is responsible for attenuation, and it will also increase the real part which is responsible for reflections at the boundary.

Inspecting equation (3.7), what is suggested in this work is that instead of setting C_K to zero, it is better to keep a relation C_M=${C_K}^{-1}$ that will totally remove the real part, in a way equation (3.7) can be rewritten in the form present in equation (3.10).

$$\boldsymbol{k} \propto \sqrt{[\frac{0}{E(1+\omega^2 C_K{}^2)} + \frac{i\rho(\omega C_K + \frac{C_M}{\omega})}{E(1+\omega^2 C_K{}^2)}]} = \sqrt{\frac{i\rho(\omega C_K + \frac{C_M}{\omega})}{E(1+\omega^2 C_K{}^2)}} = \sqrt{\frac{i\rho(\omega C_K + \frac{1}{\omega C_K})}{E(1+\omega^2 C_K{}^2)}}$$

$$= \sqrt{\frac{i\rho}{E\omega C_K}} \tag{3.10}$$

The absorbing layer properties will be calibrated using the remaining factors. Thus, *E*, C_M and C_K will be chosen in a way that optimizes the absorbing layer efficiency while always keeping C_M C_K=1.

From a rheological point of view, and using the newly defined term χ_3, the efficiency of the two assumptions discussed above is studied. By inspecting the formulation of attenuation in the Maxwell model, C_K is equal to 0 when ζ_2 is equal to 0 or *E* tends to infinity. The assumption of an *E* tending to infinity is to be discarded since this will mean a fixed boundary, and therefore the only way to achieve it is through setting ζ_2 and therefore χ_3 to zero. For the other assumption i.e. C_M C_K=1, it is only fulfilled when χ_3 satisfies the following equation $\chi_3{}^2 + \chi_3 - 1 = 0$ and therefore $\chi_3 = [(-1+\sqrt{5})/2]$ or $[(-1-\sqrt{5})/2]$. The second solution is to be discarded since it will give a negative value of attenuation. Fig. 3.5 shows a comparison between the two cases of C_K=0 and C_K=$C_M{}^{-1}$ in the Maxwell model for a fixed *E* and a frequency of 5 Hz. Fig. 3.6 shows the same comparison for a frequency of 50 Hz. For both frequencies used in the analysis, the assumption C_M C_K=1 was proven to be more efficient than the C_K=0 assumption for all values of ζ_1. A better performance on the higher frequency could be concluded when assuming C_M C_K=1.

The following parts of this work will be in order to prove the efficiency of the assumption and calibrate the most efficient absorbing layer system.

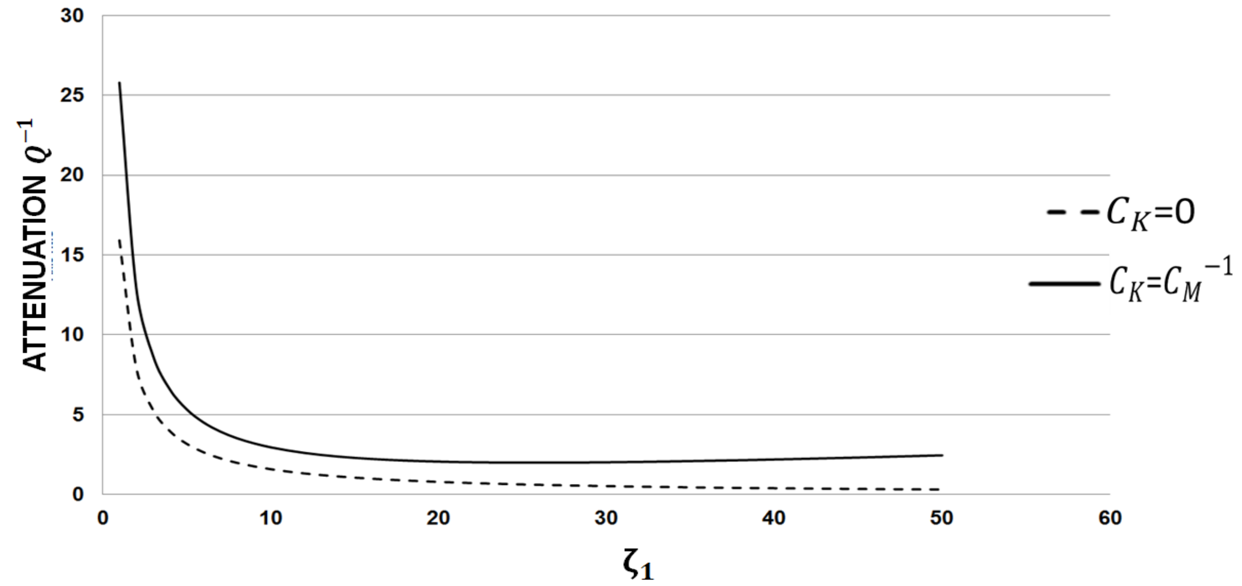

Fig. 3.5: Attenuation with respect to ζ_1 *showing the efficacy of* C_K*=0 (dashed line) vs* C_K=$C_M{}^{-1}$ *(solid line) from Maxwell Model (f=5Hz).*

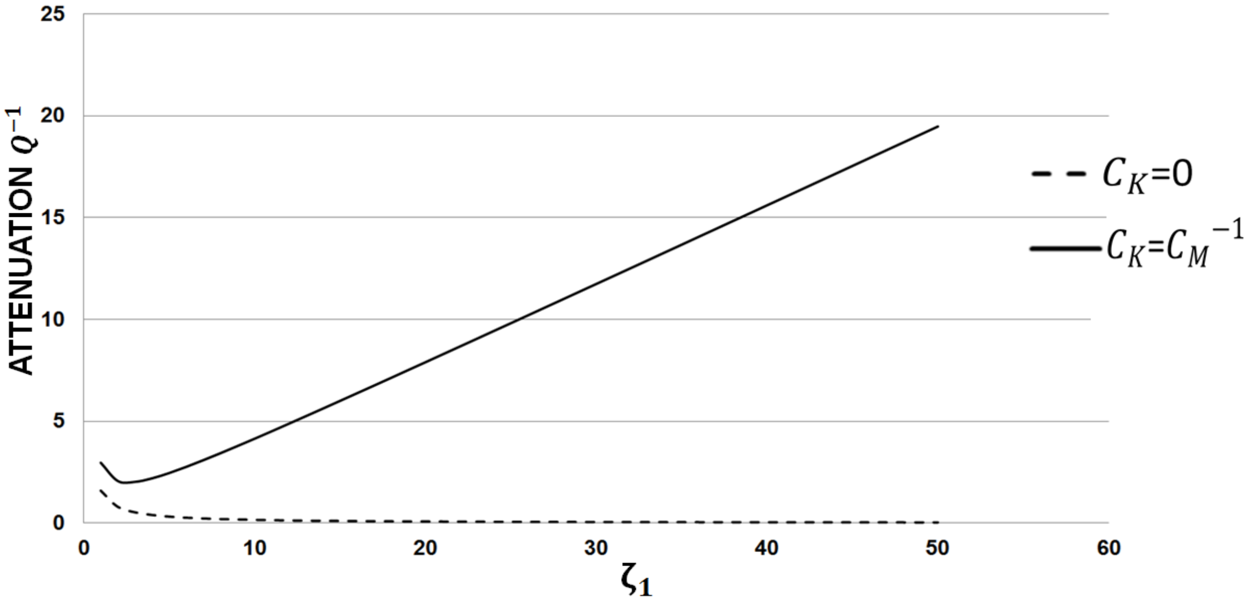

Fig. 3.6: Attenuation with respect to ζ_1 *showing the efficacy of* C_K*=0 (dashed line) vs* C_K=$C_M{}^{-1}$ *(solid line) from Maxwell Model (f=50Hz).*

3.4.3 Influence of pertinent parameters on the absorbing layer efficiency

In this section, 1D models will be assessed using the Finite Element Method. Multiple factors will be studied independently or in combination in order to check the influence of each one, leading ultimately to the best arrangement for an optimal absorbing layer. One absorbing layer having a thickness of $\lambda/4$ was applied at the boundary of the model, unless otherwise stated, where λ is the wavelength. The model is meshed with quadratic elements; the size of each element is equal to $\lambda/20$ in order to avoid wave dispersion. A total of 200 numerical simulations were carried out, the testing strategy is summarized in Fig. 3.7. A simple reference case was modeled where the absorbing layer had a constant value of E and ρ equal to that of the physical model, and values for C_K= 6.6E-04 and C_M= 377 related to a Q^{-1} =1. The material used has a shear wave velocity Vs=2200m/s.

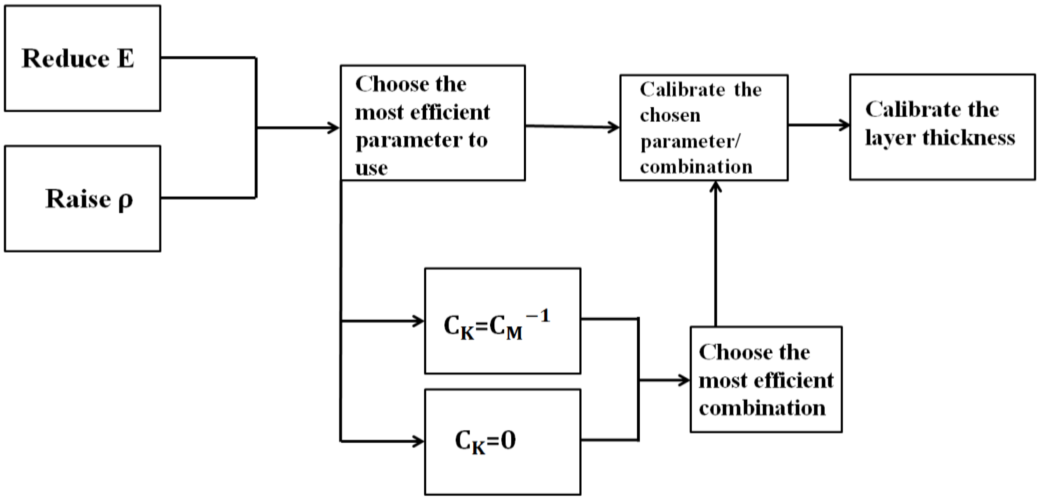

Fig. 3.7: Testing strategy involving multiple parameters.

3.4.3.1 Effect of density (ρ)

Considering equation (3.7), raising the density will normally raise the imaginary part of the equation while also raising the real part. Attenuation parameters (C_K and C_M) still have in this case a central part in defining the attenuation levels.

Fixing the remaining parameters and rising ρ improved the attenuation levels. Fig. 3.8 shows a comparison between the reference case, a 50% increase in ρ and a 300% increase in ρ respectively. The graphs represent the displacement normalized by the input's amplitude at an equidistant point between the excitation source and the absorbing layer/physical model boundary (at 40 meters distance from both sides, which is equal to around 2λ). Results are summarized in table 3.1.

Raising ρ even significantly improved slightly the attenuation level. Raising ρ to 300% of its original value improved the attenuation performance by only an average of 25%. The small effect of ρ may be, from a rheological point of view, attributed to the slight effect it will have on the elastic modulus properties of the material since E and ρ are interrelated. The rheological model presented in section 3.4.1 disregard ρ as an influencing factor.

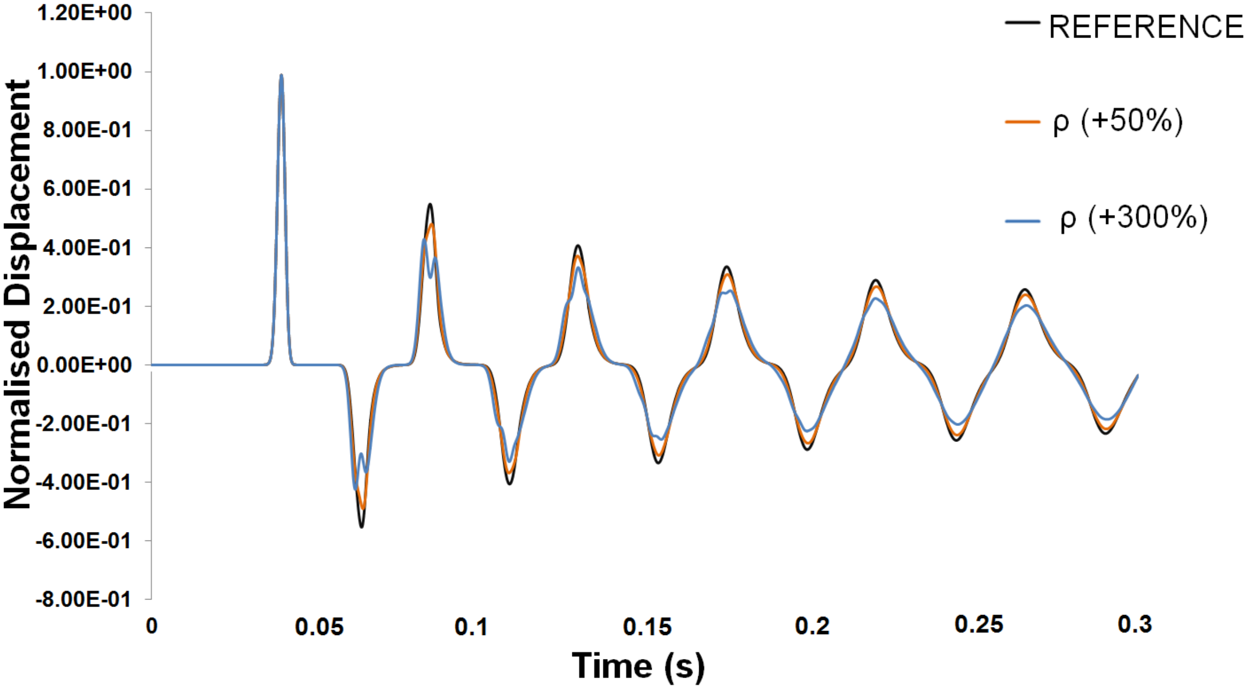

Fig. 3.8: Normalized displacement obtained by raising the value of ρ (the reference case in black, a raise of 50% in orange and a raise of 300% in blue).

	Reflection amplitude (% of the input) after 1 cycle	**Reflection amplitude (% of the input) after 3 cycles**
Reference	53%	33%
ρ(+50%)	46%	30%
ρ(+300%)	39%	25%

Table 3.1: Reflection amplitude results of increasing ρ.

3.4.3.2 Effect of modulus of elasticity (E)

Considering equation (3.7), it is clear that the more E is reduced, the bigger the imaginary part, the larger the real part as for the case of ρ. This means that while the attenuation efficiency will rise, the reflections from the absorbing layer boundaries will also rise.

In order to better assess the influence of stiffness reduction on the attenuation, all the problem parameters are fixed and the Young's modulus is reduced by different rates.

Fig. 3.9 shows a comparison between the reference case and other cases where E is reduced respectively by 30%, 70% and 90%. The graphs represent the displacement normalized by the input's amplitude at an equidistant point between the excitation source and the absorbing layer/physical model boundary (at 40 meters distance from both sides, which is equal to around 2λ).

The comparison shows that reducing E improved the attenuation in a remarkable way, and that reducing E has a much stronger effect on the attenuation than rising ρ.

Fig. 3.10 shows a comparison between the reference, a case of 90% reduction and a case of 99% reduction. It could be concluded that reducing E excessively (99%) caused reflection to rise again; therefore reducing E should be treated with caution in calibrating the absorbing layer. Table 3.2 summarizes the results of reducing E by different rates.

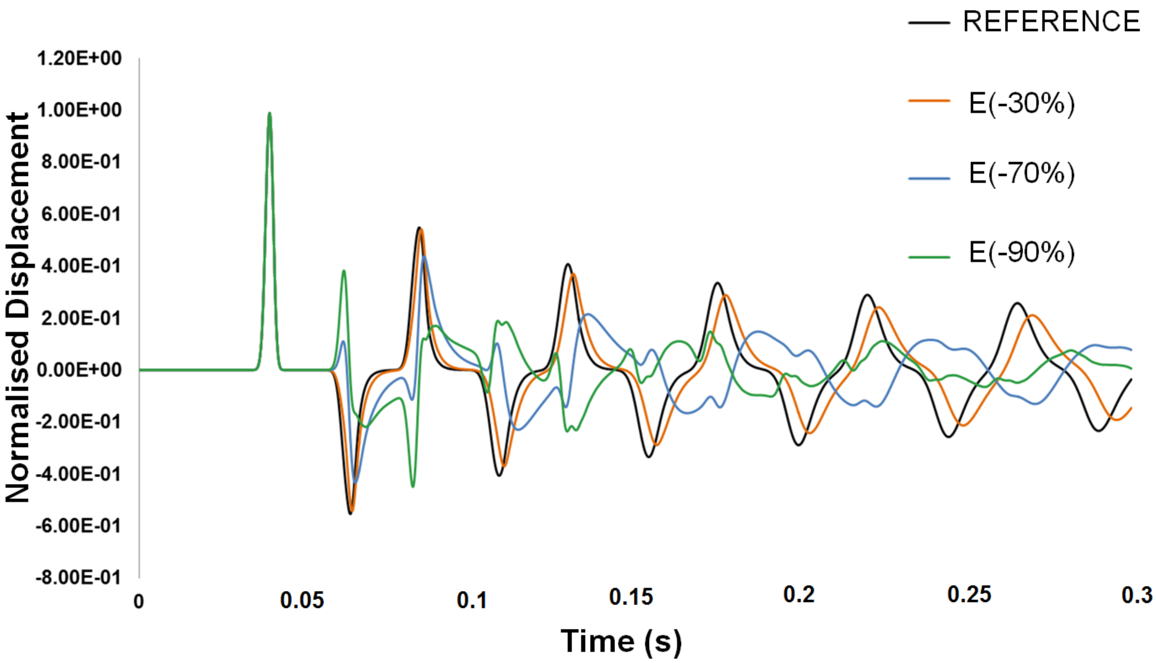

Fig. 3.9: Normalized displacement obtained by reducing the value of E (the reference case in black, a reduction of 30% in orange, a reduction of 70% in blue and a reduction of 90% in green).

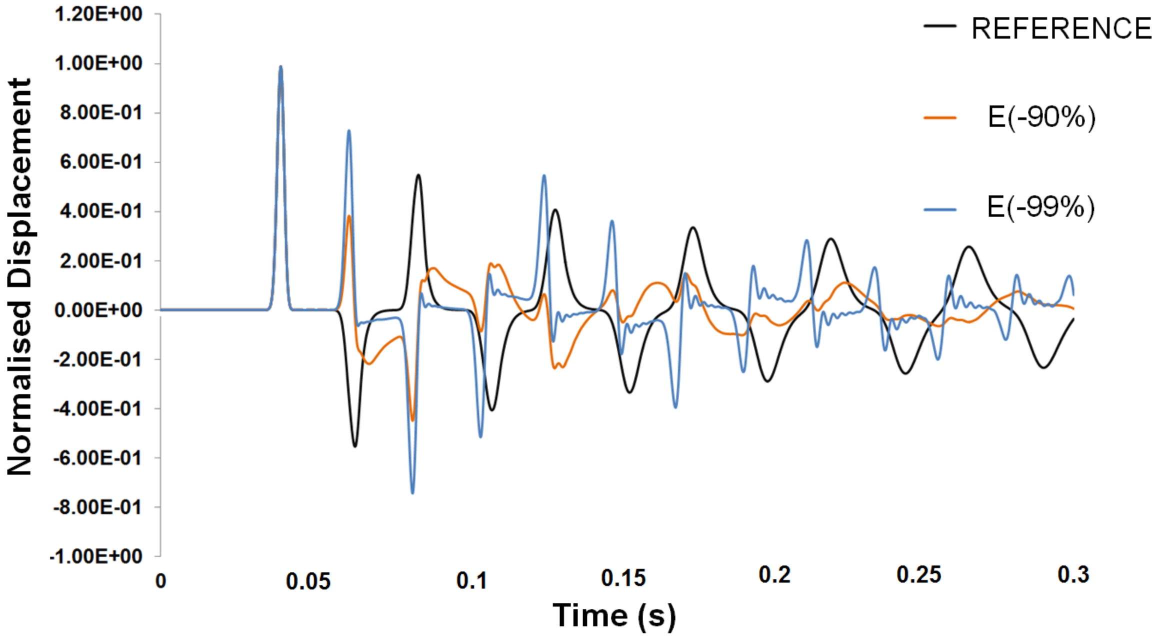

Fig. 3.10: Normalized displacement obtained by reducing the value of E (the reference case in black, a reduction of 90% in orange and a reduction of 99% in blue).

	Reflection amplitude (% of the input) after 1 cycle	**Reflection amplitude (% of the input) after 3 cycles**
Reference	53%	33%
E(-30%)	46%	30%
E(-70%)	39%	25%
E(-90%)	35%	10%
E(-99%)	70%	36%

Table 3.2: Reflection amplitude results of reducing E.

3.4.3.3 Effect C_M and C_K interrelation

From the previous two sections, it was deduced that the effect of the reduction of E is much more important than increasing ρ. In order to better assess and examine the assumption made about the C_M and C_K previously in this work, testing these two parameters will be done simultaneously while manipulating E and not ρ.

The first part will be a comparison of multiple values where C_K is set equal to ${C_M}^{-1}$ for different values of C_M compared to the same cases where C_K is set to zero (as previously suggested by Pettit et al., 2014). In section 3.4.2, a comparison between the two cases from a rheological viscoelastic constitutive relation proved the higher efficiency of C_K=1/C_M condition over the C_K=0. Fig. 3.11, 3.12 and 3.13 shows this comparison for C_M equal to 100, 200 and 500 respectively. In this part of study, a reduction of 70% of the value of E is adopted while ρ was left unchanged. The graphs represent the displacement normalized by the input's amplitude at an equidistant point between the excitation source and the absorbing layer/physical model boundary (at 40 meters distance from both sides, which is equal to around 2λ). Table 3.3 shows a clear comparison between the attenuation performances of all the six cases studied in this section.

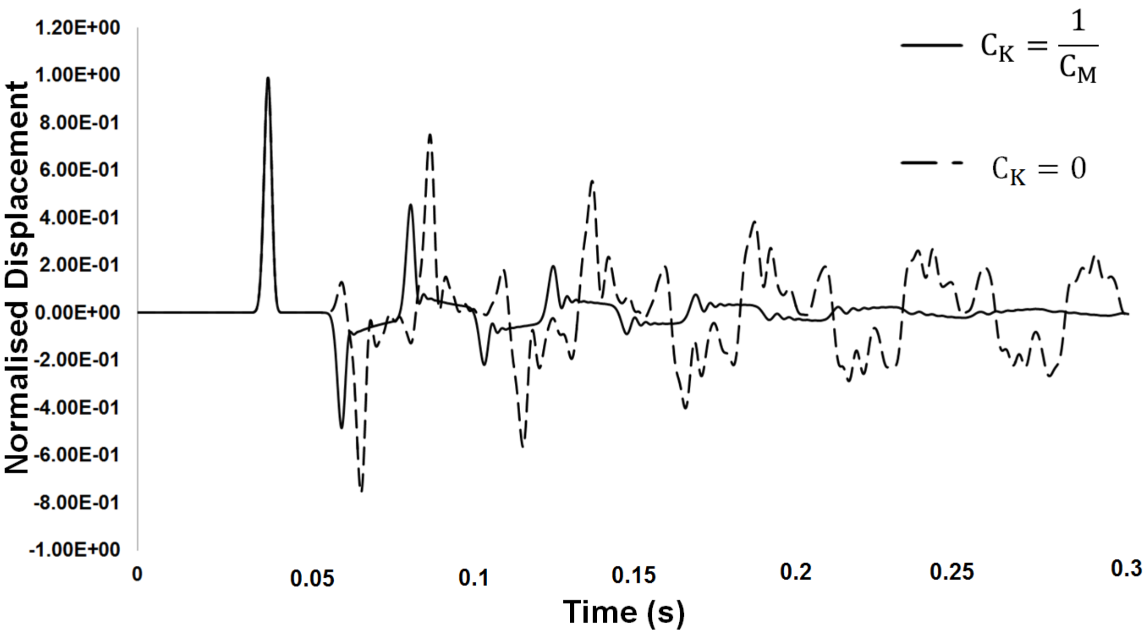

Fig.3.11: Normalized displacement obtained by a reduction a 70% reduction of E and a C_M*=100 (*C_K*=1/*C_M *represented by solid line and* C_K*=0 represented by dashed line).*

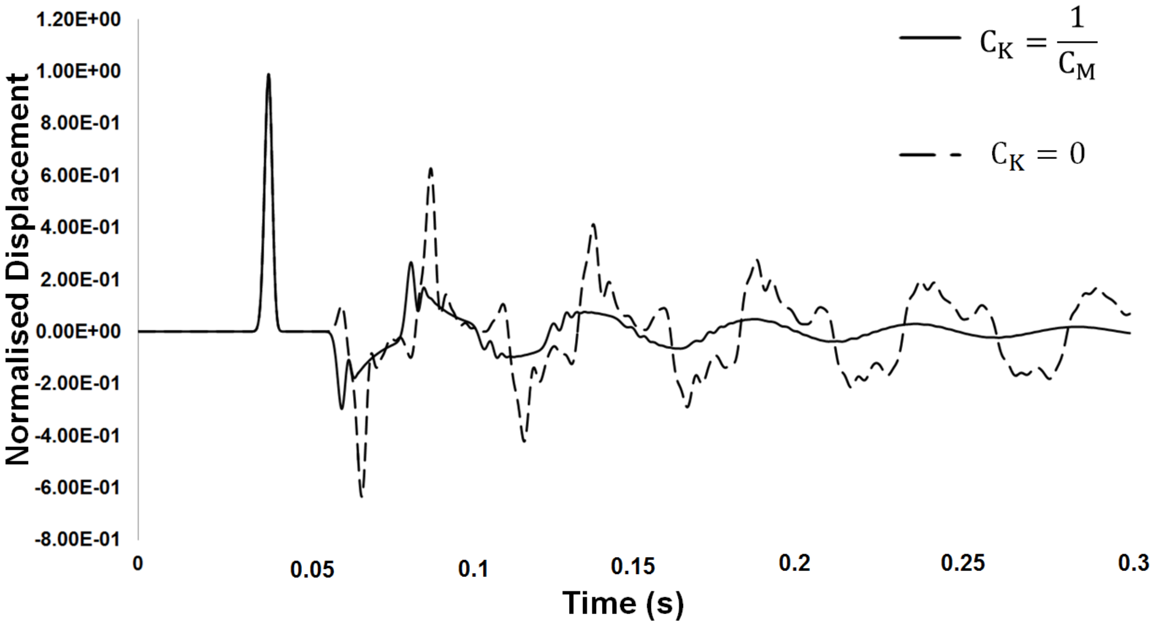

Fig.3.12: Normalized displacement obtained by a reduction a 70% reduction of E and a C_M*=200 (*C_K*=1/*C_M *represented by solid line and* C_K*=0 represented by dashed line).*

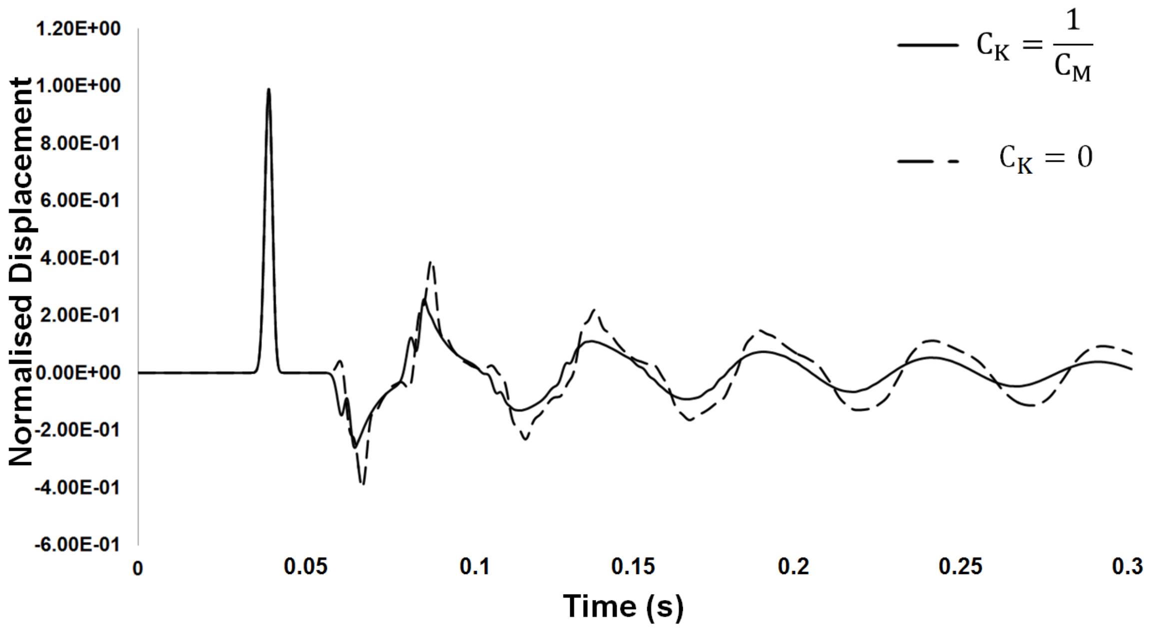

Fig. 3.13: Normalized displacement obtained by a reduction a 70% reduction of E and a C_M=500 (C_K=1/C_M represented by solid line and C_K=0 represented by dashed line).

It could be deduced that the effect of absorbing layer is much more efficient for C_K=${C_M}^{-1}$and not C_K=0. Moreover it is clear that the effect of absorbing layer is optimized at a certain value of C_M, equal to 100 in this case as shown in Fig. 3.11, 3.12, 3.13 and Table 3.3.

		Reflection amplitude (% of the input) after 1 cycle	**Reflection amplitude (% of the input) after 5 cycles**
C_M=100	C_K=${C_M}^{-1}$	45%	0.2%
C_M=100	C_K=0	75%	29%
C_M=200	C_K=${C_M}^{-1}$	27%	0.4%
C_M=200	C_K=0	61%	21%
C_M=500	C_K=${C_M}^{-1}$	23%	0.64%
C_M=500	C_k=0	39%	13%

Table 3.3: Reflection amplitude results of C_K=${C_M}^{-1}$vs C_K=0.

In order to reassure the validity of the assumption that the absorbing layer will be optimized for C_K=${C_M}^{-1}$, more parametric tests have been done where C_M is fixed and C_K is moving apart from ${C_M}^{-1}$. C_M was chosen equal to 100 since it was deduced from the previous section that for C_M=100 the absorbing layer showed the best efficacy after few cycles. Fig. 3.14 shows that for C_K=1/100 the attenuation is the best, while when moving C_K to 0.1 and 0.001 the absorbing layer is less efficient. The graphs represent the displacement normalized by the input's amplitude at an equidistant point between the excitation source and the absorbing layer/physical model boundary (at 40 meters distance from both sides, which is equal to around 2λ). Results are summarized in Table 3.4 in terms of C_K variation to a fixed C_M.

Equation (3.7) shows that when setting the real part to zero the efficiency of the absorbing layer is dependent on both E and C_M (in the imaginary part), which was also shown previously through multiple tests. In order to understand the relation between the two factors, parametric analyses have been carried out. It was noticed that for each reduction value, the optimized result was with a different C_M. It was also noticed that the more E is reduced, the smaller the relevant C_M is (see Rheological model section 3.4.1).

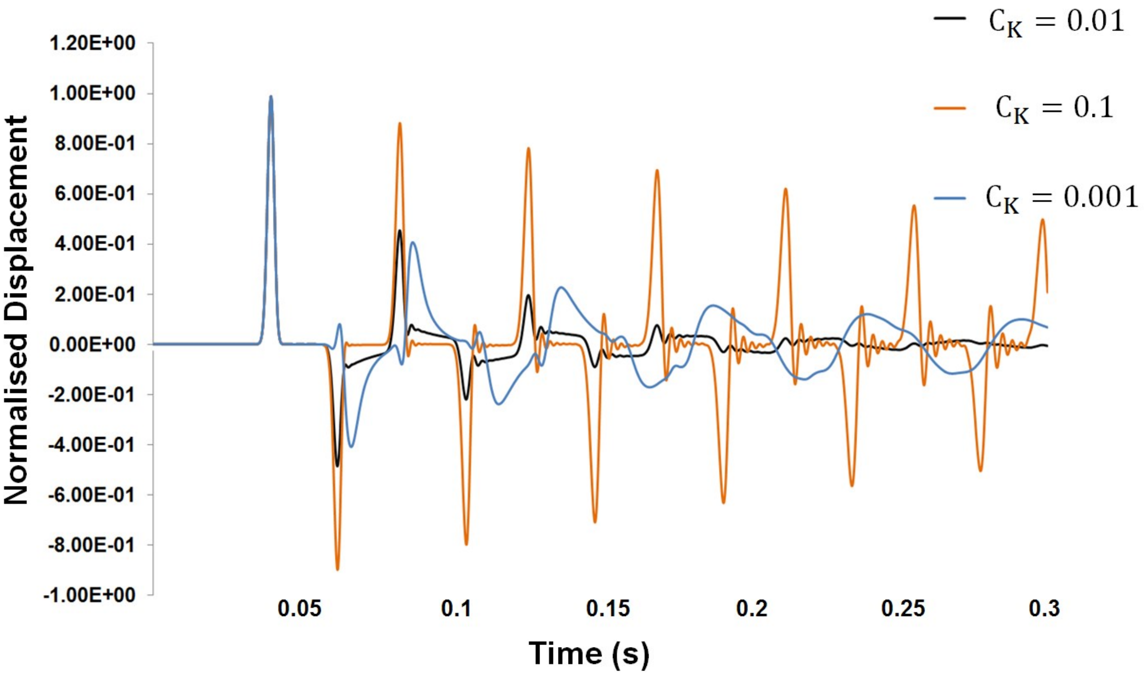

Fig. 3.14: Normalized displacement obtained by varying C_K around 1/C_M (C_K = 0.01 in black, C_K=0.1 in orange and C_K=0.001 in blue).

		Reflection amplitude (% of the input) after 1 cycle	**Reflection amplitude (% of the input) after 5 cycles**
C_M=100	C_K=0.01	45%	0.2%
C_M=100	C_K=0.1	90%	29%
C_M=100	C_K=0.001	38%	11%

Table 3.4: Reflection amplitude results of C_K sensitivity study.

Fig. 3.15 shows the efficiency of three different cases of reduction respectively 70%, 80% and 90%. The most relevant C_M value for each reduction was respectively equal to 320,160 and 100. The graphs represent displacement normalized by the input's amplitude at an equidistant point between the excitation source and the absorbing layer/physical model boundary (at 40 meters distance from both sides, which is equal to around 2λ).

The first combination (E reduced by 70% and C_M=320) reduced the incident wave by 76% after one cycle. The second combination (E reduced by 80% and C_M=160) reduced the incident wave by 85% after one cycle. The third combination (E reduced by 90% and C_M=100) reduced the incident wave by 93% after one cycle. The results are summarized in Table 3.5.

			Reflection amplitude (% of the input) after 1 cycle	**Reflection amplitude (% of the input) after 3 cycles**
E(-70%)	C_M=320	$C_K=C_M{}^{-1}$	24%	4%
E(-80%)	C_M=160	$C_K=C_M{}^{-1}$	15%	2%
E(-90%)	C_M=100	$C_K=C_M{}^{-1}$	7%	0.3%

Table 3.5: Reflection amplitude results of C_M and E calibration.

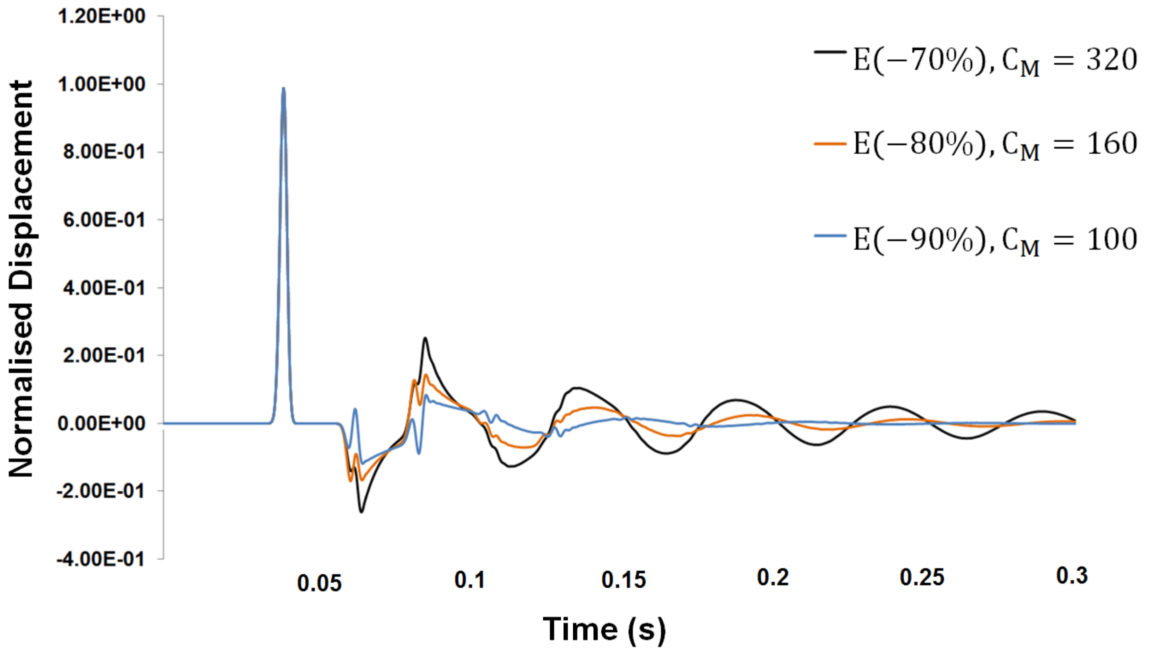

Fig. 3.15: Normalized displacement obtained for optimizing E and C_M*(a reduction of E by 70 % and a* C_M*=320 in black, a reduction of E by 80 % and a* C_M*=160 in orange and a reduction of E by 90 % and a* C_M*=100 in blue).*

3.4.3.4 Effect of layer size

The layer thickness is an important parameter in defining an absorbing layer since it is linked directly to the cost and efficiency of the FEM model. In order to better understand the relation between the layer thickness and the multiple factors studied above, multiple tests have been carried out where the multiple parameters including the layer thickness were varied.

It was shown that the larger the layer, the less E should be reduced to get a maximum efficiency. Applying an absorbing layer at the boundaries of thickness λ, the best performance of absorbing layer is reached when E is reduced by 50% and for C_M=1000. While for a layer of λ/4, the best attenuation is reached when E is reduced by 90% and for C_M=100. When reducing the layer thickness to λ /18, E could be reduced by 99% and C_M to 40 and thus the maximum attenuation is achieved.

Fig. 3.16 shows a comparison between the three cases discussed above. The best attenuation behavior is from the thinnest layer. The reflections do not exceed 6% from the input amplitude for λ /18, while for λ /4 and λ, the values were 11% and 19% respectively. For the thinnest layer

(λ /18), the reflections become equal to zero first, before the two other cases. The graphs represent the displacement normalized by the input's amplitude at an equidistant point between the excitation source and the absorbing layer/physical model boundary (at 40 meters distance from both sides, which is equal to around 2λ).

From the previous part, it was deduced that the absorbing layer size reduction requires a parallel reduction for the values of E and C_M, leading all together to a higher efficiency. This proves that the efficiency of the absorbing layer model is a multi-parameter problem.

When the size is reduced to $\lambda/180$ and E is reduced to 1.10^{-6} of its original value, while keeping the C_K=${C_M}^{-1}$ condition, it was found that C_M also should be massively reduced in order to reach the best attenuation. C_M value should be reduced to less than 1 and hence C_K increased to larger values for this case. As shown in Fig. 3.17, calibrating the thin-absorbing-layer with a reduction of E to 1.10^{-6} of its original value and setting C_M=1/22 and C_K=22, the reflections amplitudes are at 0.0001%. The summary of the results of this part is shown in table 3.6.

				Reflection amplitude (% of the input) after 1 cycle
λ	E(-50%)	C_M=1000	C_K=${C_M}^{-1}$	19%
λ/4	E(-90%)	C_M=100	C_K=${C_M}^{-1}$	11%
λ/18	E(-99%)	C_M=40	C_K=${C_M}^{-1}$	6%
λ/180	E(-99.9999%)	C_M=0.045	C_K=${C_M}^{-1}$	0.0001%

Table 3.6: Reflection amplitude results of changing layer thickness.

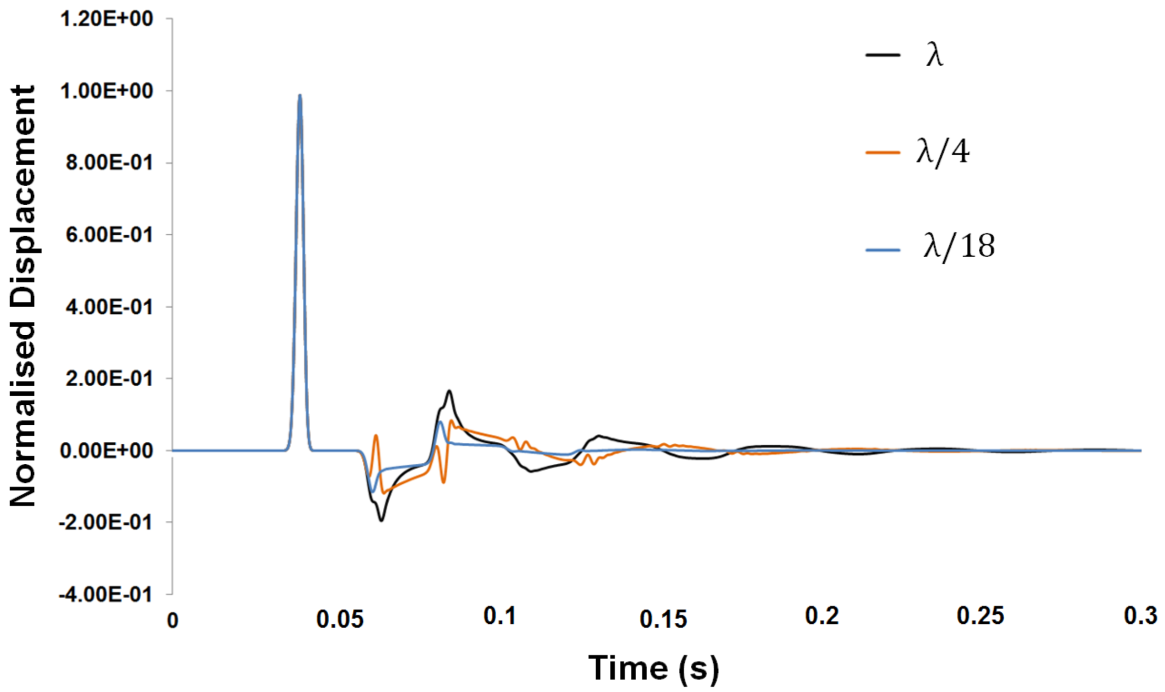

Fig. 3.16 Normalized displacement obtained for varying and optimizing thickness (black for thickness of λ, orange for λ/4 and blue for λ/18).

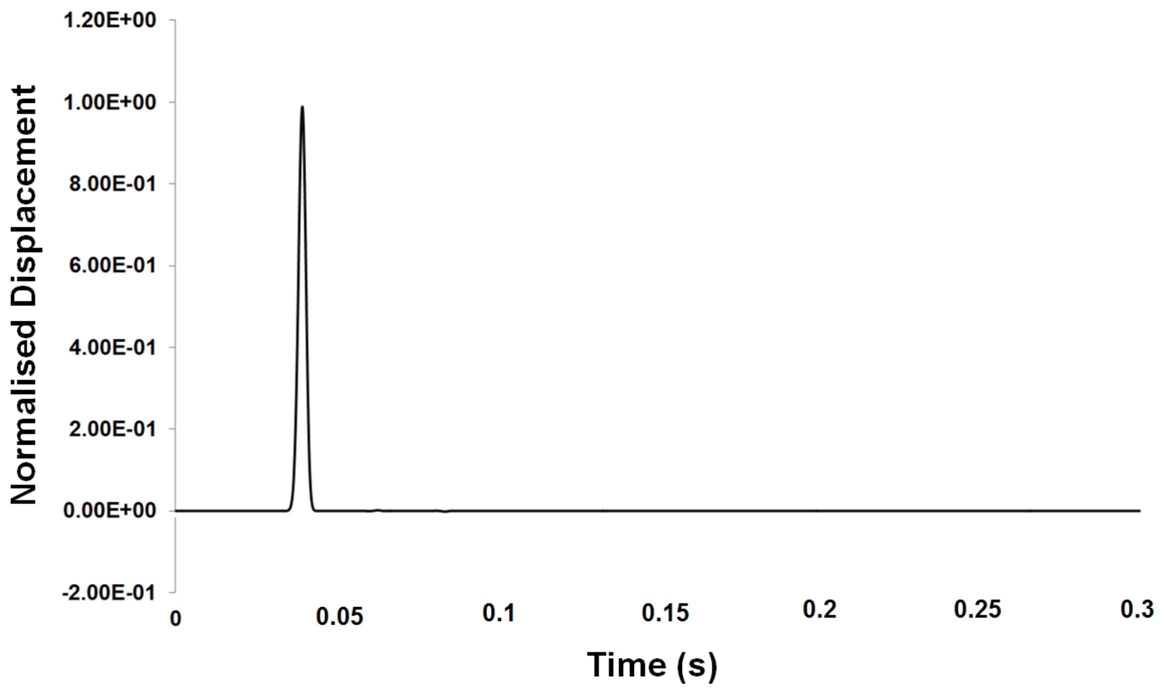

Fig. 3.17: Normalized displacement obtained for the thin-absorbing-layer.

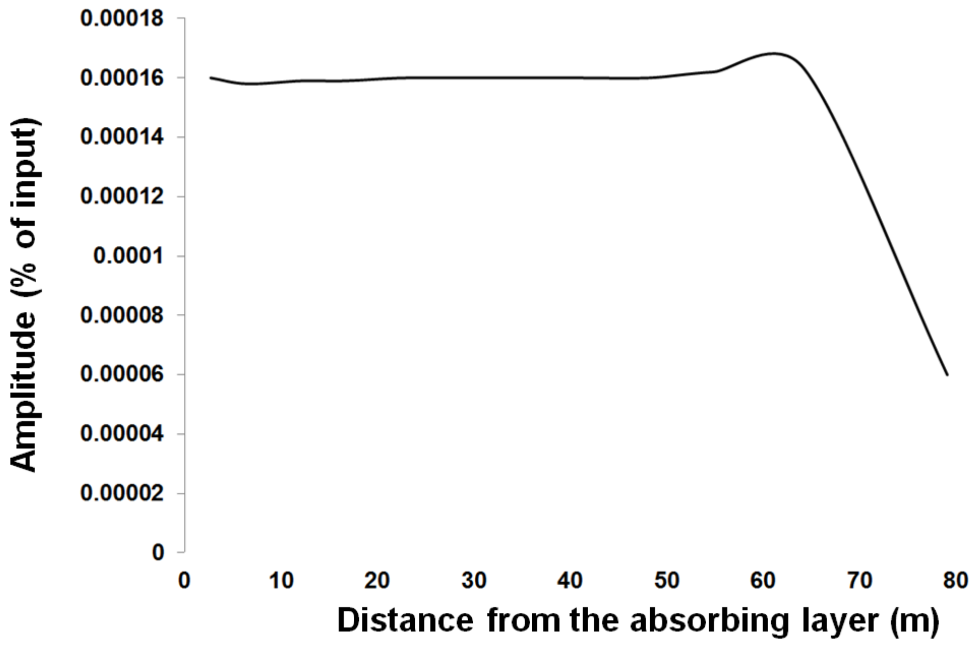

Fig. 3.18: Maximum amplitude of the reflected wave from the absorbing layer against the distance from the absorbing layer.

3.4.4 Sensitivity to different materials

Changing the studied materials in the physical domain will normally change the properties of the absorbing layers, especially that when defining and calibrating the absorbing layer previously, it was done according to a known λ associated to a defined material. Changing thus the material will change the value of λ and therefore the absorbing layer will need to be tuned with respect to the wavelengths/modulus.

Since the defined layer is already very small (λ /180) for Vs=2200m/s, and in order to study the absorbing layer for different materials, the thickness of the absorbing layer will be considered constant.

Lowering the value of Vs and thus E, and in congruence with the previous results, the optimized layer was found through decreasing C_M (and therefore rising C_K). For instance, keeping the same layer thickness and the same degree of reduction which is to 1.10^{-6} of E, the maximum attenuation for Vs=1600m/s was for a C_K equal to 40 (and C_M=1/40). In the case of Vs=1200m/s was for a C_K equal to 60 (C_M=1/60). Hence, smaller Vs require a larger C_K when fixing the thickness and the reduction rate of the layer.

3.4.5 Sensitivity to frequency content

Testing with different pulses at various frequencies showed always the same high efficiency of the absorbing layer (reflections less than 0.01%). For instance reducing the frequency content by a factor of 10 has no significant influence on the absorbing layer efficiency. Reducing the frequency content by a factor of 10 means that the thickness of the absorbing layer is equal to λ/18 and not λ/180 anymore. Higher frequencies require therefore a relatively thinner layer.

3.4.6 Absorbing Layers for 2D-models

In order to check the efficiency of the absorbing layer for FEM problems, the absorbing layer was tested in 2D models. The following models will be related to cases of rock where Vs=2200m/s. A surface excitation was applied and displacement in the vertical direction is considered. Fig. 3.19 shows a representation of the 2D models used in the analysis.

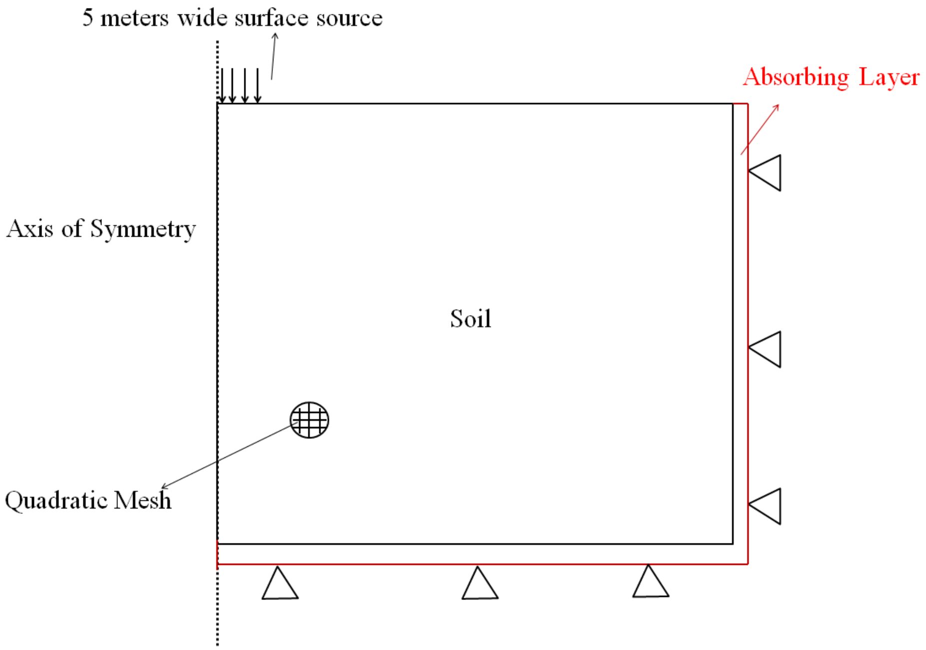

Fig. 3.19: Representation of the 2D axisymmetric model used in the analysis showing the absorbing layer, the surface source and the soil physical domain.

Fig. 3.20 shows a comparison between three cases. The first one is for the 2D model without the absorbing layer. The second is for a case where C_K=22 and C_M=${C_K}^{-1}$ and for E reduced to 1.10^{-6} of its original value (which was the optimized case in 1D). The third is for a case where C_K is doubled and therefore equal to 44, and keeping C_M=${C_K}^{-1}$ and E reduction was of 1.10^{-6} of its original value. The graphs represent the displacement normalized by the input's amplitude at an equidistant point between the excitation source and the absorbing layer/physical model boundary. While for the first case the reflection is clear and its amplitude is very high as shown, for the second and the third cases the reflections are 10% and 0.2% of the incident wave amplitude. It could be concluded that doubling the value of C_K was necessary in order to take the 2D effects in consideration.

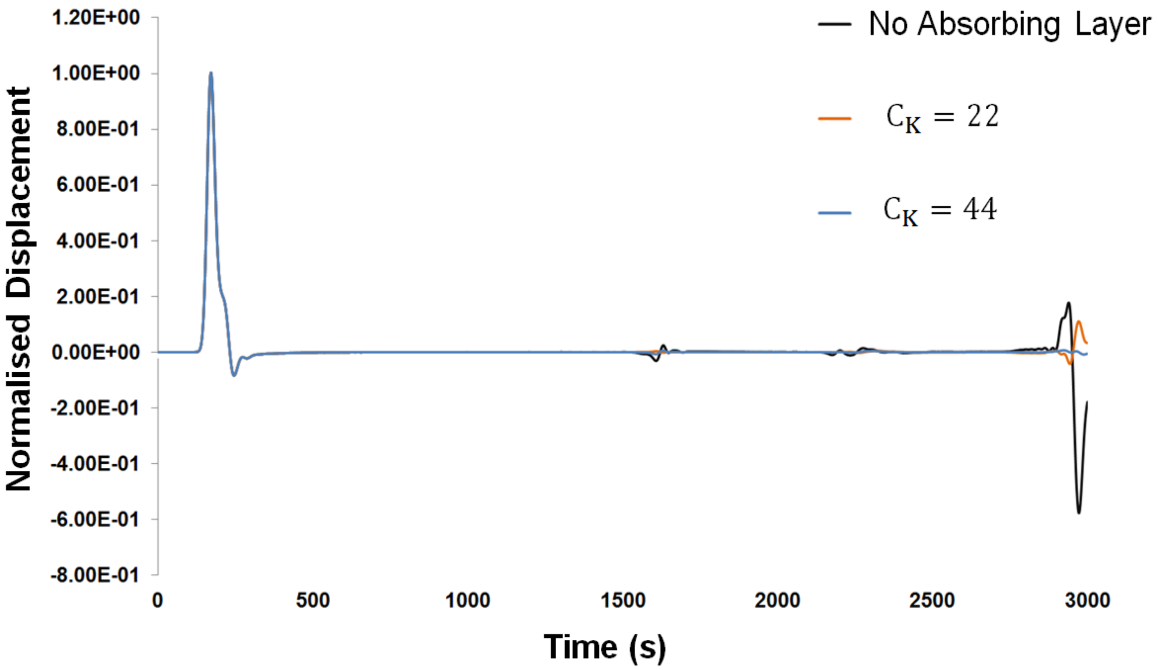

Fig. 3.20: Normalized vertical displacement obtained for 2D Comparison for high frequency pulse (black without absorbing layer, orange and blue for a stiffness reduced layer with C_K equal to 22 and 44 respectively).

Fig. 3.21 shows the same comparison as the one above for a lower frequency signal (reducing the frequency content ten times) using exactly the same absorbing layers described above (same C_K and E reduction and size). As before, without the presence of the absorbing layer the reflections were clear. The absorbing layer of the third case (C_K=44) had the best performance where reflections never exceeded 0.4% and for the second case the reflections never exceeded 1.6%. This result asserts the previous conclusion that doubling the value of C_K was necessary in order to take the 2D effects in consideration. Results from the 2D analysis are summarized in table 3.7.

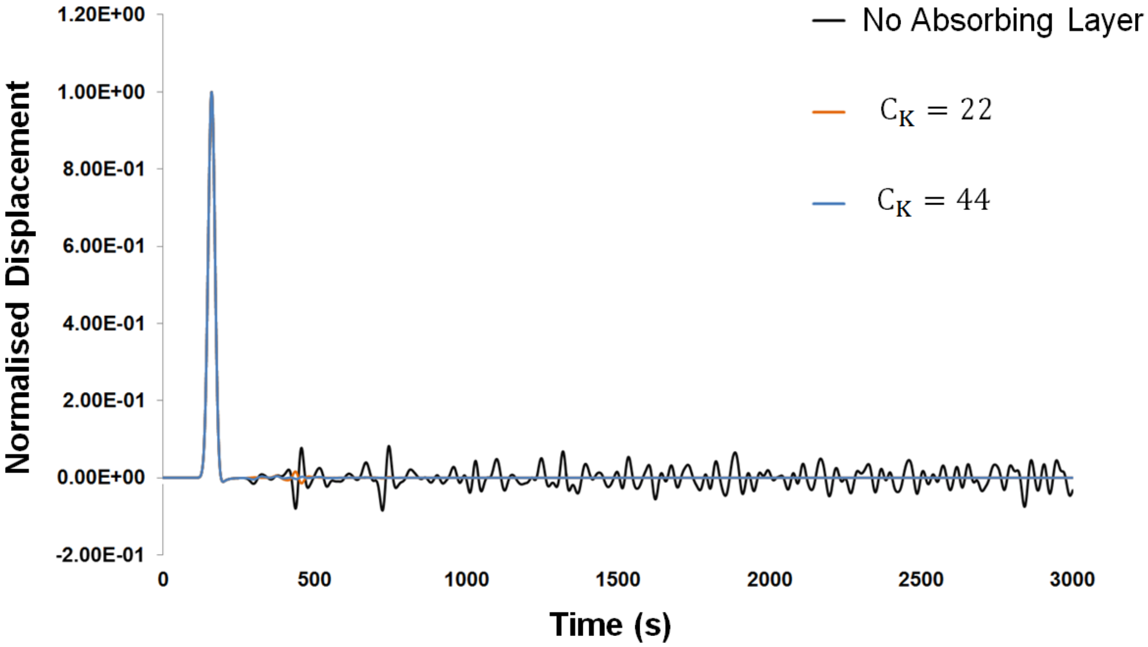

Fig. 3.21: Normalized vertical displacement obtained for 2D Comparison for low frequency pulse (black for the absence of an absorbing layer, orange and blue for a stiffness reduced layer with C_K equal to 22 and 44 respectively).

		Reflection amplitude (% of the input) after 1 cycle
High-Frequency	C_K=22	10%
High-Frequency	C_K=44	0.2%
Low-Frequency	C_K=22	1.6%
Low-Frequency	C_K=44	0.4%

Table 3.7: Reflection amplitude results of the 2D analysis.

3.5 Validation of the modelling considering a canonical problem

Sir Lamb addressed wave propagation problem in 1903 (Lamb, 1903), analytical solutions were later referred to as the Lamb problem.

In order to validate the numerical models, a Lamb solution for a vertical point load on the surface of an elastic half space using a Heaviside excitation was used. The response on the vertical direction in the far field was calculated (Fig. 3.22). Using a convolution integral the response of an excitation pulse used in numerical models could be calculated and then compared to the numerical results.

Comparisons between the results from the finite element models and the analytical solution are shown in Fig. 3.23 for a soil with *Vs*=2000m/s. The analytical model equations and procedure can be found in details in Foinquinos and Roesset (2000).

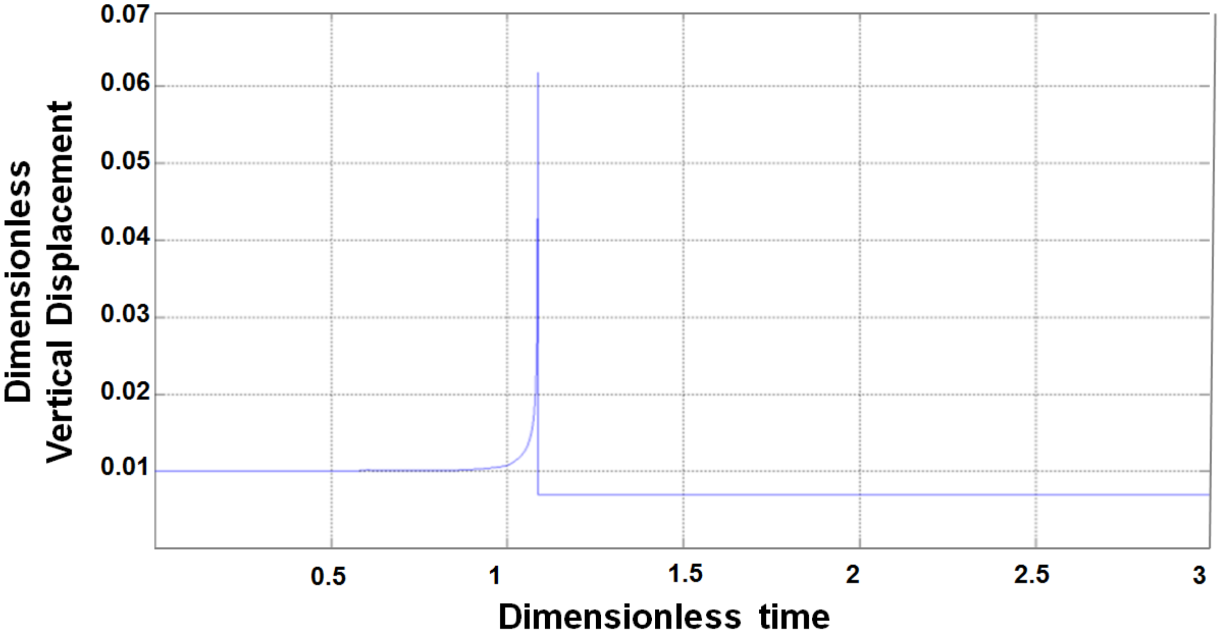

Fig. 3.22: Lamb solution for a Heaviside excitation (dimensionless vertical displacement).

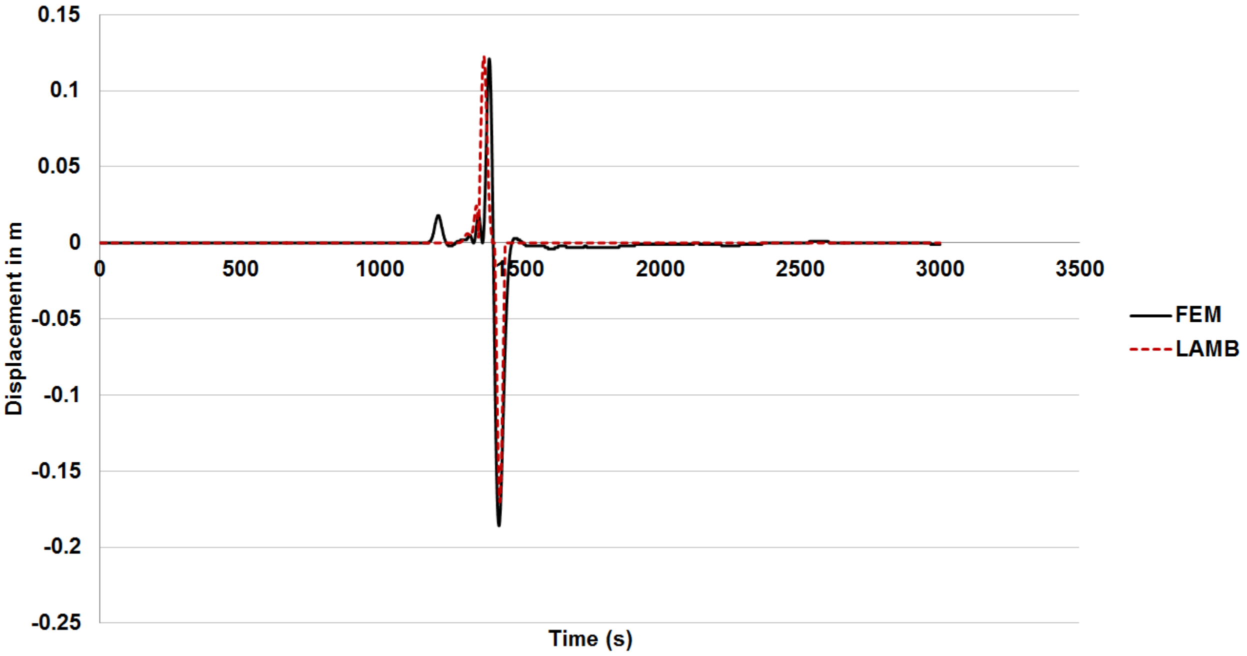

Fig. 3.23: Comparison between FEM solution of displacement (solid black) and Lamb solution (dashed red).

3.6 Conclusions and recommendations

The proposed finite element models intended a realistic simulation of vibration propagation in soils. The materials properties were chosen in coherence with formulations from the literature, meshing was refined in order to avoid numerical dispersion and a wide frequency band was imposed on the soil through a fixed surface source. Absorbing layers were applied on the physical model boundaries in order to avoid spurious reflections. A considerable part of this chapter was dedicated to the development of a new strategy for absorbing layers calibration which adds a contribution to existing CALM methods in the literature.

The design of an absorbing layer should be carefully done for each case independently i.e. when varying the modulus E and therefore the wavelength λ. It was deduced that the massive reduction of E with the absorbing layer size coupled with a convenient values for C_K and C_M could lead to a highly efficient and cheap absorbing layer.

Some general conclusions could be deduced. The values used for the calibration in this work may vary as stated before, depending on the type of materials of the study. The most important conclusions are summarized in Table 3.8.

Absorbing Layer Properties	
Materials	• The effect of increasing ρ is negligible if compared to the effect of reducing E • Reducing E as much as possible will improve the performance of the absorbing layer. C_M=${C_K}^{-1}$ must be fulfilled in order to neutralize the real part of wavenumber and therefore dilute the reflections due to the contrast between the physical model and the absorbing layer • C_M should be reduced proportionally with E (therefore C_K should be raised) • C_K will be bigger than C_M for massive *E* reduction cases. • For weaker materials (smaller *Vs*), C_K should be larger (assuming a fixed layer thickness).
Layer Size	• The absorbing layer properties and parameters are dependent from frequency and therefore of the wavelength λ. It was deduced that the higher the frequency content the thinner the absorbing layer is supposed to be (in function of λ).
Idealization	• For 2D cases, C_K should be doubled comparing to 1D cases.

Table 3.8: The most important conclusions for the absorbing layer calibration considering materials, layer size and idealization properties.

In order to facilitate the design of the absorbing layer, the size of the layer and the reduction of E could be fixed (equivalent to one node in this case and $1.10^{-6}E$ respectively in this study) and the remaining should be controlled through C_K.

It was deduced that in order to reduce E to the lowest possible value, the thickness should have been reduced significantly. While reducing E massively, C_K was to have been substantially increased (while reducing C_M proportionally), this is valid from a rheological point of view. In the Generalized Maxwell model, $C_K = (\zeta_2/E)$ and $C_M = [E(\zeta_1 + \zeta_2)/{\zeta_1}^2]$, therefore when E is reduced C_K is raised and conversely for C_M.

The probable reason why reducing the thickness along with the remaining changes (of E) caused the incident wave to disappear is the possible huge phase shift (due to much smaller E and a very small thickness). This supposedly considerable phase shift trapped the wave inside the absorbing layer. The propagation problem inside the suggested absorbing layer shows some similarity with the evanescent/inhomogeneous waves and fields, where total reflections and refractions occur and waves are considered not to propagate.

The following recommendations are given:

- more investigation of the 2D problem in order to better understand the necessity of doubling the value of C_K.
- more investigation about the relation between the frequency content and the thickness of the absorbing layer.
- more research on a coherent formulation of variation of absorbing layer properties with physical domain material properties.

3.7 Reference

Berenger, J. P. (1994). A perfectly matched layer for the absorption of electromagnetic waves. *Journal of computational physics*, *114*(2), 185-200.

Bettess, P. (1992). *Infinite elements*. Penshaw Press.

Chadwick, E., Bettess, P., and Laghrouche, O. (1999). Diffraction of short waves modelled using new mapped wave envelope finite and infinite elements. *International Journal for Numerical Methods in Engineering*, *45*(3), 335-354.

Chew, W. C., and Liu, Q. H. (1996). Perfectly matched layers for elastodynamics: A new absorbing boundary condition. *Journal of Computational Acoustics*, *4*(No.04), 341-359.

Drozdz, M. B. (2008). *Efficient finite element modelling of ultrasound waves in elastic media* (Doctoral dissertation, Imperial College London).

Engquist, B., and Majda, A. (1979). Radiation boundary conditions for acoustic and elastic wave calculations. *Communications on pure and applied mathematics*, *32*(3), 313-357.

Foinquinos, R. and Roesset J.M. (2000). Elastic layered half-spaces subjected to dynamic surface loads. *Wave motion in earthquake engineering (WIT Press)*, 141-191.

Gardner, G. H. F., Gardner, L. W., and Gregory, A. R. (1974). Formation velocity and density-The diagnostic basics for stratigraphic traps. *Geophysics*, *39*(6), 770-780.

Hastings, F. D., Schneider, J. B., and Broschat, S. L. (1996). Application of the perfectly matched layer (PML) absorbing boundary condition to elastic wave propagation. *The Journal of the Acoustical Society of America*, *100*(5), 3061-3069.

Humbert, P., Dubouchet, A., Fezans, G., & Remaud, D. (2005). CESAR-LCPC, un progiciel de calcul dédié au génie civil. *Bulletin des laboratoires des ponts et chaussées*, *256*(No.257), 7-35.

Lamb, H. (1904). On the propagation of tremors over the surface of an elastic solid. *Philosophical Transactions of the Royal Society of London. Series A, Containing papers of a mathematical or physical character*, *203*, 1-42.

Liu, G. R., and Jerry, S. Q. (2003). A non-reflecting boundary for analyzing wave propagation using the finite element method. *Finite elements in analysis and design*, *39*(5), 403-417.

Meza-Fajardo, K. C., and Papageorgiou, A. S. (2008). A nonconvolutional, split-field, perfectly matched layer for wave propagation in isotropic and anisotropic elastic media: stability analysis. *Bulletin of the Seismological Society of America*, *98*(4), 1811-1836.

Olsen, K. B., Day, S. M., and Bradley, C. R. (2003). Estimation of Q for long-period (> 2 sec) waves in the Los Angeles basin. *Bulletin of the Seismological Society of America*, *93*(2), 627-638.

Pettit, J. R., Walker, A., Cawley, P., and Lowe, M. J. S. (2014). A stiffness reduction method for efficient absorption of waves at boundaries for use in commercial finite element codes. *Ultrasonics*, *54*(7), 1868-1879.

Rajagopal, P., Drozdz, M., Skelton, E. A., Lowe, M. J., and Craster, R. V. (2012). On the use of absorbing layers to simulate the propagation of elastic waves in unbounded isotropic media using commercially available finite element packages. *NDT and E International*, *51*, 30-40.

Semblat, J. F. (1997). Rheological interpretation of Rayleigh damping. *Journal of Sound and Vibration* 206, 741-744

Semblat, J. F., and Brioist, J. J. (2000). Efficiency of higher order finite elements for the analysis of seismic wave propagation. *Journal of Sound and Vibration*, *231*(2), 460-467.

Semblat, J. F., and Pecker, A. (2009). Waves and vibrations in soils. Earthquakes, traffic, shocks, IUSS Press.

Semblat, J. F., Lenti, L., and Gandomzadeh, A. (2011). A simple multi-directional absorbing layer method to simulate elastic wave propagation in unbounded domains. *International Journal for Numerical Methods in Engineering*, *85*(12), 1543-1563.

Wang, T., and Tang, X. (2003). Finite-difference modeling of elastic wave propagation: A nonsplitting perfectly matched layer approach. *Geophysics*, *68*(5), 1749-1755.

Zafati, E., Brun, M., Djeran-Maigre, I., and Prunier, F. (2014). Multi-directional and multi-time step absorbing layer for unbounded domain. *Comptes Rendus Mécanique*, *342*(9), 539-557.

Chapter 4

Vibration Attenuation and Amplification in Soils

4.1 Introduction

Vibration prediction in soils is still a challenging task for civil engineers. The absence of a coherent methodology to quantify the amount of vibration left the complexity of the problem to be treated in a case by case manner. The aim of this part of the thesis is to establish a method using relevant parameters useful for finding a site classification and a coherent quantification approach for the induced vibration levels. Such an approach should account for attenuation phenomena and site amplification respectively.

Local site conditions and the related amplification of seismic waves represent a widely studied topic in seismology and earthquake engineering (Bard and Bouchon, 1985; Semblat et al., 2002). Site effects/amplification are directly associated to the material impedance and to geometrical irregularities or both (Semblat et al., 2005). Multiple examples of seismic wave amplifications were recorded, for instance 1985 Mexico City earthquake, 1995 Kobe earthquake and 1999 Chi-Chi earthquake.

In order to quantify site effects and therefore achieve a reliable site classification, multiple approaches and various parameters are suggested in the literature.

The most famous parameter used in the classification of soils nowadays is V_{S30}, which is the harmonic average shear-wave velocity is in the first 30 m. V_{S30} was first proposed by Borcherdt and Glassmoyer (1992) and Borcherdt (1994). V_{S30} is nowadays probably the most widely used parameter in site classification, notably in the Eurocode 8. V_{S30} appears to be agreed on in terms of its good performance when classifying sites (Boore, 2004; Idriss, 2009).
However doubts about the capability of V_{S30} to lead a good site response classification and prediction, pushed toward the research of alternative or complementary proxies.

A proxy which is V_{S10} was proposed by Gallipoli and Mucciorelli (2009) as an alternative for V_{S30} and deduced both parameters have comparable precision.

Abrahamson and Silva (2008) proposed a factor Z_{1000} along with V_{S30} in order to discriminate sites as shallow, medium and deep; Z_{1000} represented the depth at which V_S reaches at least 1000m/s.

Cadet el al. (2008, 2012) suggested a new categorization of soils using $V_{S(z)}$where z represents a given depth, in meters, in the range of 5 to 30 meters. An added factor was f_0 which is the fundamental frequency of the site. Their study yielded to consider the V_{S30} and f_0 as the best combination for site classification while upholded the possibility of classifying sites using f_0 only.

Luzi et al. (2011) analyzed factors such as average shear wave velocity to the bedrock V_{Sbed} and average shear wave velocity for different depths V_{SH}. Their study yielded to the conclusion that the best method of classification was when considering V_{S30} and f_0 (similar to Cadet et al., 2008), which he also concluded that they are independent.

Regnier et al. (2014) suggested a velocity gradient-proxy B_{30} describing the change in material contrast with depth. The gradient-factor associated to V_{S30} and f_0 showed to be a very good combination for prediction and therefore classification of sites.

In this chapter the derivation of velocity-gradient proxies relevant for the problem of vibration is discussed. After that a methodology for the vibration prediction in multilayered soils using the suggested proxies is presented under two forms: simple in the time domain and spectral. At the end, further discussions about the spectral response of soils from numerical models are presented using an H/V analysis from numerical results.

4.2 Velocity-Gradient proxies suggestion

For the purpose of analyzing the soil response under excitations with high frequencies originating from surface sources, the existing parameters used in earthquake engineering should be modified. The modifications aim to consider the peculiar aspects of the wave propagation for these kinds of sources. Higher frequencies are associated to smaller wavelength, since wavelength is inversely proportional to frequency. That will intuitively mean that the parameters will be associated to smaller scales in general and shallower depths in particular.

Unlike studies dealing with sites struck by earthquakes where the waves come from below the surface, the soil surface response for high frequencies surface sources is mainly dominated by Rayleigh waves/surface waves (R-waves). The dominance of surface waves in the case of vibrations will eliminate the idea of using factors describing the shear wave velocity at larger depths, for instance V_{s30} and V_{s20}. The alternative will be the use of a parameter capable of describing the very top layer of a complex soil system where the R-waves will be dominant. In order to find such a parameter, an approximation should be adopted that fits the best possible the wide range of soil types encountered by civil engineers. Thus this study is focalized on three soil types representing the range of soils usually encountered in shallow depths (as surface layers). The three chosen soil types are characterized by Vs=100m/s, 200m/s, 400m/s. For these soil types, the excitation was chosen to cover in the range 0-120 Hz corresponding to most of the vibrations from urban surface sources fall within.

The average of these frequencies, 60 Hz, and the average of the Rayleigh wave velocity over the chosen range of soils are the main defining parameters. The most suitable average depth which will fulfill the description of the dominance of Rayleigh waves at the surface is then calculated.

The Rayleigh wave velocities for the soils are calculated assuming a constant value of ν=0.3 and using the following equation (4.1) (Semblat and Pecker, 2009):

$$V_R = \frac{0.862 + 1.14\nu}{1 + \nu} \times V_S \tag{4.1}$$

The associated wavelength using the average Rayleigh wave velocity of the three soils and 60 Hz as mean frequency of the source is then calculated through equation (4.2):

$$\lambda_R = \frac{V_R}{f} \approx 3.5\text{m} \tag{4.2}$$

A wavelength of 3 meters was finally adopted and the mean velocity V_{s3} will be used in order to characterize the effective part of soil that controls the effects of the R-waves. The choice of V_{s3} to characterize the surface layer should be coupled with the choice of a factor that will describe the material impedance which contributes to the wave amplification in this top layer.

For the purpose of measuring the heterogeneity of the soil (the change of impedance with depth) the most pertinent factor used, as previously suggested in the field of earthquake engineering, is the gradient of the shear-wave velocity along the depth of the soil profile.

Taking into account the heterogeneity (by measuring the impedance changes with depth) of different sites will be done using gradients down to different depths. Gradients B_{Zmax} are found through a linear regression using the following equation (4.3):

$$\log_{10} V_s(z) = B_{Z\max} \times \log_{10}(z) + A_{Z\max} \tag{4.3}$$

Where z is the depth of the soil section taken starting from 1 meter, A_{Zmax} is the origin ordinate of the regression and $V_S(z)$ the shear wave velocity profile discretized at every meter. Fig. 4.1 shows an example of a soil column with a simplified representation of the gradient physical meaning.

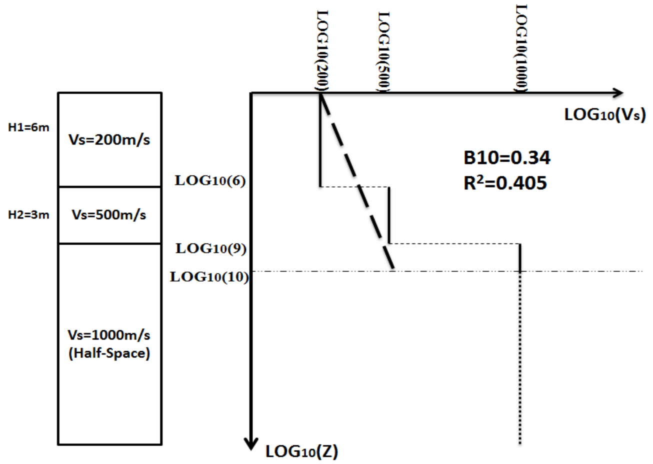

Fig. 4.1: A simplified representation of the definition of the velocity-gradient (B_{10} in this case).

Working with a wide range of high frequencies, and therefore a wide range of related wavelengths, makes it theoretically challenging to find the most relevant depth which influences the vibration prediction at the surface. Thus three types of gradients are suggested for this study related to different maximum depth: B_{20}, $B_{15}$and B_{10}.

Gradients were chosen to describe sites down to 20m. The three gradients will be studied in order to examine which one correlates better with the numerical predictions of displacement.

4.3 Testing program for the analysis of different sites

The basic idea of this section is to build a testing program that could cover the multiple aspects of the problem. For surface layers three soil types where chosen in order to describe the V_{S3}

parameter. These soils are characterized by a shear wave velocity of 100m/s, 200m/s and 400m/s respectively. Soil profiles were widely varied in order to guarantee the maximum variation of velocity-gradient factors proposed between 0 and 1. Other factors were taken into consideration in the choice of soil profiles particularly the number of layers above the bedrock/half space which was varying between one and six layers. The depth of the half-space was also varied in a wide range going from three to twenty two meters. Table 4.1 summarizes the factors defining sites characteristics. Tables 4.2 and 4.3 gives the statistical distribution for the depth of the half-space and the number of layers above it in the models used for the analysis. A total of 170 simulations were carried out where all the factors were altered in order to preserve a balanced diversification of profiles. FEM models have been carried out considering the model properties (meshes and materials) and the input solicitations described in chapter 3. Fig. 4.2 shows an idealization of the FEM models used in the study.

Profile Factor	**Range**
Vs (for shallow soils)	100-400 m/s
Vs (for deeper soils)	200-2200 m/s
Number of layers	1-6
Depth of the bedrock	3-22 m

Table 4.1: Range of variation for properties of the modelled soil profiles.

Half-Space Range of Depth	**Vs_3=100m/s**	**Vs_3=200m/s**	**Vs_3=400m/s**
0 to 5 meters	12%	18%	16%
5 to 10 meters	29%	33%	35%
10 to 15 meters	17%	15%	20%
15 to 20 meters	28%	30%	25%
Deeper than 20 meters	14%	4%	4%

Table 4.2: Statistical distribution of the half-space depth.

Number of Layers Above the Half-Space	**Vs_3=100m/s**	**Vs_3=200m/s**	**Vs_3=400m/s**
1	15%	20%	22%
2	20%	24%	24%
3	28%	33%	37%
4	34%	21%	15%
Equal or more than 5	3%	2%	2%

Table 4.3: Statistical distribution of the number of layers above the half-space.

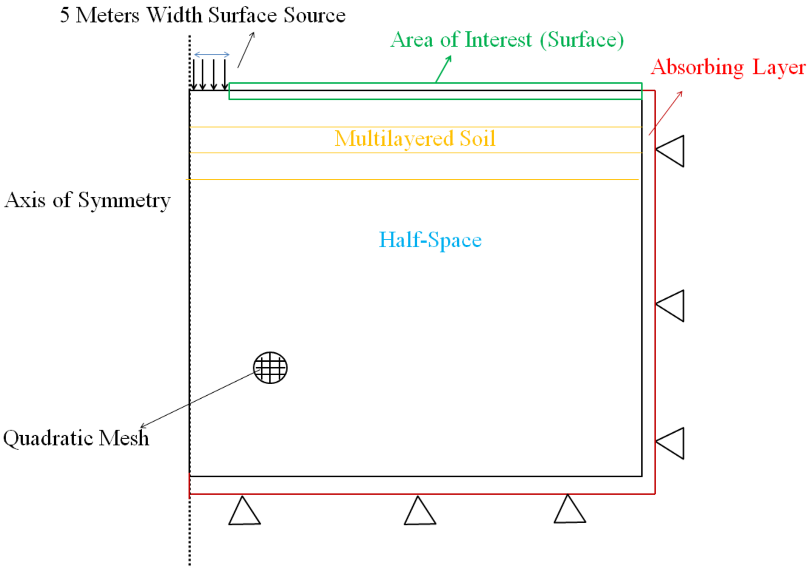

Fig. 4.2: Representation of the 2D axisymmetric model used in the analysis showing the surface source, multilayered profile and the absorbing layer.

4.4 Simple laws of attenuation and amplification in the time domain

In order to quantify the efficiency of the suggested parameters, a comparison between the multilayered cases and the homogeneous case was done. The comparison considered peak displacement values at the surface normalized by the input amplitude as a function of distance from source. For the homogeneous cases (half-space) normalized attenuation laws were established for the three types of soils as shown in Fig. 4.3 taking into consideration the material attenuation as defined in chapter 3.

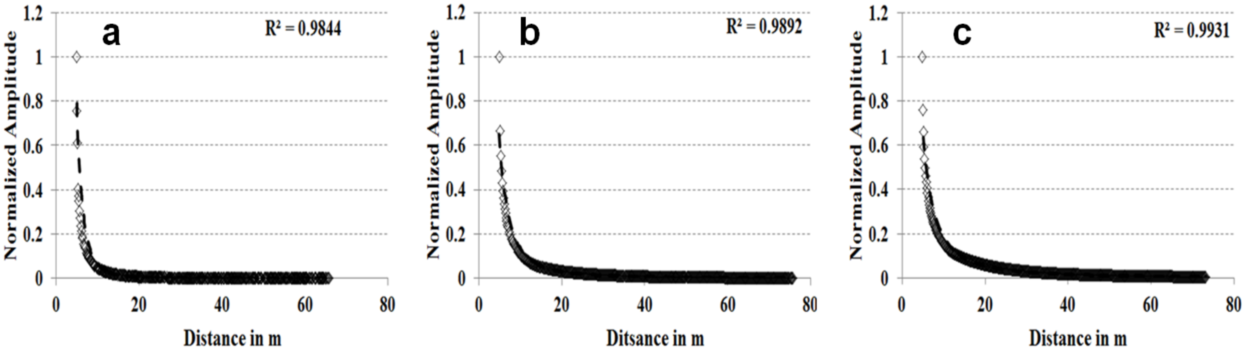

Fig. 4.3: Attenuation laws for homogeneous soils (a) Vs=100m/s,(b)Vs=200m/s,(c)Vs=400m/s.

The attenuation equations for the homogenous cases are summarized as following:

$$\textit{Attenuation Level AL} = 10.53 \times (d+5)^{-1.75} \text{ for } Vs\text{=400m/s} \tag{4.4.a}$$

$$\textit{Attenuation Level AL} = 19.15 \times (d+5)^{-2.16} \text{ for } Vs\text{=200m/s} \tag{4.4.b}$$

$$\textit{Attenuation Level AL} = 54.53 \times (d+5)^{-3.02} \text{ for } Vs\text{=100m/s} \tag{4.4.c}$$

Where the *Attenuation Level* is the normalized level of vibration after attenuation with respect to the value at the source and *d* is the distance from source.

In Fig. 4.4 a comparison is shown for the simple laws found above with laws found in the literature. The comprehensive formulation used for comparison could be found in Kim and Lee (2000) and was previously discussed in chapter 2. It could be summarized in equations (4.5) and (4.6).

$$w_2 = w_1 (\frac{r_1}{r_2})^n e^{-\alpha(r_2 - r_1)} \tag{4.5}$$

$$\alpha = \frac{\pi n f}{c} \tag{4.6}$$

Where $w_1$and $w_2$are the vibration amplitudes at the two distances r_1 and r_2; α describes the material damping where *f* is the frequency, *c* is the propagation velocity of the wave, *n* is a loss factor which varies dependently on source and wave type. For the present analysis and since a point source is the nearest idealization to compare with, and the attenuation is measured at the surface of the soil, a factor n is taken equal to 0.5, associated to a point source and Rayleigh waves.

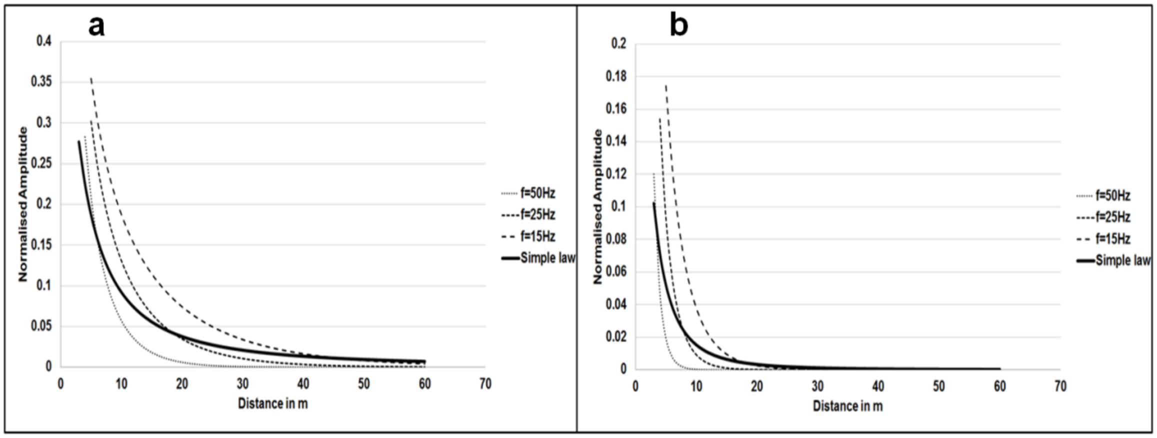

Fig .4.4: Simple and theoretical laws comparison for (a) Vs=400m/s (b) Vs=100m/s.

It could be deduced that the derived simple laws show a good correlation with the theoretical formulation. The simple laws were derived independently of frequencies (for a sum of frequencies) and it could be seen that it falls in the envelope created by a range of frequencies attenuation curves. The simple laws were derived from a surface foundation source equivalent to a point source starting from a certain distance and not exactly a point source. Moreover the simple laws represent not a single wave type but the sum of different waves which are dominated by Rayleigh waves.

For each case of V_{s3}, the amplification factor will be calculated following equation (4.7). The amplification factor describes the difference between the peak ground displacement in the multilayered case and the homogeneous case normalized with the latter.

$$\mathit{Amplification\ Factor} = \frac{PGD(\mathit{Multilayered}) - PGD(\mathit{Homogeneous})}{PGD(\mathit{Homogeneous})} \tag{4.7}$$

The amplification factors are then averaged for different segments of distance from the source and the results were reported as function of the different gradients introduced. The correlation of the calculated values for each segment plotted against the varying gradient indicates the efficiency of the chosen gradient in detecting the amplification. Fig. 4.5 illustrates the correlation variability of peak displacement values averaged for the first 20 meters next to the source for different gradients (B_{20}, B_{15} and B_{10}) for the case of V_{s3}=400m/s. The B_{10} case shows a very coherent distribution of the amplification factor versus the increasing gradient. Similarly for the case of V_{s3}=200m/s and 100m/s (Fig. 4.6 and Fig. 4.7), the best correlation is found for the B_{10} gradient.

The amplification equations are analytically summarized using B_{10} for the first 20 meters from the source in equations (4.8.a, b and c)

$$\text{Amplification Factor} = 0.34 \times \ln(B_{10}) + 1.06 \text{ for Vs=400m/s} \tag{4.8.a}$$

$$\text{Amplification Factor} = 0.314 \times \ln(B_{10}) + 1.05 \text{ for Vs=200m/s} \tag{4.8.b}$$

$$\text{Amplification Factor} = 0.323 \times \ln(B_{10}) + 0.75 \text{ for Vs=100m/s} \tag{4.8.c}$$

In order to summarize, using equation (4.4) and equation (4.8) the final prediction equation will be in the form given in equation (4.9):

$$\text{Final Vibration Amplitude} = AL(1+AF) \tag{4.9}$$

Where *AL* and *AF* are respectively the attenuation level and the amplification factor as previously defined.

Changing the segment of distance from the first 20 meters to the first 35 meters for example, shows that the consistency continues to be present as shown in Fig. 4.8 but with a small reduction in the correlation fitting value. The rather quick drop of vibration amplitudes away from source as previously seen in Fig. 4.3 makes it mandatory to be reasonable when choosing the size of window in which the values will be analyzed.

Enlarging excessively the window of distance from source will increase the imprecision due to averaging values from a very different range of amplitudes. In other words, it will underestimate the values near the source where the most severe amplification are present in terms of ground displacement, nevertheless clearly keeping the same pattern of amplification.

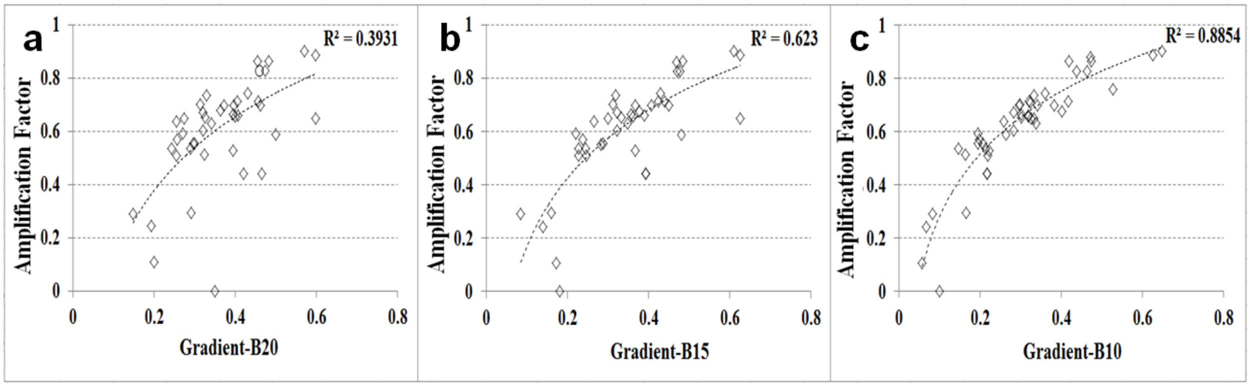

Fig. 4.5 Amplification Factors for Vs=400m/s versus Gradient (a) B_{20}(b) B_{15}(c) B_{10}.

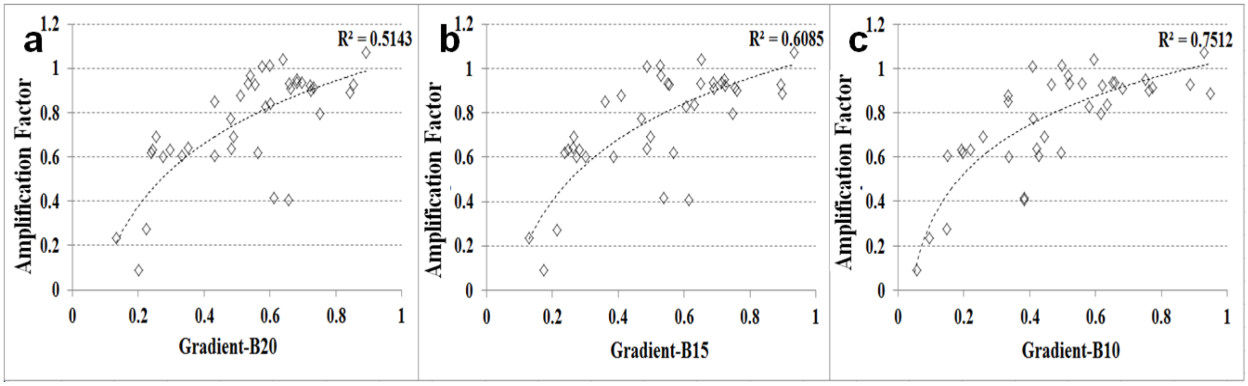

Fig. 4.6 Amplification Factors for Vs=200m/s versus Gradient (a) B_{20}(b) B_{15}(c) B_{10}.

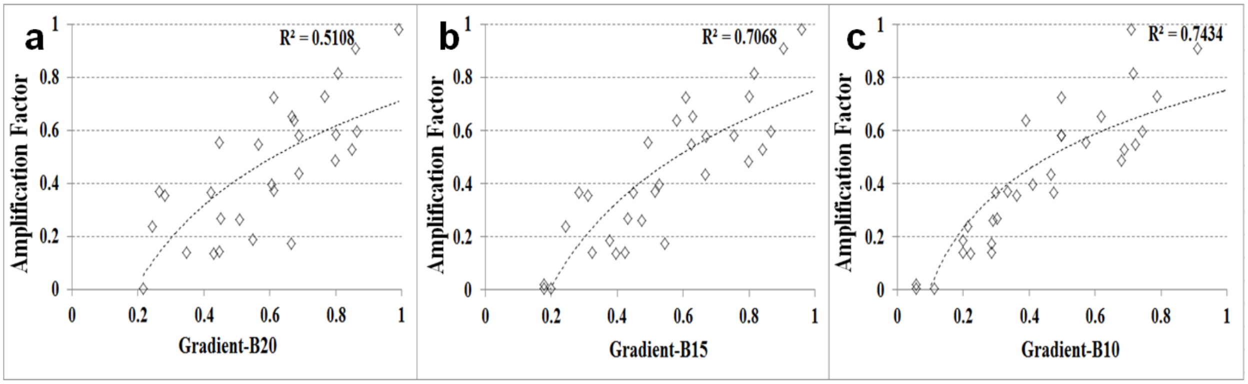

Fig. 4.7 Amplification Factors for Vs=100m/s versus Gradient (a) B_{20}(b) B_{15}(c) B_{10}.

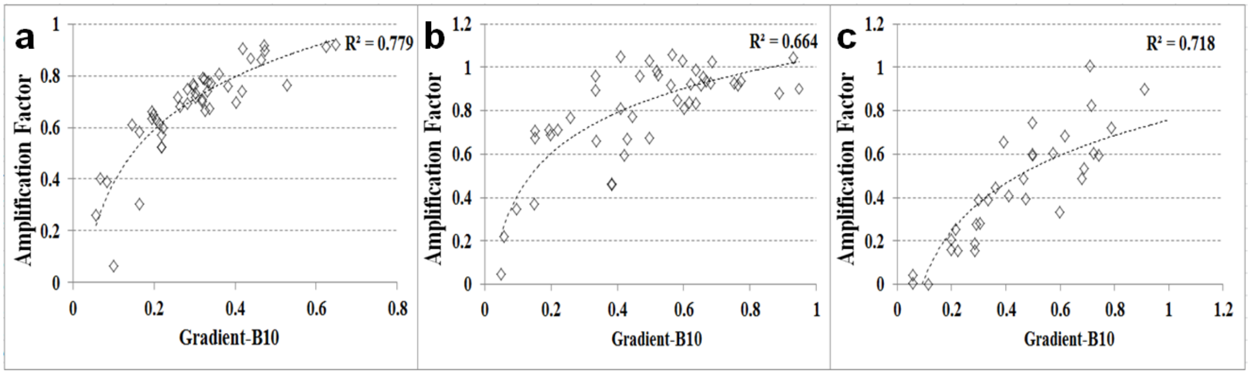

Fig. 4.8: Amplification Factors averaging the first 35m using B_{10} *for (a) Vs=400m/s (b) Vs=200m/s, (c) Vs=100m/s.*

While the near field displacement was shown to be well correlated with the variation of the gradient, it is still of clear importance to check for mid-field (20-40 meters from the source) and far-field responses (40-60 meters from the source). No precise correlation could be established when taking soil segment disrupted from the source. For the mid-field most of the amplification seems rather constant independently from the gradient. In the far-field, similarly to the mid-field, a clear correlation could not be established but it is noticed that the amplifications move toward the lower gradients. Hence the lower gradients affect more the far field than the high gradients. An example showing the amplification in a V_{s3} =200m/s soil for 20-40 meters and 40-60 meters from source segments (representing mid-field and far-field) are respectively shown in the Fig. 4.9.

It is very important to indicate that the chosen windows to define the mid and far field response are chosen independently of the properties of the site. In other words changing the soil properties whether it is the V_{s3} or the gradient will influence the frequency response and therefore the wavelengths. Wavelengths will play a crucial role in defining the response of soils in relation to the distance. For instance, weaker soils and smaller gradients will be associated with longer wavelengths/lower frequencies and therefore the distance segments choice does not represent the wavelength dependency.

The frequency dependency raises the need for more advanced analysis surpassing the established simple laws. Next sections of this chapter will be dedicated to spectral analysis addressing the problem in the frequency domain.

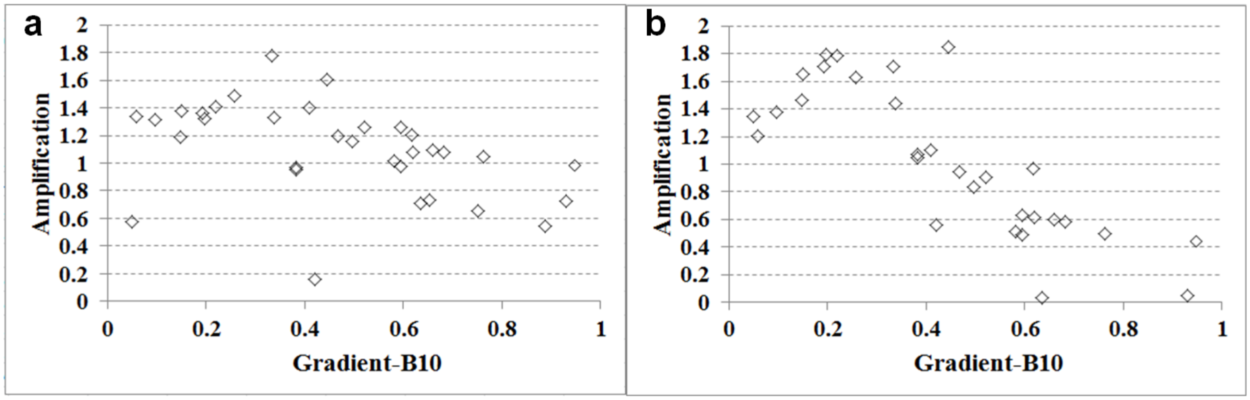

Fig. 4.9: Amplification Factors for V_{s3} *=200 m/s soils using* B_{10} *for (a) 20-40m segment (b) 40-60m segment.*

However the aim is to get a formulation capable of predicting peak vibration levels not only for the near field, without neglecting the fact that away from source, levels of vibration become very small as shown in Fig.4.3. Moreover, the most important amplifications are present near the source and the amplification pattern is clearly dominated by it (as clearly shown previously in the comparison between results from the first 20 and 35 meters).In order to check the validity in the far field of the equations which are derived from the first 20 meters, some predictions were carried out using equations (4.4), (4.8) and (4.9). The values obtained were then compared with some of the FEM results between 5 meters and 60 meters from the source.

Fig. 4.10 (a) shows the results of the standard deviation ratio between the results of FEM models and those found by the prediction equations for three different sites with different gradients where V_{s3} is equal to 400m/s. The results from the prediction equation shows a good agreement with the FEM results since most of the predicted values are within 20% of difference even at far distances (beyond 40 meters). Fig. 4.10 (b) shows the same for V_{s3}=100m/s. The deviation shows a less coherent agreement than the V_{s3}=400m/s case but the deviation is still within an acceptable range for varying distances. As a consequence, the formulas are reliable also for distances larger than 20 meters (i.e. mid-field and far-field).

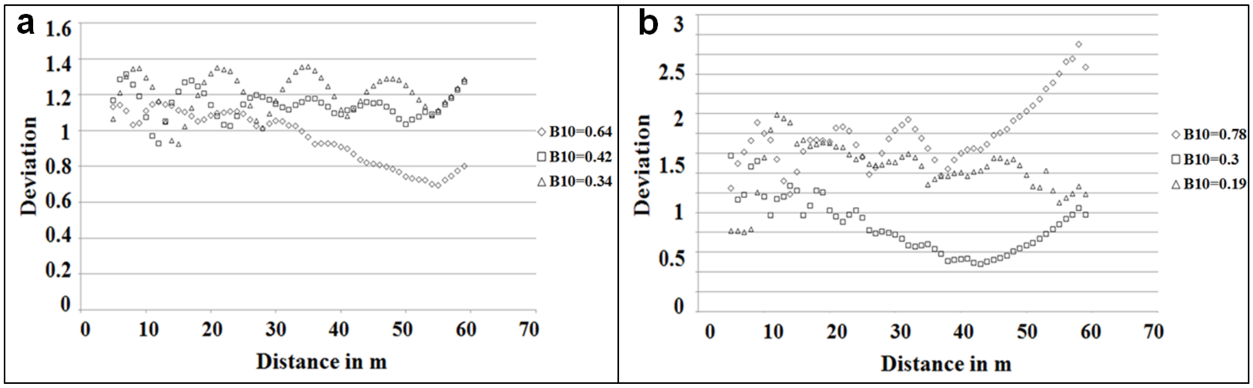

Fig. 4.10: Deviation ratio between FEM and prediction equations results for different sites (gradients) where (a) V_{s3} =400m/s (b) V_{s3} =100m/s.

4.5 Spectral Approach

As shown in the previous section, although simple laws of attenuation and amplification found from the time domain analysis could be more or less reliable, the correlation started to disappear when disrupting from the source. A more detailed and reliable prediction model is aimed for, discussing the response of multiple sites in the frequency domain.

4.5.1 Adopted Procedure

Working with a wide range of vibration, between 0 and 120 Hz, the aim is to study the spectral response of soils at various distances. The approach chosen is to divide the frequencies into bands and divide the distances into three fields: near, mid and far fields. The frequencies between 0 and 120 Hz are divided into bands of 20 Hz. The soils/sites were sorted in accordance to V_{s3} and B_{10}. In fact, taking a lot of cases with a varying B_{10} proxy will push us toward adapting an averaging process. All the cases are clustered into a known set of gradients. Each case is associated to the gradient which is closer to them. The responses are then averaged. Some examples of the site responses in the frequency domain and how it varies are shown in Fig. 4.11. The complete set of response maps could be found in Appendix A. Fig. 4.11 (left) shows the response for V_{s3}=100m/s and for three cases of increasing gradients, B_{10} equal to 0.1, 0.5 and 0.9 respectively. From these curves the higher the gradient, the higher the maximum amplitudes are and the stronger the response is at higher frequencies. A similar response could be noticed for the case of V_{s3}=200m/s, shown in Fig. 4.11 (right). In order to better quantify and assess the response of soil for different cases of V_{s3} and B_{10}, responses similar to those shown in Fig. 4.11 are further processed. Soil responses are divided into three segments of distance in order to analyze the average responses on a rather macroscopic scale. The near-field represents the first 20 meters next to the source. The mid-field represents the second 20 meters next to the source. The far-field represents the third twenty meters next to the sources. Values of normalized spectral displacement are then averaged for each frequency band. The detailed processing flowchart is shown in Fig. 4.12.

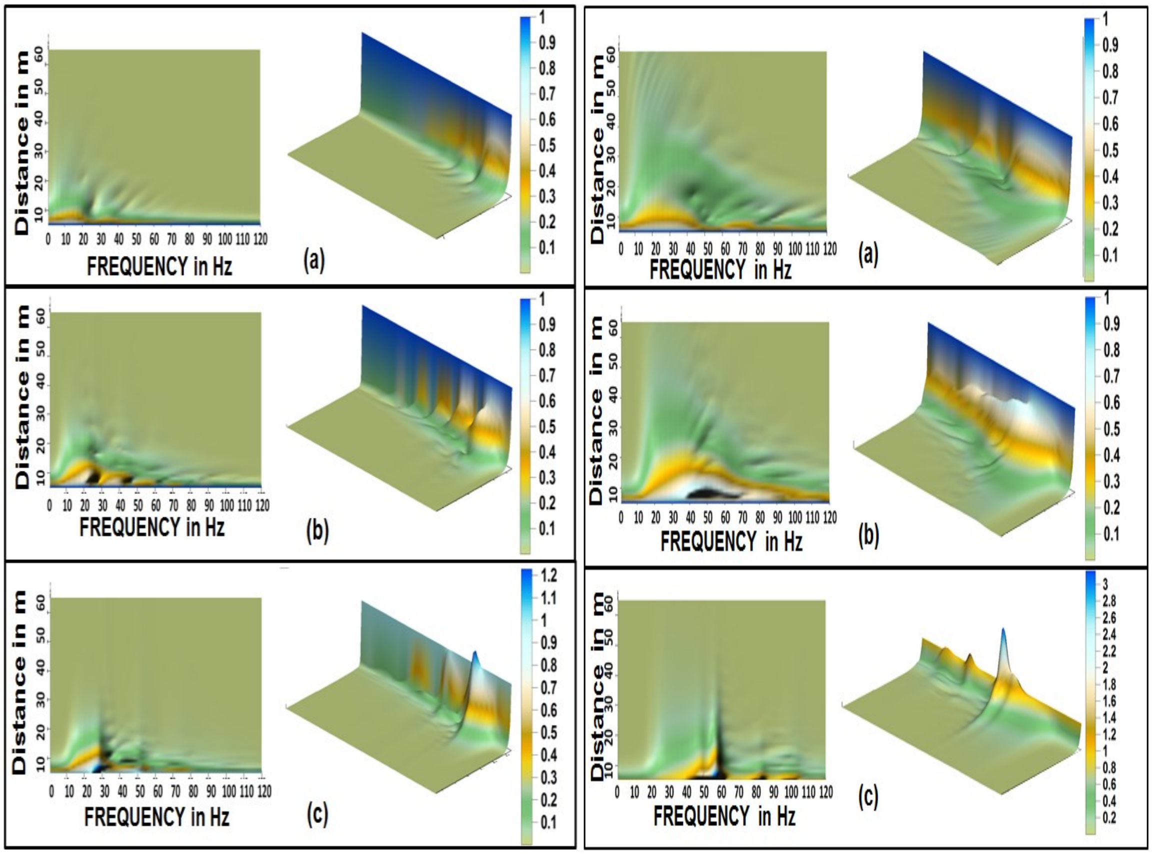

Fig. 4.11: Spectral Normalized Displacement Ratio with respect to distance for V_{s3}=100m/s (left) and V_{s3}=200m/s (right) and for (a) B_{10} =0.1 (b) B_{10} =0.5 (c) B_{10} =0.9 respectively.

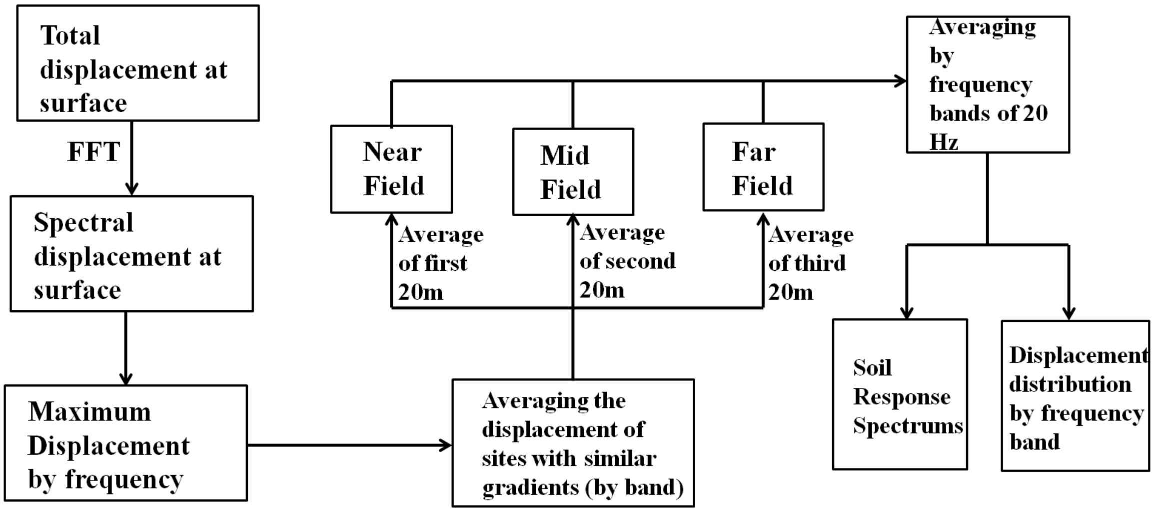

Fig. 4.12: Processing flowchart for the spectral analysis.

4.5.2 Near field Response

For V_{s3} equal to 100m/s (Fig. 4.13), it could be noticed that with an increasing gradient, the dominant frequencies are larger. Similarly the amplitudes associated with peaks are increasing with the gradient. The dominant frequencies are between 0 and 40 Hz with an increasing gradient as shown in Fig. 4.13. When the gradient proxy rises the effects of lower frequencies tend to diminish, and inversely for higher frequencies.

For V_{s3} equal to 200m/s, and similarly to V_{s3}=100m/s, the peak frequency value increases with the velocity gradient, likewise for amplitudes as shown in Fig. 4.14. The dominant frequencies are within the bands between 20 and 60 Hz. Moreover the lower frequencies (0-20Hz) are decreasing with an increasing gradient, conversely to the higher frequencies.

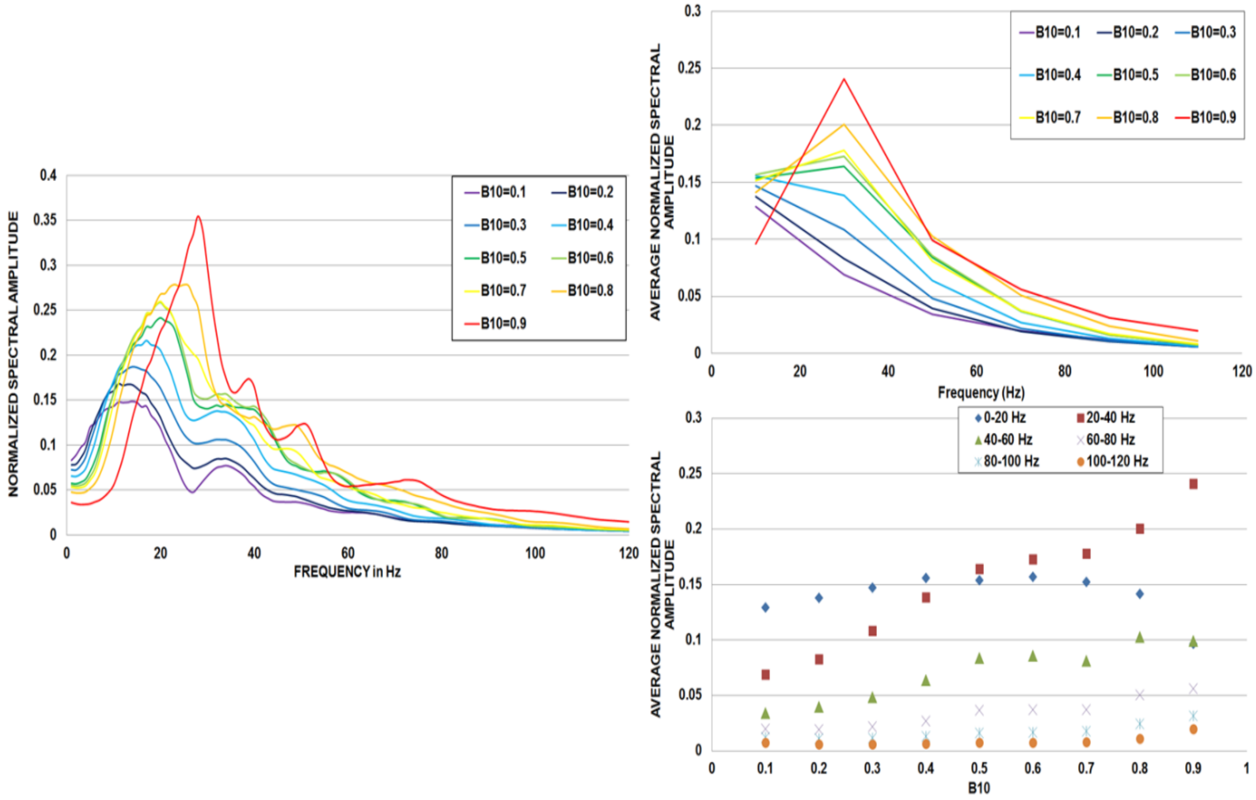

Fig. 4.13: From left to right clockwise for (V_{s3}=100m/s in the near-field): normalized spectral amplitude by frequency, averaged normalized spectral amplitude by frequency band, distribution of averaged normalized spectral amplitude by frequency band.

For V_{s3} equal to 400m/s, first it is harder to achieve higher gradients since it requires very strong material below the surface layer surpassing the stiffness of soils and rocks. Nevertheless the trend continues as for the two previous cases which is an increasing high frequency content with gradient along with larger amplitudes. In this case higher frequencies are dominating the problem (up to 100 Hz) while lower frequencies are decreasing with higher gradients. The response for V_{s3} equal to 400m/s is shown Fig. 4.15.

From all the above, it could be deduced that the lower the gradient, the smaller the influencing frequency and vice versa. Furthermore the correlation between the maximum amplitudes and the gradient is quite clear, i.e. the higher the gradient the larger the maximum amplitude.

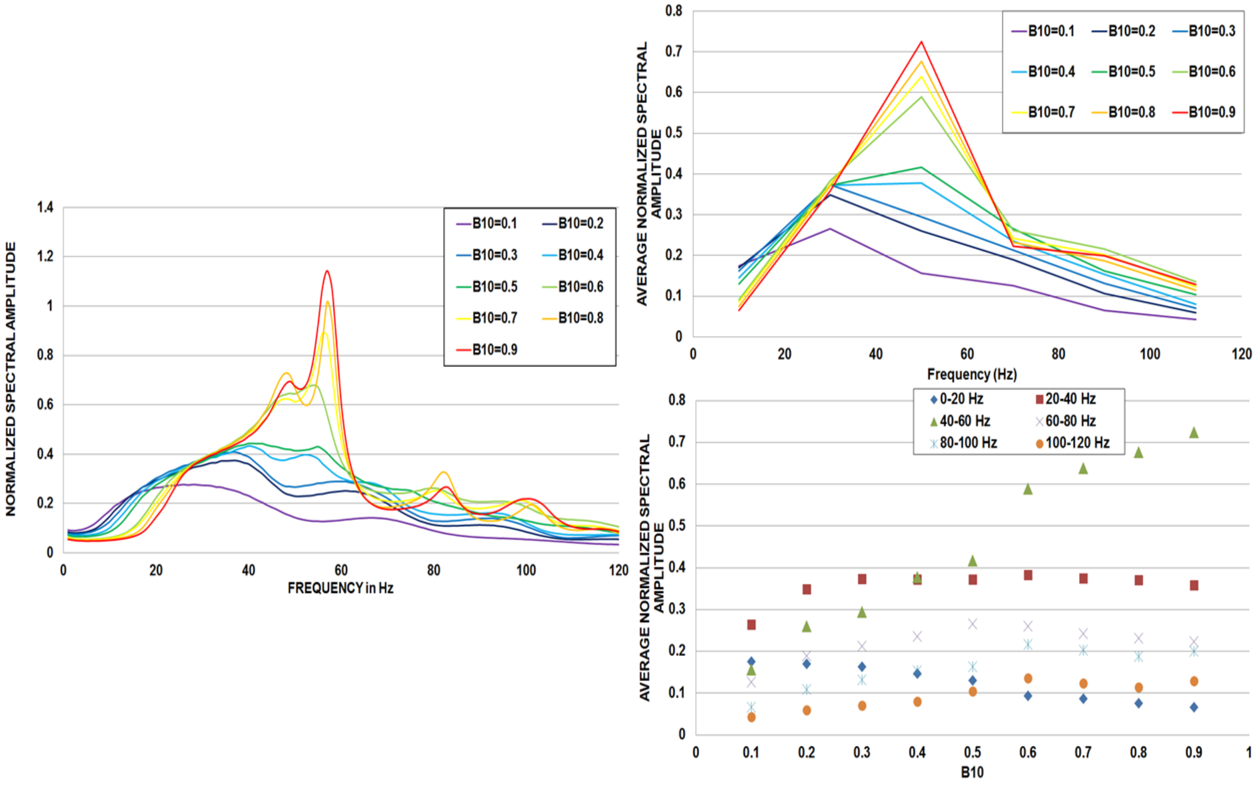

Fig. 4.14: From left to right clockwise for (V_{s3}=200m/s in the near-field): normalized spectral amplitude by frequency, averaged normalized spectral amplitude by frequency band, distribution of averaged normalized spectral amplitude by frequency band.

Inspecting individual cases before averaging and distributing frequencies by bands, for the near field, the peak frequency is always around the value V_{s3}/h_1 where h_1 is the depth of the surface layer. Hence it is concluded that lower gradients are associated with lower frequencies because they are usually associated to deeper layers (larger h_1) and weaker contrasts that tend to behave more like homogeneous cases. This fact can describe the reason why also larger B_{10} are associated with higher frequencies.

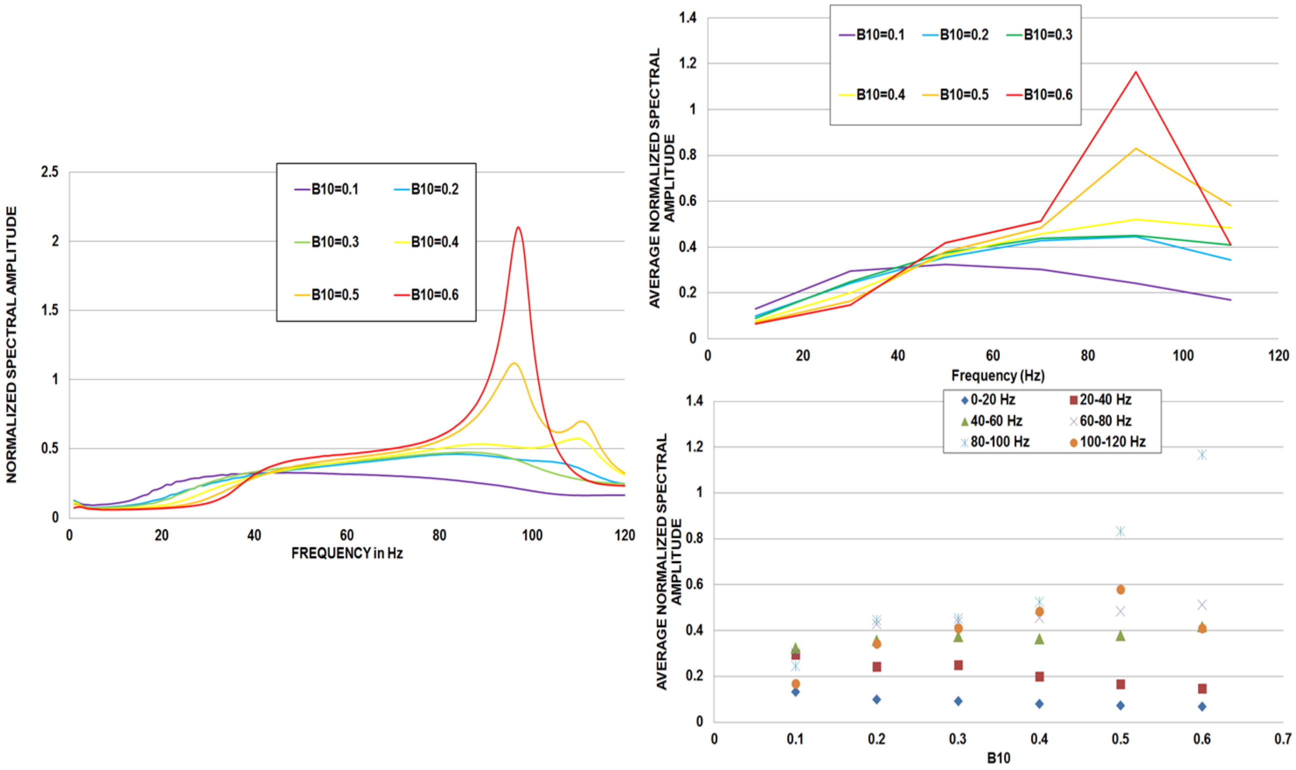

Fig. 4.15: From left to right clockwise (V_{s3}=400m/s in the near-field): normalized spectral amplitude by frequency, averaged normalized spectral amplitude by frequency band, distribution of averaged normalized spectral amplitude by frequency band.

4.5.3 Mid-field response

For V_{s3}=100m/s, as in the case of the near field, the larger the gradient the higher the most influencing frequency. For the midfield, as shown in Fig. 4.16, the predominance of the lower frequency band (0-20Hz) is extended to higher gradients (up to B_{10}=0.7).

Moreover the energy carried by the lower frequencies for the smaller gradients are very large when compared to the near-field, indicating a higher susceptibility for lower frequencies.

Inspecting the response for higher gradients, more peaks started to appear in the higher frequency range along with the decrease of lower frequencies (0-20Hz band). These peaks nevertheless do not dominate the response.

For V_{s3}=200m/s (Fig. 4.17), the effect of the 20-40Hz band is starting to become clearer and dominant up to B_{10}=0.7. The amplitude and effect of the same band becomes clearer for smaller gradients. For larger gradients a higher band of 40-60 Hz is still dominant slightly overcoming the 20-40 Hz band. Lower frequencies, 0-20 Hz band in this case, continued to decline along with the rising gradient.

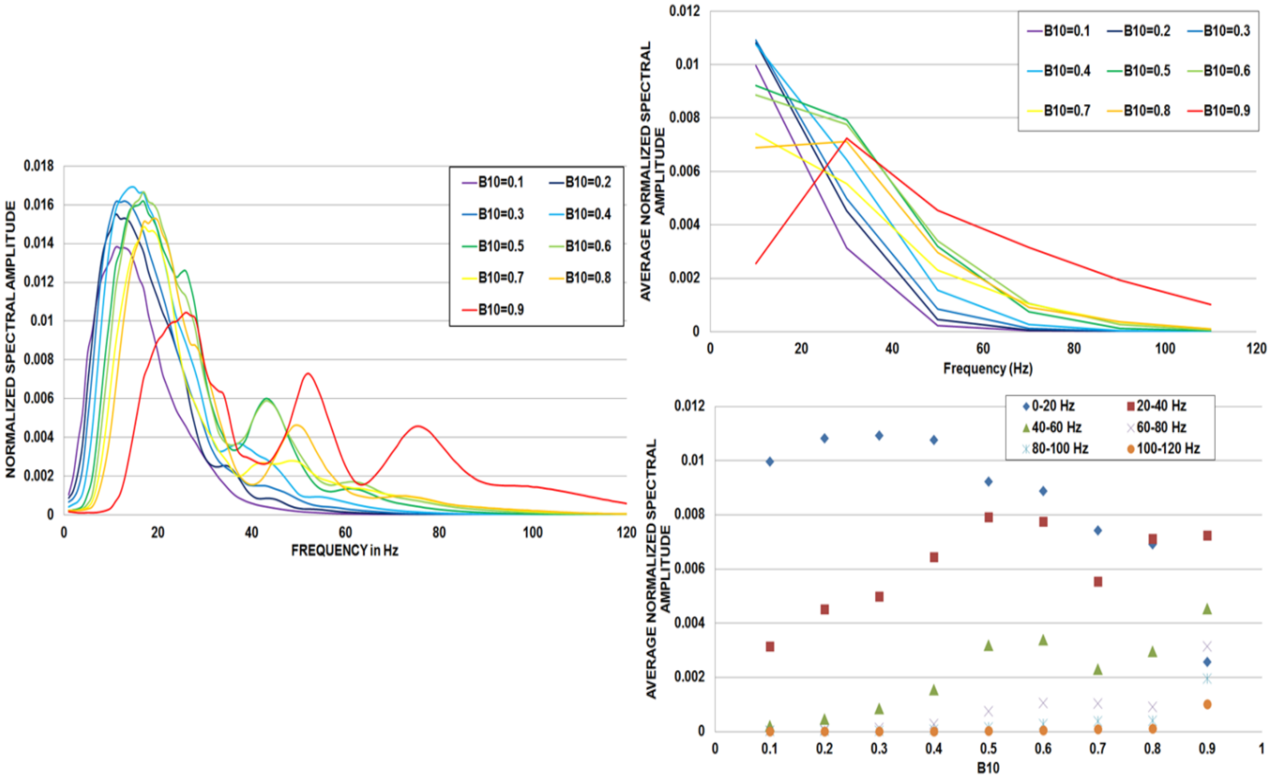

Fig. 4.16: From left to right clockwise (V_{s3}=100m/s in the mid-field): normalized spectral amplitude by frequency, averaged normalized spectral amplitude by frequency band, distribution of averaged normalized spectral amplitude by frequency band.

For V_{s3}=400m/s (Fig. 4.18), vibrations in most cases are dominated by 40-60Hz. This frequency range is equivalent to the half of the frequencies dominant in the near-field. Exceptions are for the smallest and largest gradients where 20-40Hz and 60-80Hz bands dominate respectively.

High frequencies are associated with smaller wavelengths, in the mid-field a large amount of these waves are filtered through distance and the remaining waves are associated to lower frequencies. This effect is more apparent for smaller gradients, especially in the case of V_{s3}=100m/s and 200m/s. A particular raise of certain peaks in the high frequency range for higher gradients in the case of V_{s3}=100m/s is noticed, which is contradictory to the tendency of fading high frequencies in the midfield.

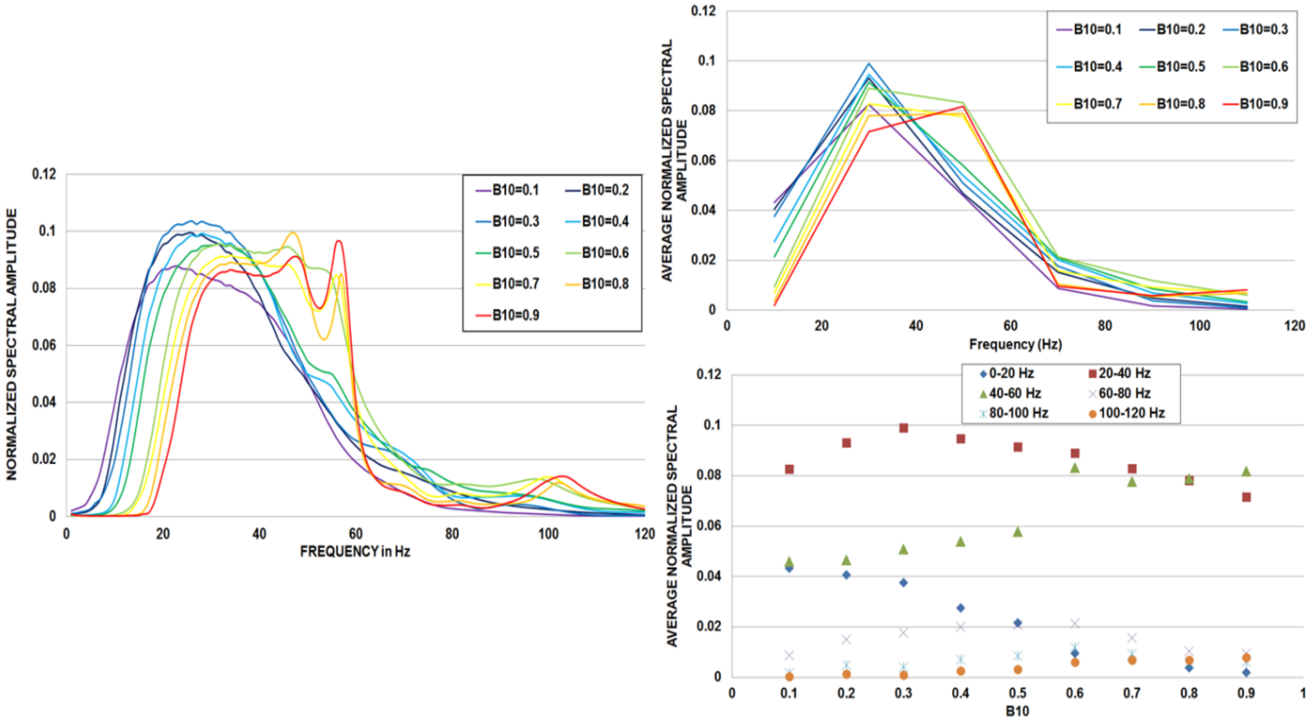

Fig. 4.17: From left to right clockwise (V_{s3}=200m/s in the mid-field): normalized spectral amplitude by frequency, averaged normalized spectral amplitude by frequency band, distribution of averaged normalized spectral amplitude by frequency band.

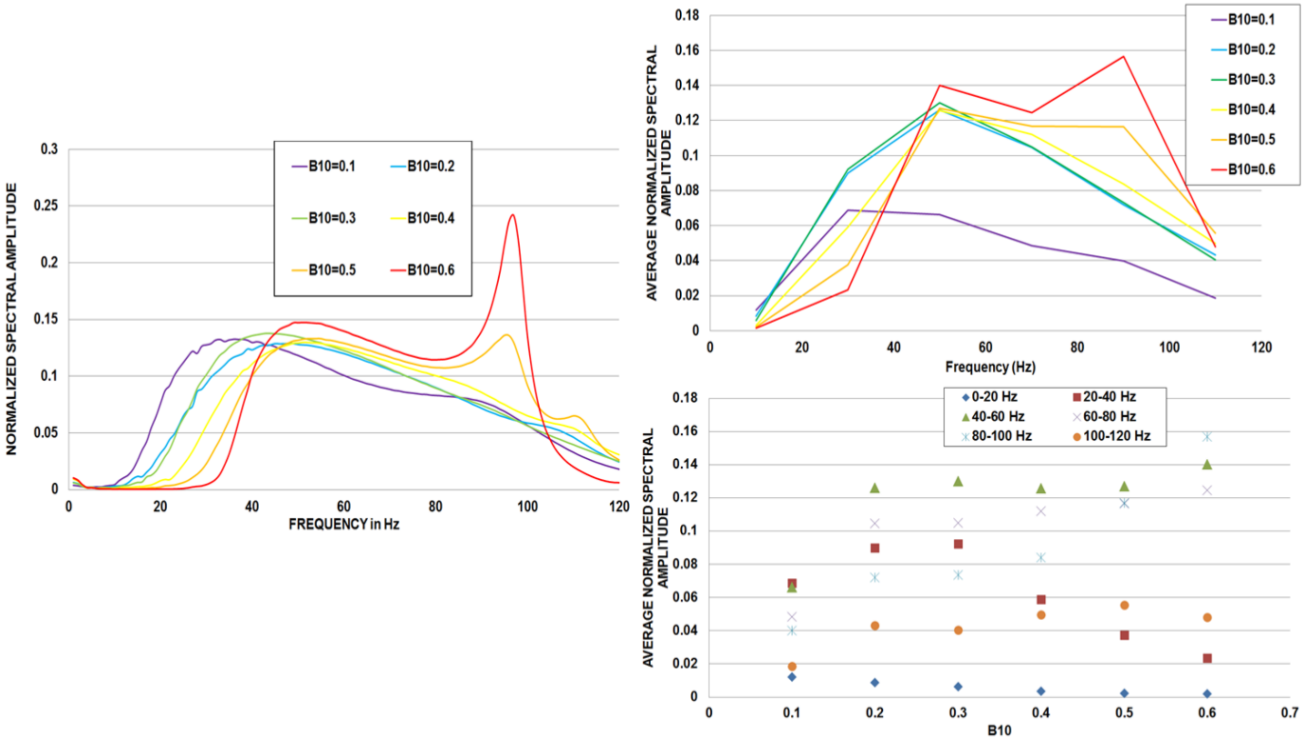

Fig. 4.18: From left to right clockwise (V_{s3}=400m/s in the mid-field): normalized spectral amplitude by frequency, averaged normalized spectral amplitude by frequency band, distribution of averaged normalized spectral amplitude by frequency band.

4.5.4 Far-field response

For V_{s3}=100m/s (Fig. 4.19), while the effects of lower frequencies are still clear, a surge of higher frequencies appears. This surge is not only for B_{10}=0.9, where the 40-60 Hz band is dominating for the first time. Starting from B_{10}=0.6, the 20-40Hz band appeared to start dominating. The small peaks detected in the mid-field for the higher frequencies started to appear more strongly in the far-field and dominate in the case of B_{10}=0.9.

For V_{s3}=200m/s (Fig. 4.20), the response is totally dominated by the 20-40Hz band and the effects of high frequencies are almost negligible. Similarly to the near and mid-field the smaller the gradient is the more the response is affected by lower frequencies.

For V_{s3}=400m/s (Fig. 4.21), the peaks are still dominated by the same frequencies as in the mid-field, except for B_{10}=0.6 which is now dominated by a lower frequency band (40-60Hz). The higher frequencies are clearly less apparent since more small wavelengths are filtered through the increasing distance.

The only unexpected change in the above results is the surge and dominance of higher frequencies for V_{s3}=100m/s for the higher gradients, especially for B_{10}=0.9. It was expected that the vibration will be dominated by lower frequencies at farther distances.

After inspecting the models where B_{10}=0.9 and V_{s3}=100m/s, it was noticed that it is usually characterized with a huge leap in soil stiffness after one or two weak thin layers. Moreover the inspection showed that the peak in the newly appearing high frequency was always around a value of $\sqrt{3}f_0$ where $f_0$is the frequency of the first peak which was dominant in the near field.

Based on this, two assumptions can be made: (1) either that the probable presence of two weak layers will cause the effects of resonance of the second one to appear at larger distances; (2) either higher modes of excitation are triggered at far distances. Moreover both assumptions could be true and valid.

In order to investigate these assumptions, a simple rheological model of a 2DOF system has been studied. The two bodies are assumed of similar properties (in order to simulate one layer with two degrees of freedom or two layers who have negligible differences comparing to the bedrock) over a fully rigid support (representing the very strong bedrock).

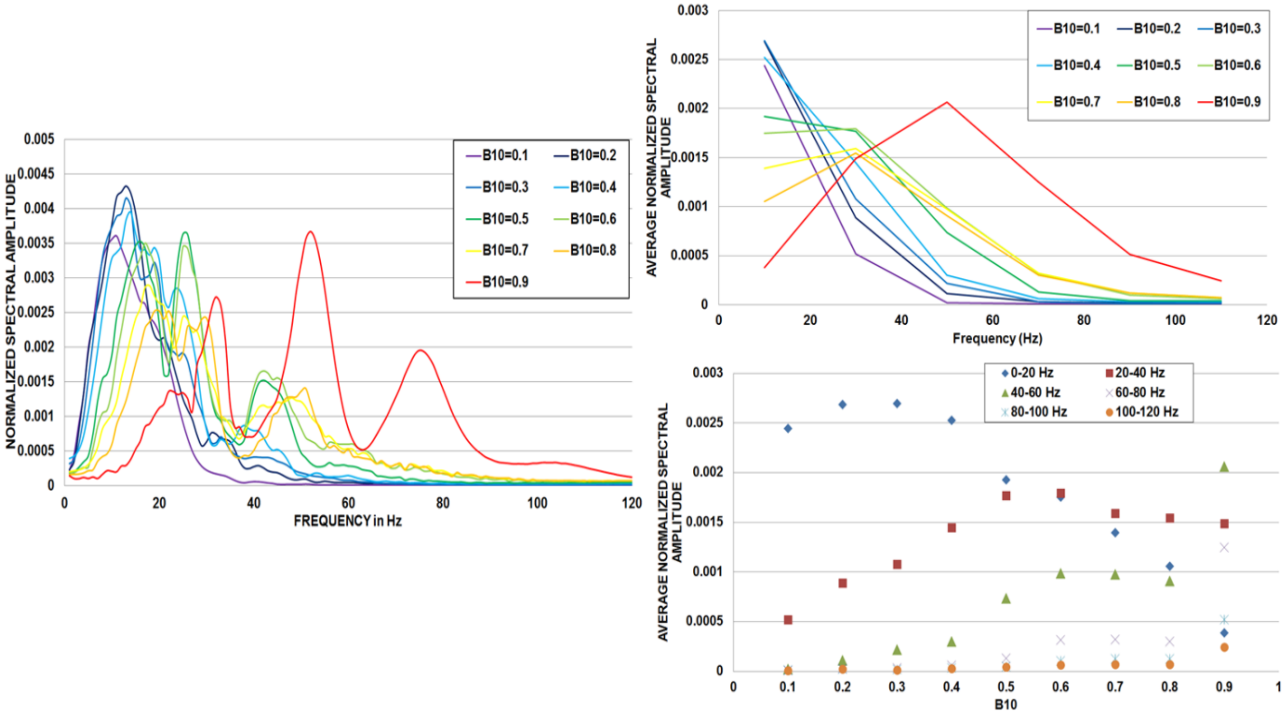

Fig. 4.19: From left to right clockwise (V_{s3}=100m/s in the far-field): normalized spectral amplitude by frequency, averaged normalized spectral amplitude by frequency band, distribution of averaged normalized spectral amplitude by frequency band.

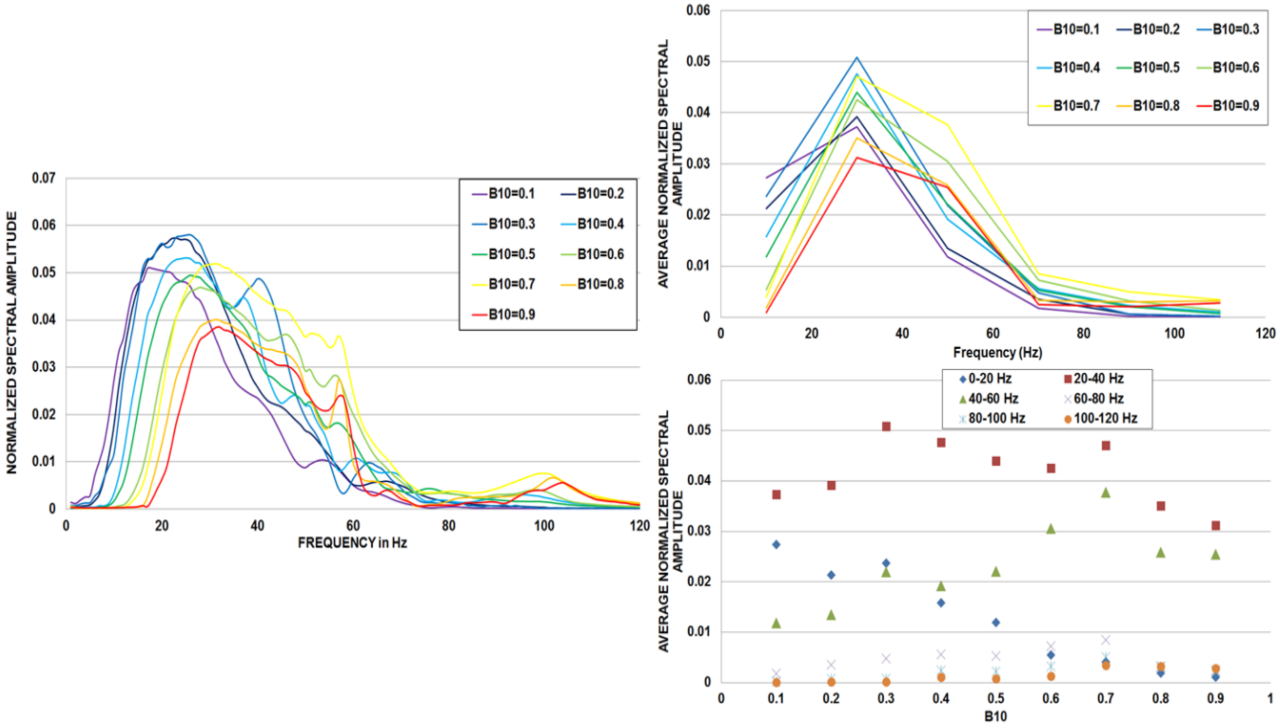

Fig. 4.20: From left to right clockwise (V_{s3}=200m in the far-field): normalized spectral amplitude by frequency, averaged normalized spectral amplitude by frequency band, distribution of averaged normalized spectral amplitude by frequency band.

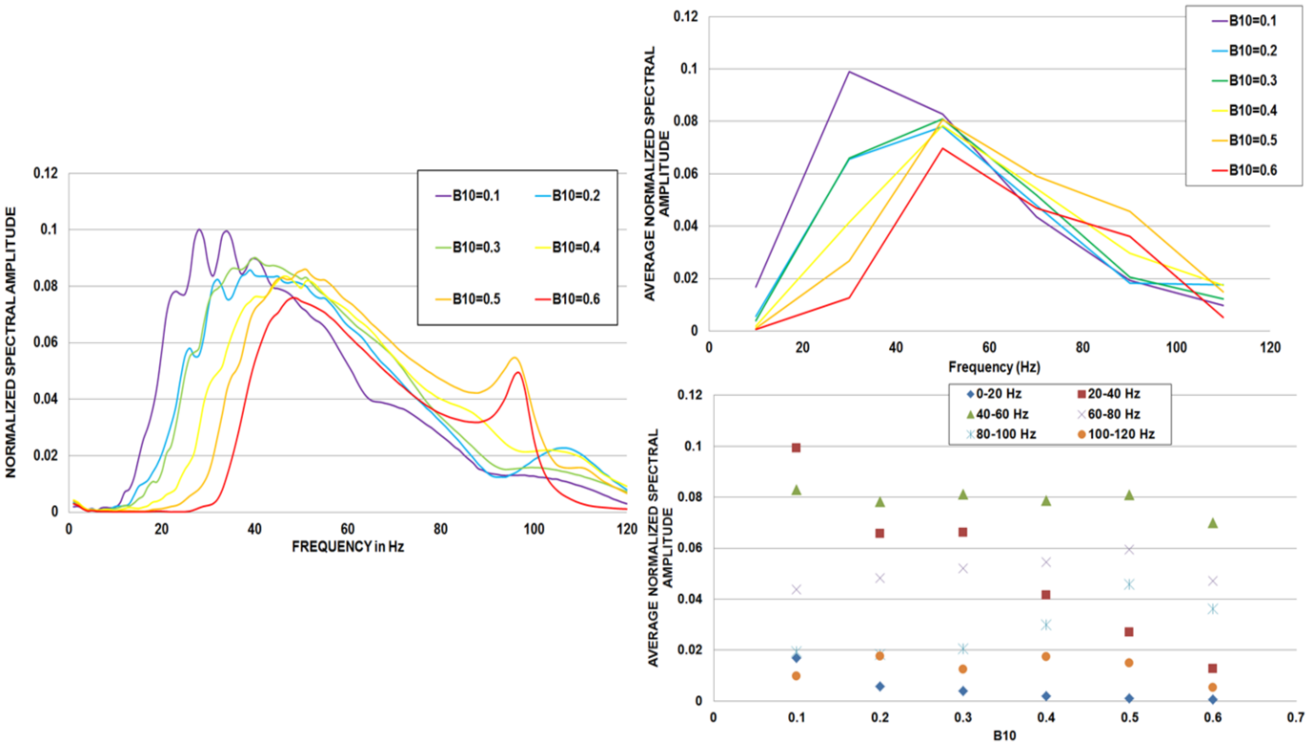

Fig. 4.21: From left to right clockwise (V_{s3}=400m/s in the far-field): normalized spectral amplitude by frequency, averaged normalized spectral amplitude by frequency band, distribution of averaged normalized spectral amplitude by frequency band.

The model is displayed in Fig. 4.22. As shown in equations (4.10) and (4.11) calculating the fundamental and the second mode eigenfrequency, it could be noticed that the frequency of the second mode is at $\sqrt{3}$ of the first as shown in equation (4.10) and (4.11). Hence, it could be deduced that at a certain distance from the source the response of the top layer will be dominated by the second mode of vibration, in this case for very weak soils with very large gradients.

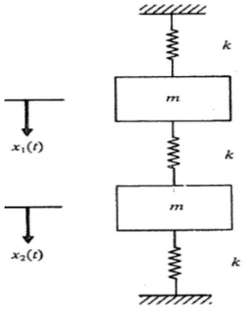

Fig. 4.22: Rheological model used for simulating two degrees of freedom of weak soils over a very rigid half-space.

$$\omega_1 = \sqrt{\frac{4km - \left[16k^2m^2 - 12k^2m^2\right]^{0.5}}{2m^2}} = \sqrt{\frac{k}{m}} \tag{4.10}$$

$$\omega_2 = \sqrt{\frac{4km + \left[16k^2m^2 - 12k^2m^2\right]^{0.5}}{2m^2}} = \sqrt{\frac{3k}{m}} \tag{4.11}$$

4.6 H/V Spectral Ratios from Numerical Results

In order to better study the excitation modes of soil and better understand its response under vibrations, the difference between the response in the horizontal and vertical direction will be studied considering the same models where the ground is excited by a surface source.

The response in the horizontal direction is generally characterized by larger peaks that do not appear in the vertical direction. These peaks were the main properties of the response as described in the previous sections of this chapter.

For V_{s3}=100m/s, a comparison between two different gradients, 0.5 and 0.9 for instance, is displayed in Fig. 4.23 (i.e. near field). It could be noticed that when the gradient is larger, the peaks in the horizontal direction become more important compared to those of the vertical direction. Moreover the peaks start to appear at higher frequencies, which is coherent with the results found in the previous section. For the case of B_{10}=0.5 the first peak appeared at 23 Hz while for B_{10}=0.9 the first peak was at 30 Hz. Inspecting the other peaks, it was found that the second peak was always at a value around 1.73 of the first (which is around $\sqrt{3}$), which was also previously concluded from both the response at the far-field of some cases and the rheological model respectively. Inspecting the third peak, that may indicate the third mode of vibration, it was constantly at 2.5 of the first and around 1.44 of the second (which is around $\sqrt{2}$).

Taking another example which is of V_{s3}=200m/s and B_{10}=0.5 and 0.9 which is shown in Fig. 4.24, similar results to those previously found were deduced. The response in the vertical direction is similar to that in the horizontal direction, except that the peaks in the horizontal direction are larger. The second largest peak was also found at a frequency equal to 1.73 of the first peak. The higher the gradient the stronger the polarisation is.

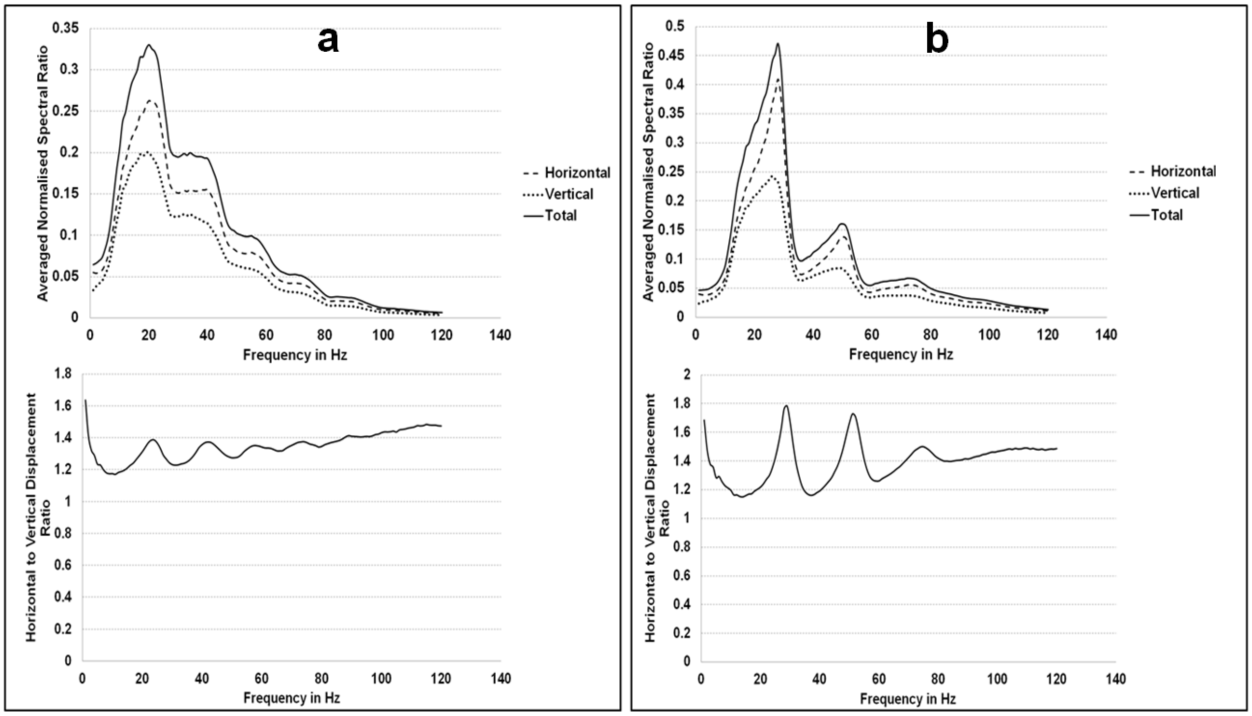

Fig. 4.23: Vertical and horizontal spectral displacement (top) and H/V spectral ratio (bottom) (a)V_{s3}=100m/s and B_{10} =0.5 (b)V_{s3}=100m/s and B_{10} =0.9.

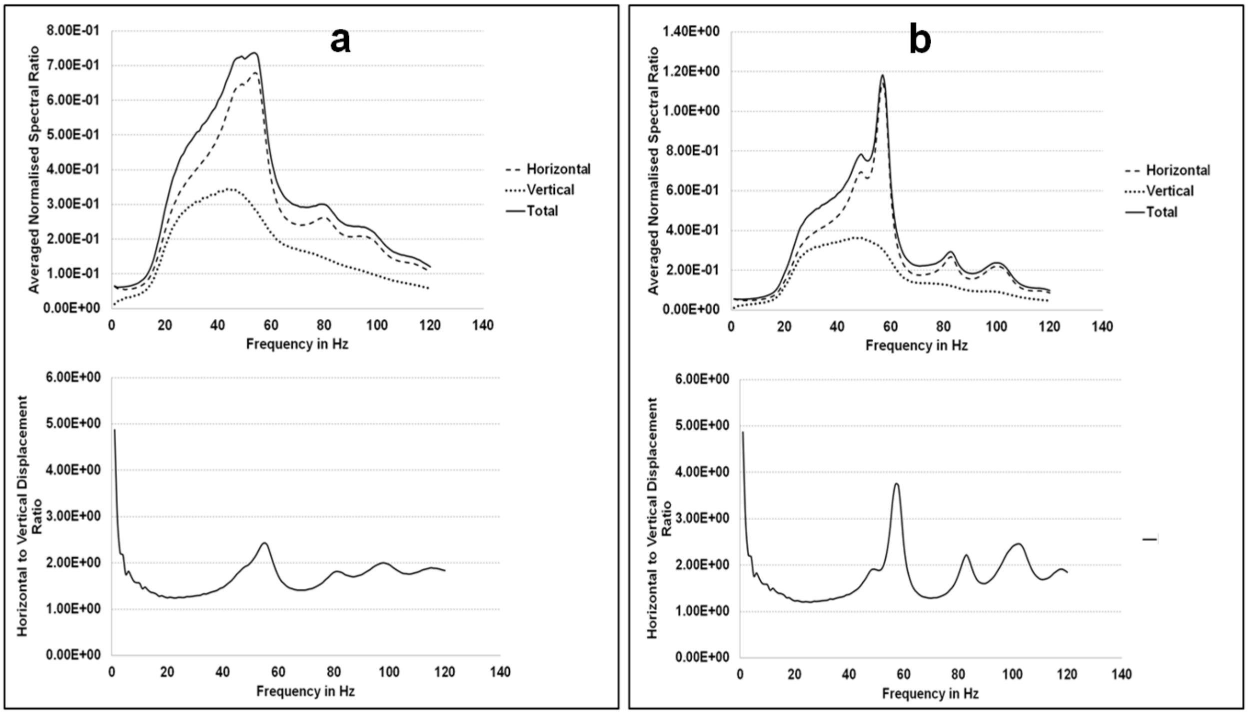

Fig. 4.24: Vertical and horizontal spectral displacement (top) and H/V spectral ratio (bottom) (a)V_{s3}=200m/s and B_{10} =0.5 (b)V_{s3}=200m/s and B_{10} =0.9.

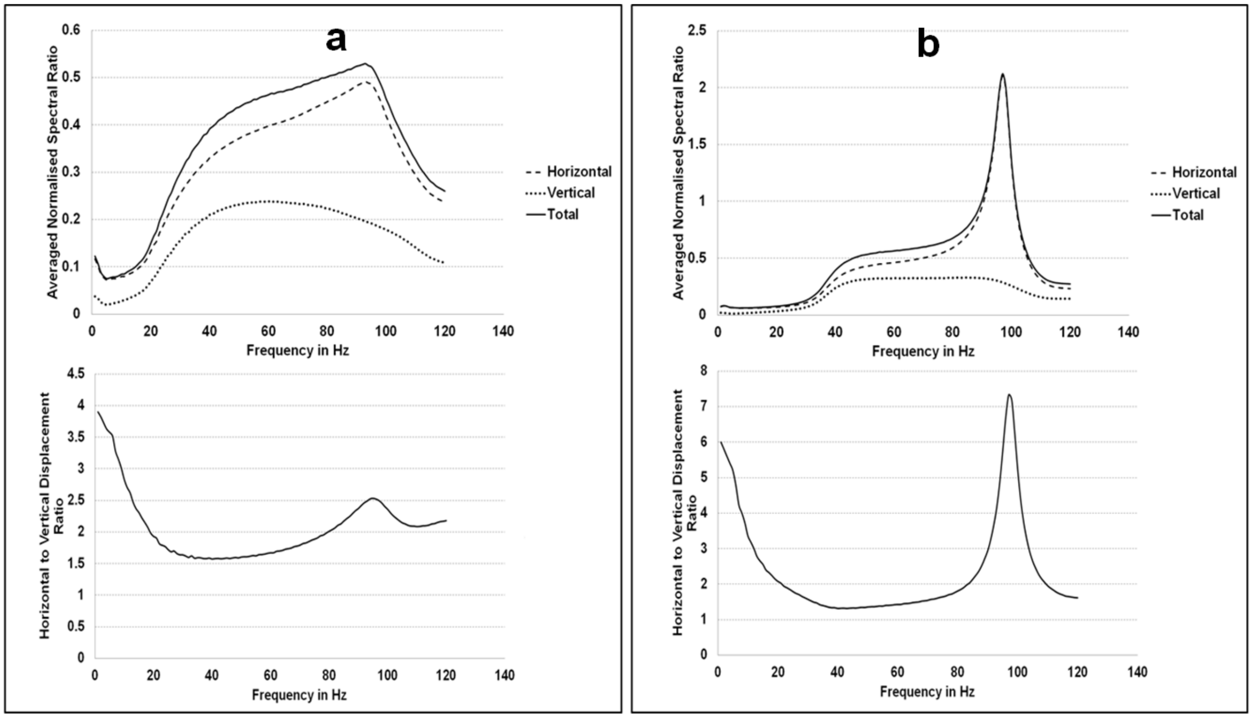

Fig. 4.25: Vertical and horizontal spectral displacement (top) and H/V spectral ratio (bottom) *(a)*V_{s3}=400m/s and B_{10} *=0.3 (b)*V_{s3}*=400m/s and* B_{10} *=0.6.*

The third example (shown in Fig. 4.25) discussed in this section is for V_{s3}=400m/s and B_{10}= 0.3 and 0.6 which was the highest gradient achieved for this value of V_{s3}. It could be seen that the peak found in the horizontal direction is very large, especially for B_{10}= 0.6, and a similar peak is nonexistent in the vertical direction. This indicates a very strong polarization which is again proven to be larger when the gradient is larger. Higher modes couldn't be detected in this case since already the resonance frequency is high, since it is proportional to V_{s3} as previously deduced.

In Appendix B two examples of H/V ratios are shown with 3D spectral maps. In the two examples it is clear that the polarisation could be seen at certain frequencies in the form of a constant ratio along the distance. These frequencies indicate the vibration modes of the soil and they are related with the same proportionality found analysing the averaged near field data.

4.7 Conclusions

The velocity-gradient proxies are reliable, robust and coherent indicators for sites classification according to their total and spectral response to surface sources.

The spectral analysis has shown that gradients B_{10} could be associated to certain frequencies. This is because gradients B_{10} are heavily influenced by layers depth along with a strong contrast between materials. This association is founded on the fact that the fundamental resonance frequency of the soil under surface excitation is strongly dependent on wavelengths and therefore on the depth and material properties of the first layer ($f_0 = V_{s3}/h_1$ where $h_1$is the depth of the surface layer). That means the deeper the first layer or the weaker the contrast, the lower the fundamental resonance frequency. The discrepancy with the case of seismic waves is large since the entire surficial layer is generally excited by seismic motions. Conversely, for surface sources, the response is dominated by surface waves and is thus highly dependent on the distance from the source. Along the distance, the effect of higher frequencies begins to fade in a proportional pattern. This relates to the associated smaller wavelengths, which are filtered through distances.

For sites associated to weak surface layers and high gradients, and starting from a critical distance, the second mode of vibration is triggered. It could be concluded that depending on V_{s3} and B_{10}, higher modes of excitation will be triggered from certain distances.

4.8 References

Abrahamson, N., and Silva, W. (2008). Summary of the Abrahamson and Silva NGA ground-motion relations. *Earthquake spectra*, *24*(1), 67-97.

Bard, P. Y., and Bouchon, M. (1985). The two-dimensional resonance of sediment-filled valleys. *Bulletin of the Seismological Society of America*, *75*(2), 519-541.

Boore, D. M. (2004). Estimating VS (30)(or NEHRP site classes) from shallow velocity models (depths< 30 m). *Bulletin of the seismological society of America*, *94*(2), 591-597.

Borcherdt, R. D., and Glassmoyer, G. (1992). On the characteristics of local geology and their influence on ground motions generated by the Loma Prieta earthquake in the San Francisco Bay region, California. *Bulletin of the seismological society of America*, *82*(2), 603-641.

Borcherdt, R. D. (1994). Estimates of site-dependent response spectra for design (methodology and justification). *Earthquake spectra*, *10*(4), 617-653.

Cadet, H., Bard, P. Y., and Duval, A. M. (2008, October). A new proposal for site classification based on ambient vibration measurements and the Kiknet strong motion data set. In *Proceedings of the 14th World Conference on Earthquake Engineering* (pp. 12-17).

Cadet, H., Bard, P. Y., Duval, A. M., and Bertrand, E. (2012). Site effect assessment using KiK-net data: part 2—site amplification prediction equation based on f 0 and Vsz. *Bulletin of Earthquake Engineering*, *10*(2), 451-489.

Gallipoli, M. R., and Mucciarelli, M. (2009). Comparison of site classification from VS30, VS10, and HVSR in Italy. *Bulletin of the Seismological Society of America*, *99*(1), 340-351.

Idriss, I. (2009). Use of VS_{30} to represent effects of local site conditions on earthquake ground motions. *Seismological Research Letters*, *80*(2), 363.

Kim, D. S., and Lee, J. S. (2000). Propagation and attenuation characteristics of various ground vibrations. *Soil Dynamics and Earthquake Engineering*, *19*(2), 115-126.

Luzi, L., Puglia, R., Pacor, F., Gallipoli, M. R., Bindi, D., and Mucciarelli, M. (2011). Proposal for a soil classification based on parameters alternative or complementary to Vs_{30}. *Bulletin of Earthquake Engineering*, *9*(6), 1877-1898.

Régnier, J., Bonilla, L. F., Bertrand, E., and Semblat, J. F. (2014). Influence of the Vs profiles beyond 30 m depth on linear site effects: Assessment from the KiK-net data. *Bulletin of the Seismological Society of America*, *104*(5), 2337-2348.

Semblat, J. F., Duval, A. M., and Dangla, P. (2002). Seismic site effects in a deep alluvial basin: numerical analysis by the boundary element method. *Computers and geotechnics*, *29*(7), 573-585.

Semblat, J. F., Kham, M., Parara, E., Bard, P. Y., Pitilakis, K., Makra, K., and Raptakis, D. (2005). Seismic wave amplification: Basin geometry vs soil layering. *Soil dynamics and earthquake engineering*, *25*(7), 529-538.

Chapter 5

Analysis of Vibration in Soils through Artificial Neural Networks

5.1 Introduction

In the previous chapter, it can be seen that the velocity-gradient B_{10} is influenced by two factors, the depth and the material contrast. For instance a strong contrast at a high depth and a weak contrast at a shallow depth may give a similar gradient value. While the effect of the deeper layers in soil is very important, the first layer plays an important role in the determination of the frequency response and the amplitudes as deduced in the previous chapter. It was proven that the effects of the thickness of the first layer h_1 is associated particularly with the dominant frequency with respect to the wavelength λ and therefore with the overall frequency response.

Fig. 5.1 shows how for a similar value of B_{10}=0.75, a different response could be found with a small variation of h_1 from 4m to 3m using the same Rayleigh damping definition of the previous chapters (V_{s3} in this case is equal to 200m/s). The change in the response is visible in terms of amplitudes and of frequency.

In order to overcome such problem, adding a factor h_1 which describes the first layer depth will help refine the prediction process. A depth factor will help segregating the effects of depth and contrast within the B_{10} gradient.

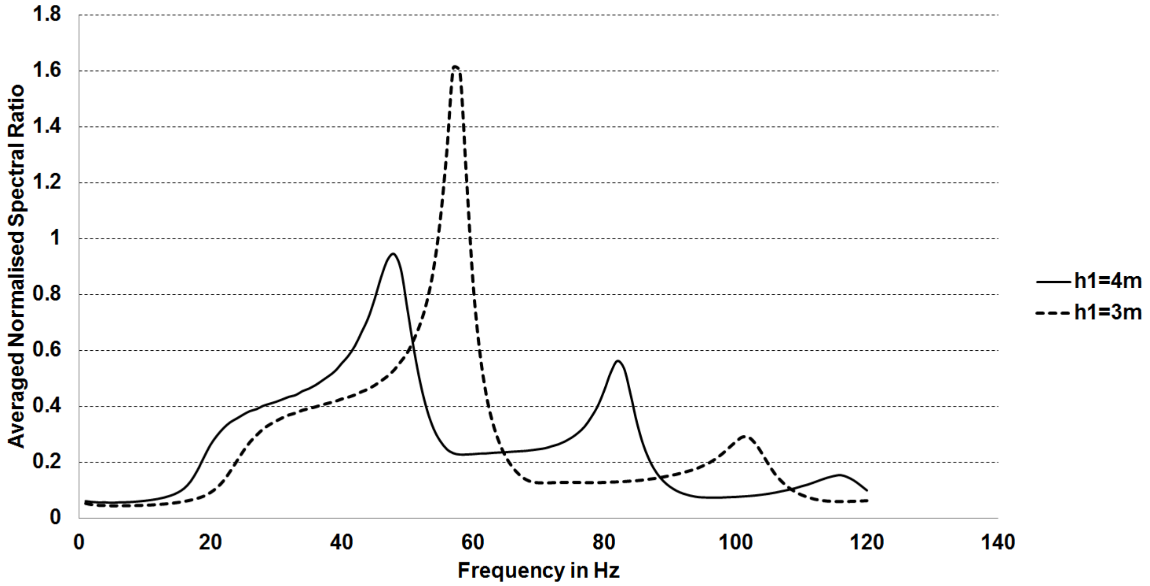

Fig. 5.1: Response for h_1=4m (solid black) and h_1=3m (dashed black) for similar V_{s3}=200m/s and B_{10}=0.75 in the near field using the same Rayleigh damping definition of the previous chapters.

In order to segregate the effects and better predict vibrations the new factor h_1 has been included in the analysis along with V_{s3} and B_{10}.

In this chapter, a prediction tool using a neural network based analysis is suggested. Later the developed tool is used in the analysis in order to deepen the understanding of the problem stated above.

The choice to work with neural networks is because of its capability to fastly interpolate, extrapolate and spouse results from other costly methods (FEM for instance). The solution speed could provide the advantage of predicting large number of cases almost instantly. The flexibility of the method is also a very important point, since it can deal with a large and widely varied number of inputs, making it suitable for theoretical studies (rare and unrealistic cases for instance). The precision of the method which will be discussed later is another motive to adopt it to avoid the excessive use of FEM that consumes plenty of time and memory storage.

5.2 Theoretical background and model architecture

Artificial neural networks are a branch of artificial intelligence domain based upon an assimilation of the human biological neural network system and was founded by McCulloch and his co-workers in early 1940's (Perlovsky, 2001). Neural networks are capable of finding patterns and recognizing similarities in a set of complex inputs through a training procedure based on prediction and comparison and auto-correction. This procedure provides the artificial neural network with a very efficient interpolation capabilities gathering the numerous properties of a very wide and varying dataset. These capabilities allow the tool to predict answers for inputs unknown to the code before and a precise prediction for wide new combinations of multiple inputs also unknown before. Neural networks were previously used for studying vibration in soils. Khandelwal and Singh (2006) studied maximum ground vibration values and frequency from blast sources using a neural network approach. Hung and Ni (2007) used neural networks to investigate the efficiency of trenches as an isolation method for railway vibration. Monjezi et al. (2011) attempted to predict blast-induced ground vibration using neural networks. Railway vibration was studied using neural networks besides numerical modeling by Connolly et al. (2014). Salameh (2016) used a neural network approach in order to analyze the correlation between damage caused in buildings at different soil and rock sites and a number of simplified mechanical and loading parameters

Back propagation technique (Hecht-Nielsen, 1992) is one of the most efficient and robust way of training neural networks and a brief description of its formulation is provided in this section. The feed-forward back-propagation neural network consists of three types of layers: input layer, output layer and hidden layer (as shown in Fig. 5.2).

The input layer has a number of neurons equal to the number of input parameters and the output layer has a number of neurons equal to the number of features of the sought solution. The hidden layers may have a varying number of nodes depending on the problem nature and size. Moreover the hidden layer could be increased to be multiple hidden layers, thus leading to a deep learning tool.

For the aim of analyzing the vibration problem from surface sources, an input layer of 5 neurons and an output layer of only one neuron are used. The five input neurons are equivalent to the following factors: V_{s3} , B_{10}, h_1, frequency and distance. The output will be for the amplitude which is the spectral normalized amplitude which was used in the previous chapter to analyze the spectral response of sites. Hidden layers will be set to three, simulating a deep learning problem.

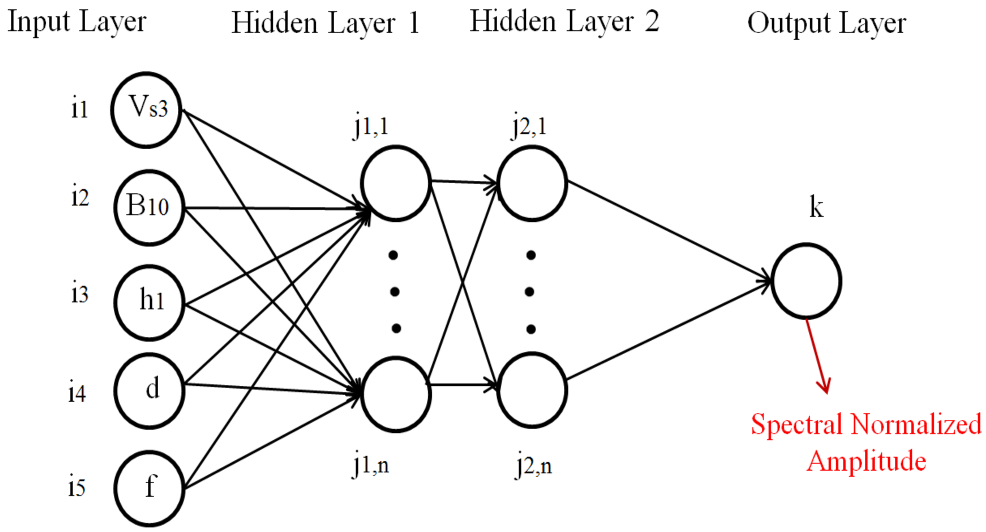

Fig. 5.2: Artificial neural network ANN deep learning tool (more than one hidden layer) diagram displaying the Input, Hidden and Output layers with respectively i, j and k are the input, hidden and output neurons.

The neurons in the hidden layers are associated with weights. These weights which are refined through the back propagation will represent the output of a neuron and therefore of the layer. These outputs will define the transfer function that associates and calculates the right output for the right input. The training process is in which the input data are driven through the hidden layers until it reaches the output layer. The calculated outputs through the hidden layers weights are compared to the real amplitudes. The difference between the predicted and the real outputs (amplitudes in this case) is then propagated back through hidden layers refining the existing weights of individual neurons/nodes. This procedure is repeated until a satisfying agreement between the calculated and real outputs is achieved. A brief mathematical description of the neural network mechanism follows. This description could be found in the literature (Khandelwal and Singh, 2006).

Let's consider an output layer *i*, a hidden layer *j* and an output layer *k* as shown in Fig. 5.2. In the hidden layer the net input values is

$$Net_j = \sum_{i=1}^{n} x_i w_{ij} + \theta_j \tag{5.1}$$

Where x_i are the input units, w_{ij} are the biases or weights on the node of the *i*th input and *j*th neuron, θ_j is the weight neuron and *n* is the number of input units.

A logarithmic sigmoid function is used to calculate the net output from the hidden layer:

$$O_j = f(Net_j) = 1/[1 + e^{-(Net_j + \theta_j)}] \tag{5.2}$$

The total input to the *k*th unit is, in an analogous fashion to the input of the *j*th unit in equation (5.1):

$$Net_k = \sum_{i=1}^{n} w_{jk} O_j + \theta_k \tag{5.3}$$

Where θ_k is the bias neuron, and w_{jk} is the weight between the *j*th neuron and the *k*th output.

Therefore, the total output from *k*th unit will be

$$O_k = f(Net_k) \tag{5.4}$$

In the training process, two patterns are presented to the system, an input pattern and a corresponding output pattern. The existing output in the network which is mostly incorrect is compared with the desired output. Hence, the error between the two outputs in a layer *k* is

$$e_t = t_k - O_k \tag{5.5}$$

With t_k the aim is output and O_k is the actual output.

The total error function will be:

$$E = 0.5\sum_{k=1}^{n}(t_k - O_k)^2 \tag{5.6}$$

The steepest descent error surface or the incremental weight is made using the following rule:

$$\nabla W_{jk} = -\eta(\delta E / \delta W_{jk}) \tag{5.7}$$

Where η is the learning rate parameter. The update of weights for the *(n+1)*th pattern is given as

$$W_{jk}(n+1) = W_{jk}(n) + \nabla W_{jk}(n) \tag{5.8}$$

The procedure will be repeated in a similar way for each layer when increasing the number of hidden layers.

Different inputs parameters have been chosen in a way to fit the multiple FEM experiments done as stated above and in order to fulfill the theoretical approach established previously. The thickness of the first layer h_1 is to be between 3 and 10 meters. h_1 beyond 10m means B_{10} is equal to zero (no change in the first 10 meters), and below 3m will not fulfill the V_{s3} parameter that describes at least the first 3m of soil .B_{10} between 0 and 1 which are the minimum and maximum values. V_{s3} values for 100, 200 and 400 m/s which usually describes the properties of shallow soils (this factor describes a combination of the Young's modulus, the density and the Poisson's ratio). The range of interest of this study was 60 meters next to the source in terms of distance. The frequency range was set between 0 and 120 Hz which is the range of interest.

Input Parameter	**Range**
Vs_3	100-400 m/s
B_{10}	0-1
h_1	3-10 m
Distance	0-60 m
Frequency	0-120 Hz

Table 5.1: Study Parameters influencing the vibration amplitude and their range.

In the models, all the three suggested factors i.e. V_{s3}, B_{10}, h_1 were integrated in a neural network tool in order to better predict vibration. Fig. 5.3 summarizes the logic of the prediction tool. V_{s3}, B_{10}, h_1 are considered interrelated while distance and frequencies are constant for all the cases.

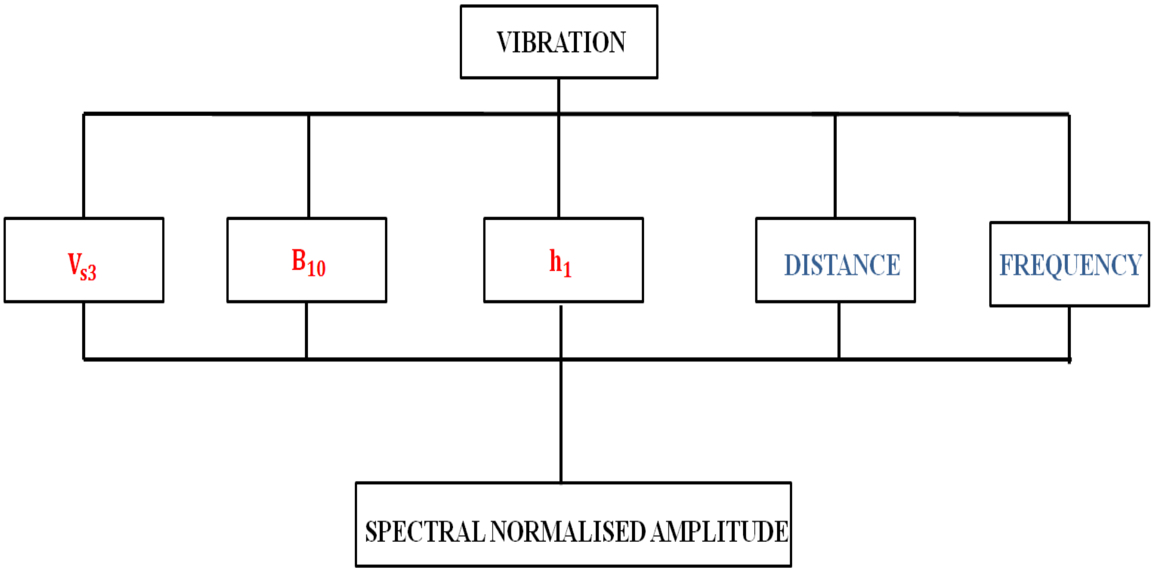

Fig. 5.3 Factors affecting the attenuation and amplification of vibration.

5.3 Assessment and validation of the neural network

The developed tool gave a fitting correlation R^2=0.93. In order to better assess the efficiency of the developed tool, a simple test was done through comparisons with FEM results. A case which was not studied before was analyzed using the ANN tool. This case is for a soil with V_{s3} =300m/s, B_{10}=0.3 and h_1=3m.

The root mean square error (equation 5.9) calculated as a measurement of precision between the two compared data (FEM and ANN) was 10%, meaning that the agreement between the two results was at 90%.

$$RMSE = \sqrt{\frac{\sum_{i=1}^{n}(prediction_i - real_i)^2}{n}} \qquad (5.9)$$

Fig. 5.4 shows the comparison between FEM and ANN results. It is clear that the results are generally consistent in terms of frequency distribution and amplification locations.

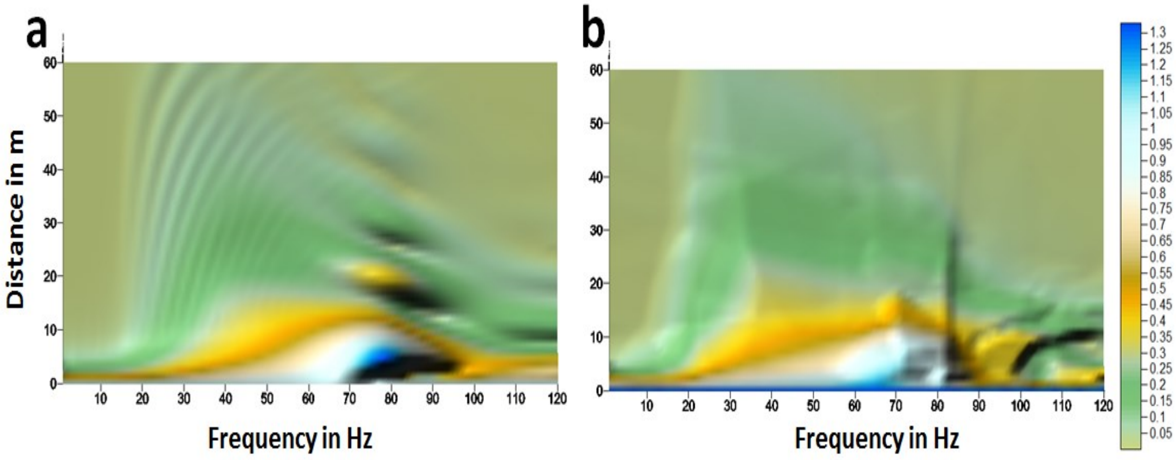

Fig. 5.4: Comparison of propagation maps between (a) FEM and (b) Artificial Neural Network.

Furthermore and in order to facilitate the prediction and improve the efficiency, the tool was modified and used to analyze and directly predict the transfer functions for the specific field of interest. Fig. 5.5, 5.6 and 5.7 show a group of results from Artificial Neural Networks (ANN) and their comparison with FEM. All these cases are totally new and the ANN tool never experienced them before. Analyzing the transfer functions raised the precision of the tool to 98%.

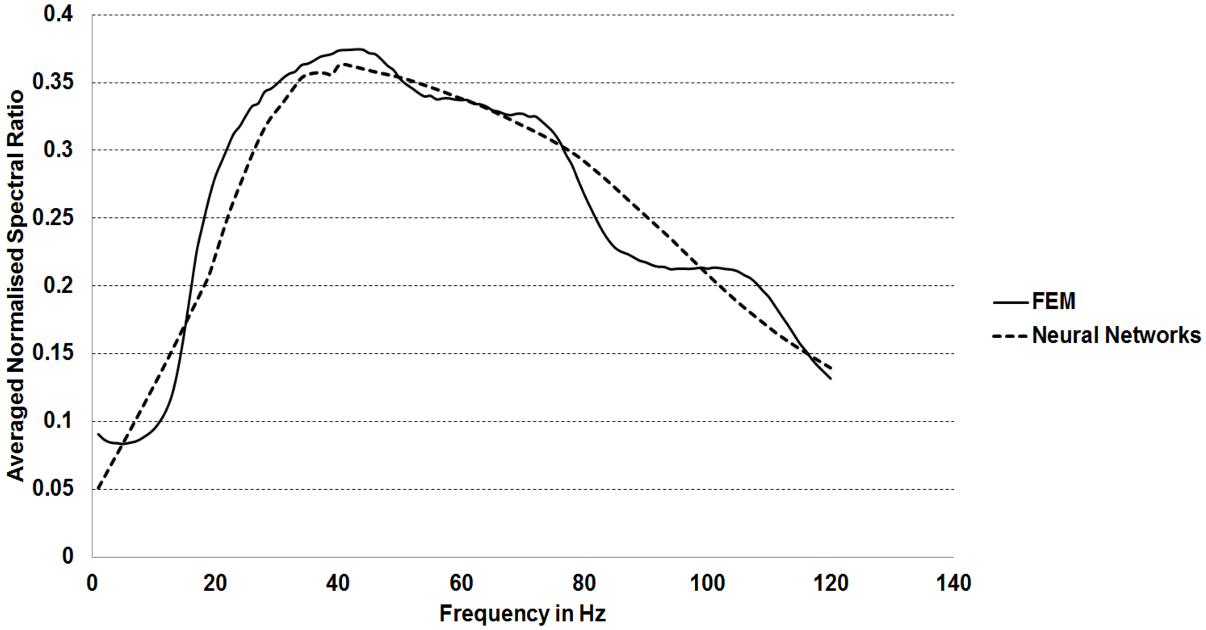

Fig. 5.5: Comparison between the results from FEM (solid black) and ANN (dashed black) for a site of V_{s3} =300m/s, B_{10}=0.28 and h_1=7m in the near field.

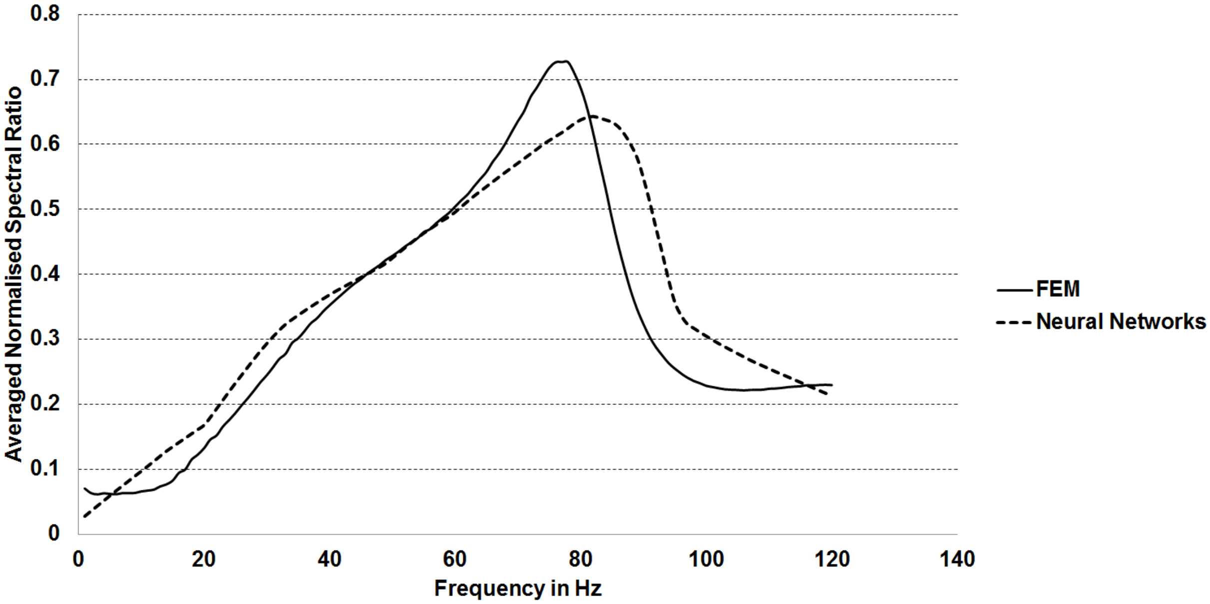

Fig. 5.6: Comparison between the results from FEM (solid black) and ANN (dashed black) for a site of V_{s3} =300m/s, B_{10}=0.302 and h_1=3m in the near field.

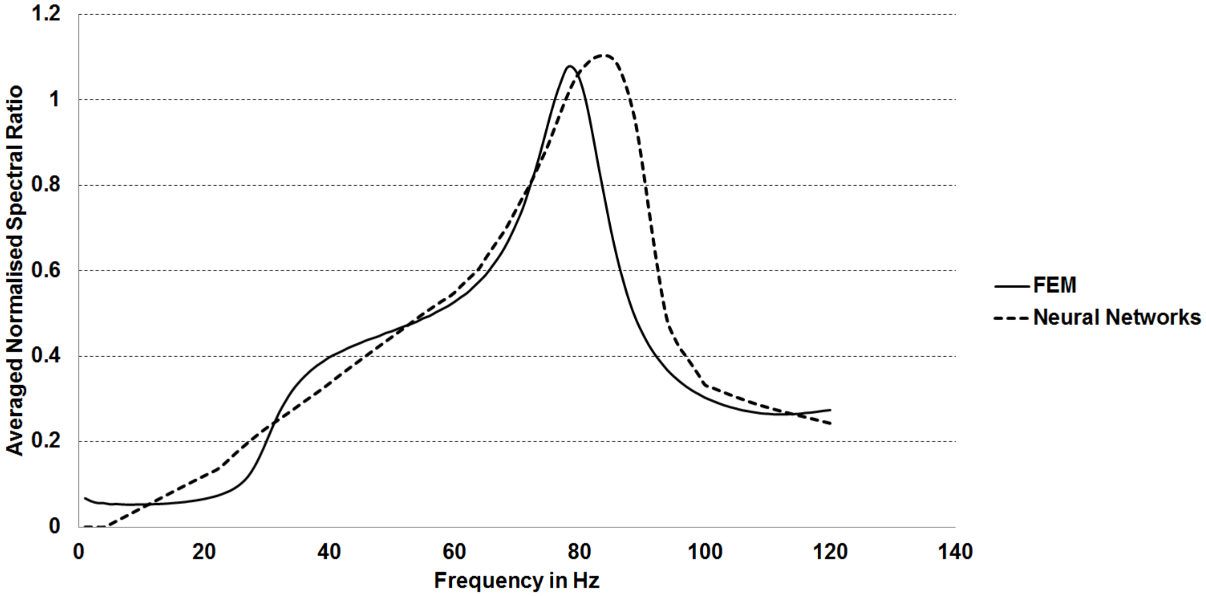

Fig. 5.7: Comparison between the results from FEM (solid black) and ANN (dashed black) for a site of V_{s3} *=300m/s,* B_{10}*=0.734 and* h_1*=3m in the near field.*

5.4 Effects of $\mathbf{B_{10}}$ and $\mathbf{h_1}$

In the following part of this chapter, the developed tool is used to deepen the analysis of the results deduced in the previous chapter. The analysis is divided into three parts, each one relevant to a specific field: near, mid and far fields respectively. The analysis will be focused on assessing the segregated effects of B_{10} and h_1. In order to comprehend the effects, the comparisons were done using two parametric types of study. The first was assessing the effects of h_1 through varying it with a fixed value of B_{10}; the second was the assessment of B_{10} through varying it along with a fixed value h_1. Two examples for the two parametric types of study are respectively shown in Fig. 5.8 and 5.9. Both examples are for Vs_3=400m/s in the near field. All the graphs of the analysis could be found in Appendix C.

The results of the analysis are summarized for all the three fields and the three types of soils along with concluding remarks for each of the fields. Only the most important observations are noted in this section.

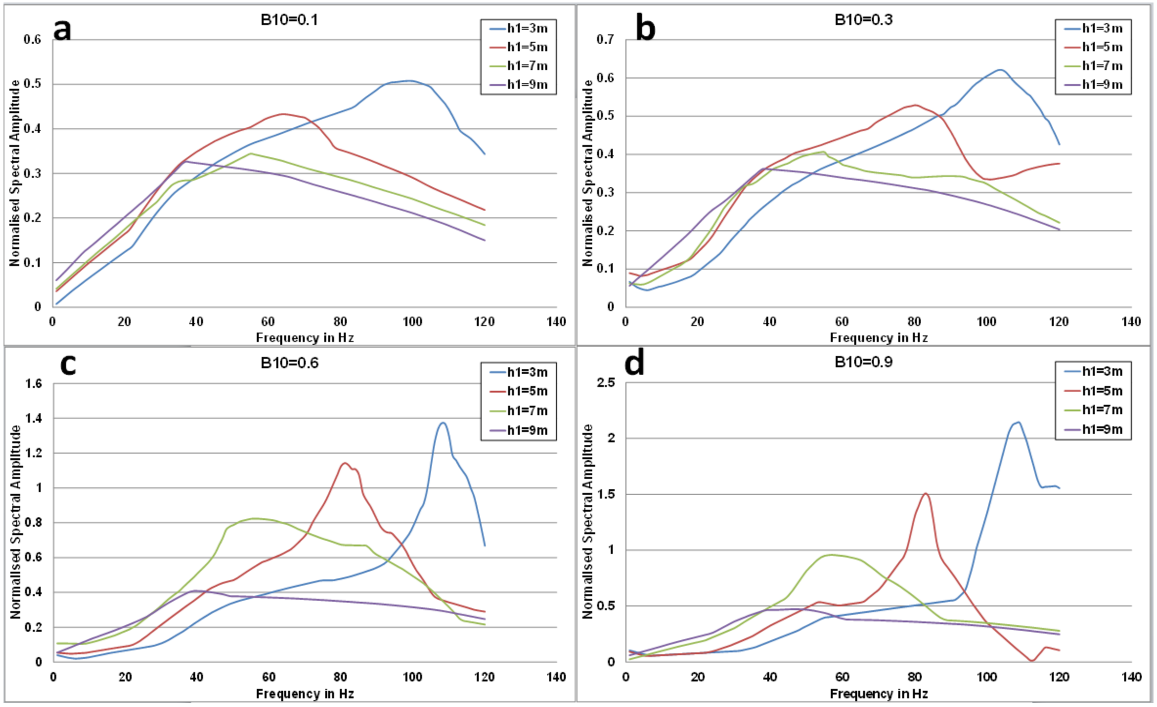

Fig. 5.8: Spectral representation calculated using ANN of Vs_3=400m/s varying h_1 for (a) $B_{10} = 0.1$, (b) $B_{10} = 0.3$, (c) $B_{10} = 0.6$, (d) $B_{10} = 0.9$ in the near-field.

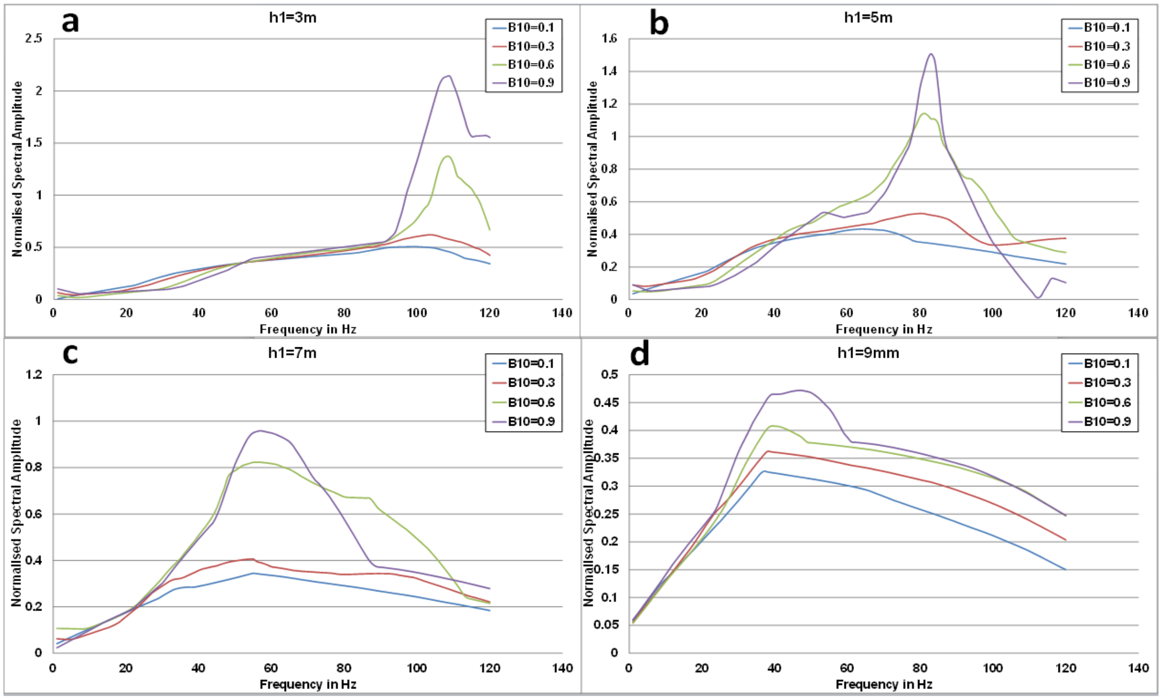

Fig. 5.9: Spectral representation calculated using ANN of Vs_3=400m/s varying B_{10} for (a) $h_1 = 3m$, (b) $h_1 = 5m$, (c) $h_1 = 7m$, (d) $h_1 = 9m$ in the near-field.

5.4.1 Effects of $\mathbf{B_{10}}$ and $\mathbf{h_1}$ in the near-field

For $\boldsymbol{Vs_3}$=100m/s, the smallest the h_1, the higher the amplitudes. The frequency associated to the peak is decreasing with a rising h_1. The effects of B_{10} started to disappear from a shallow depth which is 3m.

For $\boldsymbol{Vs_3}$=200m/s, higher amplitudes are associated with smaller h_1. The resonance frequency is varying inversely with the layer depth, following the formula Vs_3/h_1.The effects of B_{10} started to disappear from a certain depth around 5m.

For $\mathbf{Vs_3}$=400m/s, smaller h_1 are associated to larger peaks and higher frequencies. The effects of B_{10} are still clearly present till high depths, i.e. 9 m.

To summarize, the effects of B_{10} are related to the depth of the first layer h_1 and the wave velocity of this layer. For weaker soils, the effects of B_{10} will start disappearing at shallower depths and vice versa. The near field is dominated by higher frequencies which are associated to smaller wavelengths. The effects of smaller wavelengths are less influenced by the deeper layers since they are unable to reach them.

5.4.2 Effects of $\mathbf{B_{10}}$ and $\mathbf{h_1}$ in the mid-field

For $\boldsymbol{Vs_3}$=100m/s, the larger h_1, the slightly smaller the maximum amplitudes are, and the smaller their effects are on the higher frequencies. For larger B_{10}, smaller h_1 caused soil response to start appearing from a higher frequency. Moreover higher modes peaks start to appear in higher frequencies. The association between smaller h_1 and higher frequencies is still present and vice versa.

When fixing h_1 and varying B_{10} it was concluded that for h_1=3m, the higher B_{10} the higher the frequencies associated to it. Higher modes are excited by larger B_{10}.

The larger the h_1, the less difference there is between peak amplitudes, but the effect on higher frequencies could still be detected for higher B_{10} even at h_1=9m.

For $\boldsymbol{Vs_3}$=200m/s, no clear trend could be easily detected when analyzing the results from taking h_1 as the varying parameter, especially that peak amplitudes are close. The only clear trend was a shift toward higher frequencies when h_1 is equal to 3m.

When fixing h_1 and varying B_{10}, the aspects are more coherent. Higher B_{10} is associated with higher peaks independently of h_1. Lower frequencies are more sensitive to smaller B_{10}. The larger B_{10}, the response starts shifting slightly toward higher frequencies.

For Vs_3=400m/s, for B_{10}=0.1 and 0.3, the effect of h_1 is almost negligible. For higher B_{10} the effect of h_1 seems to be more apparent except the coherence is missing.

When fixing h_1 and varying B_{10}, it is noticed that the higher B_{10}, the higher the peak amplitudes are and the higher the affected frequencies. The response starts to appear from a lower frequency when $B_{10}$is smaller. The smaller the B_{10} the broader the response, higher B_{10} tend to generate a more focalized response in terms of frequency.

To conclude, for Vs_3=100m/s there is an important influence of B_{10} unlike the near field. Its effect is very important particularly on higher frequencies. The effect of the factor h_1 appeared to be less important for Vs_3=200m/s and 400m/s. It was generally limited to the case of h_1=3m which often caused a remarkable response for higher frequencies especially when associated to large gradients. The effects of B_{10} are much dominant in the midfield for these two types of soil. Larger B_{10} caused higher peaks of amplitudes. Larger B_{10} had less influence on the lower frequencies and their peaks were associated to higher frequencies. Moreover the response caused by large B_{10} was focalized around a certain frequency. This is due to the tendency of soils with smaller B_{10} to respond more similarly to homogeneous soils in this field.

Larger B_{10} has more influence on higher frequencies and less influence on lower frequencies even without the clear presence of a second mode of vibration. This may be explained by the response (and therefore the effects) of deep strong soils to larger frequencies while deep weak soils respond strongly to low frequencies and attenuate high frequencies.

The difference between the responses of soils with Vs_3=100m/s on one hand and that of Vs_3=200m/s and 400m/s on the other hand, is that the effects of gradients in the latter cases are not manifested in a clear higher mode while in Vs_3=100m/s it is. It seems that the behavior for the cases of Vs_3=200m/s and 400m/s is rather transitional while for Vs_3=100m/s it is not. For Vs_3=100m/s the variation of behavior will happen rather quickly since the soil is associated to very small wavelengths in comparison to the other two cases.

5.4.3 Effects of $\mathbf{B_{10}}$ and $\mathbf{h_1}$in the far-field

For $\boldsymbol{Vs_3}$=100m/s, the larger B_{10} the stronger the effects of h_1. The larger B_{10} and the smaller h_1, the larger the amplitudes and wider the response in terms of frequency (more effects on higher frequencies/modes of vibration)

When fixing h_1 and varying B_{10}, it was noticed that for small h_1 the higher frequency response is raising with B_{10} along with the emergence of higher modes. For large h_1, the amplitudes are declining with larger B_{10}, while the effects of higher modes is becoming negligible and differences in terms of frequency distribution is minimal. The larger h_1, the larger the gap between amplitudes caused by varying B_{10}.

For $\boldsymbol{Vs_3}$=200m/s, till B_{10}=0.6 it could be noticed that except for h_1=3m the order of amplitudes is more or less similar and the larger the h_1 the more the response is shifted toward the low frequencies. The case where h_1=3m is characterized by relatively smaller peak amplitudes and a much stronger response in the higher frequencies.

When fixing h_1 and varying B_{10}, it was noticed that for larger h_1, the effects of higher frequencies are less apparent. Rising h_1 will cause mainly the response of B_{10}=0.1 to start rising in terms of amplitudes and the conversely for B_{10}=0.9.

For $\boldsymbol{Vs_3}$=400m/s, with a rising h_1 the amplitudes associated to higher gradients starts to decline. For all cases of h_1s, smaller gradients are associated to smaller frequencies.

To conclude, the first conclusion drawn is that in the far field, both factors h_1 and B_{10} played a significant role in the determination of the response. Some components in the behavior of Vs_3=200m/s in the far-field, the appearance of second mode of vibration peaks for instance, are similar to some components in the behavior of Vs_3=100m/s in the mid-field.

In the far-field, similarly to some cases in the mid-field, when the first layer depth is very large the effects of smaller gradients are stronger than those of larger gradients. This could be attributed to the weak response of the deep stronger soils to the low frequencies (which are associated to the only waves capable of reaching them at this level). Stronger soils are more sensitive to higher frequencies and not low frequencies as it was deduced before. Deep stronger soils are allowing smaller frequencies to be transmitted into the half-space.

5.5 References

Connolly, D. P., Kouroussis, G., Giannopoulos, A., Verlinden, O., Woodward, P. K., and Forde, M. C. (2014). Assessment of railway vibrations using an efficient scoping model. *Soil Dynamics and Earthquake Engineering*, (*volume 58)*, 37-47.

Robert Hecht-Nielsen, (1992). Theory of the backpropagation neural network, Neural networks for perception (Vol. 2): computation, learning, architectures, Harcourt Brace & Co., Orlando, Florida.

Hung, C. C., and Ni, S. H. (2007). Using multiple neural networks to estimate the screening effect of surface waves by in-filled trenches. *Computers and Geotechnics*, *34*(5), 397-409.

Khandelwal, M., and Singh, T. N. (2006). Prediction of blast induced ground vibrations and frequency in opencast mine: a neural network approach. *Journal of sound and vibration*, *289*(4), 711-725.

Monjezi, M., Ghafurikalajahi, M., and Bahrami, A. (2011). Prediction of blast-induced ground vibration using artificial neural networks. *Tunnelling and Underground Space Technology*, *26*(1), 46-50.

Perlovsky, L. I. (2001). Neural networks and intellect. Oxford University Press.

Salameh, C. (2016). *Ambient vibrations, spectral content and seismic damages: new approach adapted to the urban scale. Application on Beirut* (Doctoral dissertation, Université Grenoble Alpes).

Chapter 6

Classification of Sources and Sites

6.1 Introduction

Vibrations in civil engineering are usually radiated by from the utilization of infrastructures. In order to assess in this chapter the multiple sources of vibration in the light of the site classification suggested earlier, measurements of vibrations will be analyzed. Matching the spectral properties of sources with those of a given site will facilitate the assessment of vibration hazard of the site. Recorded data from the CEREMA database were used. The data were mainly from four types of sources: pile driving, vibro-driving, truck traffic and trains traffic. All measurements used in the analysis were recorded between 3.5m and 12.5m from the source, i.e. within the predefined near-field (within the first 20m). Nearest recorded data was considered as the source. Analyzing the frequency content of the multiple sources has been performed in comparison with the near-field sites responses deduced in the previous chapters.

6.2 Spectral matching of sources and sites

Each source recording is usually characterized by a spectral content describing the amplitude associated to each frequency. This part explores a method capable of assessing the similarity between the spectral properties of both sites and sources. In order to achieve this aim, two concepts should be well defined, the spectral properties and the relative spectral properties of a given source or site. The spectral properties are the raw distribution of energy or sensitivity to a certain frequency while the relative spectral properties are the same distribution but in a relative manner to the total energy or sensitivity carried.

First the spectral content found after the Fourier transform should be represented not with the raw values but by the relative amplitude content for each frequency compared to the total amplitude carried. For the sites, the same analysis should be done except that the spectral response represents the sensitivity of the site for each frequency and not the energy carried. The relative spectral response will be calculated using the proposed equation (6.1).

$$E_f = \frac{\int_{f-1}^{f+1} R(f)df}{\int_{f_{\min}}^{f_{\max}} R(f)df} \tag{6.1}$$

Where E_f is either the relative amplitude carried by a frequency band for source spectrums or the sensitivity of the site at a given frequency for sites spectrums. The frequency ranges from 0 to 120 Hz. *R(f)* is the spectral response/content of the site or source. An example explaining of the amplitudes distribution by frequency is shown in Fig. 6.1.

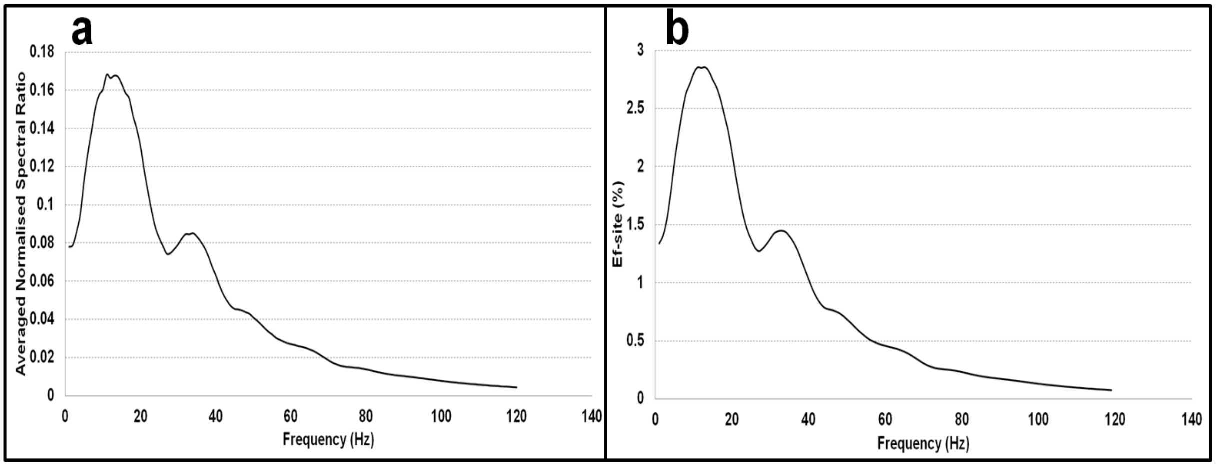

Fig. 6.1: (a) average normalized spectral amplitudes by frequency; (b) relative average normalized spectral amplitudes by frequency.

Then the matching between the spectral content of a source and a site response will be measured using a deviation factor proposed as shown in equation (6.2). The frequencies in the range of interest which is equal to 120 Hz are represented by *n* in the equation.

$$\sigma = \frac{\sum_{i=1}^{n} \left| \frac{E_{fi}(source) - E_{fi}(site)}{E_{fi}(site)} \right|}{n} \tag{6.2}$$

The more σ tends to zero the more the source and the site are matching and vice versa. The matching of the site and the source represents the hazard of resonance of a site for a given source in the near field. Fig. 6.2 shows an example of spectral matching for a pile driving source at two different sites, V_{S3}=100m/s and B_{10}=0.2 on one hand and V_{S3}=200m/s and B_{10}=0.8 in the other hand. In Fig. 6.2 (a) a strong matching between the source and the site could be seen and characterized with a small value of deviation σ equal to 0.36. In Fig. 6.2 (b) smaller matching is found between the source and the site as seen and a larger value of deviation σ is found equal to 3. The smaller matching shown in Fig. 6.2(b) indicates a smaller vibration hazard.

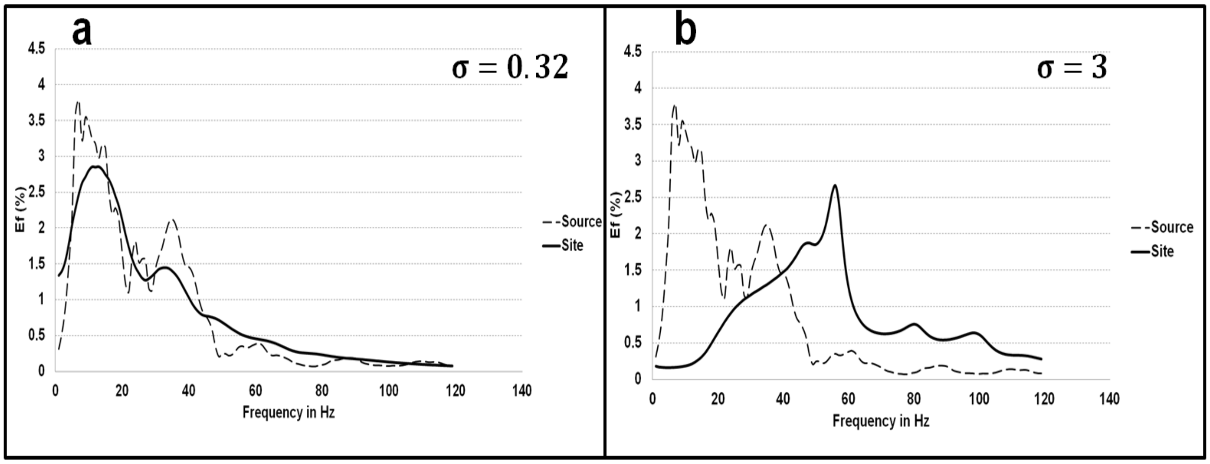

Fig. 6.2: (a) Spectral matching between a pile driving recording and a soil of V_{S3}=100m/s and B_{10}=0.2; (b) Spectral matching between a pile driving recording and a soil of (V_{S3}=200m/s and B_{10}=0.8). (Source in dashed line and site in solid line).

6.3 Sites classification by source

In the following sections, the methodology established above will be used in order to assess four different types of sources along with the twenty four sites defined in chapter 4. The four types of sources are: pile driving, vibro-driving, truck circulation and train circulation. Each recording for all these sources has three components. The sites are defined using V_{S3} and B_{10} factors.

6.3.1 Pile driving

Records for pile driving were taken at proximity of the source, at 3.5m and 4.5m. Fig. 6.3 (a) shows the deviation σ in the three directions of measurement along with their average for each site for a distance of measurement equal to 3.5 m. Fig. 6.3 (b) shows the same at a distance of 4.5 m for a different case, the difference is minimal. Fig. 6.4 shows the average deviation, for all sites, from all the recordings of pile driving.

It could be deduced that the vibration hazard in weaker sites is clear for this type of source. For V_{S3}=100m/s the deviation σ is nearly zero and almost the same independently from B_{10}, except for B_{10}=0.9 where σ rises slightly. For stronger soils i.e. V_{S3}=200m/s and 400m/s, the hazard which is inversely related to σ, is much smaller than that for V_{S3}=100m/s. For both soils i.e. V_{S3}=200m/s and 400m/s, the larger the gradient the larger σ and therefore the smaller the aggravation of the hazard in the site for pile driving sources.

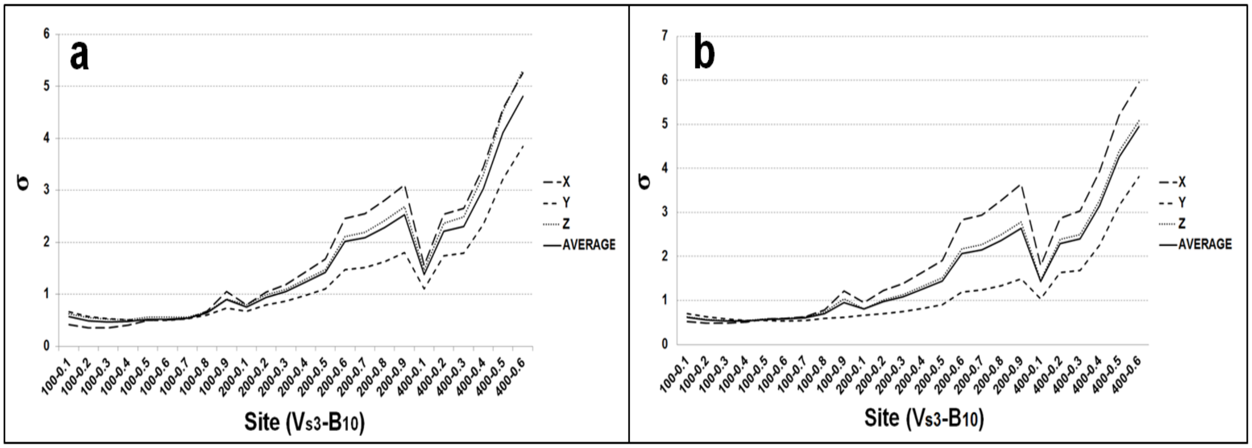

Fig. 6.3: *(a) Deviation factor by site for a pile driving measurement at 3.5m; (b) Deviation factor by site for a pile driving measurement at 4.5m.*

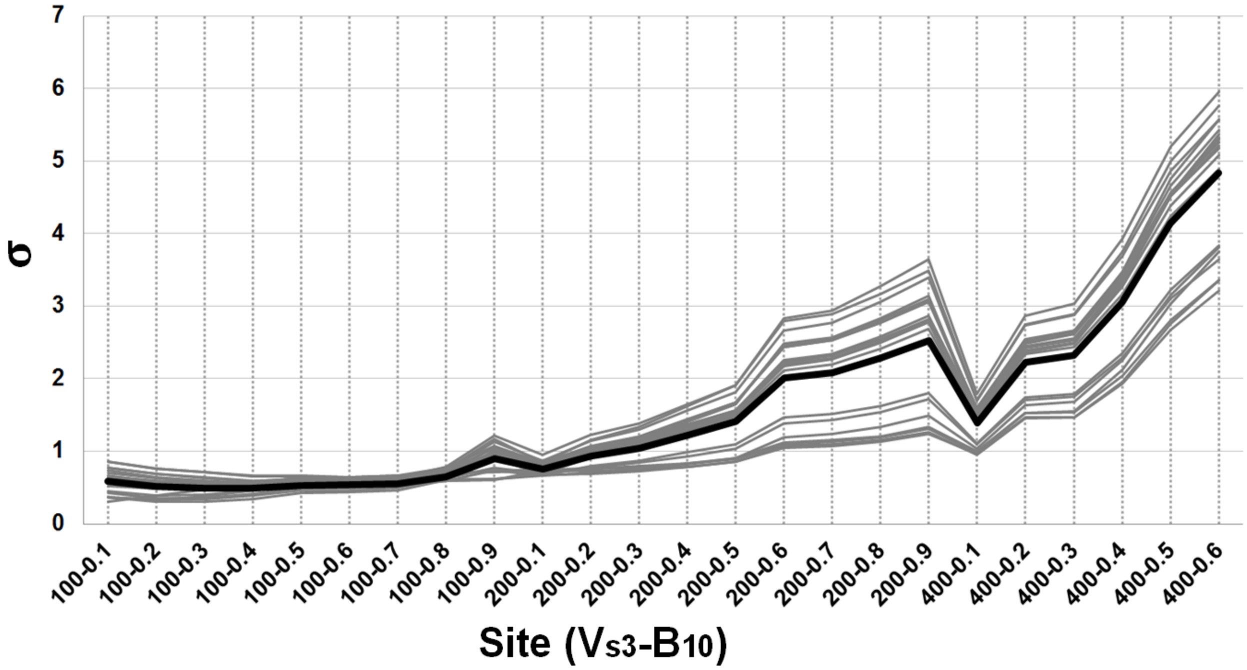

Fig. 6.4: Deviation factor by site for pile driving sources- average in bold black.

It is worth noticing that when V_{S3} is the changing factor (between 100-0.9 and 200-0.1 for instance) a remarkable variation is detected usually characterized by a reduction of σ and therefore a higher hazard. For two instances, namely between site 100-0.9 and 200-0.1 in one hand and between 200-0.9 and 400-0.1 on the other hand, it could be seen that a stronger soil with small gradient could be more sensitive than a weaker soil with large gradient.

Weaker soils are more sensitive to smaller frequencies, and as shown in previous chapters the higher the gradient for the same soil type, more the soil is sensitive to higher frequencies. For pile driving most of the energy tends to be concentrated at lower frequencies (Fig. 6.5). This explains the reason why weaker soils, i.e. smaller V_{S3} and B_{10} are more sensitive to pile driving sources.

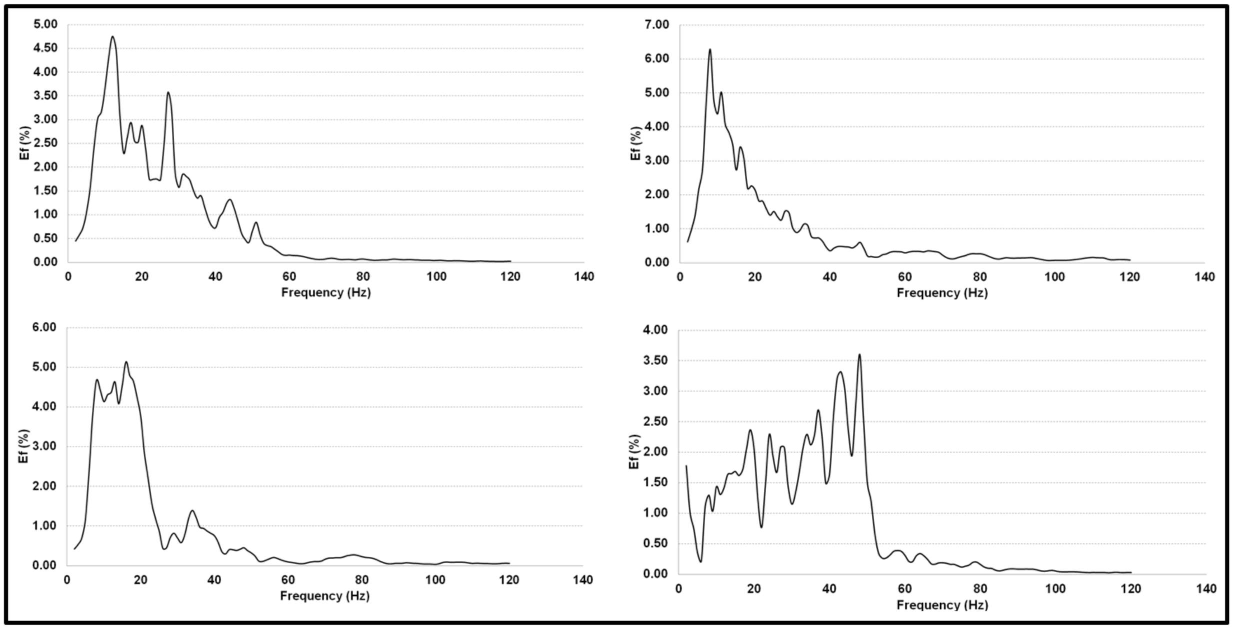

Fig. 6.5: Relative amplitude distribution by frequency for several pile driving recordings.

6.3.2 Vibro-driving

All records for vibro-driving were taken at proximity of the source, at 3.5m and 4.5m. Fig. 6.6 shows the deviation σ in the three directions for two different measurements, the similarity could be easily detected. The difference of response for different directions could also be noticed, i.e. in Fig.6.6 (a). The less influencing direction for weak soils is that of the x-direction while it was the z-direction in the second case represented in Fig.6.6 (b). Fig.6.7 shows the average deviation for all sites from all the recordings of vibro-driving.

Taking into account that measurements between normal pile driving and vibro-driving are taken at the same distances, sites responses are very different.

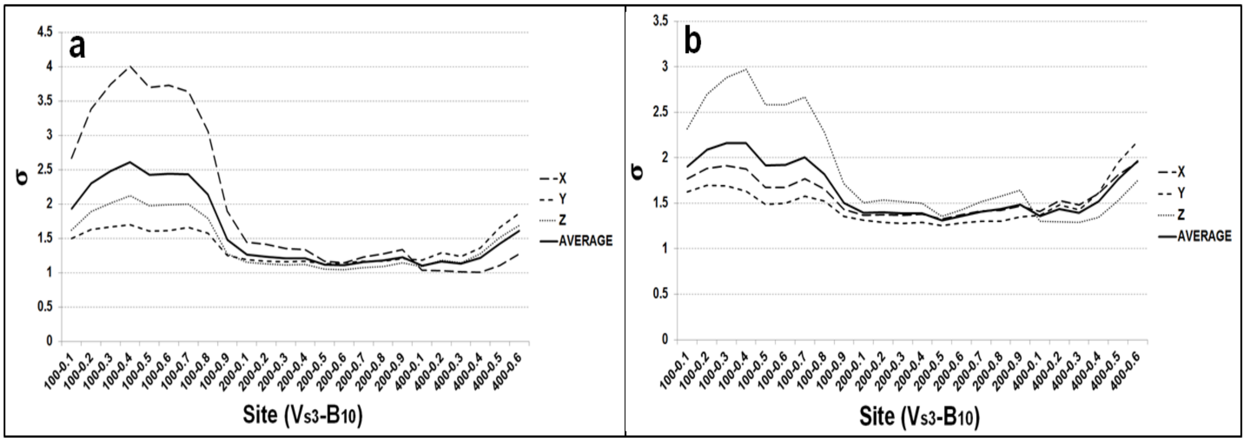

Fig. 6.6: (a) Deviation factor by site for a pile driving measurement at 3.5m; (b) Deviation factor by site for a pile driving measurement at 4.5m.

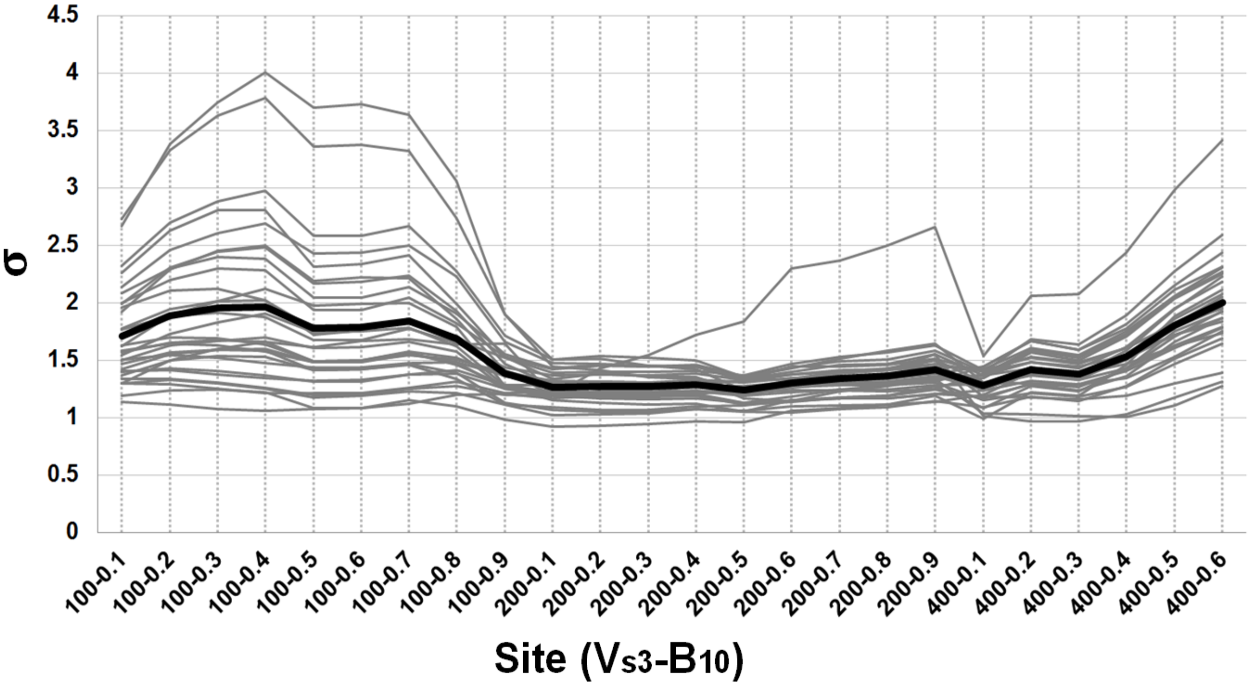

Fig. 6.7: Deviation factor by site for vibro-driving sources- average in bold black.

It could be deduced that the highest vibration hazard is at the mid-section of sites, i.e. in soils having V_{S3}=200m/s, for this type of source. For V_{S3}=200m/s the deviation σ is at its minimum value and is almost the same independently of B_{10}. For soils with V_{S3}=400m/s, the aggravation of hazard which is inversely related to σ rises with the gradient, for small gradients the hazard is similar to that of V_{S3}=200m/s. For soils with $\mathrm{V_{S3}}$=100m/s, σ has its largest values for small gradients and it tends to become smaller with higher gradients.

The responses of the different sites tend to be more or less steady and constant, with more sensitive sites in the middle section (in soils having V_{S3}=200m/s) as mentioned before. This could be attributed to the fact that the excitation coming from vibro-driving tend to be concentrated on a single or limited number of frequencies, because of the monotonic driving mechanism of the engine. Fig. 6.8 shows randomly selected spectral contents from multiple vibro-driving recordings and from different directions (vertical, horizontal and transversal). Fig. 6.8 shows that the main excitation frequency tends to be focused near 40 Hz; and secondly around 75 Hz. It was found previously that the dominant frequency is equal the ratio between the shear velocity of the first layer and its depth. In order to get a frequency equal to 40 Hz, V_{S3}=100m/s needs a very small h_1 (less than 3m) which is usually associated with very large gradient. If V_{S3}=400m/s , it needs a first layer thickness equal to 10 m in order to get a resonance frequency around 40 Hz, very deep first layers are associated with very small gradients. This explains why sites with V_{S3}=100m/s and very high gradients and sites with V_{S3}=400m/s and very low gradients had more aggravation of hazard for vibro-driving as shown in Fig. 6.7. A similar logic can explain why sites with V_{S3}=200m/s (which fall between sites with V_{S3}=100m/s and very high gradients and sites with V_{S3}=400m/s and very low gradients) are the most sensitive to vibro-driving.

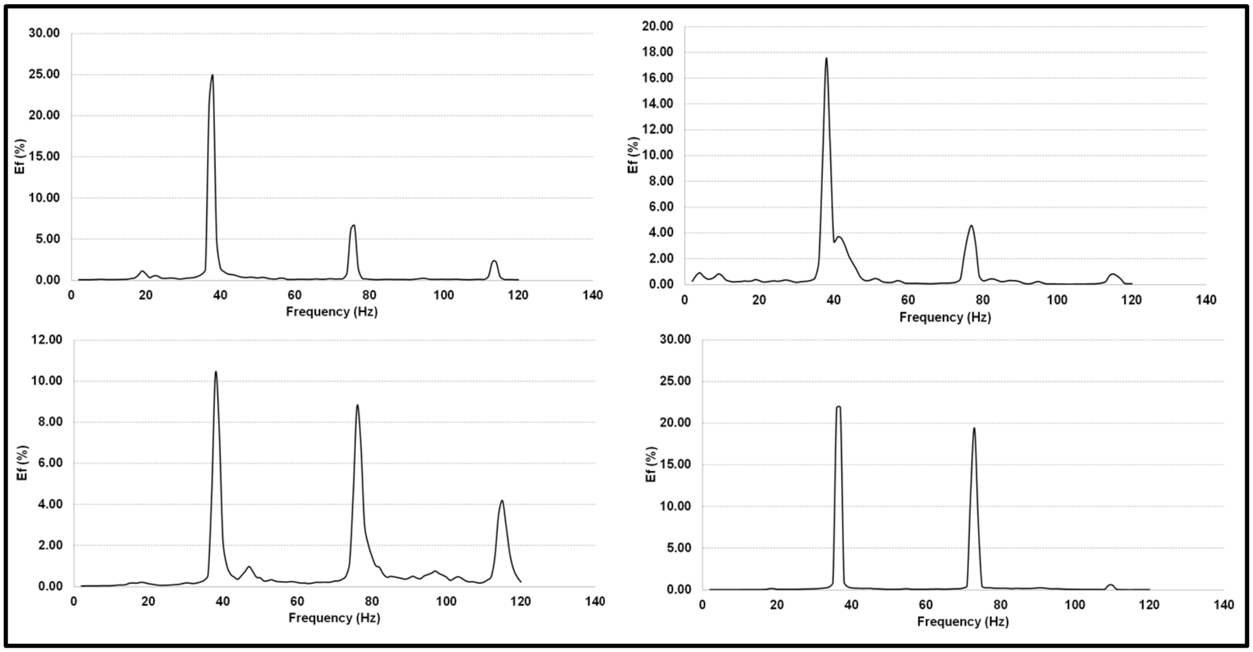

Fig. 6.8: Relative amplitude distribution by frequency for various vibro-driving recordings.

6.3.3 Trucks traffic

The available records for trucks traffic were taken at 9.4 m and 10 m, which are rather far from the source, but still in the predefined near-field. Fig. 6.9 shows the average deviation factor for all sites from all the recordings of truck circulation taken from all distances.

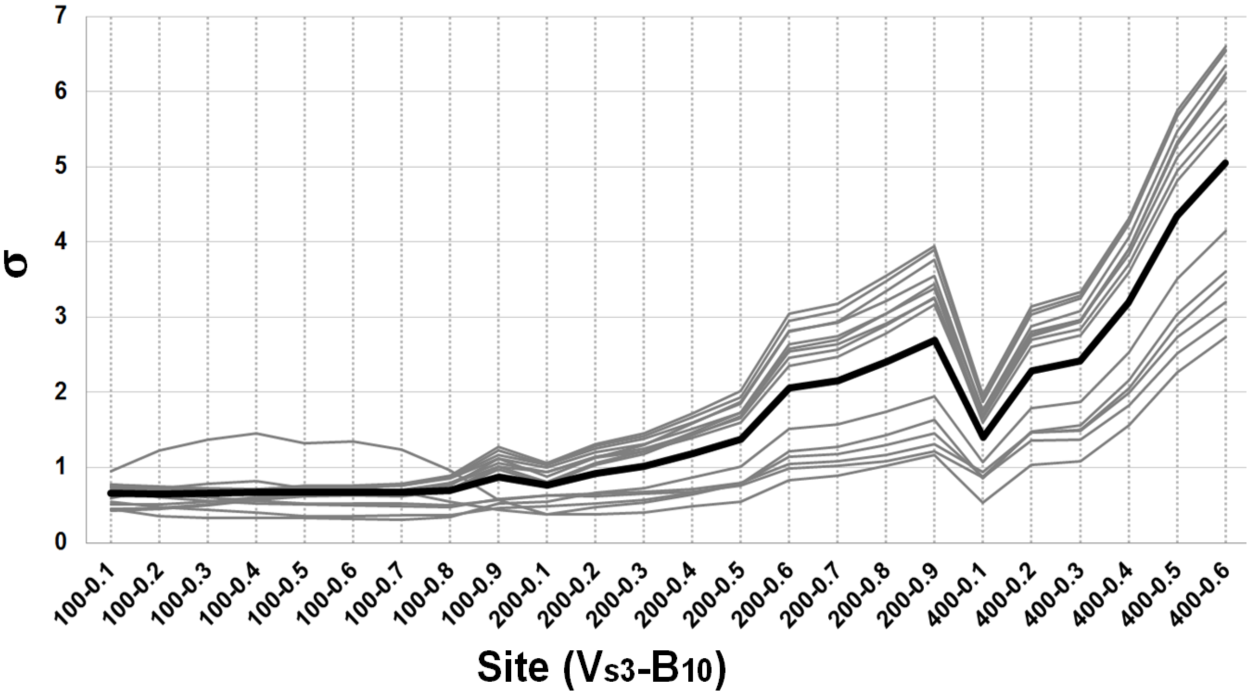

Fig. 6.9: Deviation factor by site for truck traffic sources- average in bold black.

It could be deduced that the vibration hazard in weaker sites is clear for truck circulation. For V_{S3}=100m/s, σ is near zero and almost independent of B_{10}values. For stronger soils i.e. V_{S3}=200m/s and 400m/s, the hazard is much smaller than for V_{S3}=100m/s. For both soils i.e. V_{S3}=200m/s and 400m/s, the larger the gradient the larger σ and therefore the smaller the hazard in the site for truck circulation.

It is worth noticing the similarity between sites response for truck circulation and pile driving. Weaker soils are more sensitive to smaller frequencies, and as shown in previous chapters the higher the gradient for the same soil type more the soil is sensitive to higher frequencies. For truck traffic most of the energy tends to be concentrated at lower frequencies. For instance Hunaidi (2000) mentioned that vibrations from traffic tends to be between 5 and 25 Hz. Hajeck et al. (2006) deduced that ground-borne vibrations from highway circulation is between 10 and 15 Hz. Examining the present data led to the conclusion that most of the energy content is between 10 and 25 Hz. Fig. 6.10 shows some relative amplitude distribution samples from truck traffic excitation. This type of frequency content explains the reason behind weaker soils, i.e. smaller V_{S3} and B_{10} , being more sensitive to the vibration hazard from truck traffic sources.

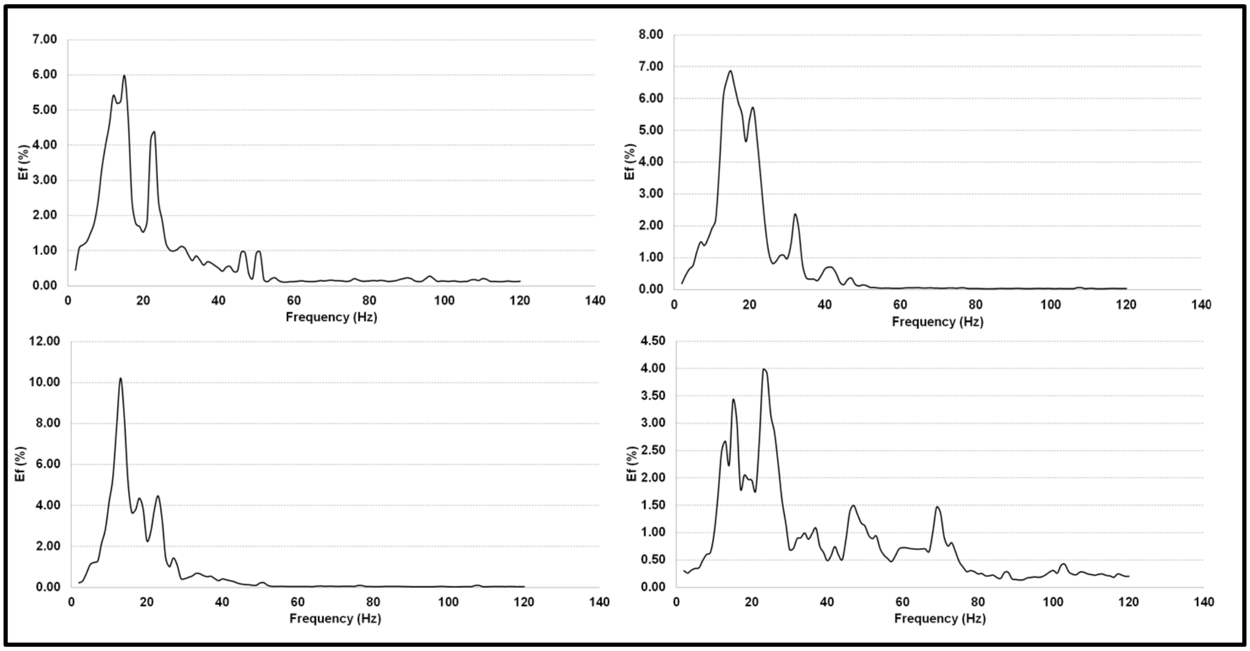

Fig. 6.10: Relative amplitude distribution by frequency for various truck traffic recordings.

6.3.4 Railways

For trains circulation the only available data were for trains with low speed (15 km/h) and medium speed (90 km/h) and at two distances 3.5 m and 12.9 m. The aggravation of hazard in sites for trains with different speeds and for recordings from different distances was very similar. Fig. 6.11 shows the average deviation factor for all sites from all the recordings of truck circulation.

Trains are very complicated sources of vibration, and their effects usually depend on multiple factors and the speed is only one of them. Other factors include the size and weight of the train, the track quality and properties.

This particular source needs more detailed studies preferably in a parametric form isolating the effects of each factor independently, which is not the main purpose of the present study. Using the limited data available it could be deduced that the speed of the train for the dataset considered hasn't affected considerably the sites response.

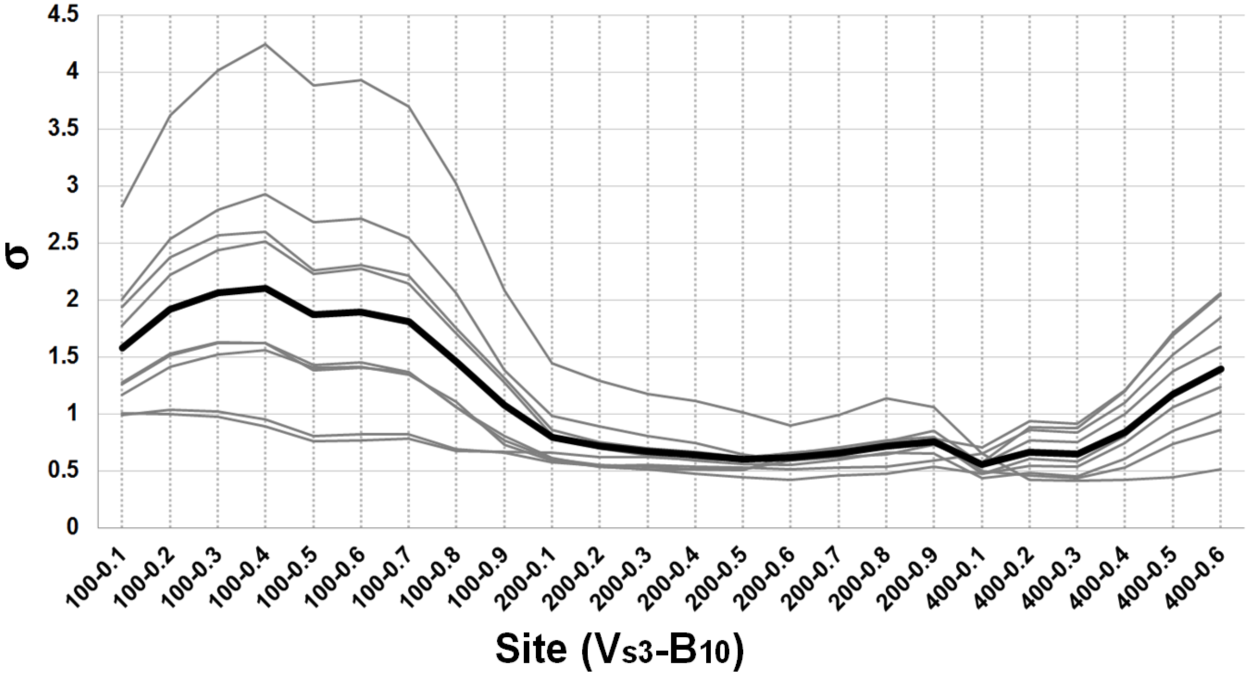

Fig. 6.11: Deviation factor by site for train sources- average in bold black.

The highest aggravation of vibration hazard was in the middle section, specifically soils with V_{S3}=200m/s in one hand and V_{S3}=400m/s with small gradients on the other hand. The less sensitive sites were the weak sites (where V_{S3}=100m/s), which is linked to the relatively high frequency content. Since the data considered do not include high speed trains (representing a super-Rayleigh mode), the absence of strong low frequency content is rather predictable. Super-Rayleigh excitation generated from very high speed trains is usually the most hazardous train excitation for weak soils. Trains exciting the super-Rayleigh mode usually happen in very weak soils and the excitation generates a cone like impulse of low frequencies (Kaynia et al., 2000; Madshus et al., 2000; Paolucci et al., 2003).

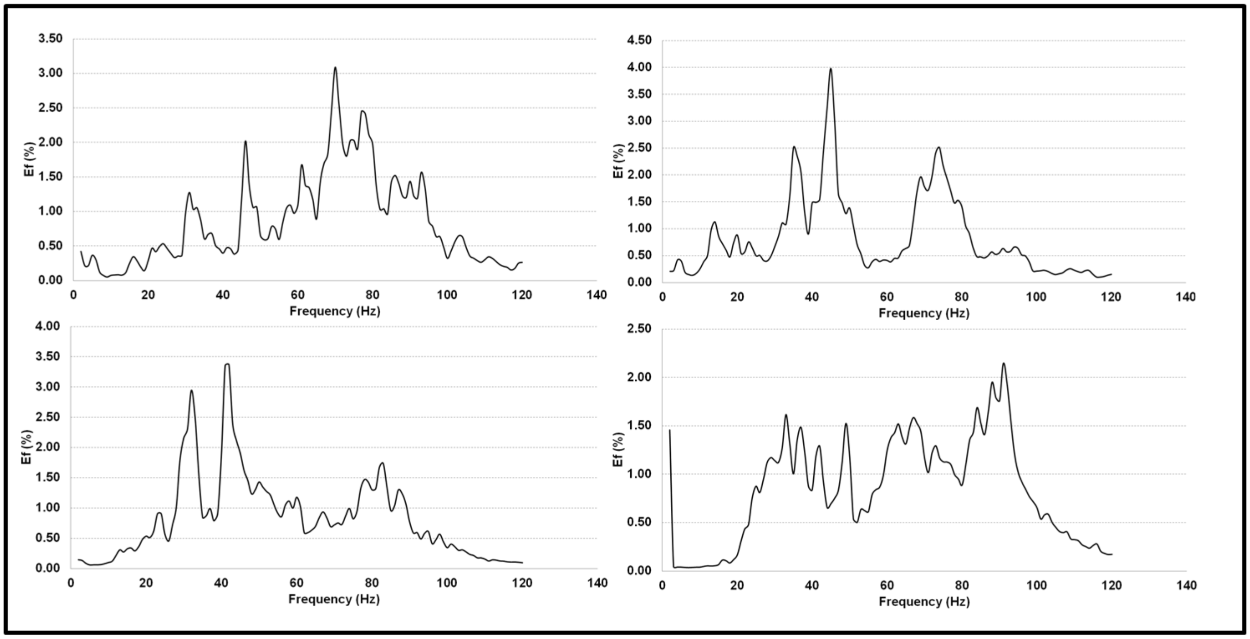

Fig. 6.12: Relative amplitude distribution by frequency for multiple train recordings.

6.4 Refinement method for spectral matching of sources and sites

A recommended way to approach the problem and to increase the prediction precision is to divide the response of sites into frequency bands similarly to what has been done in chapter 4. For each frequency band an impact factor *IF* could be assigned in order to isolate the more influencing frequencies. Such factor *IF* could be for instance the sum of the relative amplitude carried inside a certain frequency band. Therefore if a site is consisting mainly of weak soils and has a resonance frequency between 0 and 20 Hz, the impact factor for this band will be high. If this band carries 40% of the amplitude for instance, the impact factor *IF* will be equal to 0.4 and so on as shown in equation (6.3).

$$IF = \sum_{f=0}^{20} E_f(site) \tag{6.3}$$

A refined matching factor *σ'* could be the defined as shown in equation (6.4).

$$\sigma' = \sum_{i_b=1}^{n_b} IF(i_b).\sigma(i_b) \tag{6.4}$$

Where n_b is the number of frequency bands which is equal to 6 and $i_b \in [1,2,3,4,5,6]$.

In this fashion, some imprecisions could be avoided. In some cases there is a very high accord in certain frequencies between the site and the source but in a frequency segments which are not of a particular impact. For a weak soil a very good matching could be found in high frequencies between the site and the source for instance, what could reduce the value of σ and therefore indicate a high hazard. However these frequencies have a negligible influence in the propagation problem.

Fig. 6.13 shows the deviation factor for all sites from all the recordings of pile driving using the new definition σ'. It could be seen that in comparison with the previous aggravation of vibration hazard classification for this source shown in Fig. 6.4, the new classification shows better the variation of this hazard in each site. Previously the difference was appearing only when the site properties were changing massively, here the effect of the gradient B_{10} and not only V_{S3} is much more apparent. The new vibration hazard classification curves could be found in Appendix D.

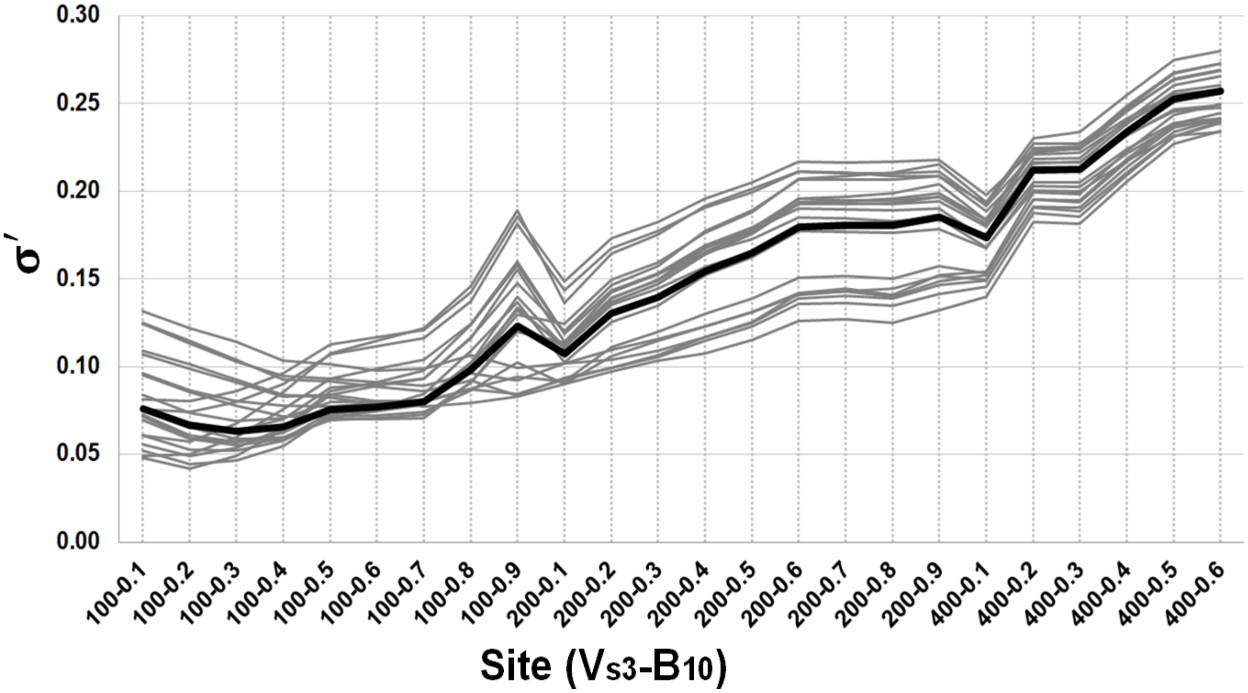

Fig. 6.13: Refined deviation factor σ' by site for pile driving sources- average in bold black.

6.5 Conclusion and recommendation

Soil vibration is highly dependent on the source of excitation. Different sites respond very differently when changing the source. Pile driving and traffic tend to cause more vibrations in weaker soils. Vibro-driving tends to cause more vibrations in medium strength soils. Vibrations caused by trains depend heavily on multiple factors, but tend to cause less aggravation of hazard in weaker soils compared to medium-strength soils for instance, except when at very high speeds.

The attenuation is stronger in weak soils and amplification rates tend to be higher in stronger soils. Despite these facts, practitioners always report more severe vibrations in weak soils. The reason behind strong vibrations detected in weak soils as seen in this chapter is that the majority of vibration sources related to infrastructure tend to carry more energy at low and medium frequencies. In some cases the frequency content of some sources almost totally matched with the responses of certain sites (weak soils) where σ and σ ' tend to 0. This accentuates the fact that from a hazard aggravation point of view and similarly to earthquake engineering, weaker soils tend to be more sensitive despite their stronger attenuation and smaller amplification capacity. For some particular sources stronger soils are more sensitive and the gradient B_{10} plays an important role in defining the vibration hazard.

A qualitative summary describing the aggravation hazard for the vibrations in soils depending on the variation of the source is represented in table 6.1. The qualitative classification ranks the hazard into five categories which are very high, high, medium, weak and very weak vibration hazard covering values of σ ' between 0.05 and 0.3 by five bands of 0.05 respectively.

Multiple recommendations could be suggested. The aggravation factor for vibration hazard should be linked with the amplification laws suggested in the previous chapters in order to make it valuable and applicable in the engineering field.

Secondly a detailed study on train sources in a parametric form is recommended. Vibrations from trains, as discussed before, strongly depend on multiple factors including the train speed, tracks quality, train size and other factors. A similar parametric study could also be suggested for traffic sources, taking into consideration the type of vehicle, pavement quality, speed of vehicle and so forth.

Thirdly the study of the vibration hazard at farther fields is also recommended. The change of vibration hazard with distance is of a particular importance along with the necessity of examining this change when changing the distance segments defining the different fields.

Site Class	**Description of Stratigraphic Profile [$V_{s3}(B_{10min}-B_{10max})$]**	**Pile-Driving** **Vibration Hazard**	**Vibro-Driving** **Vibration Hazard**	**Truck Traffic** **Vibration Hazard**	**Train Circulation** **Vibration Hazard**
1	100(0.1-0.5)	Very High	Weak	Very High	High
2	100(0.6-0.9)	High	Very Weak	High to Very High	High
3	200(0.1-0.5)	Medium	Weak	High to Medium	Very High
4	200(0.6-0.9)	Medium	Weak	Medium	High
5	400(0.1-0.3)	Weak	Weak	Weak	High
6	400(0.4-0.6)	Very Weak	Weak to Medium	Very Weak	Medium

Table 6.1: Qualitative classification of the aggravation hazard for the vibrations in soils depending on the variation of four types of sources.

6.6 References

Hunaidi, O. (2000). Traffic vibrations in buildings. *Institute for Research in Construction, National Research Council of Canada. Construction Technology Update No. 39,* 1-6.

Hajek, Jerry J., Chris T. Blaney, and David K. Hein. (2006). Mitigation of highway traffic-induced vibration. *Session on Quiet Pavements: Reducing Noise and Vibration Annual Conference of the Transportation Association of Canada*, 1-13.

Kaynia, A. M., Madshus C., and Zackrisson P. (2000) Ground vibration from high-speed trains: prediction and countermeasure. *Journal of Geotechnical and Geoenvironmental Engineering* 126.6, 531-537.

Madshus, C., and Kaynia A. M. (2000). High-speed railway lines on soft ground: dynamic behaviour at critical train speed. *Journal of Sound and Vibration* 231.3, 689-701.

Paolucci, R., Maffeis, A., Scandella, L., Stupazzini, M., & Vanini, M. (2003). "Numerical prediction of low-frequency ground vibrations induced by high-speed trains at Ledsgaard, Sweden." *Soil Dynamics and Earthquake Engineering* 23.6, 425-433.

Chapter 7

Conclusions and Recommendations

This chapter summarizes the conclusions reached from the work described in the previous chapters. Based on these conclusions, suggestions for further work are proposed.

7.1 Conclusion

For the numerical modelling of vibrations by FEM, *simple absorbing layers* have been improved through the nullification of the real part of reflected waves in the complex wavenumber domain. It proved to be very efficient especially when coupled with the stiffness reduction. Reducing excessively the stiffness along with a large increase of the stiffness factor C_K enables a large reduction in the size of the absorbing layer.

For the classification of sites for vibration problems *velocity-gradient proxies* proved to be a very good tool. Sites with larger gradients are more sensitive to higher frequencies and vice versa. Simple formulation from the time domain analysis and spectral response charts are provided and can be further used for design purposes.

The *neural network prediction* tool presented in chapter 5 enabled a deeper analysis of the problem and important conclusions to be made. The effect of the geometrical properties of the first layer proved to be important along with gradients. Both the depth of the surface layer and the gradient exhibited different effects depending on the wave velocity, *Vs*, and the distance from the source. For instance in the near field remarkably, it was deduced that the weaker the surface soil the shallower the variation of impedance should be present in order to get a response change on the surface.

Using the velocity-gradient proxies, the spectral properties of multiple sources recordings were assessed. An aggravation factor is suggested that could establish the link between the source and the amount of vibration associated with it in a site. A *classification of sources with sites* from a hazard aggravation point of view is also provided.

7.2 Recommendations for future works

More studies concerning the physical reason of higher efficiency of thinner absorbing layers with the present calibration approach is deemed necessary. The establishment of a coherent formulation should be considered regarding the calibration of absorbing layers taking into consideration the variation of materials, frequencies, stiffness reduction level and Rayleigh damping factors.

Regarding the spectral response of soils, an experimental campaign is necessary beside the numerical one in order to better assess the suggested proxies. Moreover a more focalized, less macroscopic analysis is needed in terms of distance segments. Assessing transfer functions based on new definitions of multiple fields using distance segments smaller than 20 meters is imperative. Further investigations regarding the higher modes of vibration in multilayered soils especially in relation with distance from the source is a compelling subject. Moreover important subjects were not addressed in this work, for instance the effect of the presence of a water table and its depth may eventually be a critical factor in the determination of vibration levels, however the proposed methods may be adapted to such cases. The assumption for soil impedance was a continuously increasing stiffness with depth; however some cases may be encountered where a velocity inversion may be present with depth.

The effect of deeper layers was proven to be related to the properties of the shallowest layer of soil as concluded in chapter 5. An investigation regarding the possibility of adapting more flexible gradient proxies depending on the shallow properties of sites is recommended. Gradients as, B_7 or B_5, for instance may show a good efficacy in certain cases.

In this dissertation, vibrations are studied considering they were generated by surface sources, nevertheless some important sources are body/underground sources like train tunnels for instance. The behavior of soils under excitation by this kind of sources may exhibit a different behavior if compared to that from surface sources. The upcoming waves toward the surface will follow different reflection and refraction patterns. The seismic impedance contrasts will be encountered and analyzed in an inversed order to that of surface sources since the waves are coming from below the surface. The effects of surface waves will be different in terms of amplitudes and position; moreover the definition of the velocity-gradient proxies may vary in terms of depth for example. Furthermore a more detailed research could be established assessing soil responses and the relevant proxies in relation with the depth of the source, its position from the bedrock, its geometrical shape and so forth.

Regarding the classification of sources and sites, the suggested aggravation factor should be studied in more depth and integrated in amplification formulations for each source separately. Vibration hazard for farther distance fields should be studied.

Connecting the findings of this work to the effects on structures has not been investigated in this thesis. Such investigation is highly recommended in order to assess the effect of vibrations on structures and their potential “nocivity”.

Appendix A

3D SPECTRAL MAPS FOR VIBRATION PROPAGATION

The purpose of this appendix is to provide the 3D maps of the spectral responses which were post processed in order to establish the spectral laws in Chapter 4.

A.1 V_{s3}=100m/s

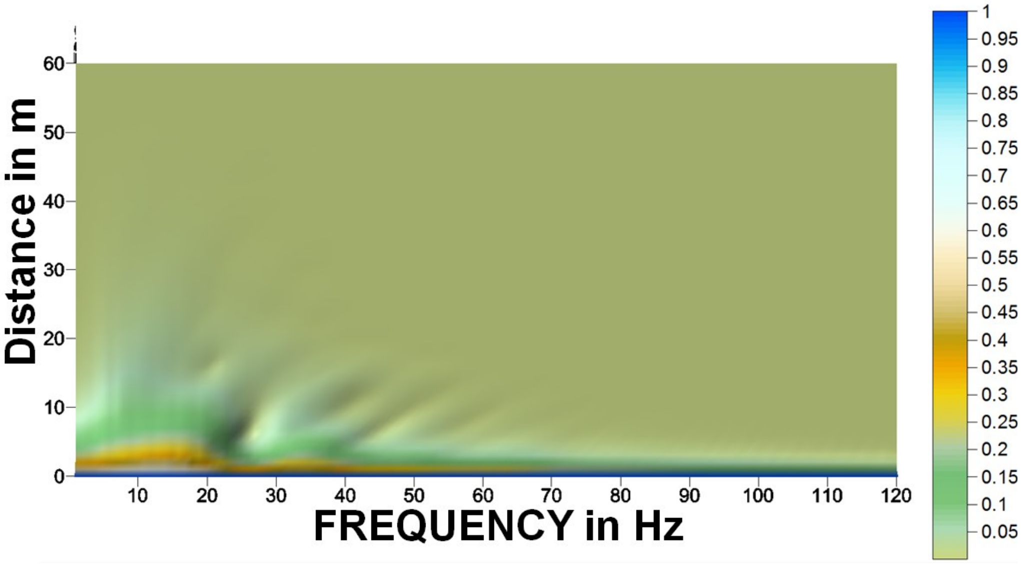

Fig. A1: Spectral propagation map for V_{s3}=100m/s and B_{10}=0.1

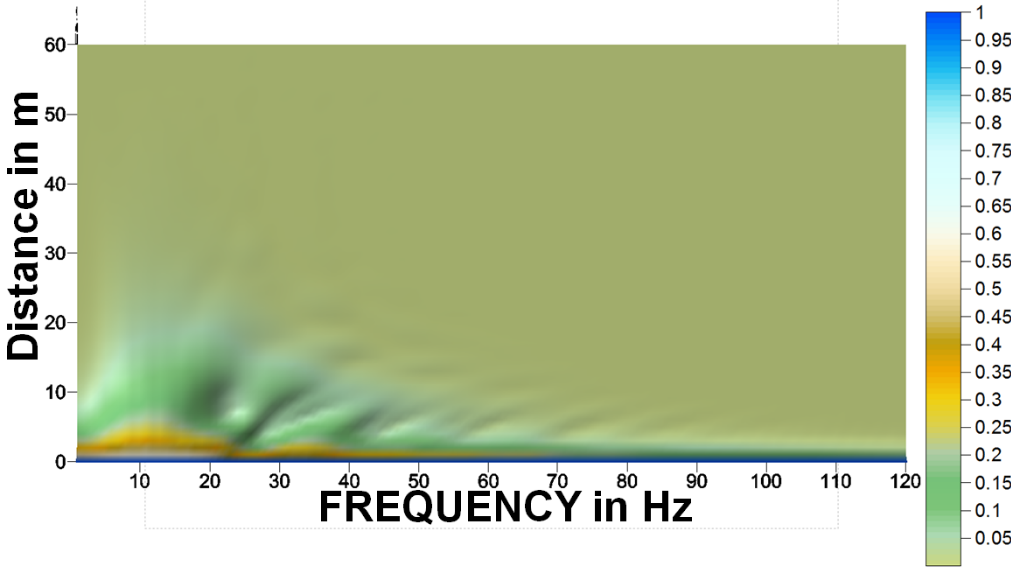

Fig. A2: Spectral propagation map for V_{s3}=100m/s and B_{10}=0.2

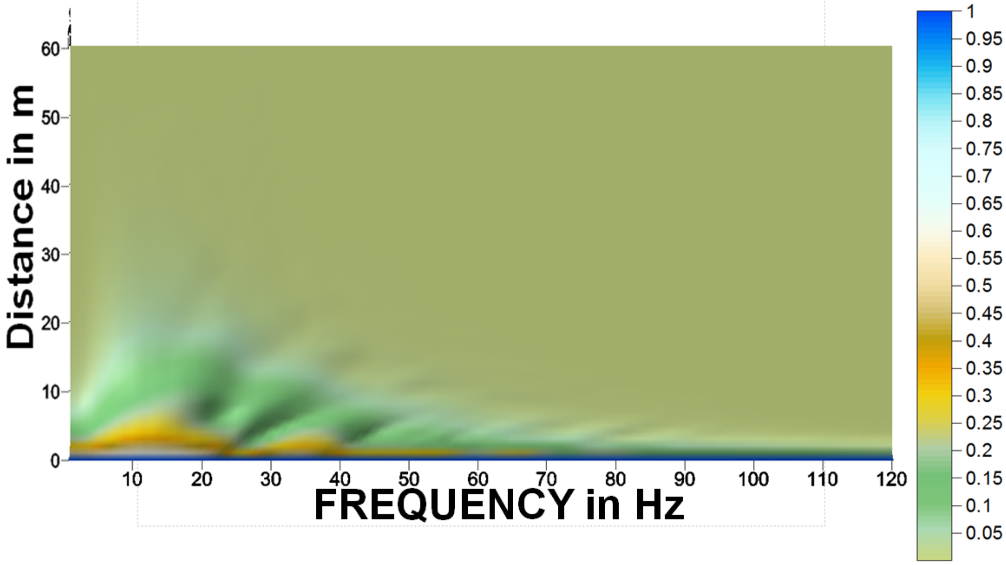

Fig. A3: Spectral propagation map for V_{s3}=100m/s and B_{10}=0.3

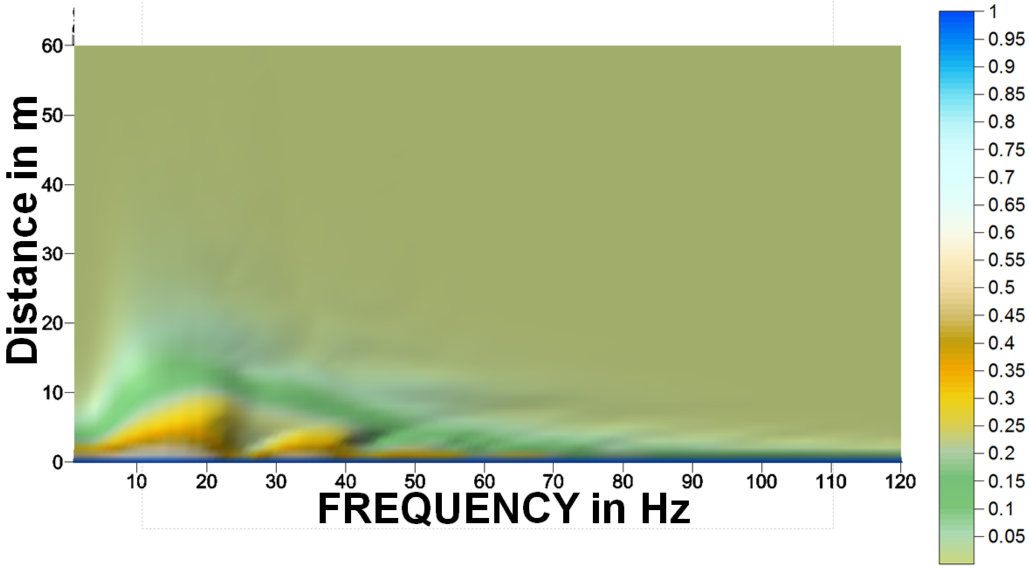

Fig. A4: Spectral propagation map for V_{s3}=100m/s and B_{10}=0.4

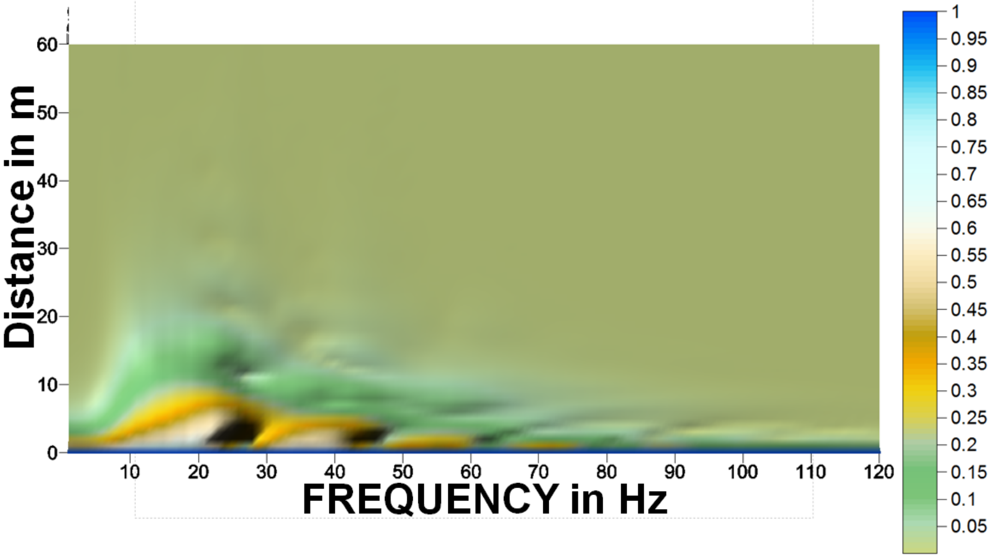

Fig. A5: Spectral propagation map for V_{s3}=100m/s and B_{10}=0.5

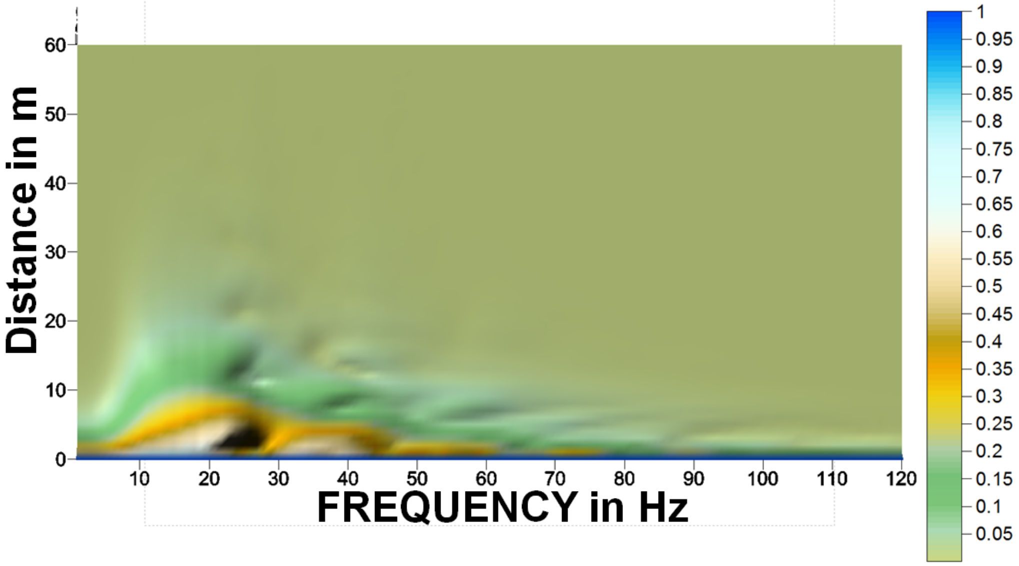

Fig. A6: Spectral propagation map for V_{s3}=100m/s and B_{10}=0.6

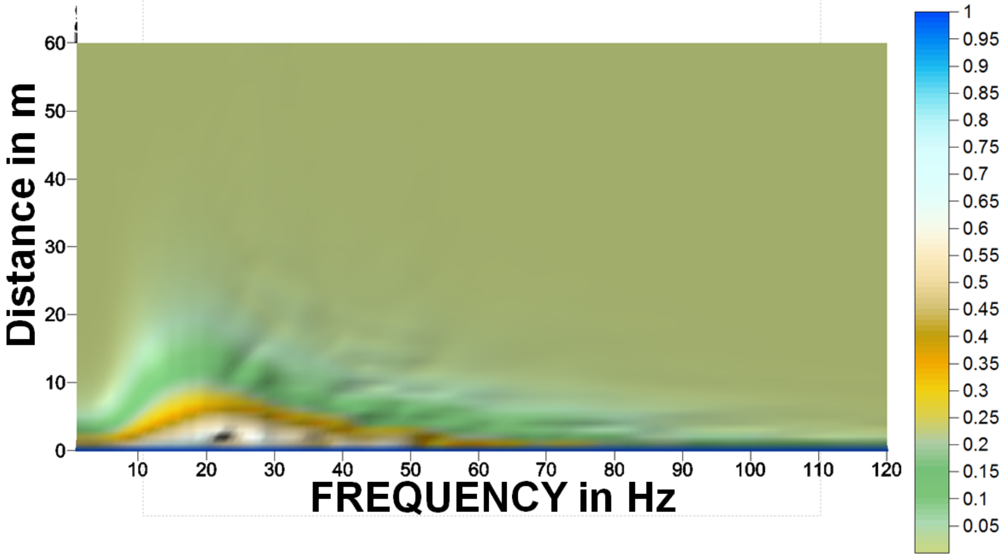

Fig. A7: Spectral propagation map for V_{s3}=100m/s and B_{10}=0.7

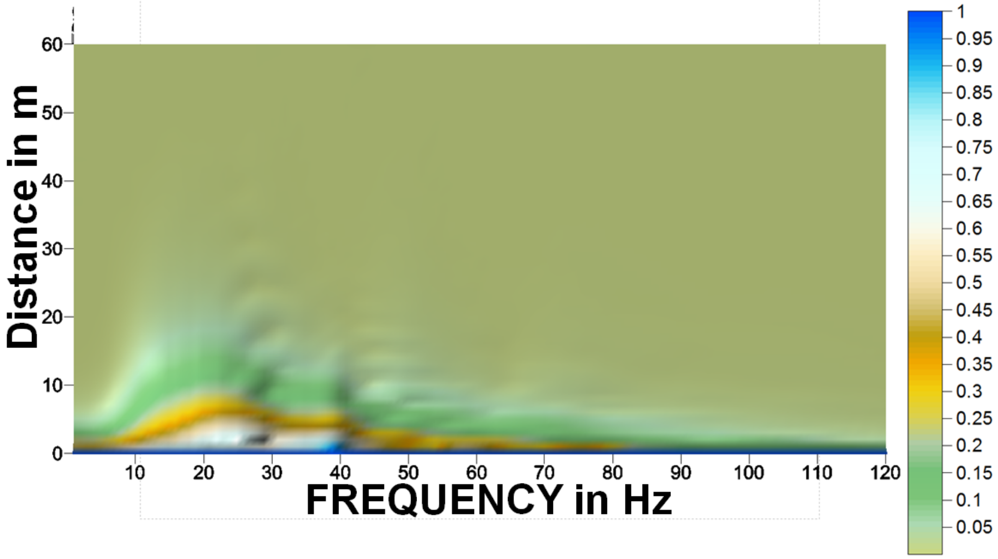

Fig. A8: Spectral propagation map for V_{s3}=100m/s and B_{10}=0.8

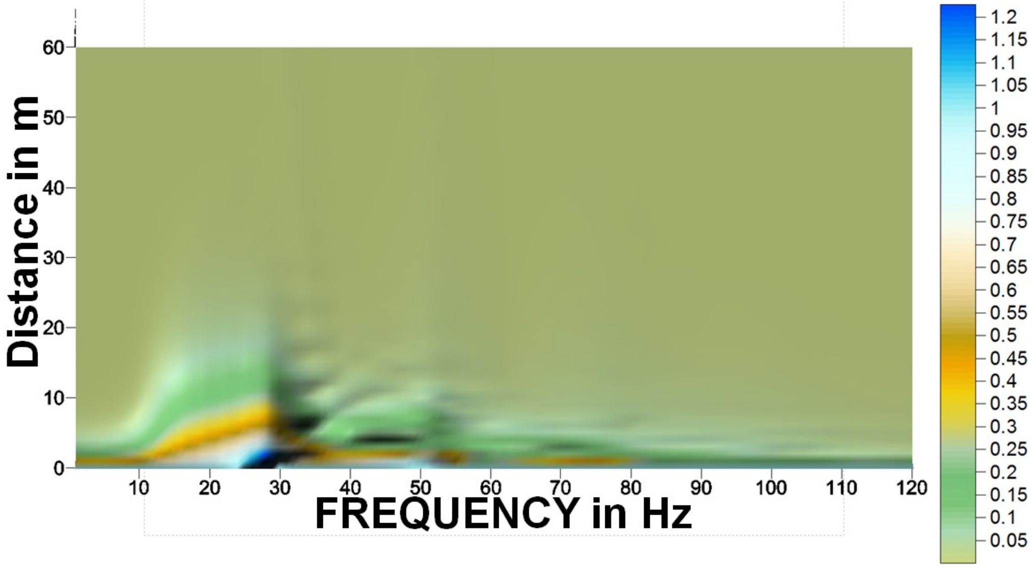

Fig. A9: Spectral propagation map for V_{s3}=100m/s and B_{10}=0.9

A.2 V_{s3}=200m/s

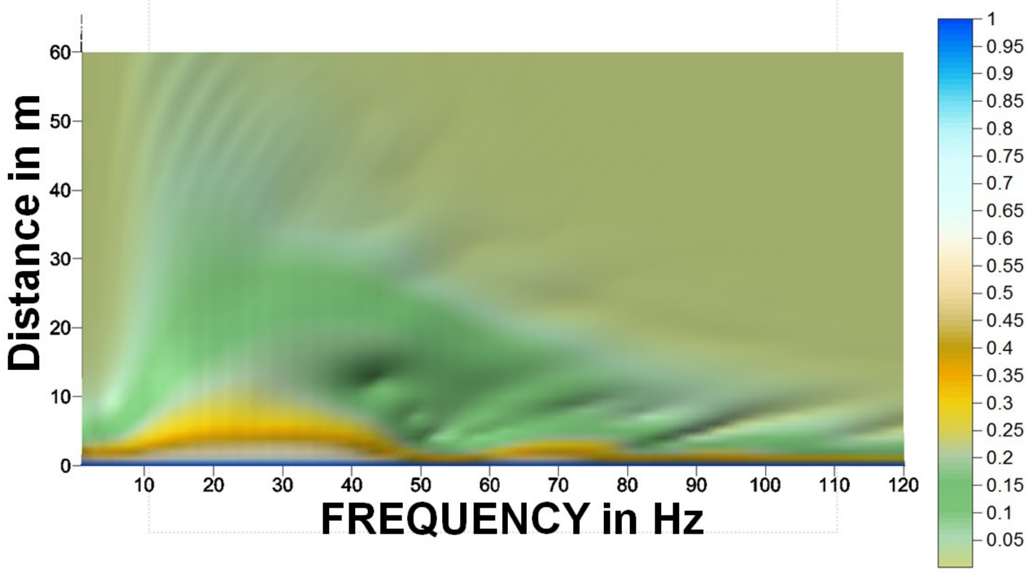

Fig. A10: Spectral propagation map for V_{s3}=200m/s and B_{10}=0.1

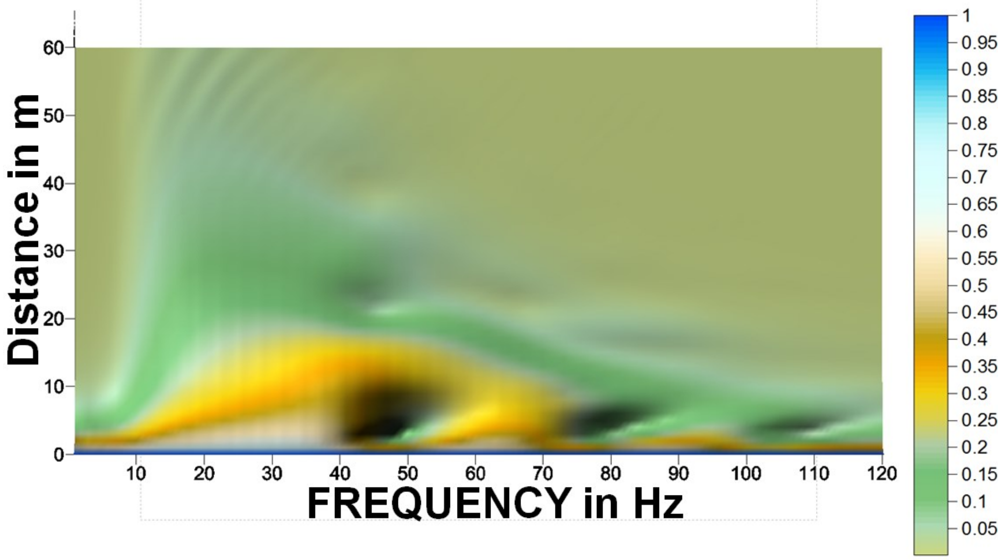

Fig. A11: Spectral propagation map for V_{s3}=200m/s and B_{10}=0.2

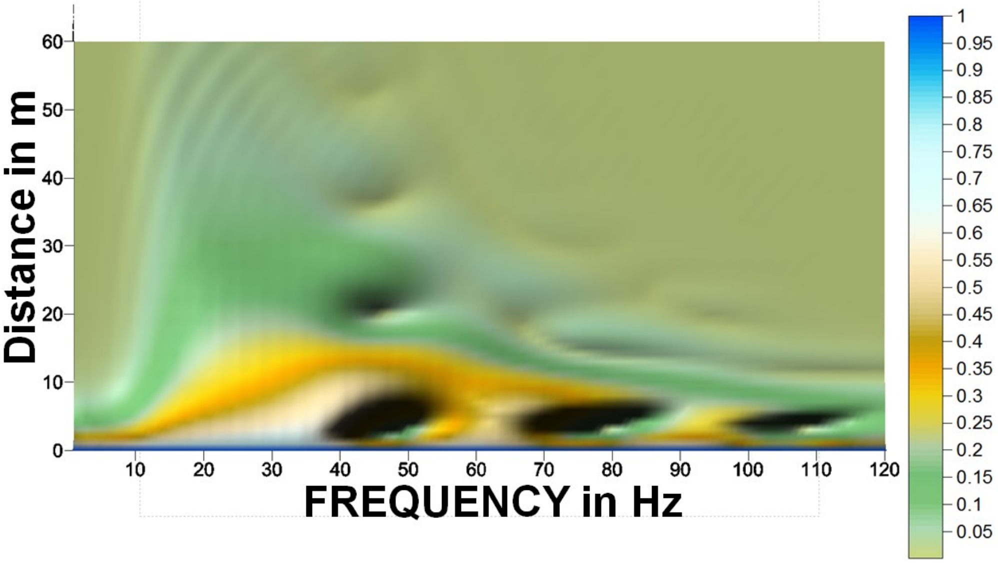

Fig. A12: Spectral propagation map for V_{s3}=200m/s and B_{10}=0.3

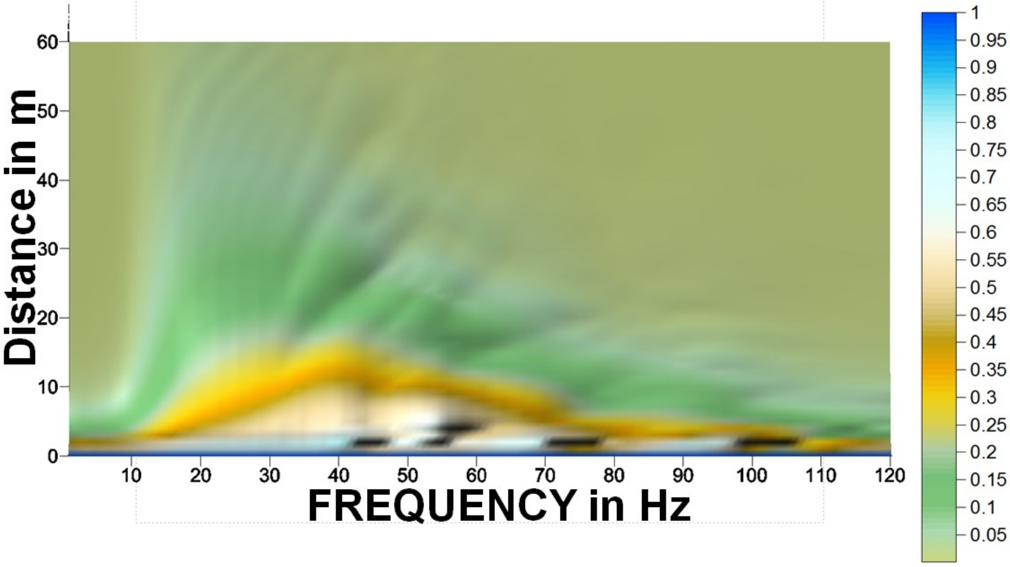

Fig. A13: Spectral propagation map for V_{s3}=200m/s and B_{10}=0.4

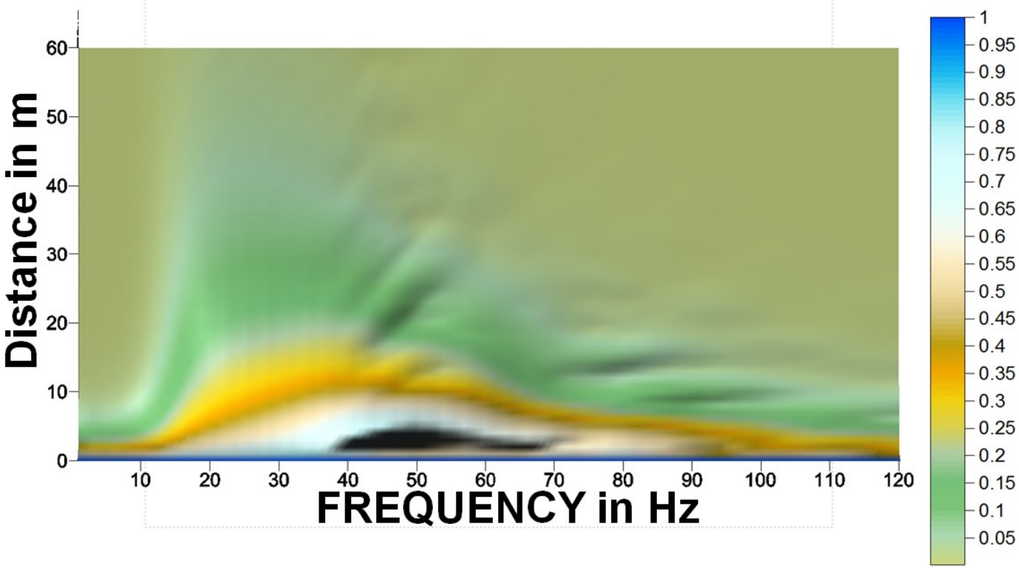

Fig. A14: Spectral propagation map for V_{s3}=200m/s and B_{10}=0.5

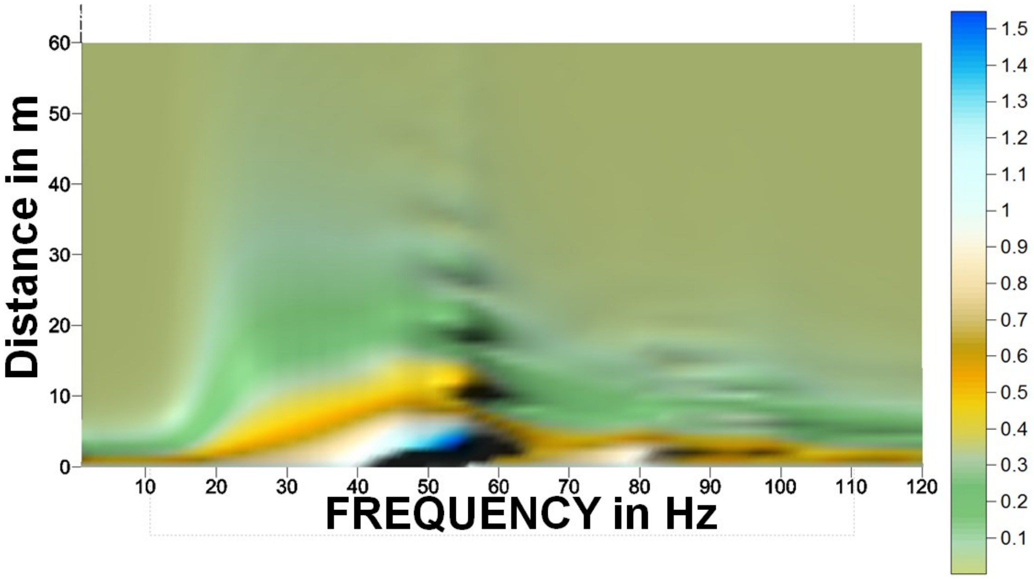

Fig. A15: Spectral propagation map for V_{s3}=200m/s and B_{10}=0.6

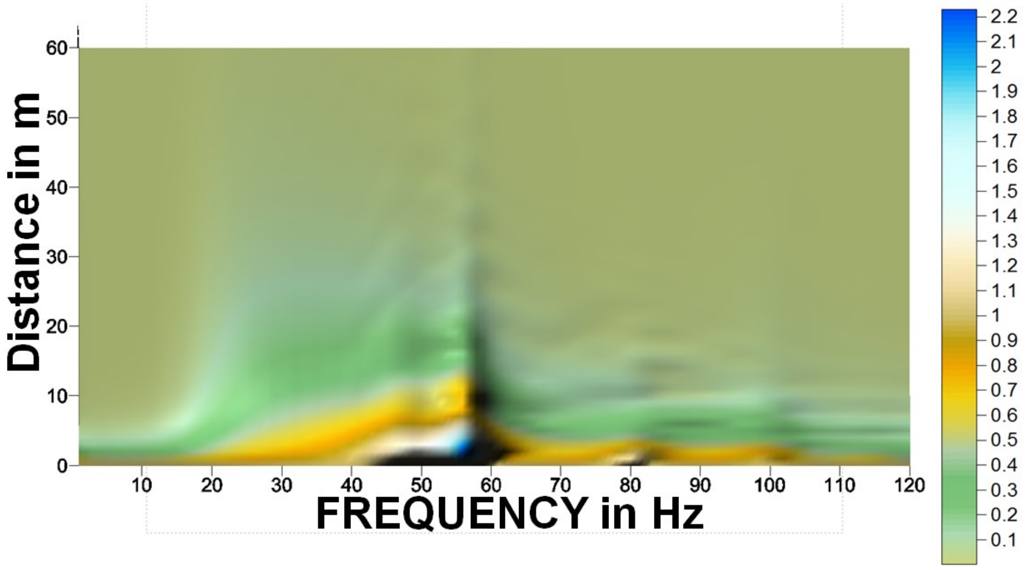

Fig. A16: Spectral propagation map for V_{s3}=200m/s and B_{10}=0.7

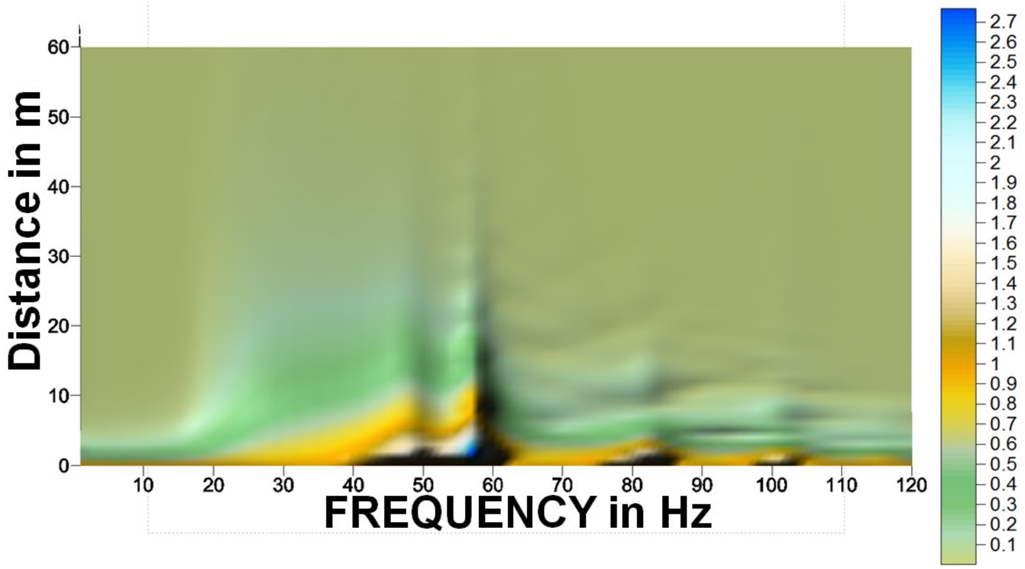

Fig. A17: Spectral propagation map for V_{s3}=200m/s and B_{10}=0.8

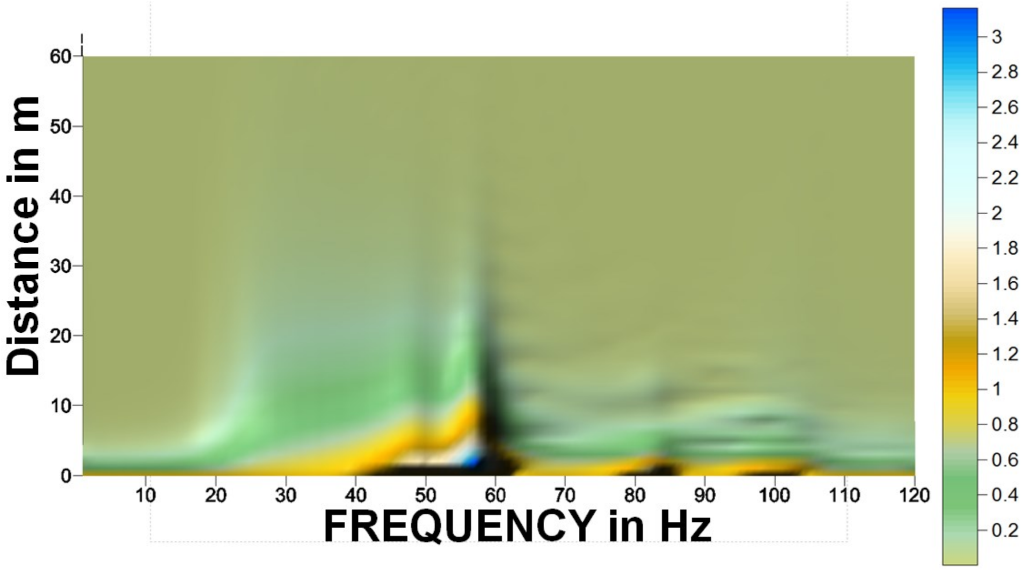

Fig. A18: Spectral propagation map for V_{s3}=200m/s and B_{10}=0.9

A.3 V_{s3}=400m/s

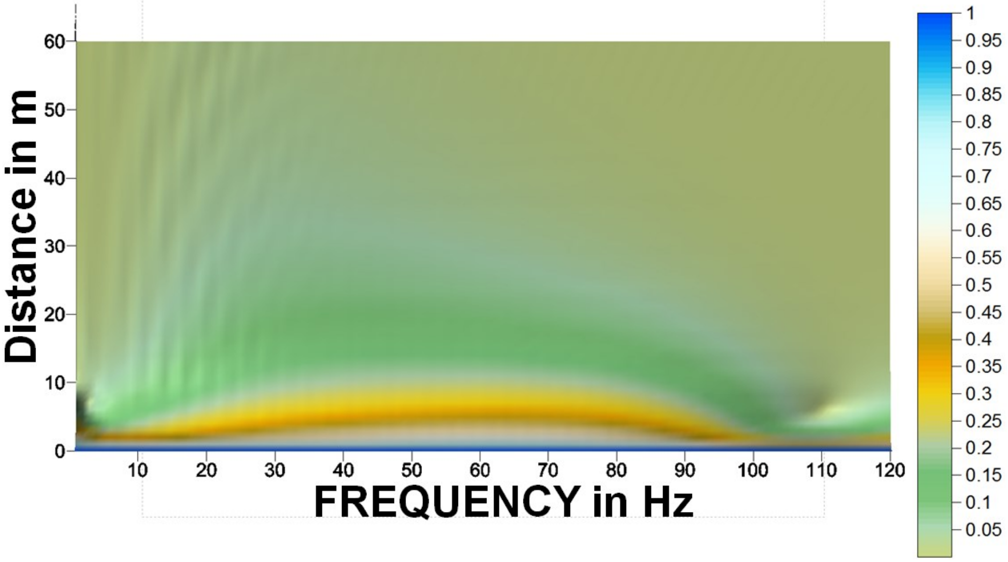

Fig. A19: Spectral propagation map for V_{s3}=400m/s and B_{10}=0.1.

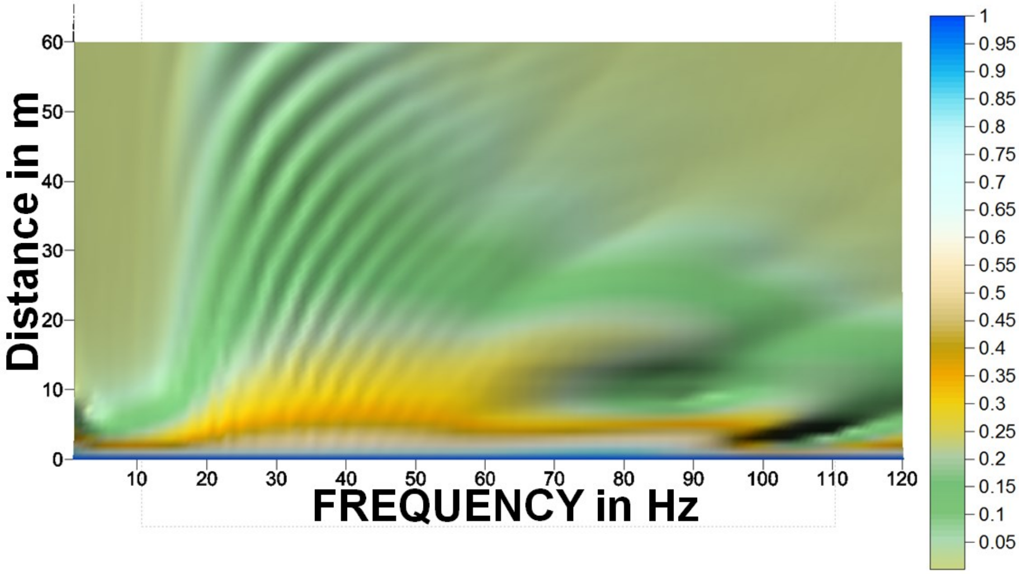

Fig. A20: Spectral propagation map for V_{s3}=400m/s and B_{10}=0.2.

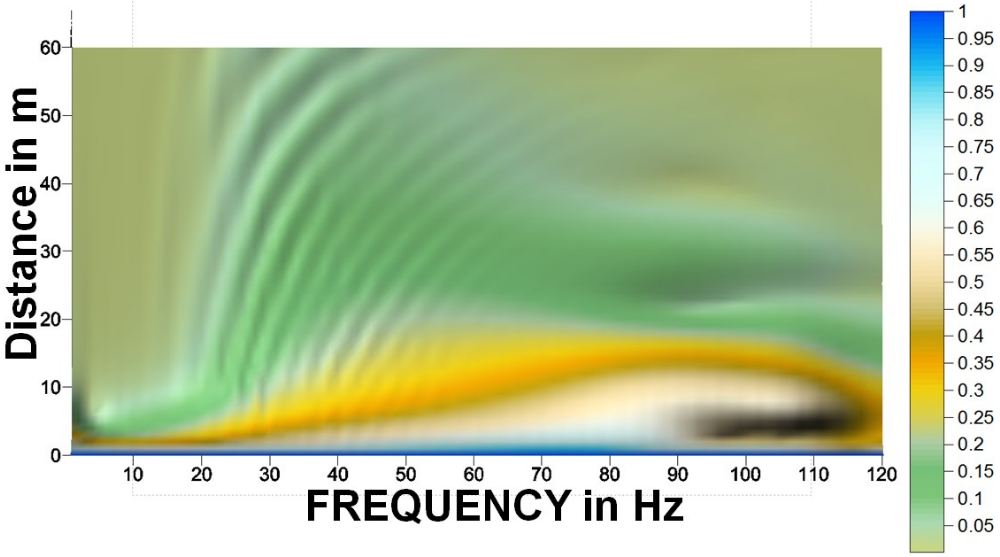

Fig. A21: Spectral propagation map for V_{s3}=400m/s and B_{10}=0.3.

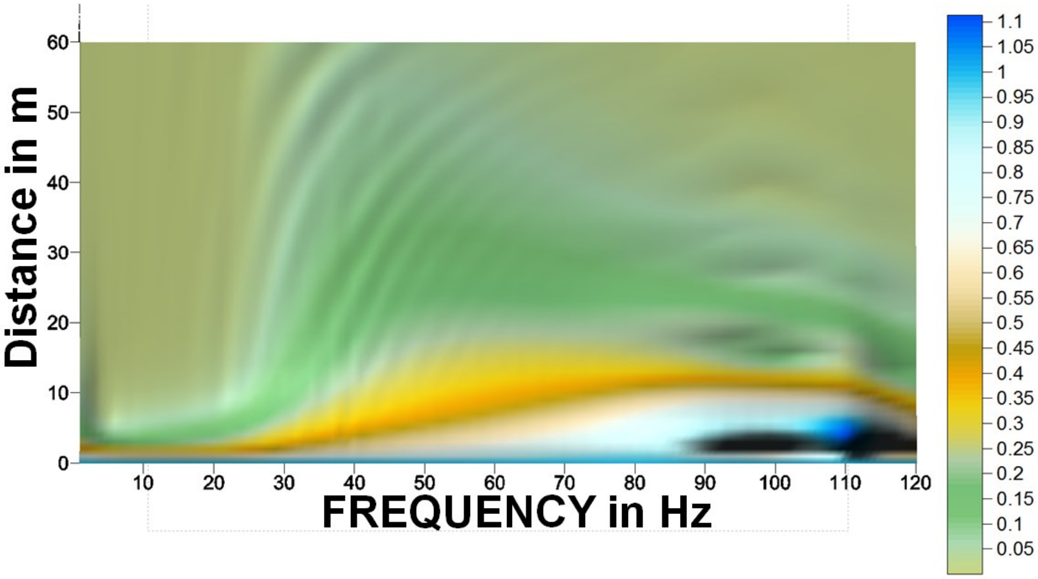

Fig. A22: Spectral propagation map for V_{s3}=400m/s and B_{10}=0.4.

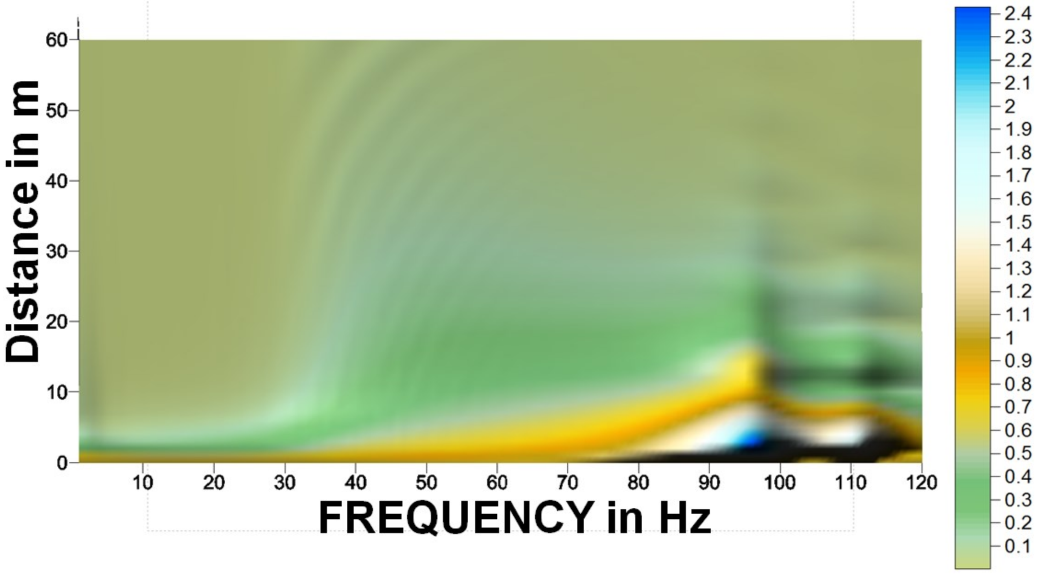

Fig. A23: Spectral propagation map for V_{s3}=400m/s and B_{10}=0.5.

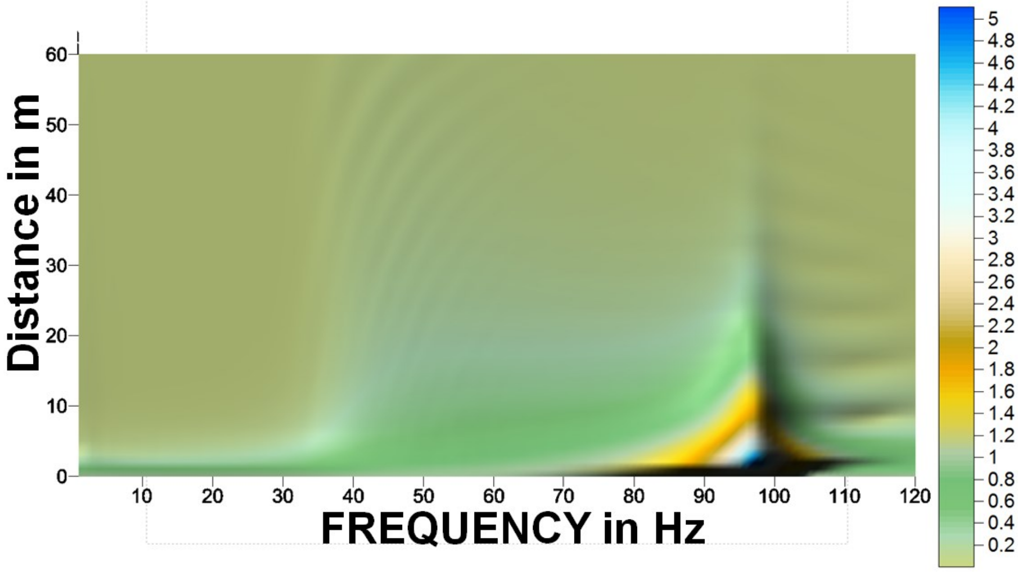

Fig. A24: Spectral propagation map for V_{s3}=400m/s and B_{10}=0.6.

Appendix B

H/V INVESTIGATION EXAMPLES IN 3D

The purpose of this appendix is to provide in 3D two examples of the H/V analysis discussed in Chapter 4 Section 6.

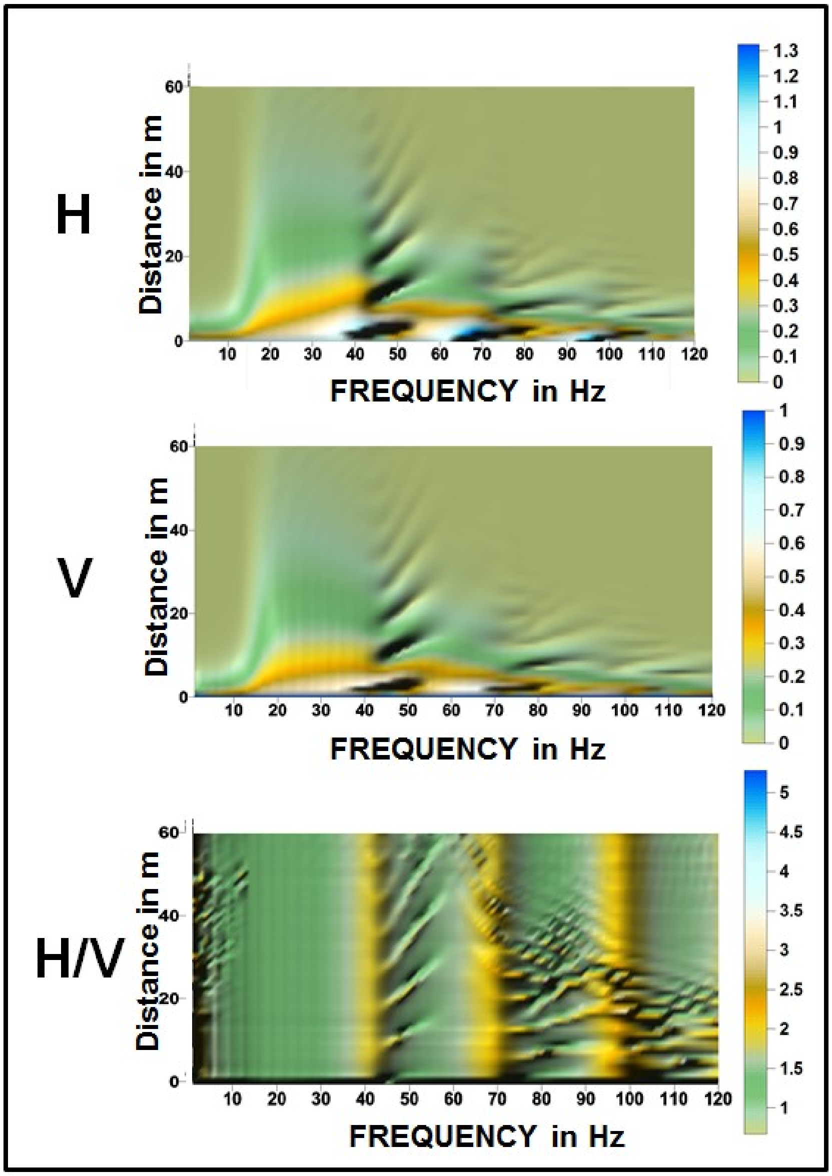

Fig. B1: H/V study for a soil with V_{s3}=200m/s and B_{10}=0.41.

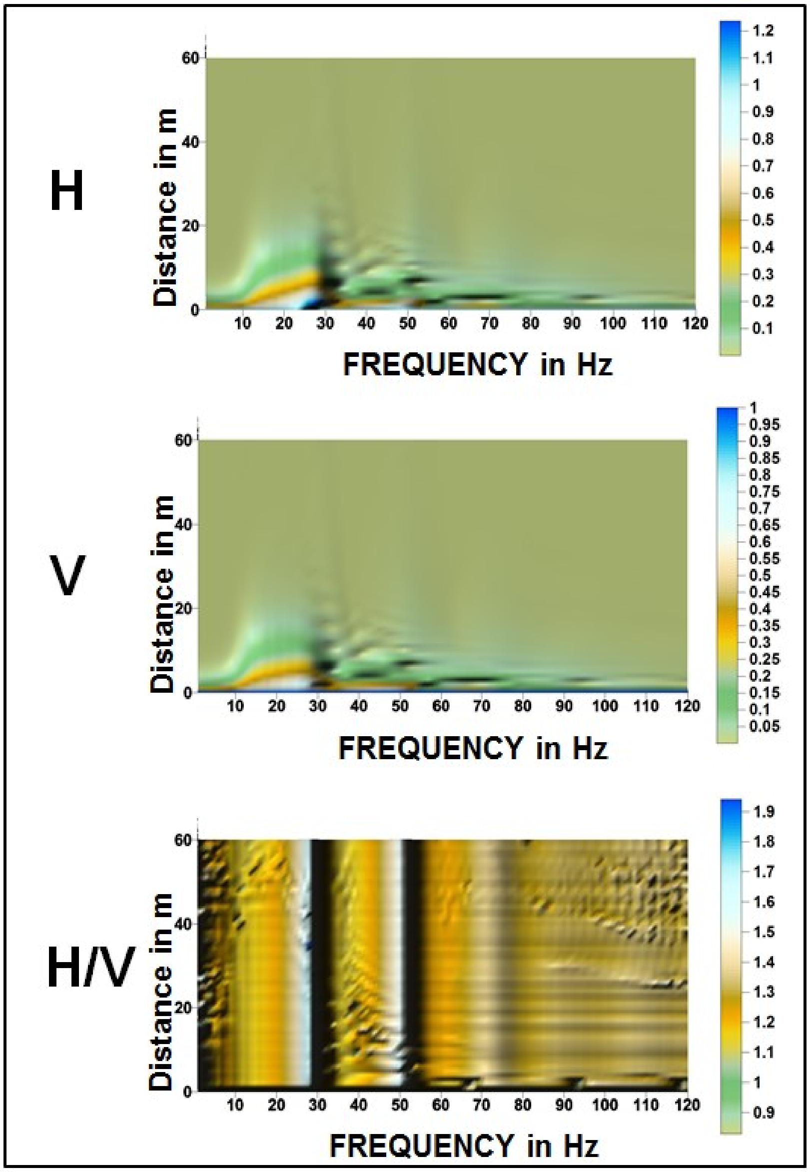

Fig. B2: H/V study for a soil with V_{s3}=100m/s and B_{10}=0.83.

Appendix C

NEURAL NETWORKS RESULTS

The purpose of this appendix is to provide the complete set of results obtained from the artificial neural networks analysis discussed in chapter 5.

C.1 V_{s3}=100m/s in the near-field

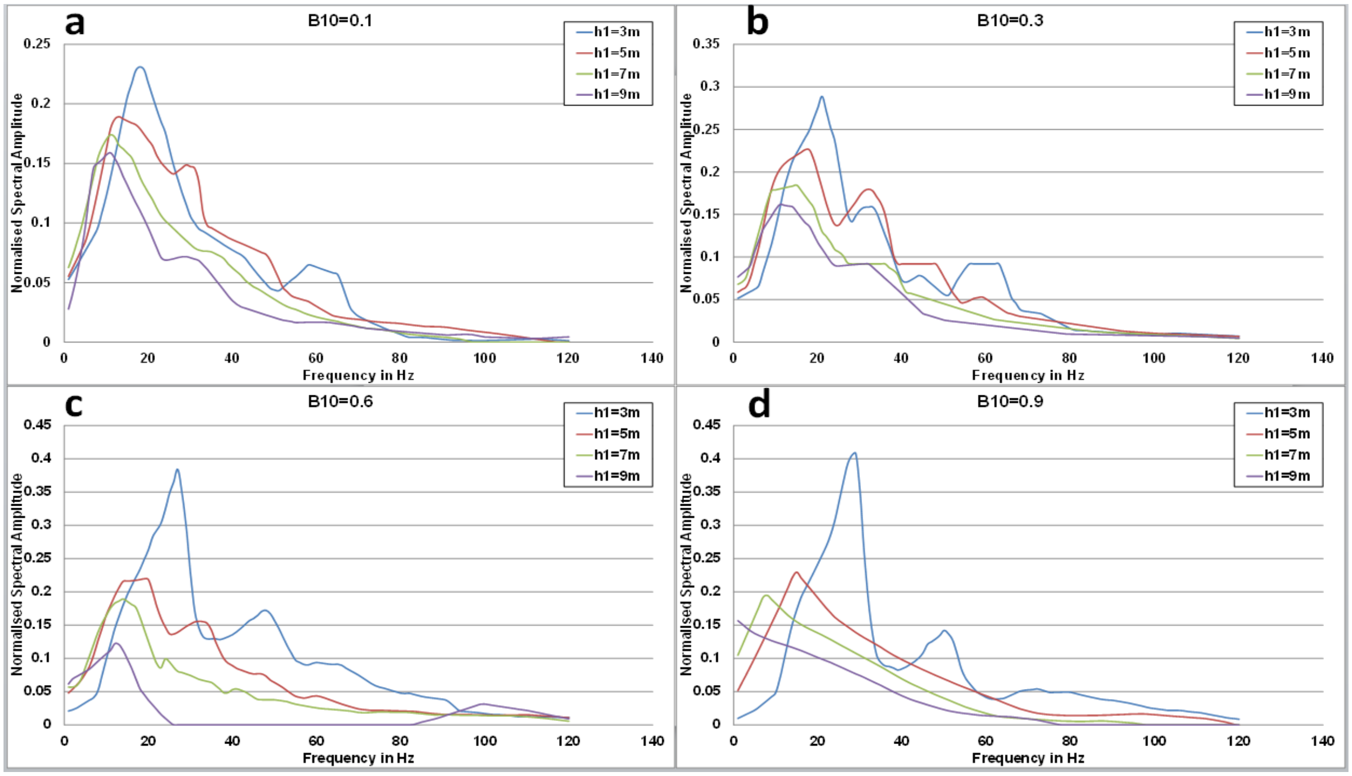

Fig. C1: Spectral representation of Vs=100m/s varying h_1 for (a) $B_{10} = 0.1$, (b) $B_{10} = 0.3$, (c) $B_{10} = 0.6$, (d) $B_{10} = 0.9$.

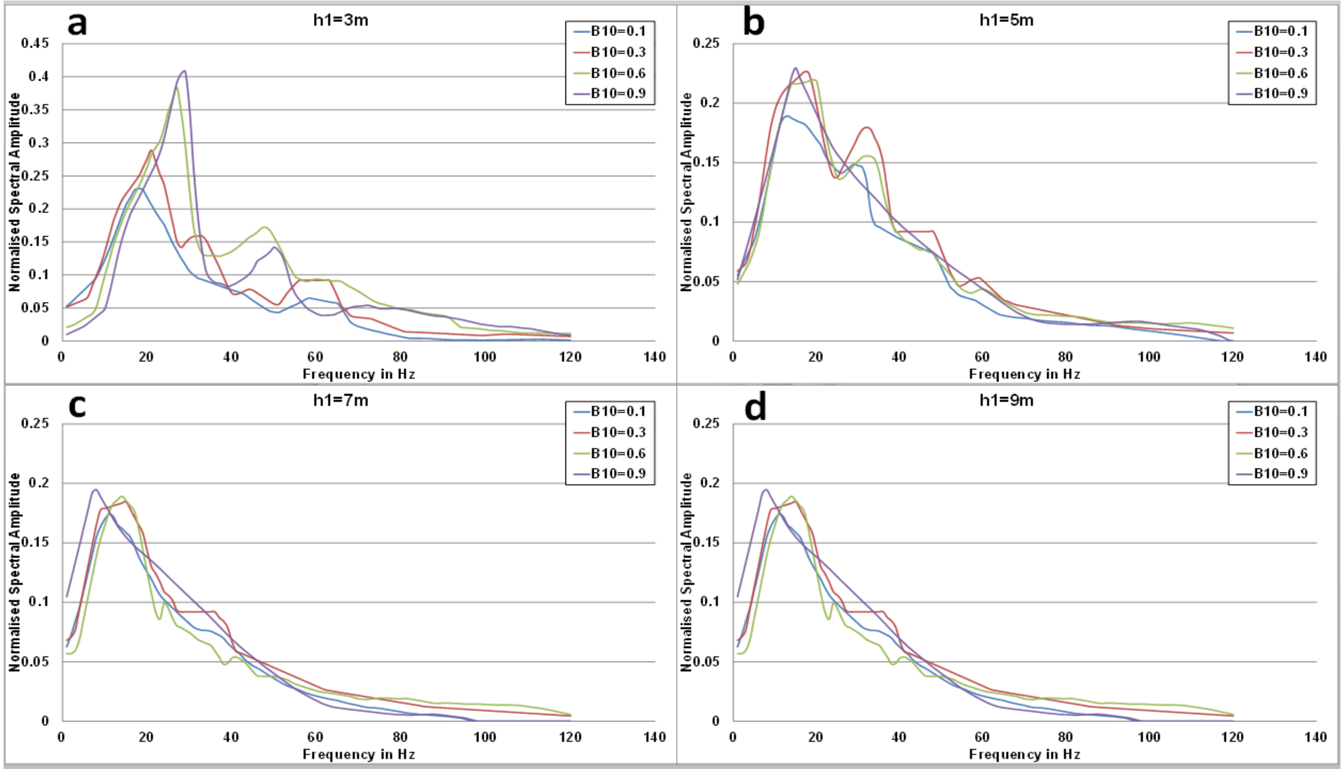

Fig. C2: Spectral representation of Vs=100m/s varying B_{10} for (a) $h_1 = 3\text{m}$, (b) $h_1 = 5\text{m}$, (c) $h_1 = 7\text{m}$, (d) $h_1 = 9\text{m}$.

C.2 V_{s3}=200m/s in the near-field

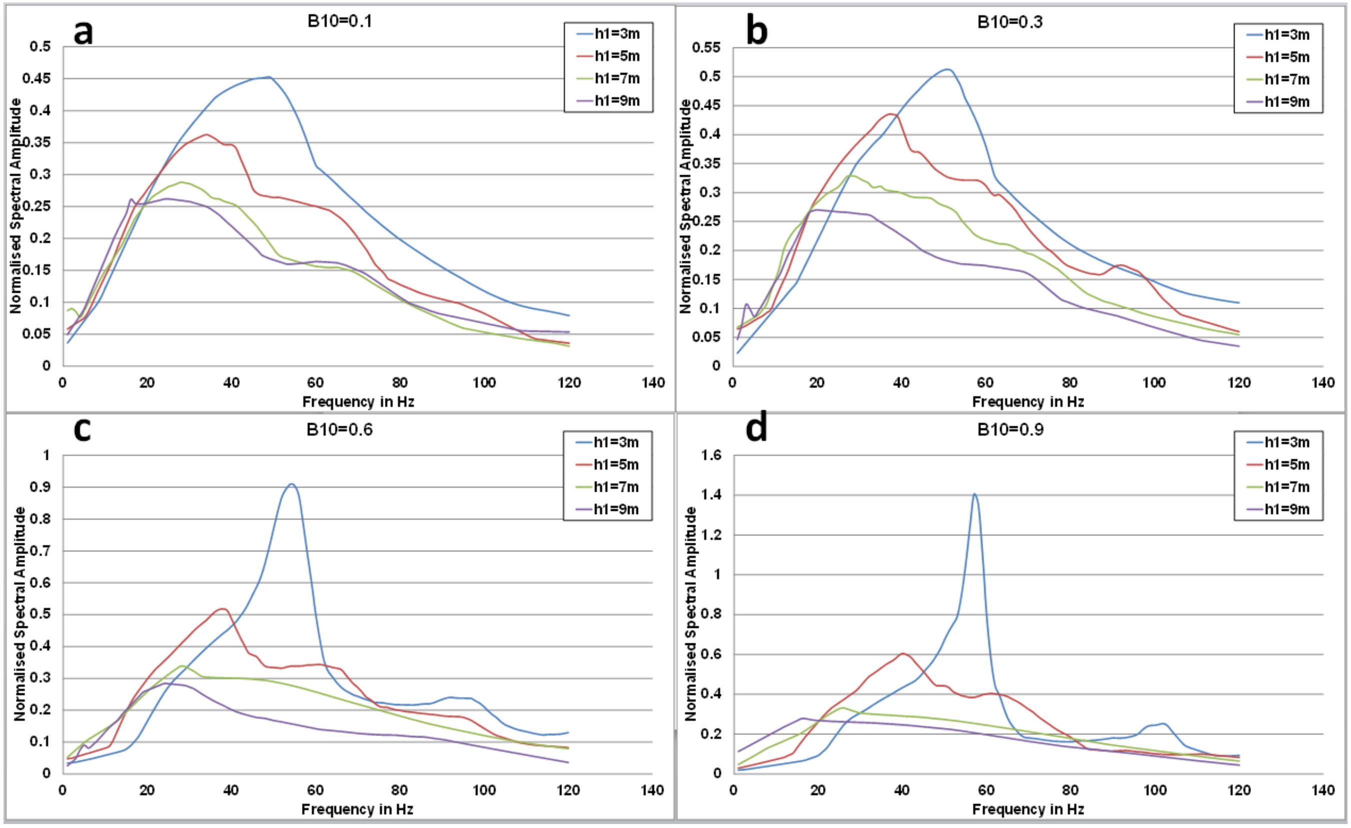

Fig. C3: Spectral representation of Vs=200m/s varying h_1 for (a) $B_{10} = 0.1$, (b) $B_{10} = 0.3$, (c) $B_{10} = 0.6$, (d) $B_{10} = 0.9$.

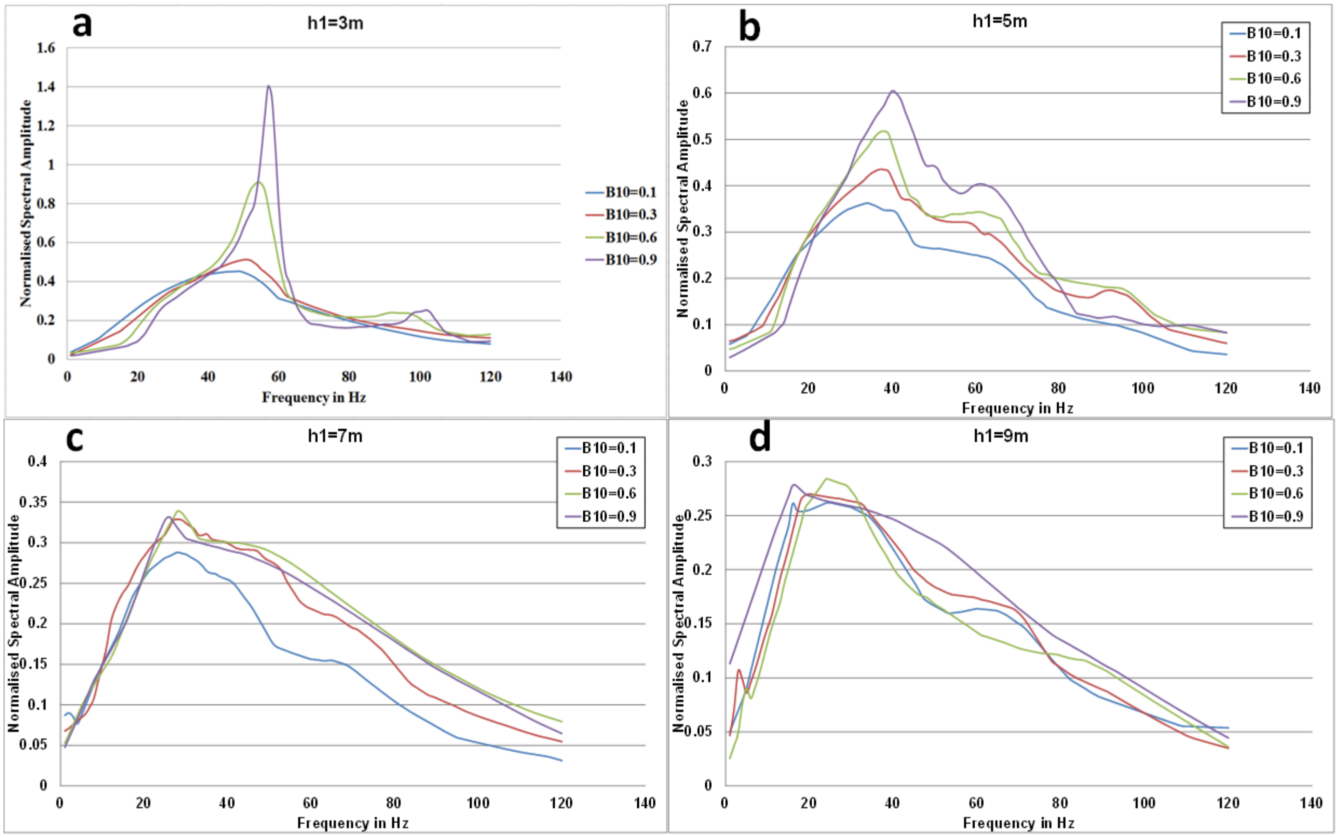

Fig. C4: Spectral representation of Vs=200m/s varying B_{10} for (a) $h_1 = 3m$, (b) $h_1 = 5m$, (c) $h_1 = 7m$, (d) $h_1 = 9m$.

C.3 V_{s3}=400m/s in the near-field

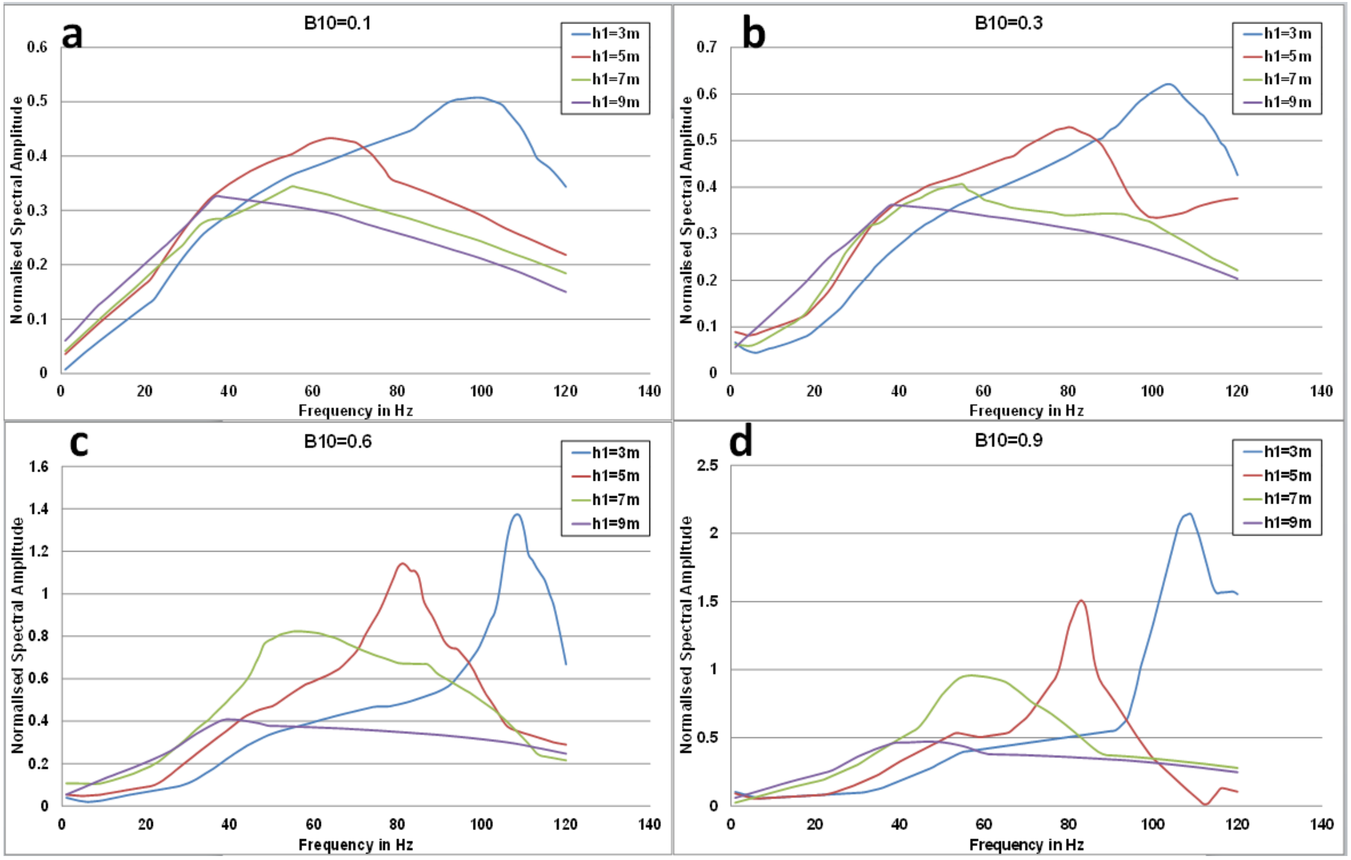

Fig. C5: Spectral representation of Vs=400m/s varying h_1 for (a) $B_{10} = 0.1$, (b) $B_{10} = 0.3$, (c) $B_{10} = 0.6$, (d) $B_{10} = 0.9$.

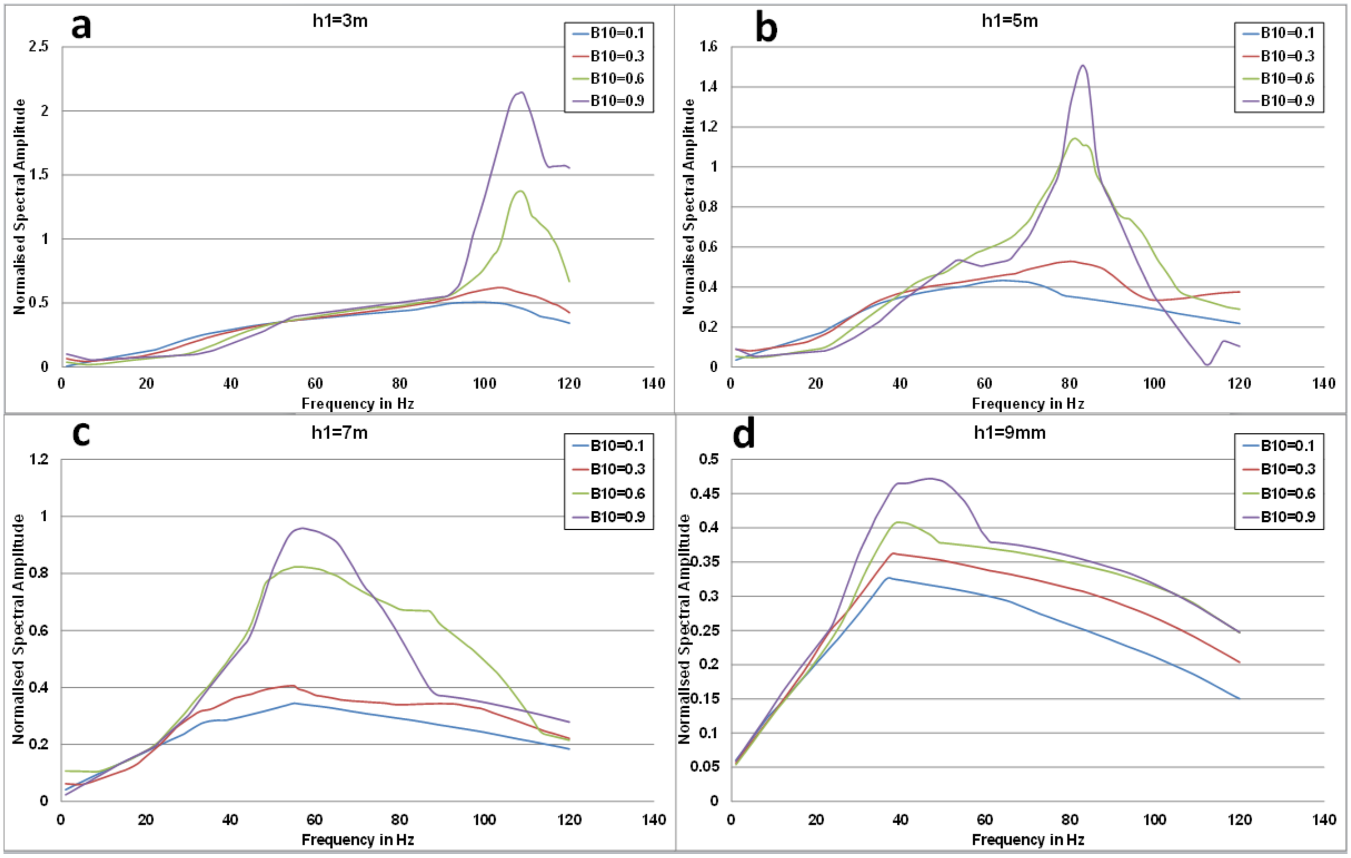

Fig. C6: Spectral representation of Vs=200m/s varying B_{10} for (a) $h_1 = 3m$, (b) $h_1 = 5m$, (c) $h_1 = 7m$, (d) $h_1 = 9m$.

C.3 V_{s3}=100m/s in the mid-field

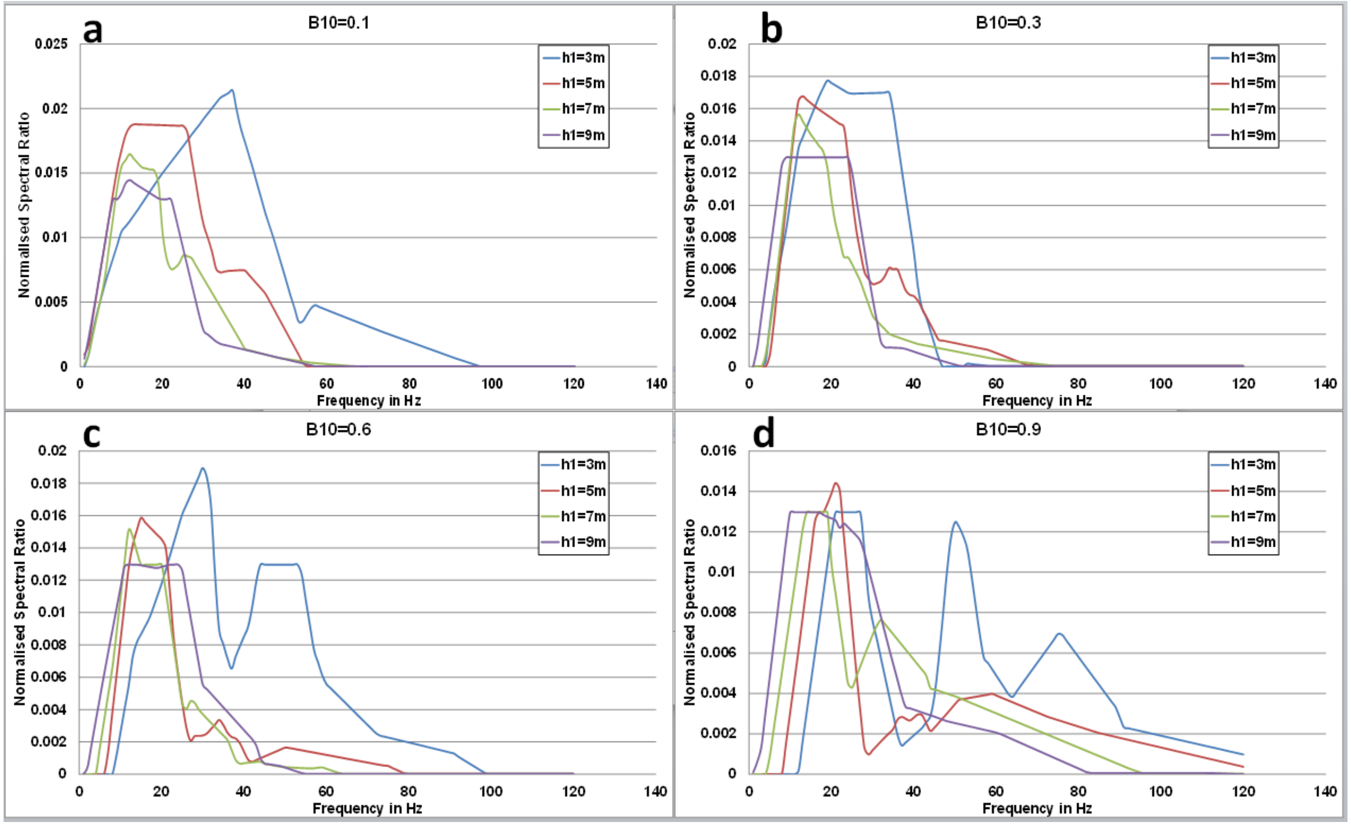

Fig. C7: Spectral representation of Vs=100m/s varying h_1 for (a) $B_{10} = 0.1$, (b) $B_{10} = 0.3$, (c) $B_{10} = 0.6$, (d) $B_{10} = 0.9$.

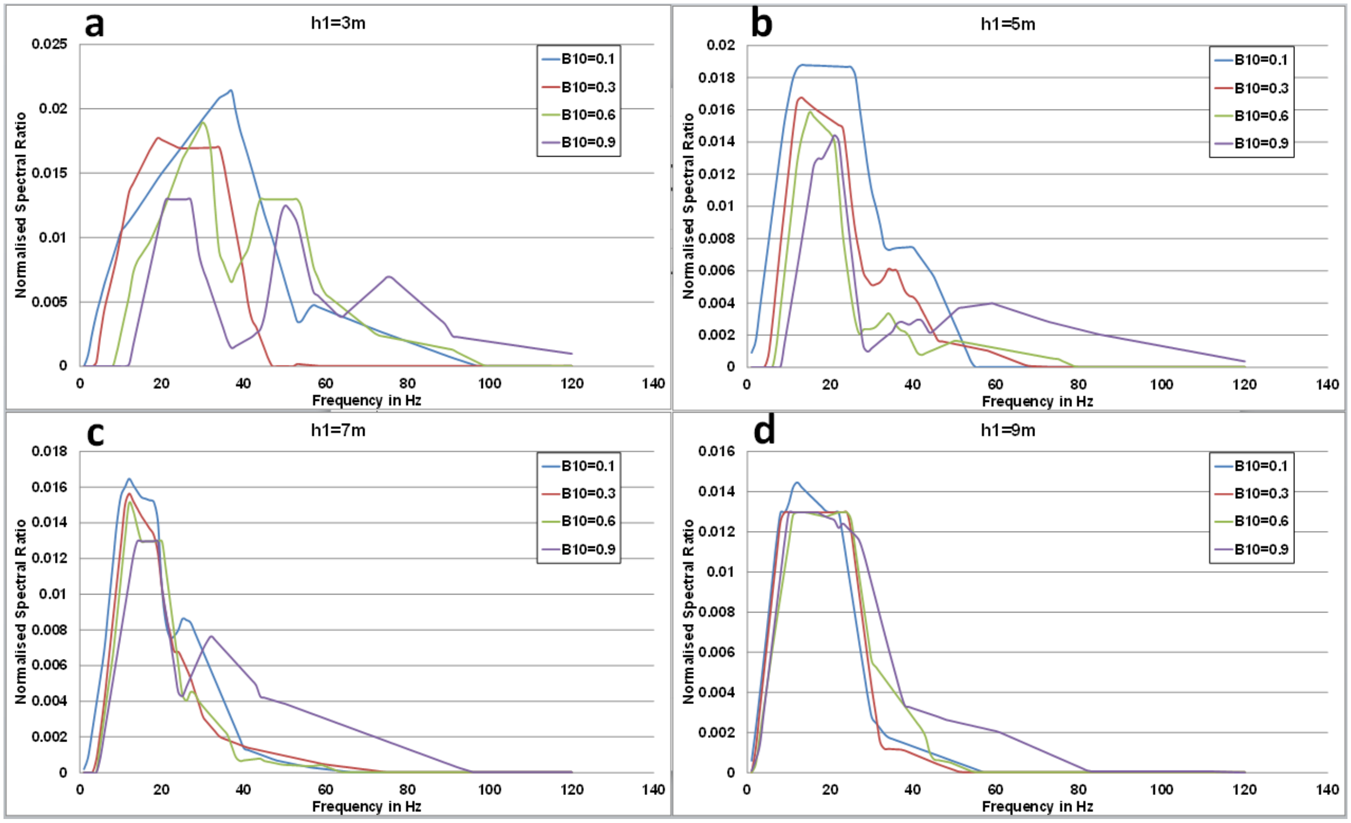

Fig. C8: Spectral representation of Vs=100m/s varying B_{10} for (a) $h_1 = 3m$, (b) $h_1 = 5m$, (c) $h_1 = 7m$, (d) $h_1 = 9m$.

C.3 V_{s3}=200m/s in the mid-field

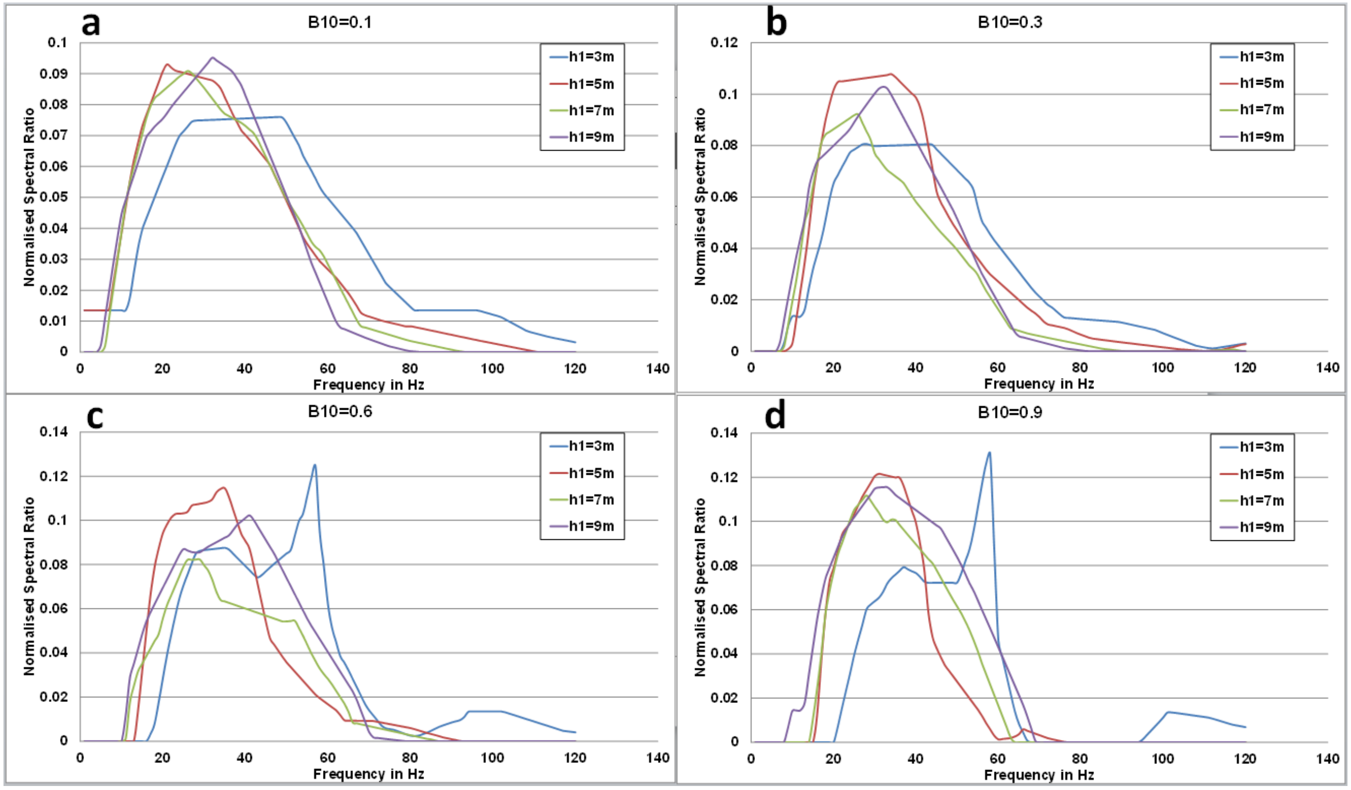

Fig. C9: Spectral representation of Vs=200m/s varying h_1 for (a) $B_{10} = 0.1$, (b) $B_{10} = 0.3$, (c) $B_{10} = 0.6$, (d) $B_{10} = 0.9$.

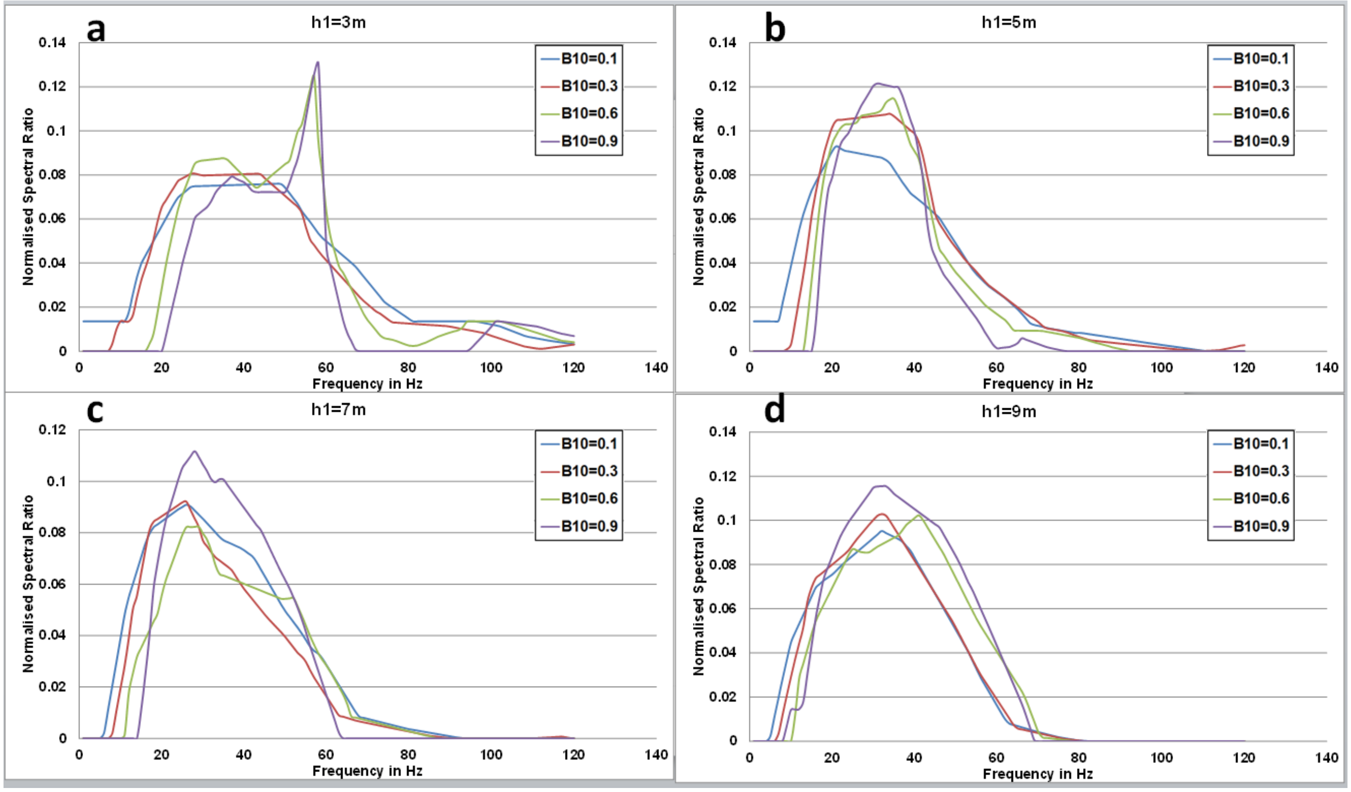

Fig. C10: Spectral representation of Vs=200m/s varying B_{10} for (a) $h_1 = 3m$, (b) $h_1 = 5m$, (c) $h_1 = 7m$, (d) $h_1 = 9m$.

C.4 V_{s3}=400m/s in the mid-field

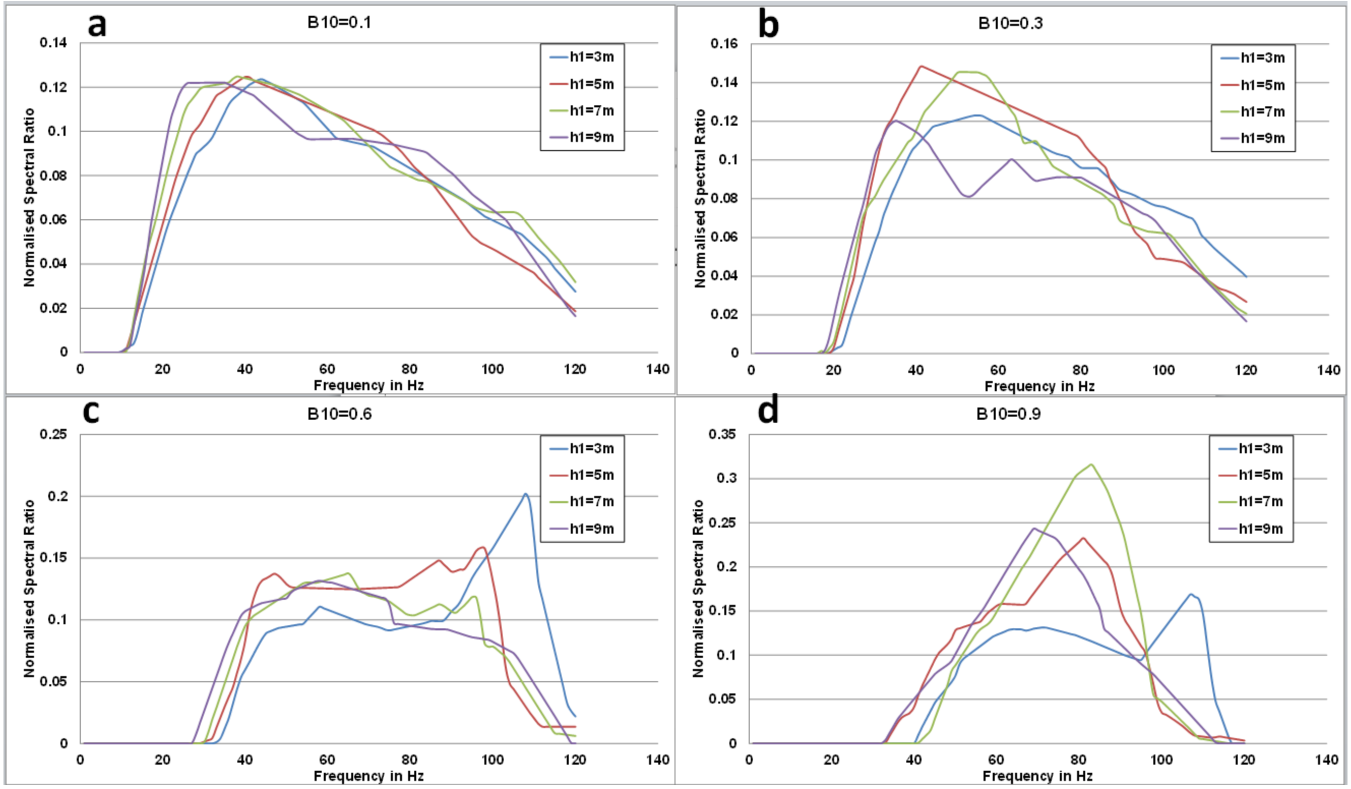

Fig. C11: Spectral representation of Vs=400m/s varying h_1 for (a) $B_{10} = 0.1$, (b) $B_{10} = 0.3$, (c) $B_{10} = 0.6$, (d) $B_{10} = 0.9$.

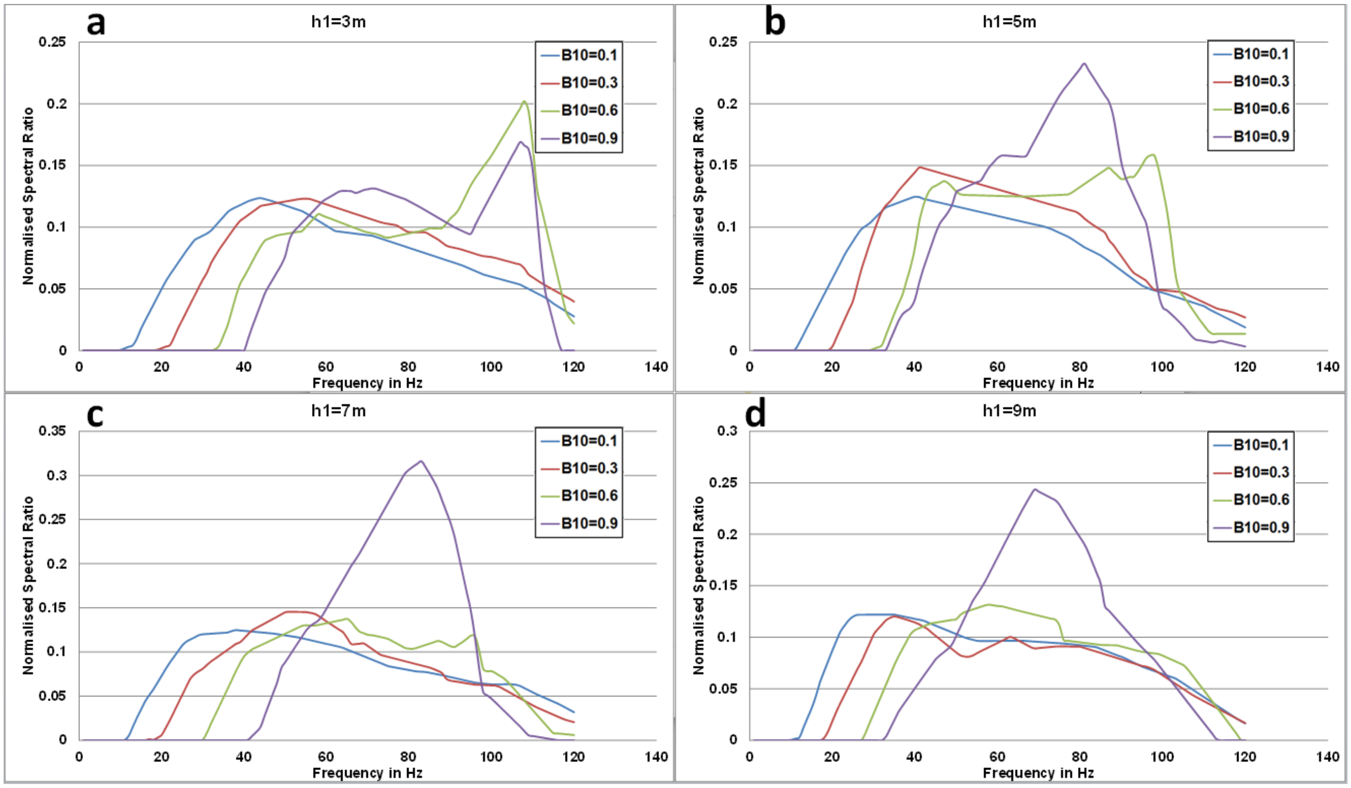

Fig. C12: Spectral representation of Vs=400m/s varying B_{10} for (a) $h_1 = 3m$, (b) $h_1 = 5m$, (c) $h_1 = 7m$, (d) $h_1 = 9m$.

C.4 V_{s3}=100m/s in the far-field

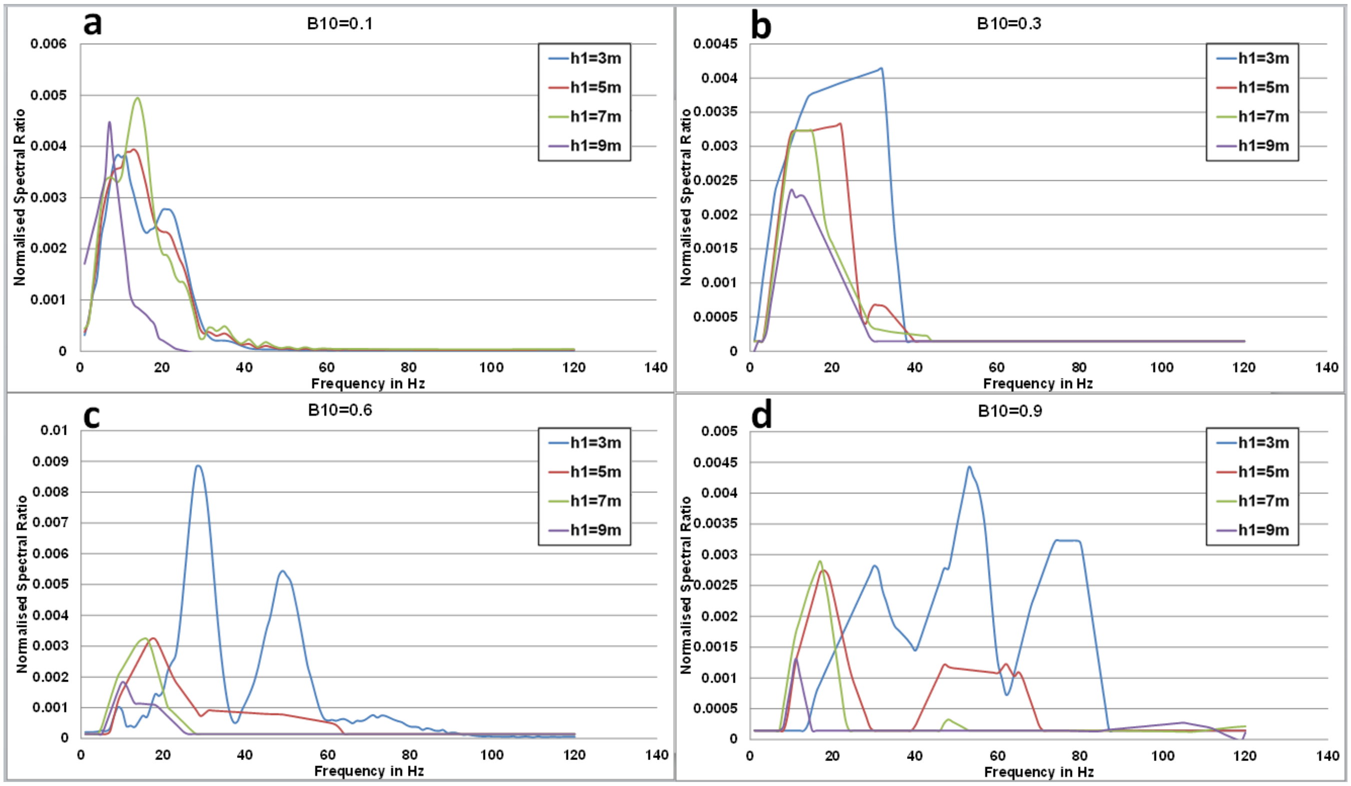

Fig. C13: Spectral representation of Vs=100m/s varying h_1 for (a) $B_{10} = 0.1$, (b) $B_{10} = 0.3$, (c) $B_{10} = 0.6$, (d) $B_{10} = 0.9$.

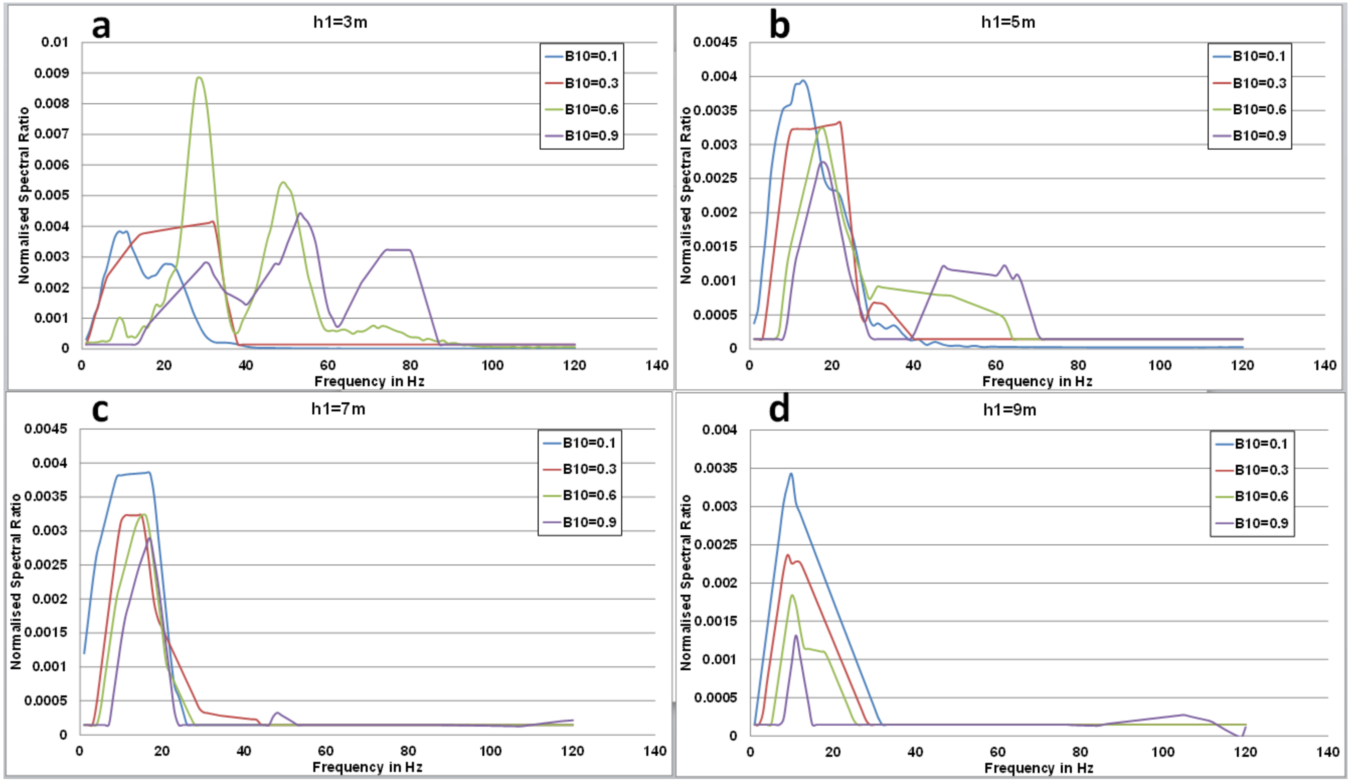

Fig. C14: Spectral representation of Vs=100m/s varying B_{10} for (a) $h_1 = 3m$, (b) $h_1 = 5m$, (c) $h_1 = 7m$, (d) $h_1 = 9m$.

C.4 V_{s3}=200m/s in the far-field

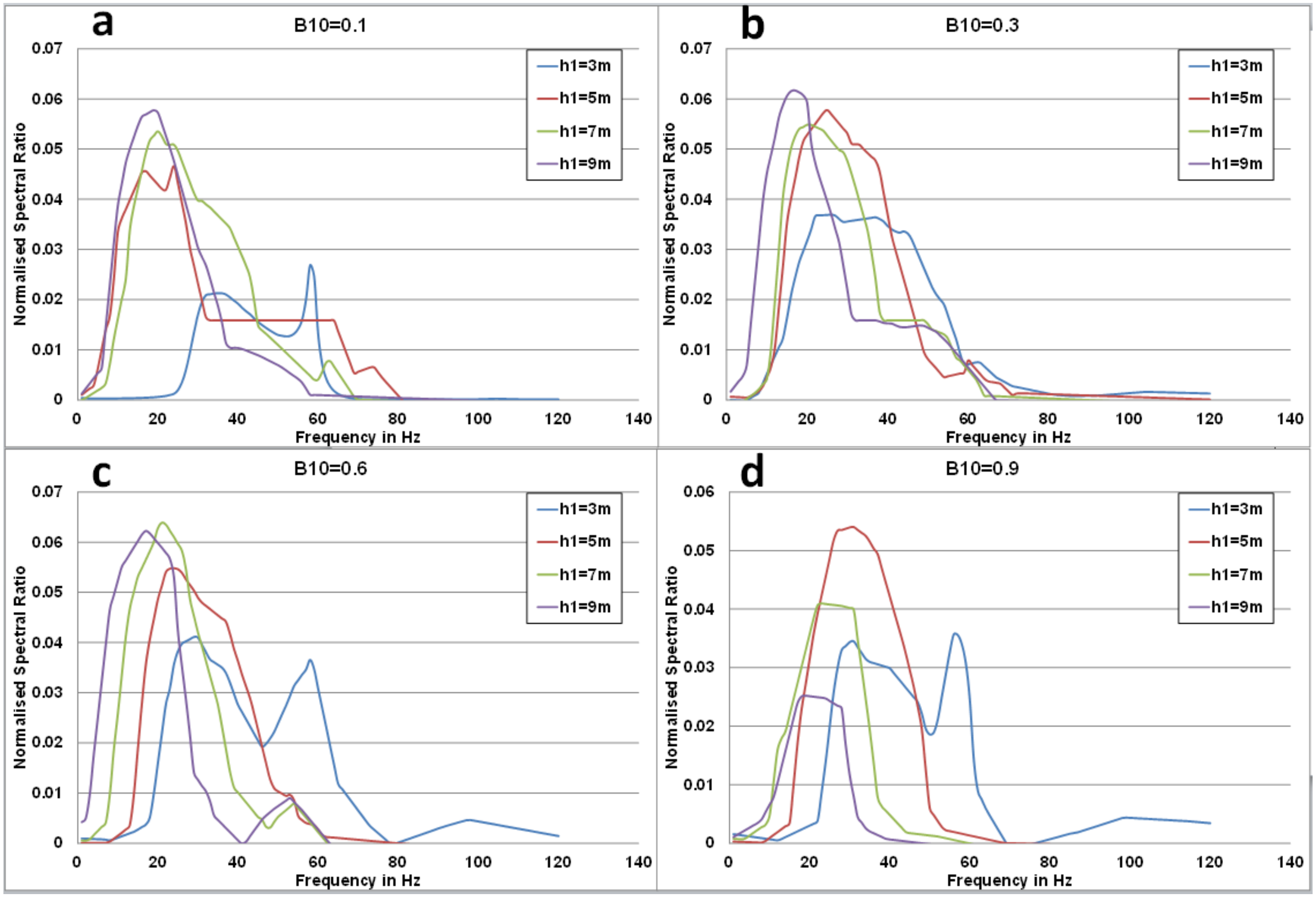

Fig. C15: Spectral representation of Vs=200m/s varying h_1 for (a) $B_{10} = 0.1$, (b) $B_{10} = 0.3$, (c) $B_{10} = 0.6$, (d) $B_{10} = 0.9$.

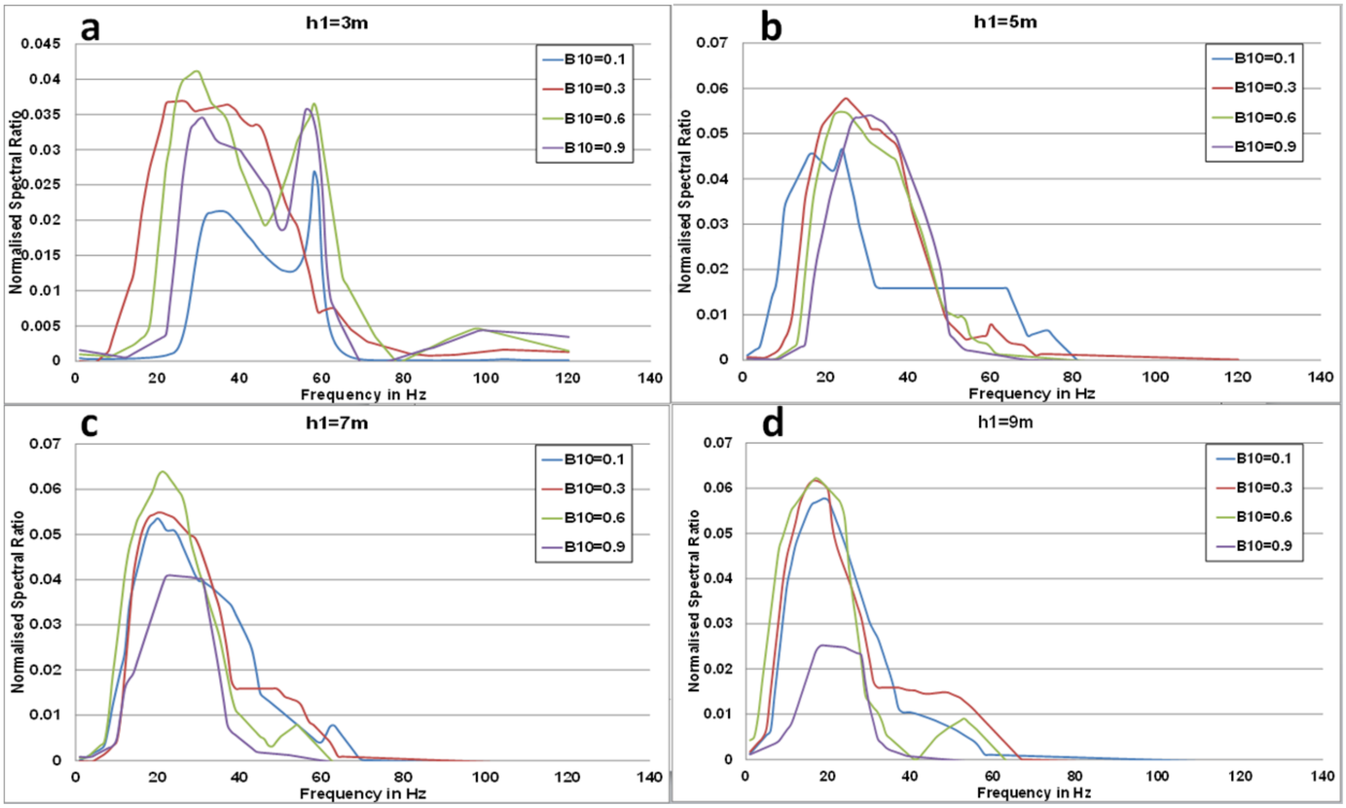

Fig. C16: Spectral representation of Vs=200m/s varying B_{10} for (a) $h_1 = 3m$, (b) $h_1 = 5m$, (c) $h_1 = 7m$, (d) $h_1 = 9m$.

C.4 V_{s3}=400m/s in the far-field

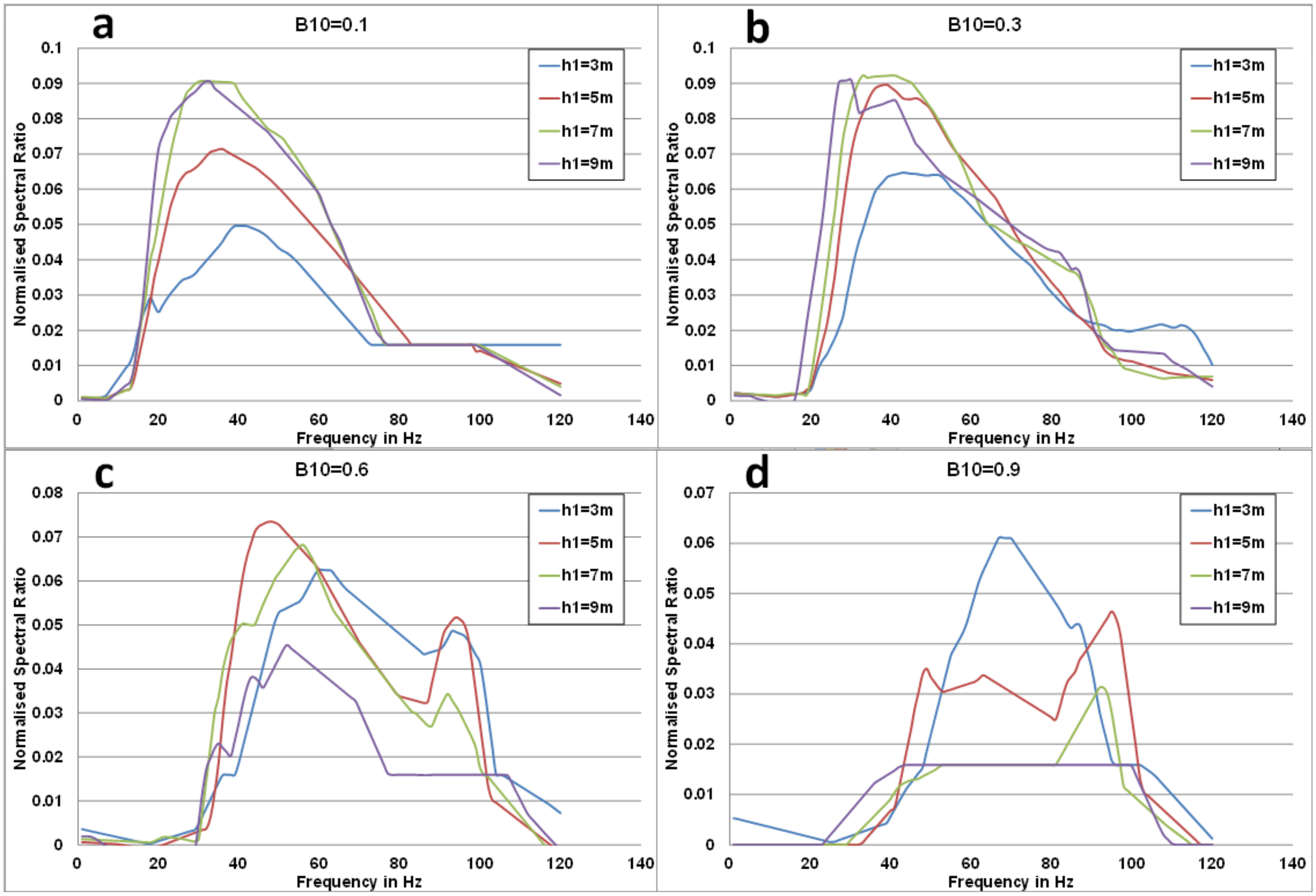

Fig. C17: Spectral representation of Vs=400m/s varying h_1 for (a) $B_{10} = 0.1$, (b) $B_{10} = 0.3$, (c) $B_{10} = 0.6$, (d) $B_{10} = 0.9$.

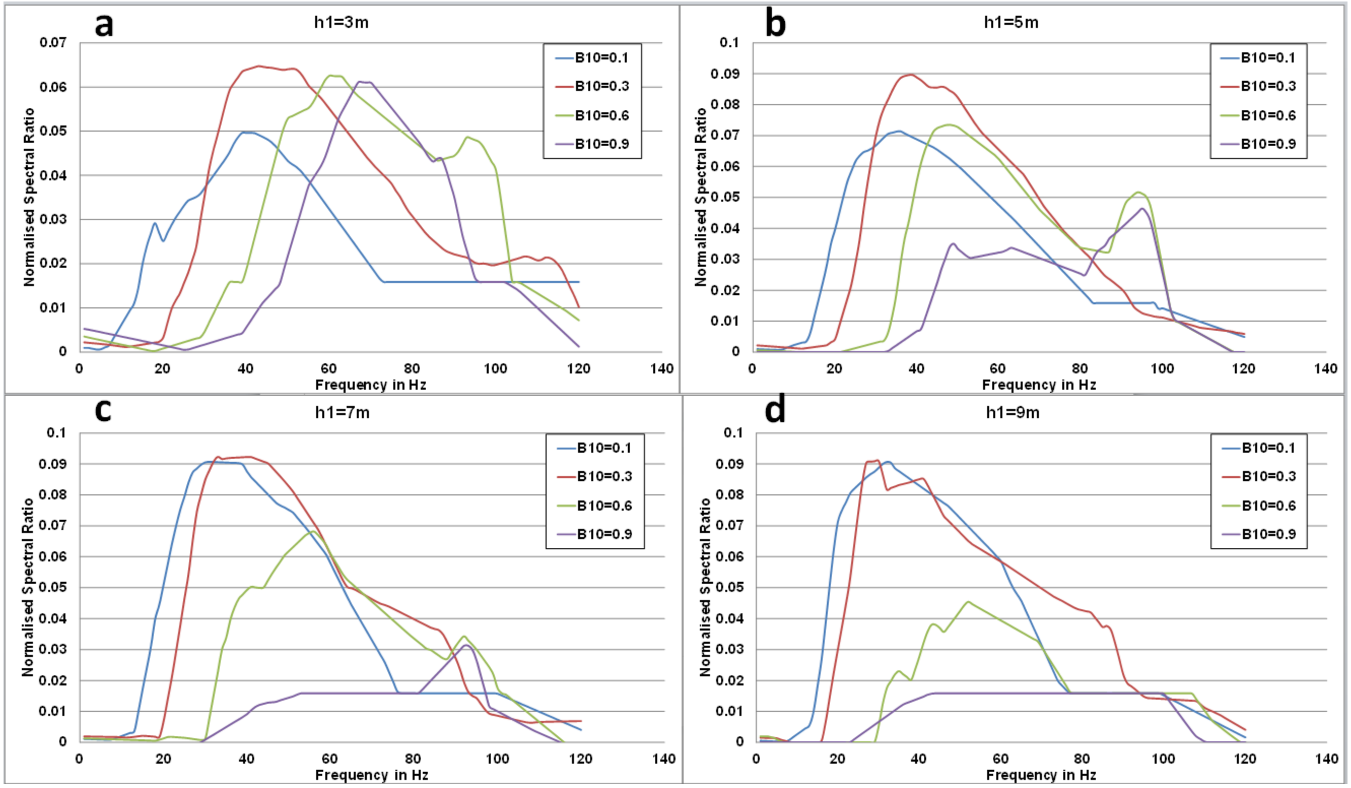

Fig. C18: Spectral representation of Vs=400m/s varying B_{10} for (a) $h_1 = 3$m, (b) $h_1 = 5$m, (c) $h_1 = 7$m, (d) $h_1 = 9$m.

Appendix D

SOURCE-SITE CLASSIFICATION CURVES USING *σ'*

The purpose of this appendix is to provide the source-site classification curves using the new definition of the spectral matching discussed in Chapter 6 Section 4.

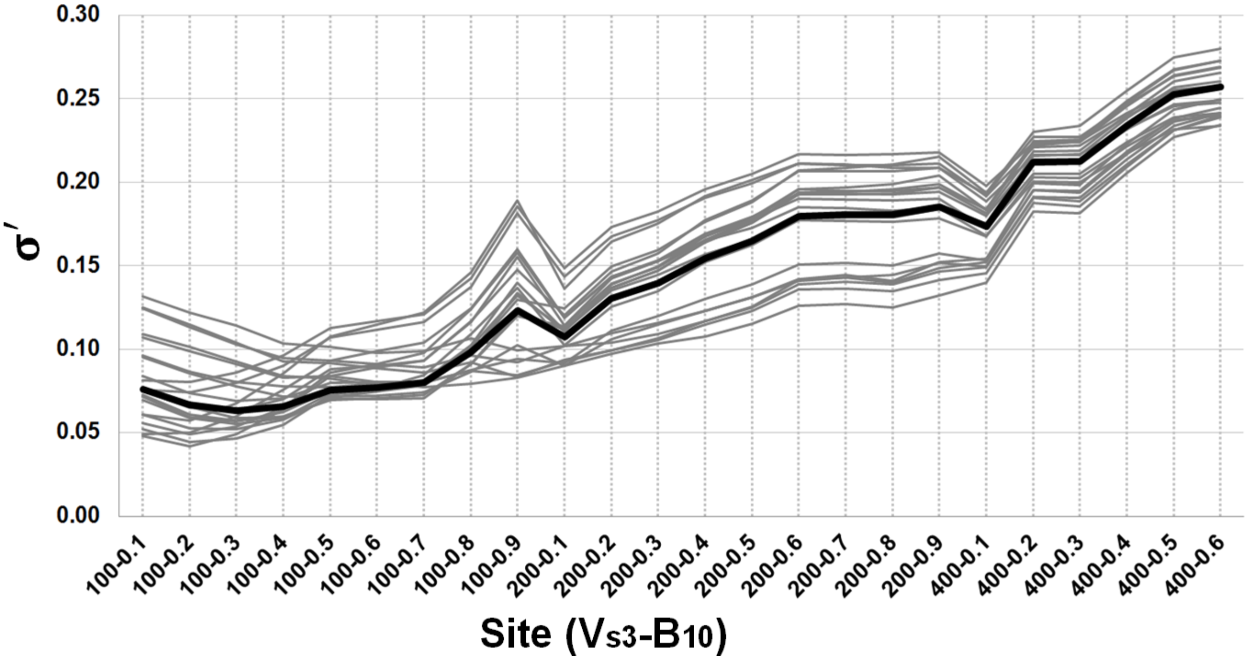

Fig. D1: Deviation σ' by site for pile driving sources- average in bold black.

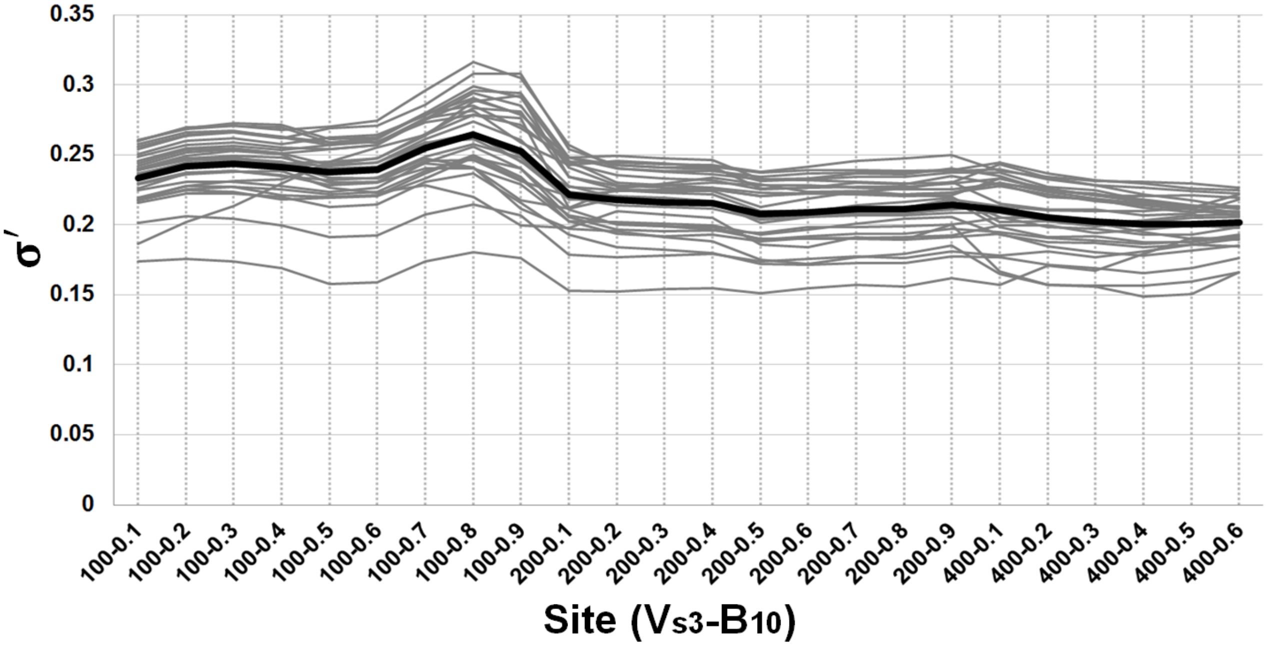

Fig. D2: Deviation σ' by site for vibro-driving sources- average in bold black.

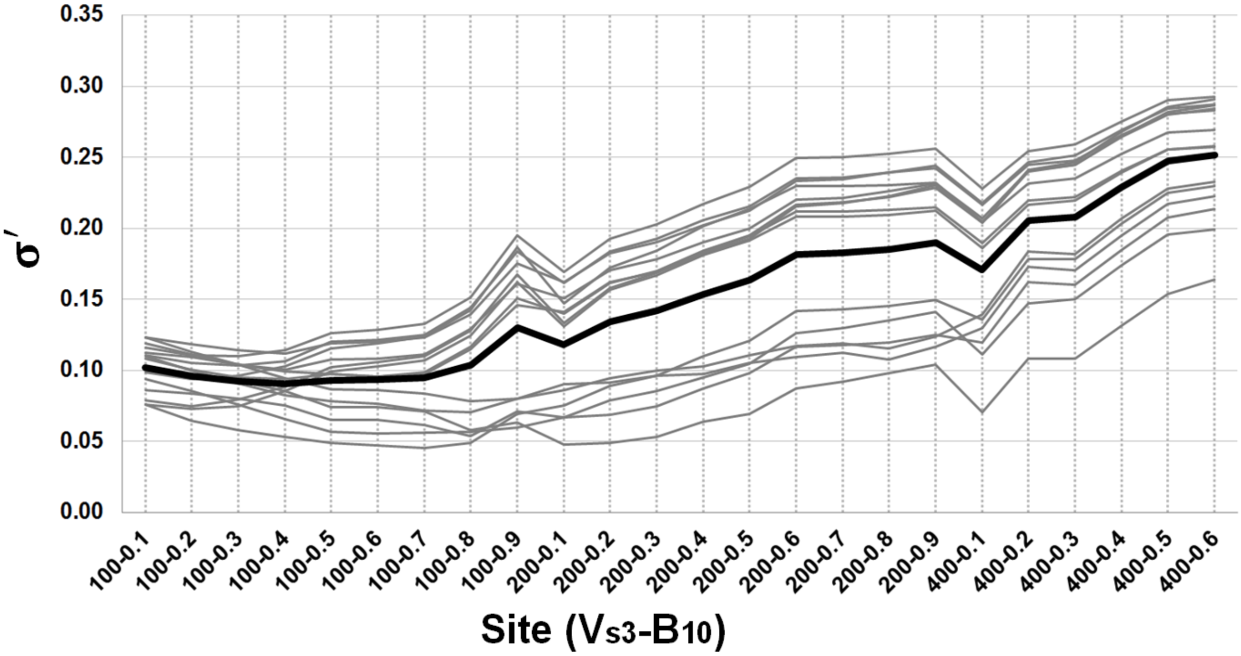

Fig. D3: Deviation σ’ by site for truck traffic sources- average in bold black.

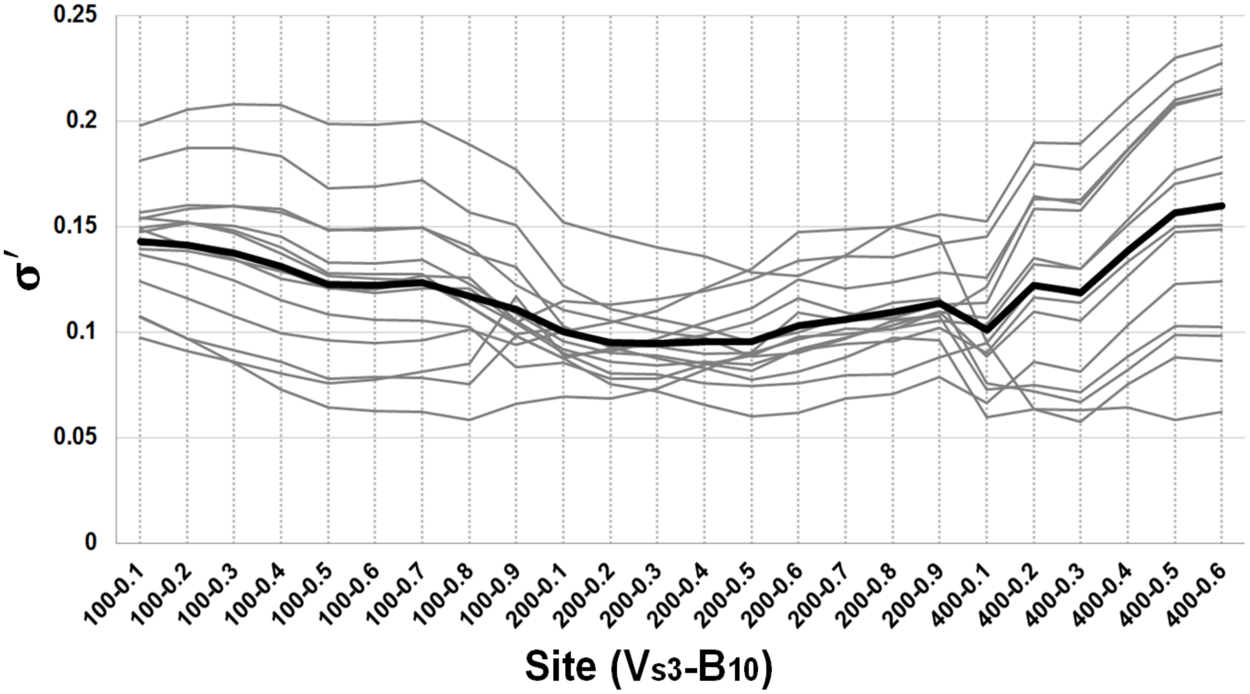

Fig. D4: Deviation σ’ by site for train traffic sources- average in bold black.